Department
of Physics

Spectroscopic analysis of structural and chemical properties of solid thin film lubricants

Dissertation

submitted in partial fulfillment of
the requirements for the degree of

Dr. rer. nat.

to the Faculty of Physics
TU Dortmund University, Germany

by

Carl Arne Thomann

born in Oldenburg

Dortmund, October 2023

Date of the oral examination: 08 December 2023

Examination board:

Prof. Dr. rer. nat. Matthias Schneider, *chairman*
Dr. rer. nat. Jörg Debus
Prof. Dr. rer. nat. Carsten Westphal
PD Dr. rer. nat. Jörg Bünemann

Table of Contents

List of Figures

List of Tables

Abstract

There is a variety of solid thin films available to tailor surface properties for a given lubrication application; two common classes are amorphous carbons (a-C) and molybdenum disulphide (MoS_2). Upon tribological loading in a given working condition, especially at elevated temperatures or in humidity, chemical transitions and structural processes are known to take place in a-C and MoS_2 thin films and to critically limit their performance. To accommodate those restrictions and to suit thin film properties for a specific application, a selection of element-modifications are applied on a regular basis. Their impact on structure and chemistry are commonly studied by different spectroscopic methods in publications. General aim is to analyse structural and chemical properties in a-C and MoS_2 thin films and property changes with respect to chemical modification via Raman microscopy. The setup shall allow for spatially-resolved studies on wear debris and for investigation on structural and chemical transitions, which occur as consequence of over-boarding tribological loading or excessive temperatures.

The understanding of those transitions is a prerequisite for the scientific conception around tribo-film formation, which is identified as critical part of the tribological system and as tribological benefit. For this, Raman microscopy provides a realm for possible measurands with respect to structure and chemistry. It is augmented by an additional setup for optical temperature tuning via a nanosecond pulsed laser and a calibrated pyrometer for local temperature measurements. This work summarises the Raman-accessible film properties and the changes after element-modification and thermal impact. For a-C, the following properties are (indirectly) measurable: internal stress, sp^3 content, silicon content, and degree of graphitisation. In contrast, some core properties like hardness, adhesion behaviour, and film thickness remain inaccessible. In studies of optical temperature tuning in a-C, two ordering mechanisms are found, which are affected by element-modification. As initial reaction upon heating, graphitic clusters within an amorphous matrix increase in number and, subsequently, in size upon further heating. This allows for a spectra-based definition of onset temperatures for solid-to-solid transition from a-C to defected nano-crystalline graphite. A Five Stage-model of structural relaxation in a-C is proposed. For MoS_2, it is found that the formation of tribo-films is strongly dependent on the working environment, the tribo-film gains temperature resistance over untouched thin film material, and tribo-film formation is affected by element-modification. In studies of optical temperature tuning in MoS_2, an initial ordering process of amorphous MoS_2 and subsequent chemical reaction to distinct oxides of molybdenum were detected. The occurrence of such oxides with deviating hardness values in an otherwise intact MoS_2 thin film hints at a possible structure- and chemistry-based wear mechanism. A Five Phase-model upon heating in MoS_2 is proposed.

The results are useful for identification of defect mechanisms and possibly for gauging the status of wear in a-C and MoS_2 thin films. Element-modification in a-C with previously unknown effects may now be interpreted within a found Five Stage-model; similarly, the behaviour of MoS_2 spectra upon heating can now be evaluated.

Chapter 1

Introduction and Motivation

Brief history in tribology: past, present, and future

Tribology (greek: τρίβω, tribo, "I rub") is a modern branch of science and engineering revolving around lubrication, friction and traction, and wear. Friction and wear, of course, are an inescapable hindrance to all practical intentions, the usage of (mostly) animal fats and oils for remedying lubrication is archaeologically secured throughout history of mankind [1], and even its hominid ancestry used primitive lubrication [2][3, p. 791].

First verified scientific efforts in quantitative studies on friction were conducted by Leonardo da Vinci by the end of the 15th century, in which the fundamental aspects of friction laws were found before being enunciated by Guillaume Amontons by the end of the 17th century. [4] Charles Coulomb investigated the main influences on friction in the 18th century, which includes the previous efforts in parts and recognises an ageing or environmental component. [3, p. 793] His findings are now commonly known as Coulomb friction. In those times, intricate details on contact mechanics were inaccessible. First studies on those started in 1882, when a model of elastic contact was proposed by Heinrich Hertz, who was studying the effect of compressive stacking on the compound optical properties of glass lenses. [5] His model disregards surface energies like adhesion, which are taken into account by its modern successors for adhesive surfaces, e.g. the Johnson-Kendall-Roberts (JKR) theory [6] or Derjaguin-Muller-Toporov (DMT) theory [7], both in 1970s. Still, the hertzian contact is a convenient explanation of natural surface in a simplified manner: rough surfaces are pictured as flat with miniscule asperities interacting and interlocking with one another, all of which are at their basis hertzian contacts. [8, 9] Wear, on the other side, was studied in an observation-based manner in the past. Early scientific studies on coin wear were on commission of the UK mint by the end of the 18th century: Charles Hatchett and Henry Cavendish could not find a way to hinder wear in coins, but stated observations on the quality of wear, which depend on the material pairing. [10] Early quantitative approaches were made by John Frederick Archard proposing the proportionality of wear debris volume to applied work in 1950s [11], which is fundamentally based on the energy dissipative hypothesis by Karl Theodore Reye in 1860 [12] and on the asperity model.

The term *tribology*, however, was coined at first in 1960s in a report of Peter Jost, who is regarded the founding father of the modern discipline. The report estimates the cost of friction, wear, and corrosion to the economy of the UK. In the last decades, modern tribology science aims for intrinsic and structural-based reduction in friction and wear, like superlubricity or the usage of mechanical vibrations [13]; key objective in nano-tribology is connecting the underlying effects from nano-sphere to observable macroscopic phenomena.

Solid thin film lubricants: prospects and challenges

Lubrication is often oil- or grease-based. Such fluid lubrication is vastly successful, but poses a point-of-failure in highly critical machine parts and requires scheduled maintenance. When such fluid lubricants are no option, a modern approach to intrinsic lubrication are fluid-free thin film lubricants. This work focusses on two classes of such thin films, namely amorphous carbons and molybdenum disulphide.

Amorphous carbons (a-C) are comparatively novel materials, which gained scientific and economic interest in the last decades for their manifold and outstanding properties for various aspects, but first and foremost for their **exceptional tribological performance**. [14, 15] Easy manufacturing and the degree of adaptability for application-specific properties made amorphous carbons a well-courted solid thin film of interest, its intrinsic friction and wear is valued in sectors like automotive industry, aeronautics, and biomedical applications. **Molybdenum disulphide ($\mathbf{MoS_2}$)** is a representative of transition metal dichalcogenides (TMDC), a relatively old material group whose structure was well-studied through the last century. [16, p. ix] In modern engine oils, which feature a highly-engineered mixture of compounds beside their base (oil), MoS_2 and related TMDC were historically used for prolonged friction reduction even when the primary oil circulatory system is diminished. MoS_2 is applied as-is or as precursor compound leading to (mostly) **$\mathbf{MoS_2}$ *tribo-films*** upon usage, which drastically reduce friction and prevent wear.[17, 18, 19] The formation of such tribo-films is the key benefit in both conventional MoS_2 powders and MoS_2 thin films.

Both thin film classes have considerable shortcomings, which critically limit their application. Thin films of a-C are critically limited by thermally-induced phase transitions, which occur in most carbon allotropes and organic compounds. [20, 21, 22, 23] Thermal limit is estimated to roughly 400 °C, upon which structural phase transitions take place. [24, 25, 26] In most recent research, these phase transitions are studied in self-forming carbonaceous materials upon heating [27, 28]; likewise, numerous related effects and phenomena were described in earlier studies. For MoS_2, thin films are additionally chemically sensitive to the working environment, especially its humidity and oxidation potential. Element-modification expands the realm of thin film properties of both a-C and MoS_2. Such modification is done to tailor properties for a specific application, like silver in a-C:Ag for bio-compatibility or nitrogen in MoS_2:N for an amorphous structures. Most importantly, however, element-modification may help counteracting the shortcomings of a-C and MoS_2 thin films.

Objective of this work

General aim is to analyse the **structural and chemical properties** in a-C and MoS_2 thin films and property changes with respect to chemical modification via a Raman microscopy setup. The setup allows for spatially-resolved studies on occurring wear debris and for investigation on **thermally-induced** structural and chemical **transitions**; both are dependent on **tribological loading** or **contact temperatures**. Gaining understanding of those transitions is a key requisite for the scientific conception around tribo-film formation, which is still object of research: until now, the structural mechanisms within an a-C thin film for lubrication purposes were not examined in a full range of temperatures or with element modification. In MoS_2, the full mechanism of tribo-film formation is still unclear as it is occurring *in situ* and being mostly inaccessible. [29, 30]

For such measurement tasks in structure and chemistry, **Raman microscopy at micrometer** scale provides a realm for possible measurands. It is augmented by an **additional setup for local temperature tuning** via a nanosecond pulsed laser in a pump&probe-style and by a calibrated pyrometer for local temperature measurements.

Structure of this work

The sub-structure of the upcoming chapters are presented in their introduction paragraph, all sections may be read independently.

Chapters 2 and **3** provide an overview of the required theoretical understanding of the topic and of the involved methodology.
Chapter 4 demonstrates the exclusive usage of Raman spectroscopy in structural and chemical analysis of pure and chemically-modified thin films in their as-deposited situation. Additionally, wear- and stress-related defected thin films (after ball-on-disk tribometry and adhesion test) are exemplarily investigated.
Chapter 5 motivates Raman spectroscopy analysis in combination with optical temperature tuning via a nanosecond pulsed laser, which gauges the thin film's reaction towards thermal energy in combination to element-modification.
Chapter 6 summarises the findings and suggests possible further studies.

Chapter 2

Theoretical background

This chapter presents a basic understanding for the theoretical background, spanning multiple disciplines: physics, chemistry, and mechanical engineering. For sake of clarity, it is grouped in sections on materials 2.1, on methodology 2.2, and on tribology 2.3. The upcoming sections do not follow a hierarchy and can be read independently.

2.1 Foundation of material science: crystalline structure, vibrational dynamics, chemical and phase transitions

Fundamental structures of solids (crystals) with both long-range and short range-order are modelled as (direct) lattice, vibrations in this lattice rudimentarily constitute its dynamics. The type of bonding between lattice points strongly influences the macroscopically perceived properties of materials: Figure 2.1 coarsely summarises the bonding type (corners) and the typical material classes (vertices). The two material classes in this thesis are mostly covalently bonded, in-depth coverage of bonding type is not crucial for the scope of this work.

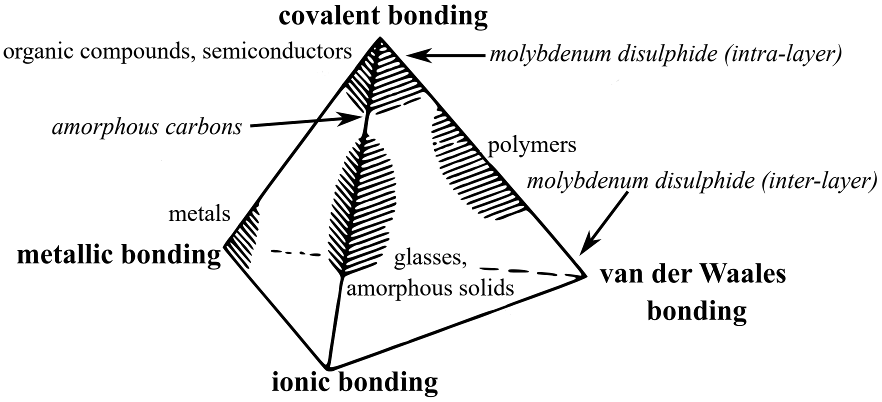

Figure 2.1: Bonding types and typical material classes. Adapted from textbook [31].

An introduction to lattices and vibrational dynamics can be found in literature of solid state physics. [32, 33, 34] The two material classes in this thesis are amorphous carbon (a-C) and sputtered molybdenum disulphide (MoS_2) thin films, both are industrially used for fluid-free lubrication. Further information on their chemistry and phase transitions are found in standard references [16, 35, 36, 37] and textbooks [38].

2.1.1 Fundamental structure of crystals and basic dynamics

Crystals are characterised by a long range-ordered structural fundament, its **lattice**. In short, the lattice is fully accessible by a linear combination $\vec{G}$ of base vectors $\vec{x}_i$. At each lattice point, a **basis** of atoms, molecules, or ions is added. For basis with j atoms (or molecules or ions) at the lattice point, the j parts are taken into account with coordinates A_i of the basis $\vec{g}_j = \sum_{ij} A_{ij}\vec{x}_i, A_{i1} = 0, A_{i,j\neq 1} \in]0,1[$. The combination of lattice and basis forms the rigid crystal. [33]

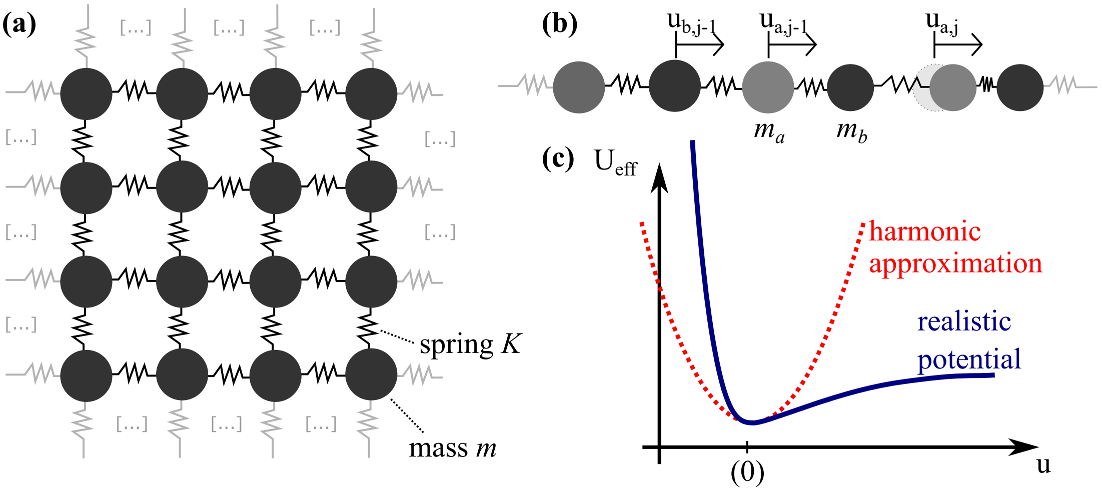

Figure 2.2: Ball and spring-model for crystal dynamics in **(a)** a two-dimensional quadratic lattice and in **(b)** a one-dimensional chain with alternating masses, **(c)** For small deviations from their equilibrium position, the bonding potential in solids is approximated as harmonic.

The ***ball and spring* model** is a simple model for crystal dynamics. Bonding between basis element is described as harmonic potential, only, which is sufficient for the scope of this thesis. Figure 2.2(a) gives an example for this model: a two-dimensional quadratic lattice with monatomic basis ($j = 1$, mass m) and with generalised spring constant K, in which the atomic displacement from their inscribed equilibrium is u. The springs K denote an effective potential U_{eff}, which is dependent on the actual position $\vec{R}$ of an element in the lattice of N elements. In more detail, the actual position $\vec{R}$ is comprised of the equilibrium position of lattice elements $\vec{G} + \vec{g}_j$ and their individual displacement $\vec{u}_{\vec{G},\vec{g}_j}$, giving in total $\vec{R} \equiv \vec{G} + \vec{g}_j + \vec{u}_{\vec{G},\vec{g}_j}$. The Hamiltonian $\hat{\mathcal{H}}$ of the solid is the sum of all contributions with counting index $\{l\} = \vec{G}, \vec{g}_j$

$$\hat{\mathcal{H}} = \sum_{\{l\}} \frac{p^2_{\{l\}}}{2m_{\{l\}}} + U_{\text{eff}}(\vec{R}_{\{l\}}). \tag{2.1}$$

Applying the approximation of small displacements u, the effective potential $U_{\text{eff}}(\vec{R}_{\{l\}})$ is then expanded as

$$U_{\text{eff}}\left(\vec{R}_{\{l\}}\right) = U(\vec{G}+\vec{g}_j) \tag{2.2a}$$

$$+\sum_{\{l\}} \partial_u U(\vec{G}+\vec{g}_j)\cdot \vec{u}_{\{l\}} \tag{2.2b}$$

$$+\frac{1}{2}\sum_{\{l\}\{l'\}} \partial^2_{u,u'} U(\vec{G}+\vec{g}_j)\cdot \vec{u}_{\{l\}}\vec{u'}_{\{l'\}} + O(u^3) \tag{2.2c}$$

The equilibrium condition $u = 0$ yields by definition the minimum potential U_{eff}, which leads to vanishing contributions in term (2.2b). Cutting higher contributions $O(u^3)$ in term (2.2c) then yields the harmonic approximation, in which the second derivates $\partial^2 U(\vec{G}+\vec{g}_j)$ in term (2.2c) span the dynamical matrix. Eigenvalues of the dynamical matrix are the fundamental frequencies of motion. [33, pp. 41 sqq.]

A more vivid example of these fundamental frequencies is now given for molecules[1], see Figure 2.3(a). A molecule shall have three degrees of freedom for each compound, bonds and molecule geometry act as constrains. For the given linear molecules of carbon dioxide $CO_2(N = 3)$ and hydrogen $H_2(N = 2)$, $3N - 5$ normal modes are expected, so 4 and 1, respectively. While all vibrational motion in molecules can be described as superposition of the fundamental modes, the situation is more complex in solids, note that N is the size of Avogadro's number. Before demonstrating an example [32, pp. 108–112], the effect of a polyatomic basis ($j > 1$) has to be considered. The basis elements j are not necessarily static with respect to each other, but have the additional freedom to move in-phase or

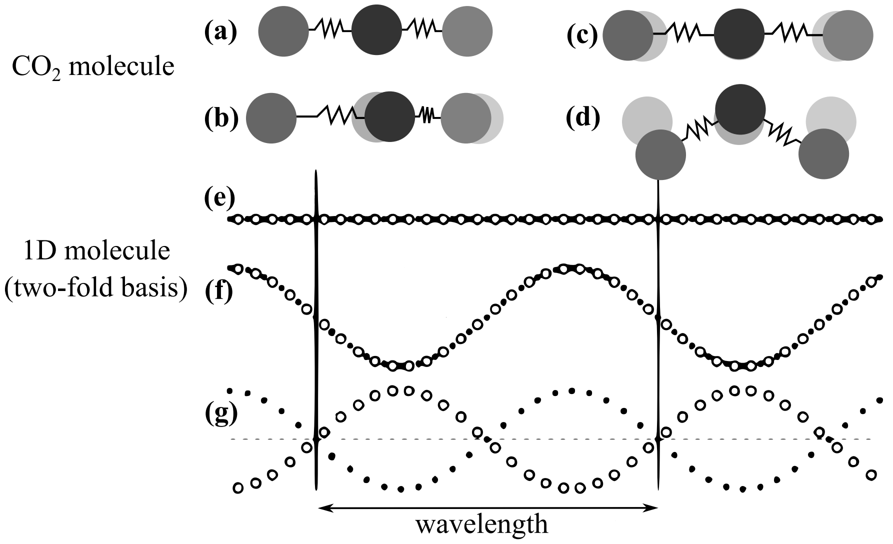

Figure 2.3: Examples of vibrational modes: **(a)** carbon dioxide CO_2 molecule at rest with its vibrational modes **(b)-(d)** and **(e)** a molecular chain with two-fold basis at rest with an **(f)** acoustical and **(g)** optical vibration. Adapted from publication [39].

---

[1] Visit interactivephonon.materialscloud.io for animations of lattice dynamics in solids

out-of-phase, see Figure 2.3(f-g). These are historically regarded as **acoustic** and **optical modes** as discussed in section 2.2.2 on the Raman effect.

Consider an one-dimensional solid with alternating masses m_a, m_b and a common spring constant K, as depicted in Figure 2.2(e). With standard assumptions and conventions (lattice constant a, i the square root of -1) and the ansatz of a travelling wave of displacement in form $u_{\mathrm{a/b};j}(k,\omega) = u \exp(ijka)\exp(-i\omega t)$, one finds the two equations of motions for the displacements u_a and u_b, which has a unique solution when the determinant of its coefficient matrix

$$\underbrace{\begin{pmatrix} 2K - m_\mathrm{a}\omega^2 & -K(1+\exp(-ika)) \\ -K(1+\exp(ika)) & 2K - m_\mathrm{b}\omega^2 \end{pmatrix}}_{\text{coefficient matrix, related to the dynamical matrix}} \begin{pmatrix} u_\mathrm{a} \\ u_\mathrm{b} \end{pmatrix} = \vec{0} \tag{2.3}$$

vanishes. This gives the dispersion relation

$$\omega^2 = \frac{K}{m_\mathrm{red}} \pm \sqrt{\frac{K^2}{m_\mathrm{red}^2} - \frac{4K^2}{m_\mathrm{a} m_\mathrm{b}} \sin^2\left(\frac{ka}{2}\right)}, \qquad m_\mathrm{red} = \frac{m_\mathrm{a} \cdot m_\mathrm{b}}{m_\mathrm{a} + m_\mathrm{b}}, \tag{2.4}$$

which is plotted in Figure 2.4. It describes the travelling wave of displacement through the crystal and links the periodicity of the time component $\omega = {}^{2\pi}/T$ with the periodicity of the space component $k = {}^{2\pi}/\lambda$. The two edge cases of long travelling wave with $k \approx 0$ and the shortest $k = {}^{\pi}/a$ (alternating bases are exactly out of phase) are also imprinted. The two solutions of equation (2.4) directly translates to acoustic and optical phonons. This example would yield very similar results for an universal mass m with different spring constant k_i. In general, one expects $3j$ modes with 3 modes being **acoustical** (A) and the remaining **optical** (O).

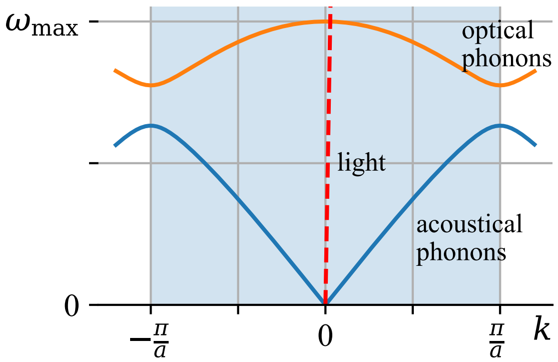

Figure 2.4: Dispersion relation of a simple solid with two-fold basis, see Figure 2.2(b), yielding an **optical** (orange branch) and **acoustical phonon band** (blue branch), shaded region denotes the first Brillouin zone. For comparison, the red dotted line describes the dispersion relation of light.

Another classification of vibrations regards the orientation of motion with respect to the propagation direction $\vec{k}$, **longitudinal** (L) and **transversal**, **in-plane** (T) or **out-of-plane** (Z). The types of modes, but not the frequency, are largely determined by the lattice alone. Exploiting its symmetry, the depiction of lattices in reciprocal space will become handy.

There, the set of possible vibrational modes are unique within $k = 0$ and $k = \pi/a$, which is called the first **Brillouin zone** for the exemplary one-dimensional solid with lattice constant a. The reciprocal lattice and the vibrational dispersion relation of a solid are commonly measured by scattering spectroscopy, e.g. neutron scattering.

2.1.2 Considerations of defected or amorphous solids

The section above describes a solid without any irregularity, perfect ordering and no boundary conditions, i.e. a single crystal. Real solids are bounded by their interfaces and surfaces and contain a considerable amount of defects in their structure. Such errors may have a considerable *positive* impact on the macroscopic properties of the solid, although being negatively connoted. As example, a misaligned crossover from three layers to two allows for dynamic shearing of the structures in the nano-sphere and bending flexibility in the macro-sphere. The defects are free to travel and may be seen as mediators of mechanical load, for example in bending or straining. In contrast, a perfect crystalline solid would be surprisingly hard and brittle. A variety of defect types and disorder are known and studied, but only a selection becomes important in the scope of this work. They are nominally introduced for both material classes in sections 2.1.3 and 2.1.4.

Highly defected solid can still be modelled as accumulation of smaller crystallites (domains) with defects or boundary surfaces in between. Size, shape and orientation of those ordered domains may be comparable to each other. These solid structures are called micro- or nano-crystalline, depending on the size of the ordered domains. [34] In the edge case of extremely high defect density, however, a solid is called amorphous (greek ἄμορφος, amorphos, “without shape” or “without form”) and can no longer be treated as nano-crystalline. First and foremost, amorphous structures lack long range-order of their lattice. This lack also overturns the definition of lattice defects, so a new definition is needed and introduced later. In close vicinity of the constituents of an amorphous structure, bonds to other species may be constituted similarly to the situation in a fully ordered crystal of the same material. The major differences are variations in bonding length a and angle ϕ, which ultimately result in variation of bonding strength. This, characteristically, leads to internal stress. [40] As important note, an amorphous structure must not be termed simply as unstructured or (completely) disordered, because, on the one hand, a short range-order is still present, meaning that the environment of the constitutional element is comparable to its neighbour. On the other hand, local ordered clusters may be embedded in the system. The differentiation between amorphous and nano-crystalline solids is mainly attributed to the density of the ordered domains. [34] The prototypical class of amorphous materials are glasses, which in Figure 2.1 are in the vertex between covalent and ionic bonding. It lacks structural “imperfections” as predetermined breaking point for mediating mechanical load, for example, architectural glass is, in fact, hard and brittle just as stated above.

Defected structures are often still measurable by methods requiring crystal symmetry and characterisable by key parameters of crystals. For example, a defected crystal may still yield X-ray or neutron scattering signatures comparable to a pristine reference sample, although aforementioned methods rely on the crystal symmetry. Other experiments fail if they require a long range-order like X-ray scattering yielding no Bragg peaks. The vibrational modes also face significant impact, see subsection 2.2.3 on Raman spectra of amorphous solids for details.

2.1.3 Carbon and carbon allotropes, amorphous carbons (a-C)

Different structures of same elements are called **allotropes**; lattice basis and bonds do not necessarily define the lattice structure uniquely. As a prime example, there are a few bonding types in carbon, but a realm of various structures. Carbon has four (valence) electrons in their outer shell in the configuration [He] $2s^2 2p^2$. Both the $2s$ orbital and a certain number x of $2p$ orbitals often combine to sp^x hybridised orbitals, which are characterised by the number $x \in \{1, 2, 3\}$ of participating p orbitals, see Figure 2.5. Two highly ordered allotropes of carbon are **diamond** (sp^3, cubic crystal system) and **graphite** (sp^2, hexagonal crystal system), which are representative for their hybridisation.

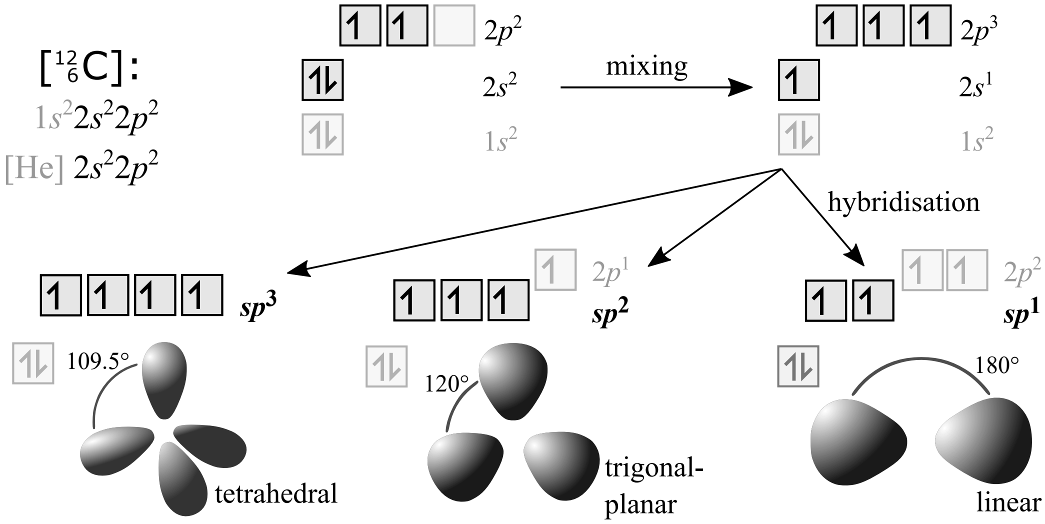

Figure 2.5: Overview on hybridisation of electronic states of carbon. The electronic configuration [He] $2s^2 2p^2$ is first mixed to [He] $2s^1 2p^3$, before the orbital $2s$ and a number of $2p$ orbitals energetically assimilate (hybridisation). The geometry of sp^x orbitals with $x \in \{1, 2, 3\}$ also determines the geometry of bonding, i.e. linear, trigonal-planar, or tetrahedral, respectively.

Graphite, strictly speaking, is defined as a structure of parallel aligned, long-reaching layers of hexagonally arranged, planar sixfold-rings of sp^2 carbons (IUPAC recommendations [36]). Materials with regions (domains) of graphite are differentiated as *graphitic materials*, when the perfect graphitic lattice structure overall is missing.[2] Besides those allotropes, under extreme conditions, liquid carbons or carbon vapours are possible [41]. A stable phase is found using the **Gibbs free energy** G, which is the lowest for the stable phase at constant temperature T and pressure p. Phase transitions lead to changes in G, which are divided into changes in enthalpy ΔH and in entropy ΔS, giving in total $\Delta G = \Delta H - T\Delta S$. The Gibbs free energy G, however, does not provide information whether a reaction is taking place. [38, pp. 287–289] In carbons, graphite is more stable than diamond, diamond is metastable. Yet, diamond structure is preserved up to roughly 1500 °C in vacuum due to kinetic barriers. [38, p. 514] The transition of diamond to graphite is enhanced by graphitic impurities or by certain metal inclusions. [42, p. 13]

---

[2] Notably, in the publication, the incorrect use of the term "graphite" for "graphitic materials" is criticised.

In recent studies [27], the structural evolution of carbon materials from their molecular precursors over defective and amorphous regimes to highly-ordered crystalline structures are discussed, as in Figure 2.6:

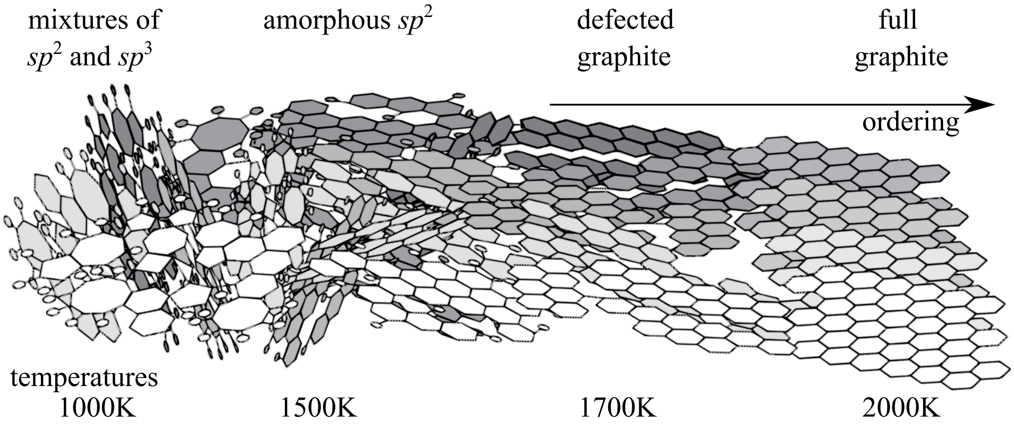

Figure 2.6: Schematic of the ordering process of graphitic carbons when formed from molecular carbonaceous precursors. **From left to right**: mixture of carbon components, which upon heating become more and more ordered. Carbons then reach an amorphous/highly defected state, further heating yields nano/micro-crystalline graphite to (full) graphite with long range-order, eventually. Modified from publication [27].

Starting from the high-temperature end with highest ordering, all carbon atoms are residing in their natural hexagonal layers closely resembling graphite. Further decreasing the lattice area will yield amorphous structures, which still are fully sp^2 hybridised.

An even more diverse system is obtained, however, when parts of the sp^2 hybridisation is replaced by sp^3 sites. The ability to form sp^3-sp^2 mixtures in amorphous solids is unique for carbon among group IV elements (e.g. carbon, silicon, germanium) [43]. Other group IV elements form completely sp^3 bonded amorphous structures like amorphous silicon (a-Si), while the maximum sp^3 content in amorphous carbons is 88%. [44]

Graphitising and non-graphitising carbons, glassy carbon

Glass made of carbon (**glassy carbon**) exists, but is only discussed as contrary and delimiting example in this thesis. In short, it features locally structured carbons in complete sp^2 hybridisation with the key property of being non-graphitising.

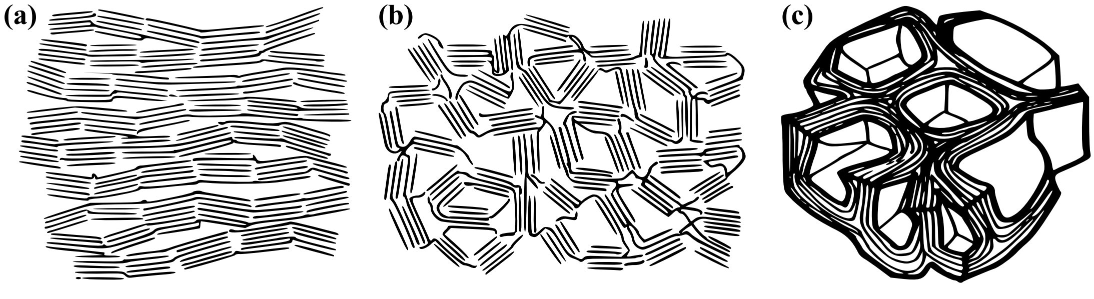

Figure 2.7: Schematic of graphitic layers in different carbon allotropes. **(a)** Graphitising carbons allow for further reorientation, while **(b)** non-graphitising carbons are sterically hindered; for example, the structure of **(c)** glassy carbon is non-graphitising. Adapted from textbook [42] and publication [45].

Graphitising carbon allotropes are characterised by their reaction upon heating or pressure: they enrich in ordered sp^2 hybridised sub-structures and/or existing ordered domains enlarge. Ideally, the final state of highest ordering and symmetry is graphite, which by IUPAC definition [36] is a perfect, long-ranging crystal. Defects are starting as reduction of coherent graphitic lattice area and loss of the graphitic nature, i.e. delocalisation of electrons in p-orbitals. The generic structure of graphitising and (non-)graphitising carbon allotropes is depicted in direct comparison in Figure 2.7 along with the structure of glassy carbon (non-graphitising).

Amorphous carbons

Amorphous carbon is a collective term for a large group of carbon allotropes for thin films. With all allotropes combined, amorphous carbons span an extreme structural variety with key properties of ceramics, metals, or polymers. [42, p. 108] Generally, they are a metastable networks with varying content of sp^2 and sp^3 hybridised carbons with short range-order and a varying degree of ordering, see Figure 2.8, plus possible chemical modifications.[24, 46, 47] The (usual) content and contribution of sp^1 hybridised bonding is rather small compared to those with sp^2 and sp^3 hybridisation, which in contrast largely determine the properties and especially the mass density [42, p. 108][48]. Another common term is **diamond-like carbons (DLC)**. It suggests that the amorphous carbon samples show comparable properties of completely sp^3 hybridised, highly ordered diamond like a high band gap E_g (electrically isolating), optical transparency, and, a high(est) stiffness and hardness [42, pp. 35, 104].

With the two exemplary carbon allotropes diamond and graphite in mind, one may expect bonding lengths a and bonding angles ϕ of amorphous carbon to be a mixture of both. In fact, however, a-C bonding characteristics show a more intricate radial and angular distribution rather than discrete values like for diamond and graphite, see Figure 2.9.

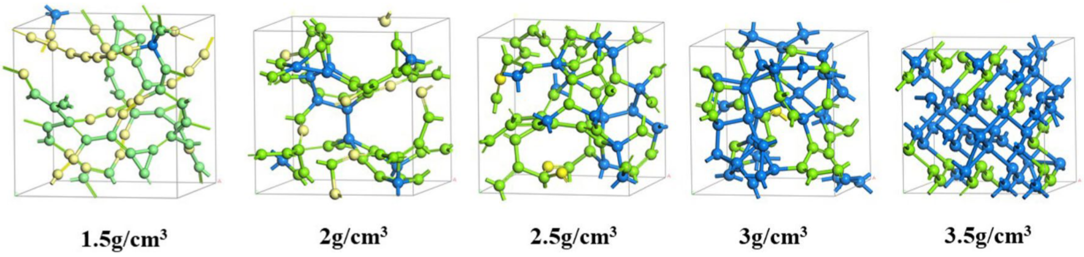

Figure 2.8: Mass density dependency of carbon hybridisation in amorphous carbon thin films. Yellow, green and blue atoms depict sp^x hybridised carbons with $x \in \{1, 2, 3\}$, respectively. Increasing the density of the thin films shifts the hybridisation balance from *sp* over sp^2 to sp^3 hybridisation. Density of this work's samples is in range (1.9-3.0) g/cm^3. Figure taken from publication [48].

Local maxima of the bonding characteristics are in between those of diamond and graphite. The global maximum in bonding length distribution suggests a closer sphere of neighbouring atoms than in diamond, which is known for its high density with respect of atomic packing. This alone gives a explanation for the considerable amount of internal stress on the network due to mismatching stable bonding characteristics. Now, one might see amorphous carbons as a a supercooled liquid state of carbon, which is also suggested in literature [42, p. 23]. In harsh contrast, this picture suggests falsely a glass-like behaviour upon heating of a-C, that is, the avoidance of crystallisation and a phase transition to a liquid. This is a core difference between glass-like carbon and amorphous carbons.

Keeping in mind, that amorphous carbons are better described as being short range-ordered over disordered, the term "defect" may then be applied to (a) partially ordered sites in an amorphous matrix and (b) within the amorphous matrix as distribution of bonding characteristics. Thereto, **topological** and **structural defects** are distinguished. Structural disorder is the deviation from graphite bonding characteristics and topological disorder is linked to a heterogeneous distribution of graphitic cluster size. [49]

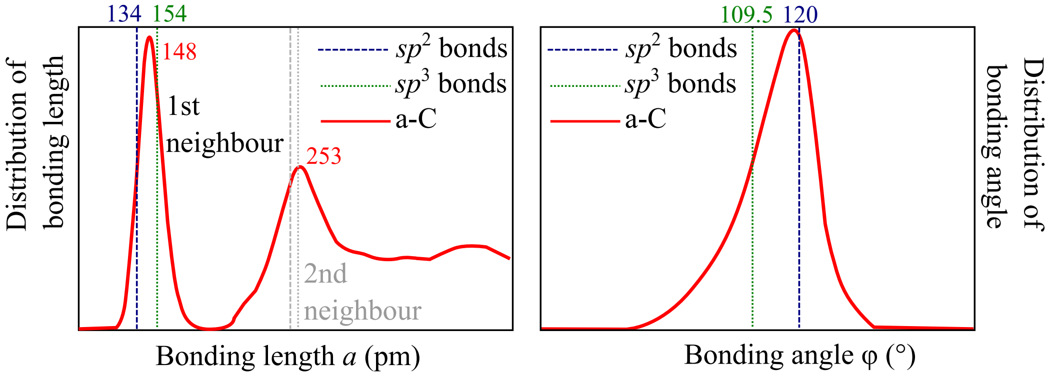

Figure 2.9: Bonding characteristics of amorphous carbons, distributions of **(a)** bonding length a and **(b)** bonding angle ϕ. For comparison, vertical lines denote the natural bonding characteristics for purely sp^2 and sp^3 hybridised carbons, e.g. ideal graphite and diamond, respectively. Adapted from publications [50, 51].

Tetrahedral and hydrogenated amorphous carbons, chemical modifications

Allotropes with high sp^3 content are called **tetrahedral amorphous carbons (ta-C)** in remembrance of the tetrahedral bond structure of carbons in diamond. Besides the ratio between sp^2 and sp^3 hybridisation, fundamental work also uses the content of hydrogen and clustering to group carbon thin films [52]. For overview, possible samples of carbons are filed in a ternary diagram (original by Jacob and Möller [47, 53], often adapted) in Figure 2.10.

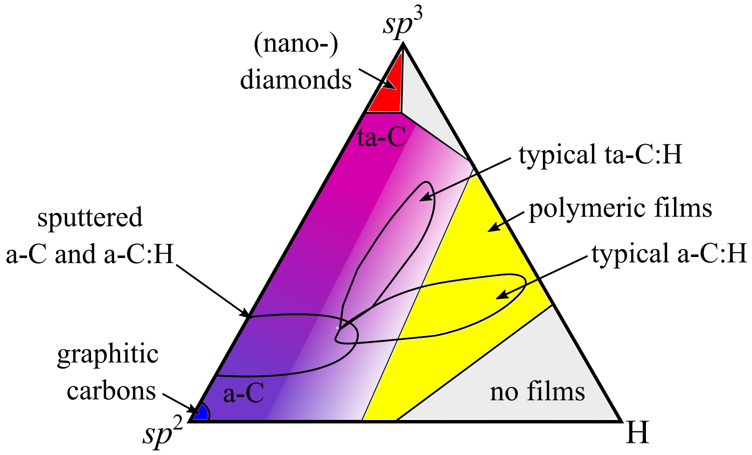

Figure 2.10: Ternary diagram of carbon thin films. Adapted from textbook [42] and publication [54].

The original encompassed hybridisation and hydrogen content [53] and was expanded to clustering or ordering dimension [47], which is often skipped for simplicity. **Hydrogenation** in amorphous carbon (**a-C:H**) shows drastically different properties depending on the hydrogen content. Lower hydrogen content, for example, preserves the dominance of sp^2 hybridisation and leads to comparatively soft samples with respect to ta-C and its hydrogenated counterpart ta-C:H. Such samples are sometimes called hydrogenated graphite-like carbons (GLCH) or, directly, soft a-C:H. Higher hydrogen content leads to an increase in hardness, so the terms are accordingly hydrogenated diamond-like carbons (DLCH) or hard a-C:H. [42, p. 177]

As thin films, a-C feature a considerable density of **dangling bonds**, especially at the surface. The adsorption of water or ambient air molecules usually saturate these, the implications are discussed in section 2.3.4. A small amount of hydrogenation in the film is usually sufficient for a controlled saturation. For hydrogenated samples with hydrogen content below 20%, the internal structure of a-C and a-C:H are comparable [55]: a-C:H still contains sp^2 clusters [56] and has mostly compensating ordering and disordering effects [49]. Of technical relevance, the addition of hydrogen leads to the reduction of internal stress, which is the limiting factor for film adhesion in thin film with thickness of a few µm. [46] Upon heating a-C:H, hydrogen leaves the carbon network which yields a porous non-graphitic structure; limit of thermal stability is approximately 500 °C.[46] Chemical modifications offer an useful extension of the already huge variety on (hydrogenated) amorphous carbons for addressing different aims. These are thoroughly introduced in chapter 4, section 4.1.

2.1.4 Molybdenum disulphide (MoS_2) and molybdenum oxides (MoO_x)

Molybdenum disulphide MoS_2 is one well-known and well-investigated representative of the class of lamellar solids and of **transition metal dichalcogenides** (TMDC). It is chemically classified as chalk, i.e. the product of a metal and a group VI element (chalcogenides, “chalk-forming elements”) like oxygen or sulphur. Application of MoS_2 and related TMDCs as dry lubricant is owed to the layered structure and weak van der Waales-bonds between layers [16, p. 29], see Figure 2.11. Modern applications span from battery components to semiconductor physics, all of them utilise the rich electronic and optical properties. [16, 37]

With its layered structure, one might be reminded of graphite, and in fact, some modern allotropes of carbon like nano-tubes also have a TMDC equivalent. [37, p. 123] Disregarding those specialised allotropes, the major structural differences in MoS_2 bulk material are confined to the stacking order, mostly. Powders are characterised by their plethora of boundaries and exposed vertices, which in MoS_2 are a point of contact for chemical reaction. As result thereof, powders and alike are considerably more sensitive to introduced heat, which leads to oxidation in standard environments.

When oxidised in ambient air, MoS_2 reacts to molybdenum trioxide MoO_3

$$2\,MoS_2 + 7\,O_2 \longrightarrow 2\,MoO_3 + 4\,SO_2\uparrow, \tag{2.5}$$

which is the preferred oxidation product of MoS_2. Besides MoO_3, molybdenum dioxide MoO_2 is formed from MoS_2 under reducing conditions with scarcity of sulphur or, industrially, as reduction of MoO_3 to Mo and subsequent oxidation to MoO_2 at 670 °C [58]:

$$MoS_2 + 6\,MoO_3 \longrightarrow 7\,MoO_2 + 2\,SO_2\uparrow, \tag{2.6}$$

$$2\,MoO_3 + Mo \longrightarrow 3\,MoO_2. \tag{2.7}$$

MoO_2 is usually monoclinic (m-MoO_2), but hexagonal structures (h-MoO_2) and phase transitions between those are reported. [59]. It is also known that MoO_2 is formed in the presence of water vapour at 800 °C. MoO_2 is unstable in ambient air with introduction of heat [60],

$$2\,MoO_2 + O_2 \longrightarrow MoO_3. \tag{2.8}$$

Chemical formula	Mineral name	Mohs hardness	crystal system
Mo	*element*	5.5	cubic
MoS_2	Molybdenite	1-1.5	hexagonal
MoO_2	Tugarinovit	4.5	monoclinic
MoO_3	Molybdite	3-4	ortho-rhombic
$MoO_3 \cdot 2H_2O$	Sidwillite	2.5	monoclinic
MoS_2	Jordisite	1-2	amorphous

Table 2.1: List of occurring molybdenum compounds, corresponding mineral name, Mohs hardness, and crystal system. Note that this list is restricted to compounds in minerals and neglects possible Magnéli phases [57] of oxides or poly-molybdates [38, pp. 819–822].

Sputtered MoS_2 thin films may be considered structurally as microcrystalline MoS_2 with varying degree of domain size, growth orientation (basal or columnar) and defect density. Some element-modifications like nitrogen or copper lead to amorphous films; these are introduced in chapter 4, section 4.2. The microcrystalline nature act as onset point for chemical reactions as discussed for powders earlier.

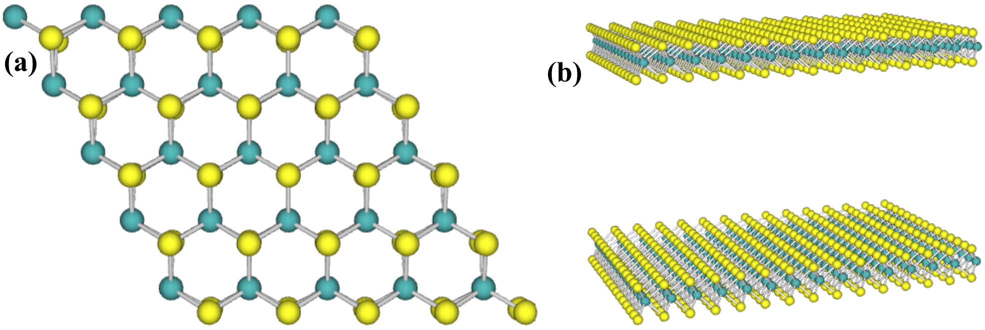

Figure 2.11: Overview on molybdenum disulphide structure (yellow: sulphur atoms, blue: molybdenum atoms): **(a)** top-down view on monolayer, **(b)** side-view on layers with layer distance to scale. Taken from PhononVisualizer software [61], under Creative Common Attribution License [62].

2.2 Fundamentals of chosen methods: general optics, Raman spectroscopy, optical temperature tuning

For the scope of this thesis, interaction of light and matter refers to interaction between light(-fields) and electrons. This section uses both the wave and particle nature of light, that is, light as a wave in electric field $\vec{E}$ as $\vec{E} = \vec{E}_0 \cdot \cos(\omega_{\mathrm{Ph}} t - kx + \phi)$, and light as photon particle with inscribed energy $E_{\mathrm{Ph}} = \hbar\omega_{\mathrm{Ph}}$. Phase differences ϕ as well as spatial component kx in light waves are disregarded, because the form of Raman spectroscopy in this work does not require coherence.

2.2.1 Considerations on interaction between light and matter

Interaction between light and matter can be described in two concurring systems: from the perspective of light and of the material.

From the perspective of light, encountering matter results in refraction, absorption, reflection, scattering, or transmission. Refraction and transmission are disregarded from here, scattering is discussed in detail later. The optical constant $n^* = n + ik, \quad n, k \in \mathbb{R}$, in which i is the square root of -1, can be separated in two components, optical density n and the optical extinction coefficient k. These two components describe transmission behaviour of light through matter and absorption of the light's energy into the matter, respectively. Key requirement for **reflection** on surfaces is an appropriately small band gap E_g and miniscule absorption. In a shortened and drastically simplified picture, the band gap E_g is a material property, which acts as a minimum required energy barrier for interaction.

Incident light without sufficient energy and in low intensity likely passes through the material, rendering the material transparent. As prime example, diamond has a notoriously high band gap E_g of 5.5 eV [3] and is transparent for optical light, while metals have by definition no band gaps and high reflectivity with characteristic gloss. The simplified *Jablonski* diagram on the right displays absorption, fluorescence and non-radiative transitions (e.g. vibrational relaxation). Bold horizontal lines represent electronic energy states, thin lines the vibrational energy states. The deposited energy of the incident light is stored and subsequently re-emitted as fluorescent light. No energy is ultimately transferred, this type of scattering is termed *elastic*. Absorption is the summation of all energy dispersive mechanisms, which involve energy transfer; the exact mechanisms of energy absorption or energy dissipation are irrelevant here. Resulting dampening of light is modelled in Lambert-Beer's law with the absorbance A_λ as

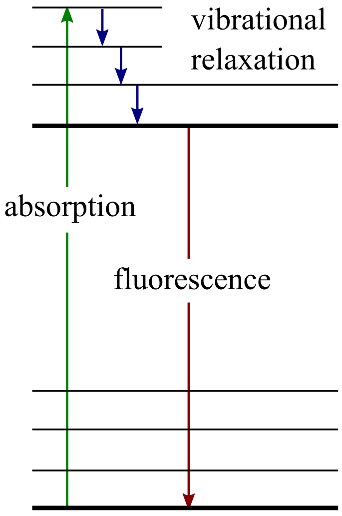

Figure 2.12: Jablonski diagram

$$A_\lambda = \log\left(\frac{I_0}{I}\right) = \alpha_\lambda d, \tag{2.9}$$

---

[3] equivalent energy of UV light with wavelength $\lambda = 225\,\mathrm{nm}$

in which the transmitted light intensity I is reduced over the incident intensity I_0 as a function of a specific absorption coefficient $\alpha_\lambda = 4\pi k/\lambda$ and light path length d. This can be used to estimate the light penetration $\delta = \alpha_\lambda^{-1}$ in highly absorbent materials. For the involved materials, the laser penetration depth δ is estimated to no more than 100 nm for MoS_2 and equally for a-C.[4]

From the perspective of matter, the electric field $\vec{E}$ of incoming light leads to electronic displacement, which is summarised as electric displacement field $\vec{D}$. This displacement field

$$\vec{D} = \epsilon^* \vec{E} = \epsilon_0 \vec{E} + \vec{P} \tag{2.10}$$

is constituted of the external electric field $\epsilon_0 \vec{E}$ (vacuum permittivity $\epsilon_0 = 8.85 \times 10^{-12}\,\mathrm{F\,m^{-1}}$) and the material polarisation $\vec{P}$. The polarisation $\vec{P}$ is the (transient) effect of the external field on the material. It is linked to the electric field $\vec{E}$ of light via

$$\vec{P} = \underbrace{(\epsilon^* - \epsilon_0)}_{=\epsilon_0 \chi} \vec{E} \tag{2.11}$$

with the dielectric function $\epsilon^*(\omega)$, $\epsilon^* = \epsilon' + i\epsilon''$, $(\epsilon', \epsilon'' \in \mathbb{R})$. This function ϵ^* is commonly (and conveniently) separated into various parts arising from involved mechanisms. For visible light, to which this chapter is curtailed, a key mechanism is the electronic polarisation in resonance to vibrational states [66, p. 1]. The real and imaginary part of the dielectric function ϵ^* are known as storage ϵ' and loss modulus ϵ'', respectively, which are equivalent to n and k from the light's perspective above.

2.2.2 Inelastic scattering of light, the Raman effect

Raman spectroscopy is centred around the Raman effect, which is named after indian physicist and 1930 Nobel prize laureate Chandrasekhara Venkata Raman (1888-1970). It was predicted by austrian physicist Adolf Smekal (1895-1959) in 1923 [67] and experimentally found in 1928 by C.V. Raman and co-worker Kariamanikkam Srinivasa Krishnan (1898-1961), when using filtered sunlight on liquids and vapours [68][69, pp. xix–xx][70, pp. 7–13]. This was co-discovered almost simultaneously by Soviet physicists Grigory Landsberg (1890-1957) and Leonid Mandelstam (1879-1944), when investigating quartz crystals with mercury vapour lamps [71, 72]. Landsberg and Mandelstam acknowledged the prior findings of Raman in their publications, but were not certain to confirm a relation. The Raman effect describes the energy loss (or gain) of scattered light, in which molecular vibrations are involved. For those to interact, a general requirement is the change in polarisability: a (static) electric field $\vec{E}$ yields a polarisation $\vec{P}$. On an elementary level, an electric dipole moment $\vec{p}$ is induced from $\vec{E}$ as

$$\vec{p} = \alpha \vec{E} + \frac{1}{2}\beta E^2 + \frac{1}{6}\gamma E^3 + O(E^4) \tag{2.12}$$

via polarisability tensors α, β, γ. As the strict considerations of the vectoral nature are only vital for polarisation-sensitive efforts, the vectors and tensors can be reduced to scalars for

---

[4] In more detail, 40 nm and 80 nm for mono-or and bulk-MoS_2 at resonant excitation $\lambda = 632.8$ nm , 50 nm for a-C at excitation with $\lambda = 532$ nm [63, 64, 65]

the purposes of this thesis. This scalar polarisability α is now described as Taylor expansion over a general vibrational normal coordinate u as

$$\alpha = \alpha_0 + \sum_j \left(\frac{\partial \alpha}{\partial u_j}\right)_{(0)} u_j + \sum_{jk} \left(\frac{\partial^2 \alpha}{\partial u_j \partial u_k}\right)_{(0)} u_j u_k + O(u^3), \tag{2.13}$$

in which j, k are indices of different normal modes and symbol (0) denotes the ground state condition $u = 0$. This is a natural assumption, because the dynamics of the lattice elements (vibrational movement) and the surrounding electrons are strongly coupled via the dielectric function ϵ. Likewise, the linearisation of polarisability α is sufficient. With the model of harmonic oscillation of the displacement u_j of the j-th normal mode as $u_j(t) = u_{j,0}\cos(\omega_j t)$, the combination of all expanded and linearised equations (2.12), (2.13) directly yields

$$p = \alpha_0 E_0 \cos(\omega_{\mathrm{Ph}} t) \tag{2.14}$$

$$+\frac{1}{2}\left(\frac{\partial \alpha}{\partial u_j}\right) E_0 u_j \cos\left((\omega_{\mathrm{Ph}} - \omega_j)t\right) \tag{2.15}$$

$$+\frac{1}{2}\left(\frac{\partial \alpha}{\partial u_j}\right) E_0 u_j \cos\left((\omega_{\mathrm{Ph}} + \omega_j)t\right) \tag{2.16}$$

for each normal mode j. The superposition of the oscillation in electric field $|\vec{E}| = E_0 \cos(\omega_{\mathrm{Ph}} t)$, and the oscillation in polarisability α so gives three terms: First term (2.14) stems from the excitation of a dipole and describes the subsequent re-emission of light with unchanged frequency ω_{Ph}. This contribution is referred to as Rayleigh scattering and is the most prominent contribution to the spectra, even if unimportant for this work. The latter two terms in (2.16) only differ in sign of the frequency modulation $\omega_{\mathrm{Ph}} \pm \omega_j$. These terms encompass the subsequent light emission with reduced or increased energy and are referred to as Stokes or Anti-Stokes contribution, respectively. In picture of particles, the photons scatter inelastically on vibrational quasi-particles (phonons), onto which they transfer a part of energy and momentum. The conservation of momentum requires that photons and phonons are equal in (quasi-)momentum, which yields a Raman selection rule for contributing phonons: $q \approx 0$ or, in other words, only phonons close to the Brillouin centre Γ (with a few notable exceptions). Another selection rule requires non-constant polarisability with respect to normal mode u_j, which is directly visible for equation (2.15). Compared to Rayleigh scattering, Raman scattering is miniscule: one photon scattered in Stokes scattering is overshadowed by 10^6 to 10^8 photons scattered elastically. [20][70, p. 3]

Vibrational modes can also be excited directly. The energetic gap between vibrational states are comparatively small to the band gap E_g, their excitation wavelength is usually in the infrared (IR) region of light. The coupling of light to vibrational modes is indirectly mediated by the change of dipole moment p in a similar manner as demonstrated above. For a intuitive picture [70] and clear distinction between scattering and excitation, see Figure 2.13. The key difference lies in the requirements ${}^{\partial\alpha}/_{\partial u_j} \neq 0$ for so-called Raman-active modes and ${}^{\partial p}/_{\partial u_j} \neq 0$ for so-called IR-active modes. Vibrational modes may therefore be selectively measurable by Raman or IR spectroscopy. The fact about inversion-symmetrical molecules being only one of both is commonly beneficial, making Raman and IR spectroscopy complementary and rendering ambient gas molecules impeding on IR -, but not on Raman spectroscopy.

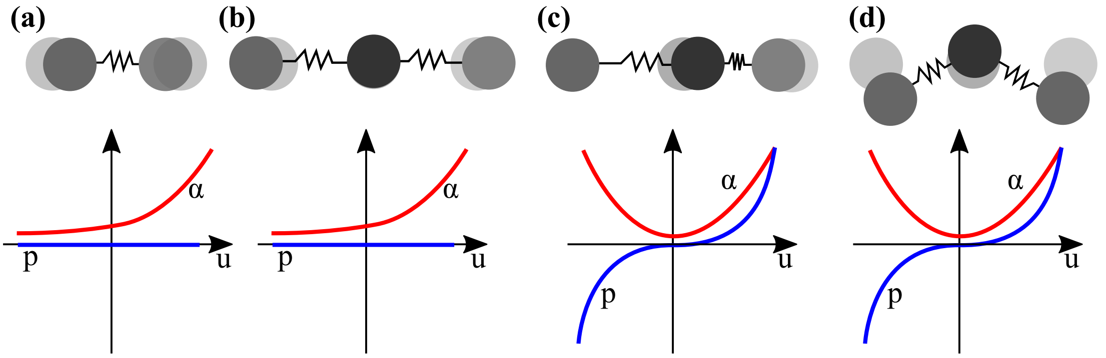

Figure 2.13: Polarisability change as key requirement for Raman effect. In vibrations of **(a)** a di-atomic molecule and **(b)** in one vibrational mode of a tri-atomic molecule, the polarisability α changes along the normal coordinate u, while the dipole moment p is unchanged. The situation is reversed for other vibrational modes in **(c)**+**(d)**. Adapted from textbook [70].

Resonant Raman spectroscopy, Double Resonance Raman process

Resonant Raman spectroscopy takes advantage of a vastly increased scattering cross-section, when the energy of an incident photon matches an electron energy state of the sample. Quantitatively, the scattering probability $\lambda_{i \to f}$ from initial state i to the final state f is captured in Fermi's Golden Rule

$$\lambda_{i \to f} \propto \rho(E_f) \cdot |V|^2 \tag{2.17}$$

with an incident photon as perturbation V, the transition probability $\lambda_{i \to f}$ to the density of states ρ at the final state energy E_f and a matrix element $|V|^2$ of the perturbed energy matrix. Qualitatively, the matrix elements $|V|^2$ contain the difference of energies, for example of the excitation energy as initial state energy and the electron states, in the denominator.[5] When in resonance, that is, the excitation energy is equal to an electron state, both energies match and drastically increase the matrix elements and therefore the scattering probability.

2.2.3 Characteristics of a Raman spectrum

The earliest "detectors" for the Raman effect were photographic paper, on which the Stokes components were visible as darkened lines.[75, p. 339] This, of course, did not allow at all for precise investigations of today, but give a hint on the origin of the term "line" for what is today referred to as *Raman peak*.

Generally, a Raman spectrum is subject of interpretation. Figure 2.14 shows a simple Raman spectrum besides a Jablonski-type schematic of the involved scattering process. In this simple spectrum, Raman spectrum of silicon wafer shows one strong Raman feature at 520.5 cm^{-1}, a Raman peak at the absolute frequency $\omega_{\mathrm{Ph}} \pm \omega_j$. In a simple model, the **Raman shift** ν (peak position) represents a measure of the involved atomic masses and interatomic bonding strength, that is, phonon energy $W \sim \sqrt{\frac{k}{m}}$. Raman shift is

---

[5] Details are not important for the scope of this work, but are well described in publications [47, p. 176][73, pp. 2276–2279][74, pp. 136–137]

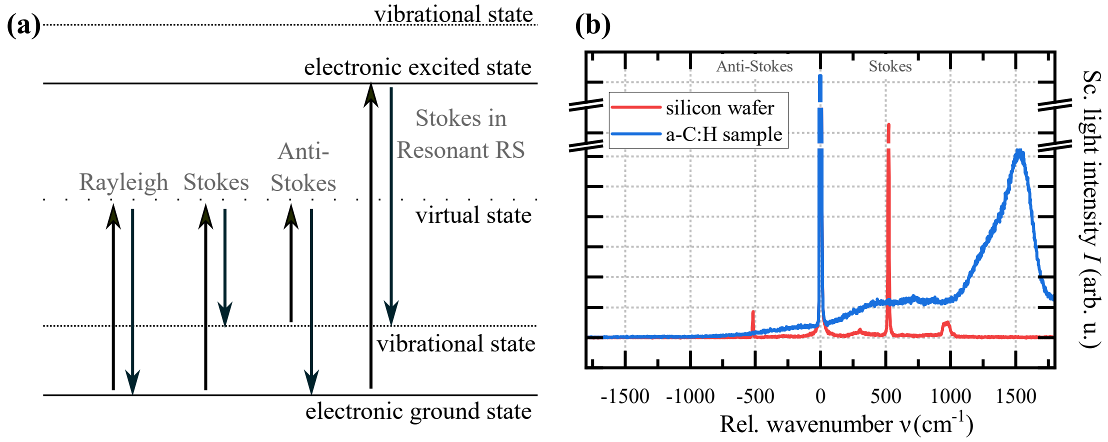

Figure 2.14: Overview in Raman scattering process and resulting Raman peak. **(a)** Jablonski-type diagram of involved energy levels in the involved scattering processes: Rayleigh scattering, (resonant and non-resonant) Raman scattering as Stokes and Anti-Stokes components, **(b)** spectrum of Raman scattering process, which are linked to the equation components (2.14) to (2.16).

conveniently calculated as $\nu = \lambda^{-1}_{\text{excitation}} - \lambda^{-1}_{\text{Stokes}}$ in relative inverse centimetre (cm^{-1}), With rare, but noticeable exception in Resonant Raman spectroscopy, the usual range of Raman shift is $-100\,\text{cm}^{-1}$ to $3600\,\text{cm}^{-1}$. [70, pp. 76, 211] Raman spectra of pristine crystals feature most likely peaks with peak widths of a few cm^{-1}. This is measured as full width at half maximum (**FWHM**) in cm^{-1}. The line width is affected by multiple phenomena, for example, the duration of the underlying vibration is inversely related to the line width. Also, a distribution of Raman modes with similar, but different Raman shifts ν gives rise to a broad spectral feature. In specialty cases, the FWHM is linked to certain types of disorder or crystallinity, which will be discussed later. In a ideal solid, Lorentzian-type **line profiles** of variable widths are a natural choice, because the involved mechanisms originate from (damped) vibrational (mostly-)harmonic resonances like in the lorentzian oscillator model. [76] From this starting point, some sample characteristics introduce broadening, for example distortions of bonding characteristics and internal stress, which appear as Gaussian profile.[77] So, a natural choice for unknown or mixed samples is the convolution (Voigt profile) or superposition of both line profiles (Pseudo-Voigt profile). The Pseudo-Voigt profile reads

$$I(x)/A = \underbrace{(1-\alpha)\,\frac{1}{\tilde{\sigma}\sqrt{2\pi}}\exp\left(-\frac{(x-\nu)^2}{2\tilde{\sigma}^2}\right)}_{\text{gaussian}} + \underbrace{\alpha\,\frac{1}{\pi}\left[\frac{\sigma}{(x-\nu)^2+\sigma^2}\right]}_{\text{lorentzian}} \tag{2.18}$$

with common amplitude A, common measure of width $\tilde{\sigma} = (2\log 2)^{-1/2}\,\sigma$, Raman shift ν and form factor α. For more intricate samples as amorphous carbon matrices with graphitic inclusions, more sophisticates, but computationally challenging line profiles are presented in recent studies. [43, 78]

The **intensity** of the Raman peak (in standard forms of Raman spectroscopy) is dependent on both sample and instrumentation characteristics. [69, p. 19][79] This means on the one hand that the experiment design can be optimised for a given measurement task, but also on the other hand that most minute sample signals remain hard to detect. For a start, refer to equation (2.15) and recall the power emission P_{dipole} of a Hertzian dipole being connected the second derivative in time of electric dipole moment $|\ddot{p}|^2$. So, from equation (2.15), the bare intensity of a Stokes-shifted line reads

$$I \propto E_0^2 \cdot \left(\frac{\partial \alpha}{\partial u}\right)^2 \cdot (\omega_{\text{Ph}} - \omega_j)^4 \tag{2.19}$$

with averaging over time, $\cos^2(...) = \text{const.}$ [70, p. 52] On the sample side, the second factor gives rise to a key Raman selection rule,

$$\left(\frac{\partial \alpha}{\partial u}\right) \neq 0. \tag{2.20}$$

Combined with the frequency of the phonon ω_j, information about the sample can be derived. Aside from the equation above, the concentration and inspected volume, in other words, the number of contributing specimen, have a direct impact on the intensity. On the instrumentation side, the choice of excitation frequency ω_{Ph} strongly influences the intensity. It plays the dominant role in the difference $(\omega_{\text{Ph}} - \omega_j)$, usually orders of magnitude, while the phonon frequency ω_j is unchanging[6] with respect to the excitation. In this regard, using the second harmonic (doubled frequency) of a given excitation yields a sixteen-fold increase of intensity if no other effects apply, see chapter 3.2.1. Finally as for the omnipresent, the factor E_0^2 will translate to a proportionality of Raman intensity and excitation power if no other effects come into play [70, p. 52] The yield of a given Raman signal may be further enhanced via complex setups or derived Raman spectroscopy measures. The benefits of such setups are presented later.

Unwelcomed phenomena: fluorescence and signal losses

Naturally, the simplified case in Figure 2.14 neglects possible unwelcome features like spectral background and technical artefacts besides the Raman peaks.

The most disruptive effect in Raman spectroscopy is **fluorescence**, which easily oversaturates the detection equipment on occurrence. It is the key opposing factor in the choice of excitation frequency ω_{Ph} for optimal intensity in equation (2.19): it suggests the usage of highest possible frequency for maximum intensity, but the choice is limited by the minimum required energy for absorption and/or fluorescence, the band gap E_g. Resonant Raman spectroscopy deliberately exceeds this limit for an intensity boost without fluorescence because of non-radiative (forbidden) transition pathways. *Photobleaching* or *fading* is a method to avoid fluorescence at a large scale, which is based on optically-induced and typically irreducible reactions in the sample. At smaller manifestations of fluorescence, the effect is restricted as vastly more broad feature in the background of the spectrum. In that case, a polynomial fit and, especially for a narrow spectral window, a linear fit for background removal is usually sufficient. Besides weak fluorescence, the background *slurs* other unaccounted contributions like broad Raman peaks or stray light.[7] Fluorescence, stray light

---

[6] This is true with a few notable exceptions of dispersive peaks, for example in graphite [80]

[7] Still, some publications estimate sample parameters based on the background, e.g. the hydrogen content in a-C [81].

and unwanted signals of substrates are instrumentally damped by the implementation of confocal Raman microscopy, see details in subsection 3.2.2.

Signal loss in Raman spectroscopy are grouped in instrumental and sample-related. [69, p. 19] Instrumental reasons encompass losses in optical devices, especially a pinhole or entrance slit, and efficiency values of grating or detection equipment. [70, p. 74] Besides the intensity, the widths of the peaks are not only ascribed to sample characteristics. The resulting peak width is the geometric average of peak widths contribution of the instrumentation and of the natural peak widths of the sample. [70, p. 123] For signal loss being poorly-selective, it is strongly recommended to not evaluate the absolute intensity of a Raman peak for solid samples. The relative intensity of Raman peaks is less problematic, that is usage of the intensity ratios between Raman peaks or an ordered list peak intensity.[69, p. 48]

Raman spectral features of amorphous solids

Up to now, the discussion above is centred around solid and (mono-)crystalline samples; additional effects have to be taken into account for nano-crystalline or amorphous solids. Figure 2.15 shows the Raman spectrum of an amorphous material and its components: deviating Raman peaks, Rayleigh wing, and boson peak.

In most energetically diverse cases, that is amorphous solids or powders for example, Raman peaks feature a Gaussian-type line-shape with distinct widths. This is also a natural choice, because the contributing processes are distributed around a centre energy. In the light of the central limit theorem, the nano-crystalline parts of a powder act as independent scattering centres, which sum up to the spectrum. For unknown samples or samples of mixed crystallinity, it is advisable to use a Voigt profile, that is the weighted convolution of Lorentzian- and Gaussian- line profile and assess the weight parameter for the decision of Lorentzian- or Gaussian-type fit model, or Pseudo-Voigt profile as in equation (2.18).

Spectral behaviour in the background close to the Rayleigh peak is strongly non-linear. One contribution stems from the overly strong Rayleigh peak overshadowing the Raman spectra, the Rayleigh wing, which is easily suppressed by the usage of filters. The other contribution stems from a particular feature in amorphous solids: a more-or-less universal peak with characteristic line shape in the spectral region close to the Rayleigh peak. In 1980s [83], such behaviour was described as “boson peak” in experimental or numerical studies of amorphous materials[84, 85, 86]. The information in this peak, however, is challenged with the core argumentative that such peak is the manifest of a feature in the density of states of phonons (or vibrational DOS, VDOS), which naturally evolves with increasing disorder in the force constants. [87] In this work, this particular spectral region is disregarded; background removal as stated above is not affected.

2.2.4 Raman peak allocation in carbons and in a-C thin films

The earliest study of carbons in Raman spectroscopy was published 17 years after the initial publication of the Raman effect (1928, [68]) and two years after its application to crystals (1943, [88]), in which Raman’s assistant and co-author R. S. Krishnan used mercury vapour lamp and photographic film for study of diamonds. After three days of exposure, the first and second order of a Raman line at 1332 cm^{-1} was found. [89] One year after, a temperature

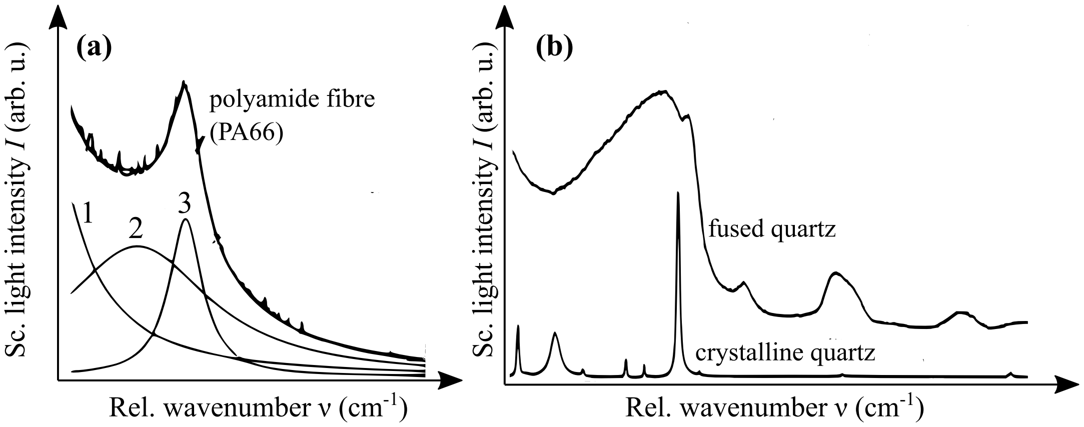

Figure 2.15: Effect of disorder on Raman spectra: **(a)** elements of a Raman spectrum of amorphous solids, example on a polymer (PA66 polyamide): (1) non-linear background (Rayleigh wing), (2) Gaussian-type and (3) Lorentzian-type contribution, **(b)** Effect of crystallinity on Raman spectra: both samples are quartz. Most of the crystalline sample show sharp Lorentzian-type Raman peaks, while features in fused quartz is vastly softer. Adapted from publications [39, 82].

dependence of this Raman line was published. [90] Studies of black carbon allotropes, however, required a laser as excitation source to overcome high absorption. Among those, Tuinstra and Koenig in 1970 noted an “omnipresent” Raman line at $1575\,\mathrm{cm}^{-1}$, which they related to single crystals of graphite, and another Raman line at $1355\,\mathrm{cm}^{-1}$ for other materials like pyrolytic or commerical graphite, activated charcoal, lampback, and vitreous carbons. [91] In this work, the occurrence of the Raman line at $1355\,\mathrm{cm}^{-1}$ and its width was linked to degree of organisation in carbon, in more detail, they found inverse proportionality of the crystallite size L_a to the intensity of the Raman line. A contrary hypothesis based on the similarity to the diamond Raman spectrum was noted, but the lack of temperature dependence, which was found by Krishnan, and the poor thermal stability of diamond powder falsified the hypothesis of being diamond-related.

Raman spectroscopy developed over the last decades to become to the go-to standard in the study of carbons today. [47, 52, 73, 93, 94, 95, 96, 97] It taps into the characteristics of sp^2 structures mostly and into sp^3 structures indirectly, which both define a realm of optical, electronic and mechanical properties [95, 48], and by this allows for an in depth study of sample characteristics. [98] Exploiting the facts that Raman spectra are generally linked to the behaviour of atomic or molecular bonding and that carbon allotropes may have different hybridisations, various allotropes of carbon show a manifold of different, but still finite Raman spectra. The limit of Raman spectroscopy in carbons is the ambiguity of its (few) spectral features. [20] Figure 2.16 shows the Raman spectral of defective graphite, amorphous carbon, and a partially ordered allotrope of carbon, *biochar*. [92]

The spectrum of amorphous carbon features most prominently the D- and G-Raman peak at roughly $1380\,\mathrm{cm}^{-1}$ and $1560\,\mathrm{cm}^{-1}$, respectively, and the second-order 2D-Raman peak (not shown). They are broad and over-lapping and thus, challenge the exact ascription to elemental peaks. For a specialised applications, one may use a manifold of underlying

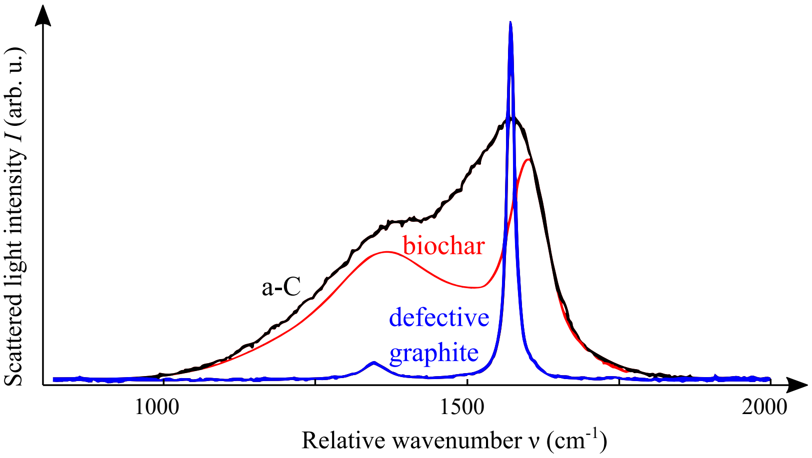

Figure 2.16: Selection of Raman spectra in carbon allotropes with different crystallinity, from highest in (defective) graphite to lowest in a-C. Adapted from publication [92].

Raman peaks [99, 100], even up to ten elemental peaks in the spectral range 960 cm^{-1} to 1700 cm^{-1}[21] For the scope of this work, the following Raman peaks are of interest: G-, D- and 2D-Raman peak.

G-Raman peak

The underlying vibrational mode of the G-Raman peak is the E_{2g} mode in sp^2 hybridised carbon pairs, so it is usually found in all graphitic materials [91]. Its excitation mechanism and vibrational mode are depicted in Figure 2.17: an incident photon with E_{Ph} excites an electron from the filled **Dirac cone** (a feature in the electronic band structure of graphite with linear dispersion and vanishing band gap) into or close to the unfilled. The involved phonon for the scattering event is close to the Γ-point of the Brillouin zone, so the momentum conservation criterion is always fulfilled. No defects or multi-phonon requirements

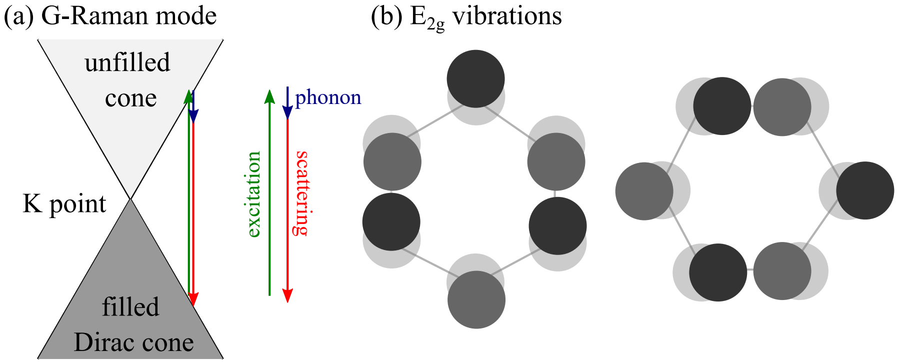

Figure 2.17: Excitation mechanism of G-Raman mode in carbons: **(a)** the Dirac cone at the K point ensures resonance for all excitation wavelengths, **(b)** the involved vibrational mode E_{2g} in sp^2 hybridised carbon pairs.

are needed for this procedure. For amorphous carbons, its Raman shift is centred around roughly 1580 cm^{-1}, but may appear in the spectral range of 1550 cm^{-1} to 1600 cm^{-1} for a-C and even in the spectral range of 1500 cm^{-1} to 1680 cm^{-1} for ta-C. This large variance of the Raman shift $\nu(G)$ stems from the strong dependence on sp^3 content and distribution. Other factors, albeit considerably more shallow in effect, are reported for internal stress in the order of a few cm^{-1} per GPa, or structural phenomena like sp^2 clustering or rearranging into chains. [101] Only for amorphous carbons, the G-Raman peak is dispersive in excitation wavelength, when it is non-dispersive in more ordered allotropes like graphite or nano-crystalline graphite. [97] The characteristic widths FWHM(G) spans 50 cm^{-1} to 175 cm^{-1}, which is (a) an indicator of the disorder in bonding characteristics and (b) a measure of the characteristic crystallite size L_a, see Figure 2.18.

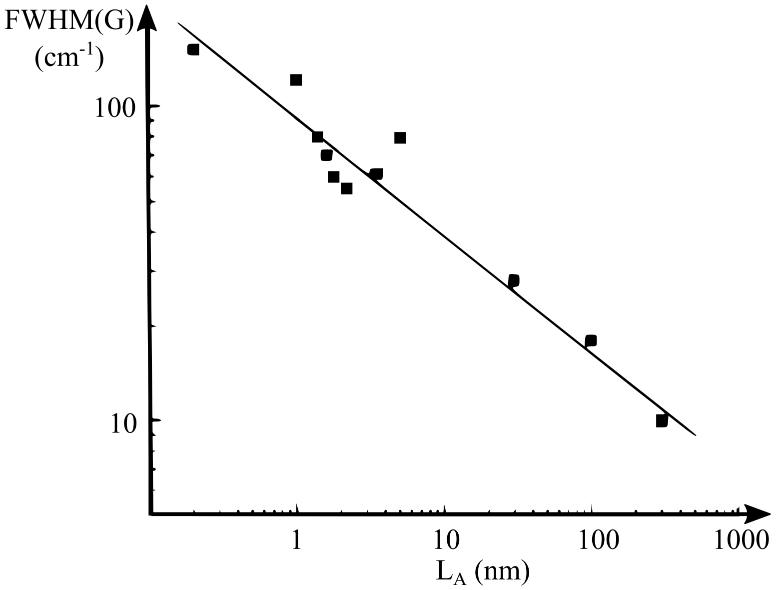

Figure 2.18: Dependency of FWHM(G) on crystallinity, for which the inter-defect distance L_A serves as a measure. Adapted from review [47, p. 171].

The line shape is traditionally a Breit-Wigner-Fano profile, which covers the naturally occurring skewness of the line. [101] Raman lines do not naturally have a skewness, literature assumes a peak at 1600 cm^{-1}, which results in the shoulder in G-Raman peak. A natural choice of the G-Raman peak line shape is a gaussian or (pseudo-)voigt profile.

D-Raman peak

The origin and theoretical understanding of the D-Raman peak was an object of debate, see publication [52] for a concise overview.

The underlying vibrational mode of the D-Raman peak is a A_{1g} breathing mode aromatic sixfold rings, which is depicted in Figure 2.19 along with its intricate excitation mechanism: an incident photon with E_{Ph} excites an electron from the filled Dirac cone onto to the Fermi surface of the unfilled cone at energy E_1, a phonon with momentum $q = k$ shifts the electron from cone at K to another at K', before back-scattering on a defect and

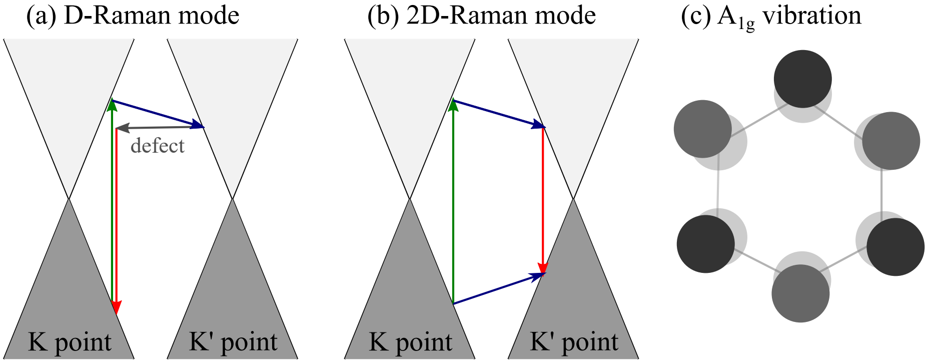

Figure 2.19: Excitation mechanism of D- and 2D-Raman mode in carbons: **(a)** the involved phonon provides momentum to scatter from cone at K to another cone at K', for which a local defect is required. **(b)** The 2D-Raman mode involves two phonons of opposite momentum, but no local defect site. **(c)** Vibrational mode A_{1g} in six-fold carbon rings for both D- and 2D-Raman mode.

recombination with the electron hole. In this last step, the scattered photon is emitted with energy E_2, which is the initial energy E_1 minus the energy of the phonon. [73] For this process, a partial screening effect of electrons with respect to atomic vibrations is required, which, in a metal, is unstable for certain vibrations in the Brillouin zone. This instability, the so-called Kohn anomaly [102], occurs in graphite for the modes $\Gamma - E_{2g}$ (G-Raman peak) and $K - A_1'$. In the phonon dispersion, these anomalies are visible as kinks at their respective Brillouin zone point [52, 103, 104], which translates to a spike in VDOS and thus to a dense concentration of possible vibrational states for scattering events. In the perspective of Resonant Raman spectroscopy as described above in equation (2.17), two processes are resonant: the initial excitation (green arrow) and scattering on the phonon (blue arrow), while the defect scattering (gray arrow) and recombination (red arrow) are non-resonant. [73] Such processes are called Double Resonance Raman processes. In fact, due to resonance-enhanced scattering yield, carbon allotropes are few of the rare materials, which show Raman signatures of order higher than two.

In a nutshell, a defect is required to satisfy the conservation of momentum with the involved phonon momentum $q = k$. [91]. For amorphous carbons, its Raman shift is centred around roughly $1375\,\mathrm{cm}^{-1}$, but may appear as low as $1350\,\mathrm{cm}^{-1}$ for a-C after an vast rearranging and ordering process. The characteristic widths FWHM(D) spans $50\,\mathrm{cm}^{-1}$ to $400\,\mathrm{cm}^{-1}$ in graphitic materials and a-C. The line shape is traditionally a Lorentzian profile. [101]

Intensity ratio of D- and G-Raman peak, selective excitation band gap openings

The earliest description of graphitic materials in Raman spectroscopy by Tuinstra and Koenig in 1970 already used the intensity of the D-Raman peak for analysis. From the behaviour of the intensity ratio between D- and G-Raman peak in a-C, a three stage model of amorphisation [101] was proposed, see Figure 2.20. Within this framework, the sp^3 content and the rough topology of the carbon clusters, rings and chains, can be estimated.[106] The crystallite size is also accessible, which was previously found in graphitic materials. The

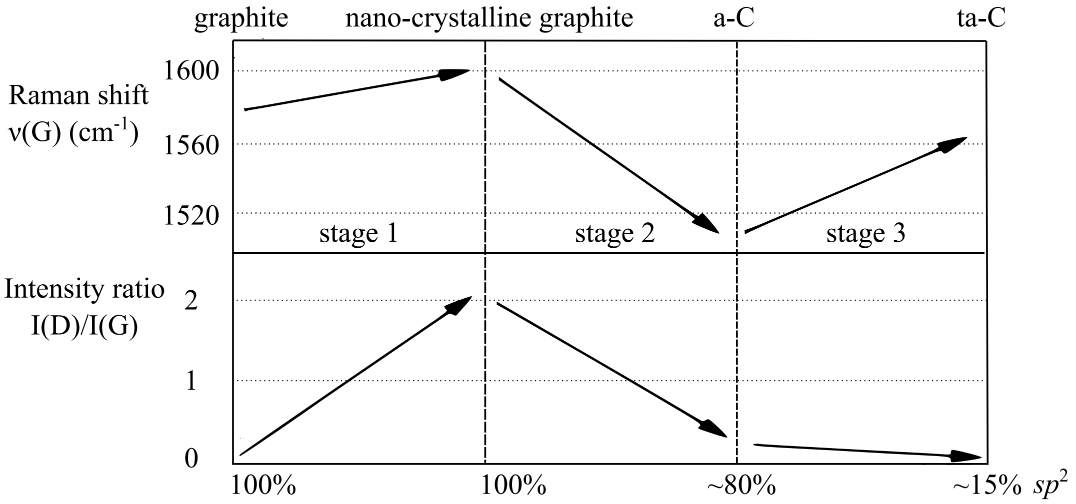

Figure 2.20: Three stage-model of amorphisation by Ferrari and Robertson. Behaviour in stage 1 and 2 are dispersive in excitation energy, this path describes the situation for 532 nm excitation. Thin films of a-C in this work are located in stage 2. Adapted from review [101] and publications [97, 105].

relation of Tuinstra and Koenig, $R_{\mathrm{Int}} \propto L_A^{-1}$ between crystallite size L_A and intensity ratio R_{Int}, however, is only valid for graphitic materials and breaks for highly defected samples like a-C, which were verified by comparison. [96] For those, a similar relation $R_{\mathrm{Int}} \propto L_A^2$ was introduced by Ferrari and Robertson, the onset point between the two regimes is at roughly 20 Å. [101]

Raman shift is not dispersive in excitation energy in a *regular* Raman scattering process, as in gauging a maximum in the phonon density of states close to the Brillouin zone centre Γ. From the finding of being dispersive, it was found that involved Raman peaks in carbon are the result of a more intricate Raman scattering process. In Resonant Raman spectroscopy of amorphous carbons, the dispersion is based on resonance with a particular cluster of different size. A shorter wavelength, and therefore higher energy, is resonant with a smaller carbon cluster, because smaller clusters have a larger band gap opening. This band gap is non-existent, of course, for long-range ordered graphite, for which the Raman peaks are not dispersive.

Second-order Raman peaks, 2D-Raman peak

In the spectral region around 2700 cm^{-1}, second order or combination peaks found, of which only the 2D-Raman peak is investigated. As caveat, multiple unrelated phonon modes by C-H stretching vibrations, typically with Raman shift of around 2900 cm^{-1} and a regional width of more than100 cm^{-1}, are overlapping the second-order Raman peaks.

The 2D-Raman peak, although resembling the second order of the D-Raman peak, has an unique excitation mechanism, which is depicted in Figure 2.19: an incident photon with E_{Ph} excites an electron from the filled Dirac cone onto to the Fermi surface of the unfilled cone, a phonon with momentum $q = k$ shifts the state from one cone K to another K', before back-scattering on a defect and relax to the ground state. The back-scattering does not require a defect as in the case of the D-Raman peak, but another phonon of $q = k$. For this mechanism to occur, a long-range ordering in graphitic clusters is required. So, the appearance of the 2D Raman-peak is a clear indication that these graphitic structures had evolved. [52]. For amorphous carbons, its Raman shift ν is centred around roughly $2680\,\mathrm{cm}^{-1}$, the dynamics of the 2D-Raman peak, besides its appearance, is disregarded for the scope of this work. The characteristic widths FWHM(2D), on occurrence in thermally-treated a-C, closely resembles that of FWHM(D).

Further spectral features peaks, low frequency peaks

Two spectral features at Raman shifts ν of $450\,\mathrm{cm}^{-1}$ and $720\,\mathrm{cm}^{-1}$ are low-frequency peaks L_1 and L_2, which are mainly sp_1-related and typically found in sputtered samples. [107, 97] They may be fitted using a gaussian profile [108], but are disregarded in this work.

Peaks of C-H stretching vibrations are investigated in detail in literature for identification or advanced measurements in organic molecules [109, 110, 111, 112] and especially for proteins [113]. For the scope of this work, they are noted but no further analysed.

2.2.5 Raman peak allocation in MoS_2 thin films and their oxides

A detailed Raman analysis of MoS_2 and its oxides is omitted for this work, because the occurrence of different chemical phases is sufficient for analysis. For completeness, the underlying vibrational modes in the MoS_2 and Mo oxides Raman spectra is briefly summarised.

Samples of TMDCs have a two-dimensional structure of point group D_{6h}, see corresponding vibrational symmetries in Table 2.2. [16] This point group contains vibration modes

symmetry	Raman active	IR active
A_{1g}	$409\,\mathrm{cm}^{-1}$	not active
E_{2g}^1	$33.7\,\mathrm{cm}^{-1}$	not active
E_{2g}^2	$383\,\mathrm{cm}^{-1}$	not active
E_{1u}	not active	$384\,\mathrm{cm}^{-1}$
E_{1g}	$287\,\mathrm{cm}^{-1}$	not active

Table 2.2: Table of vibrational modes in bulk-MoS_2 crystal, Infrared- and Raman-active modes. Values from textbook [16, p. 47] and publications [114, 115].

with A_{2u}, A_{1g}, E_{2g}^1, E_{2g}^2, E_{1u}, and E_{1g} symmetry, of which the modes E_{1g}, both E_{2g}, A_{1g} are expected to be Raman-active, that is, fulfil Raman selection rules. Figure 2.21 shows the (resonant) Raman spectrum of a pristine sample of MoS_2, in which more features than expected are found. For a start, the **expected optical modes** are visible and well-identifiable, namely, intra-layer vibrational modes E_{1g} at $286\,\mathrm{cm}^{-1}$, E_{2g}^1 at $383\,\mathrm{cm}^{-1}$, A_{1g} at $408\,\mathrm{cm}^{-1}$. The inter-layer vibrational mode E_{2g}^2 at $32\,\mathrm{cm}^{-1}$ is also Raman-active, but usually inaccessible for being close to the Rayleigh peak. In sputtered samples, in contrast to pristine (bulk) samples, **acoustical phonons** like LA(M) at $188\,\mathrm{cm}^{-1}$, and ZA(M) at

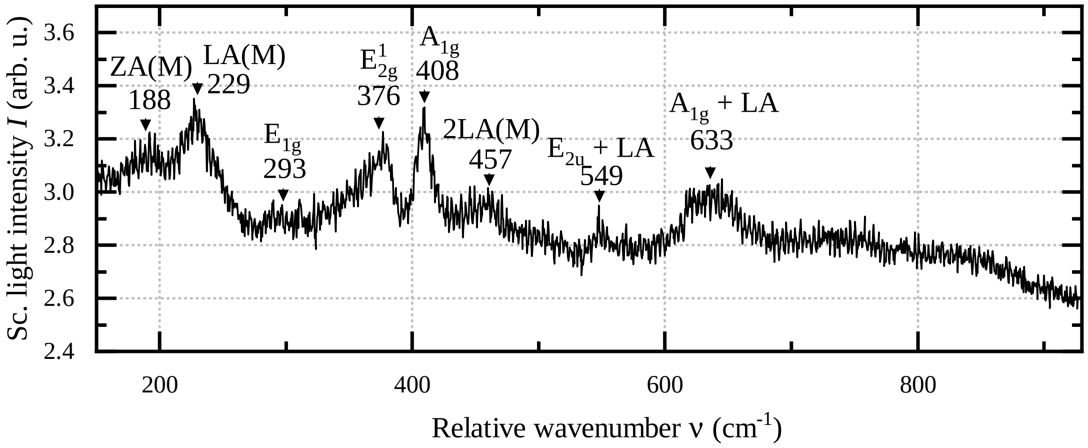

Figure 2.21: Typical Raman spectrum of sputtered MoS_2 thin films, symbols indicate the vibrational mode symmetry for identification.

229 cm^{-1} are visible. With resonant excitation, **second-order spectral features** are accessible [116], the excitation wavelength $\lambda = 632.8$ nm is chosen for being close to exciton absorption bands A_n at 652.6 nm and B_n at 590.5 nm [117]. Of those higher-order peaks, most noticeable are (a) an overtone of a longitudinal acoustical mode at the M point of the Brillouin zone, the $2LA(M)$ mode at 466 cm^{-1}, (b) the combination of $LA(M)$ with the A_{1g} mode at 645 cm^{-1}, and (c) a subtraction of LA(M) from the the A_{1g} at 179 cm^{-1} (not indicated). [118] The spectrum of MoS_2 contains peaks whose Raman shift is dispersive in excitation energy, which, as stated above, is not an element of *regular* Raman scattering process and give a hint towards a Double Resonance Raman process, see section 2.2.2 above.

The occurrence of acoustical phonons like TA(M), LA(M), and ZA(M) in the Raman spectrum of MoS_2 is uncommon; it is factually impossible in pristine samples. As such, they are usually only visible in defected samples, which meet the requirement of momentum conservation. Residual peaks in the spectral region 140 cm^{-1} to 180 cm^{-1}, which are usually poorly resolved, may stem from oxidation products of molybdenum. The occurrence of higher-order Raman features like combination and subtraction peaks under resonantly excited is curious. In recent research [119], this was explained by an inter-valley scattering mechanism, in which acoustic phonons connect different valley states within a Double Resonance Raman process. This, in a way, resembles the scattering mechanism of the *D*-Raman peak in (defective) graphitic materials and in amorphous carbons. From this, the occurrence of such peaks is useful to detect disorder or stacking-faults. [63] For the two commonly occurring oxides of molybdenum, Figure and Table 2.22 give an overview on their Raman spectra and involved vibrational mode.

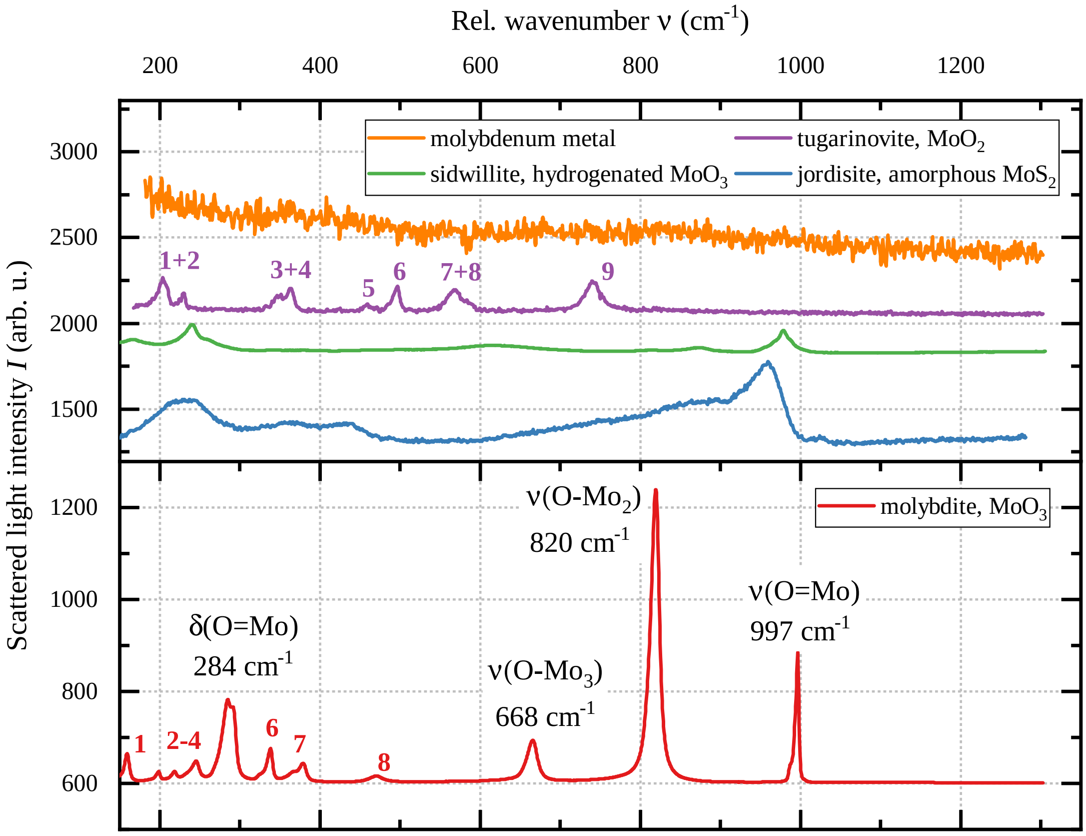

Sample	peak ID	Raman shift ν/cm^{-1}	symmetry	notes
MoO_2	1	203		
	2	228		
	3	345	a_g	$\delta(\mathrm{O{-}Mo_3})$
	4	363	a_g	$\delta(\mathrm{O = Mo})$
	5	461		
	6	495		
	7	571		
	8	589		
	9	744		
MoO_3	1	159.5	a_g	$\delta((\mathrm{O_2Mo_2})_n)$
	2	198.5	b_{2g}	$\delta(\mathrm{O{-}Mo_2})$
	3	218.8	a_g	$\delta(\mathrm{O{-}Mo_2})$
	4	245.3	b_{1g}	$\delta(\mathrm{O{-}Mo_2})$
	6	338.4	a_g	$\delta(\mathrm{O{-}Mo_3})$
	7	378.9	b_{1g}	$\delta(\mathrm{O = Mo})$
	8	471.9	$a_g\&b_{1g}$	$\nu(\mathrm{O{-}Mo_3})$

Figure 2.22: Raman spectra of molybdenum derivates and molybdenum oxide minerals. Reference data by RRUFF project database of minerals [120], peak identification data via [121, 122, 123, 124]. Symbol δ: deforming vibrations (rocking, wagging, twisting, scissoring), symbol ν: symmetric and anti-symmetric stretching vibration.

2.3 Basics in tribology: science of friction, wear, and lubrication

The basics of material science and contact mechanics as well as basics in tribology are presented, but only for the required minimum scope of this thesis. For contact mechanics and tribology, the textbooks and public lectures of the renominated researchers Horst Czichos [125] and Valentin Popov [126, 127] are cordially recommended. Besides the chemical and physical properties, which are already presented for MoS_2 and a-C in section 2.1, here the mechanical properties are introduced in general terms as well as specifically for both thin films.

2.3.1 Macroscopic mechanical properties, comparison of thin film materials

Mechanical properties capture the solid's behaviour upon a applied force. For the sake of conciseness and simplicity, a selection of thin film properties for general purpose usage are regarded. For this, the mechanical properties of thin films are hardness, toughness, and strength; elasticity, ductility and fracture behaviour, and film adhesion.

Hooke's law (Robert Hooke, 1678), the linear proportion of spring deflection and applied force, is surely common knowledge in science and engineering. By extension from mechanical springs to a slim body, a generalised deflection as **strain** ϵ (deformation per unit length along the load, dimensionless) and generalised tension force as **stress** σ (force per unit area, dimension of pressure) are introduced. Further natural reactions like tapering (transversal contraction), volume contraction, and shearing have to be taken into account in engineering, but are disregarded for the scope of this work.

Plotting those in Figure 2.23 shows the law's validity range: the **linear elastic** range.

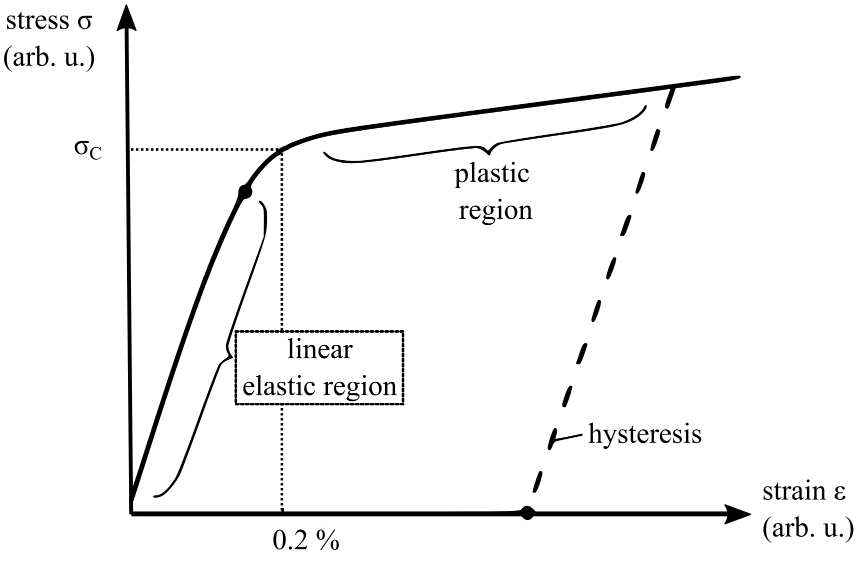

Figure 2.23: Generic stress-strain diagram for a ductile material. In this curve, elastic and plastic deformation are recognisable. Adapted from textbook [126, p. 11].

In three dimensions, Young's modulus, bulk modulus, and shear modulus describe the solid's reaction to generalised tension[8]. **Young's modulus** E (modulus of elasticity) is the equivalent of the proportionality constant of Hooke's law and so a measure for the stiffness macroscopically. In the microscopic picture, it is based on stretching of interatomic bonds and is, therefore, a measure of the interatomic bonding strength. As result, diamond with its densely packed, strong sp^3 bonding has among the highest Young's modulus $E = 1000\,\mathrm{GPa}$, while polymers like PVC, whose intra-molecular bonding is the weakest link, is orders of magnitude lower, like 1 GPa to 3.5 GPa. Ideally without fatigue, the deformation in the elastic range is fully reversible. On the brim of the linear elastic region, non-reversible, plastic deformation takes over. It is microscopically connected to the breaking of bonds, presumably at defects or dislocations as weakest links first. Within the plastic deformation range, the global maximum of stress is reached, which serves as definition of **material strength**. In more detail, one distinguishes the maximum stress without leaving the elastic range as the **yield strength** and the global maximum as **ultimate tensile strength**. This, notably, is not necessarily the strain value at rupture. The maximum strain is qualitative estimation for **ductility** of a solid, that is, its the willingness to plastically deform before rupture. When rupture occurs above 0.05 (as rule of thumb), a solid is termed **ductile**, and **brittle** otherwise. The concept of **toughness** adds the stress levels to the ductility and is defined as area under the stress-strain curve. As example, architecture glass has high Young's modulus, high ultimate tensile strength and hardness, but still a low toughness for being brittle. **Hardness** is used to describe plastically deformed area per applied load. For surfaces especially, hardness is the resistance against penetration.

For an overview, Table 2.3 contains the material properties of common steels and polymers and an overview on modified a-C and MoS_2 thin films. Thin film engineering falsely relies on the hardness of thin films to quantify the sample quality. [128, p. 953] The idea of depending on hardness value as sole quality measure solely is challenged recently [129]; for tribological purposes, a application-specific compromise of ductility and hardness is usually the objective [130] - besides chemical and thermal resistance as well as film adhesion [128, p. 953]. The capability of ductility in this scenario is useful to accommodate deformation

Table 2.3: Comparison of material properties of common steels, polymers, thin film systems of this work.

Sample		Typical values of	
	density	elastic modulus	hardness
16MnCr5	$7.85\,\mathrm{g\,cm^{-3}}$	200 GPa	8.4 GPa
Ti6Al4V	$4.43\,\mathrm{g\,cm^{-3}}$	114 GPa	4.5 GPa
PEEK	$1.32\,\mathrm{g\,cm^{-3}}$	3.6 GPa	0.2 GPa
SiO_2 glass	$2.5\,\mathrm{g\,cm^{-3}}$	70 GPa	8.6 GPa
a-C	$(1.9\text{-}3.0)\,\mathrm{g\,cm^{-3}}$	(240 ± 10) GPa	(23 ± 2) GPa
a-C:H	$(0.9\text{-}2.2)\,\mathrm{g\,cm^{-3}}$	(215 ± 8) GPa	(24 ± 1) GPa
MoS_2	$\approx 5\,\mathrm{g\,cm^{-3}}$	(14 ± 2) GPa	(0.14 ± 0.02) GPa
MoS_2:N		(93 ± 6) GPa	(5.3 ± 0.3) GPa

---

[8] Bulk - and shear modulus are disregarded here. They are defined in a similar fashion as Young's modulus with generalised volume changes and shearing, respectively.

and serves as interception against initial cracking, which in brittle materials would otherwise lead to fraction. [128, p. 953]

2.3.2 Friction and wear: two cornerstones in tribology

Friction and wear are two of the three often quoted cornerstones of tribology; the third, lubrication, has its own subsection in this work, the forth (and often omitted) cornerstone, corrosion, is woven into the former. Friction and wear are omnipresent, earliest recorded studies go back to Leonardo da Vinci in 15th century. The modern branch of science, *tribology*, was coined in the Jost report about 500 years later. It took so long for the thoroughly scientific exploration of friction and wear to gain momentum, because the underlying mechanisms are in the nano-sphere, which became accessible in the last decades with the upcoming of solid state physics of surfaces and modern experimental equipment like atomic force microscopy. Detailed investigation for an sophisticated model requires contact mechanics.

Prerequisites: contact mechanics and surface properties

One of the factors, that renders scientific modelling in tribology difficult, is the manifold of factors, which flow into the extensive picture of a tribo-contact and a tribo-system. First studies on contact mechanics started in 1882, when a model of elastic contact was proposed by Heinrich Hertz, who was studying the effect of compressive stacking on the compound optical properties of glass lenses. [5] A force acting on the stack compresses the lenses in their contact area, which impacts, e.g., the effective focal length. The models rather rigorous assumptions are (i) two convex bodies in (ii) not to high compression and in their elastic regime, which (iii) are not interacting via friction or (iv) via surface forces. In reality, a number of forces are lead up to the interaction between two contacting bodies: fundamental forces like electrostatic interaction or van der Waales-forces are the basis of friction. The last assumption, in other words, disregards phenomena like adhesion, which are taken into account by its modern successors.

Figure 2.24 depicts a naturally occurring surface. Although the Hertzian contact is very

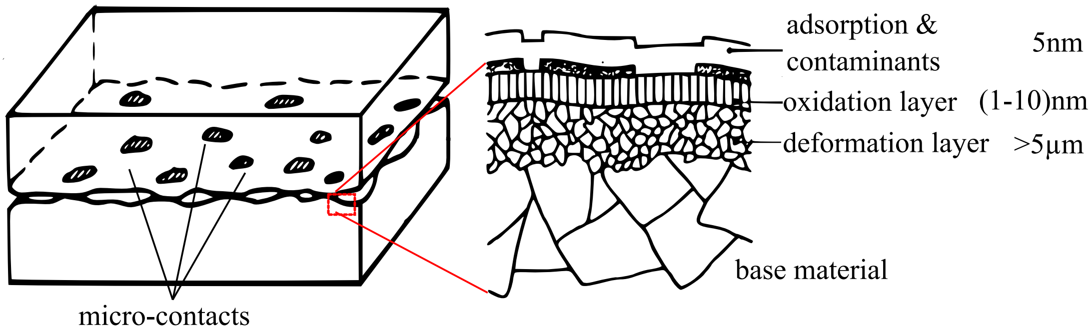

Figure 2.24: See-through schematic contact of two surfaces with tomography of a technical surface. The actual contact area is vastly smaller than the apparent contact area. Adapted from textbook [125].

basic[9], it is a convenient explanation of natural surface is simplified manner: rough surfaces are pictured as flat with miniscule asperities interacting and interlocking with one another, all of which are at their basis hertzian contacts. [8, 9] Friction is heavily dependent on the actual contact are, which is a function of the surface roughness, or figuratively of the asperities, and the contact pressure rather than the apparent contact area alone.

Friction mechanisms on surfaces

First verified scientific efforts in quantitative studies on friction were conducted by Leonardo da Vinci by the end of the 15th century, in which the fundamental aspects of friction laws were found in a more phenomenological manner. These findings were later enunciated by Guillaume Amontons by the end of the 17th century. [4]

Charles Coulomb investigated the main influences on friction in the 18th century, the material properties in contact, the surface area, the normal force, the duration of stationary contact, and ambient conditions. In this study, Coulomb identified the main contributing factors of friction behaviour and (re-)discovered an independence of friction from sliding velocity, system size, and surface roughness. [3, p. 793] His findings are now commonly known as Coulomb friction, simply summarised in equation (2.21): in macro-sphere, friction force F_{fric} in solid-solid contact is relative to the applied normal force F_{N},

$$F_{\mathrm{fric}} = \mu F_{\mathrm{N}}, \tag{2.21}$$

in which μ is defined as **coefficient of friction** (COF). While there are multiple mechanism in (macro-)friction (refer to textbook [125] for details), the situation in the nano-sphere is more transparent. For static and dynamic friction, the Prandtl-Tomlinson model gives a basic understanding of the gross picture: an atomically flat surface is comprised of an periodically potential landscape, sliding a singular point across the surface requires overcoming a potential trough in this landscape. The potential is the summary of all mechanisms acting on the surface. For surfaces, the fundamental mechanism of friction are (a) (all types of) van der Waales interaction, (b) hydrogen bonding, and (c) open molecular bonding (dangling bonds). Those fundamental forces can also be summed into other, more phenomenological categories like adhesion or capillary forces. [131] In carbons, especially, adhesion can become overly strong. If adhesion was not hindered by surface roughness, adhesion has characteristic energies of $1\,\mathrm{J\,m^{-2}}$ [126], or more visually, the contact of highly polished metal etalons with actual area of about $3\,\mathrm{cm}^2$ and a distance of $20\,\mathrm{nm}$ can carry a load of $1\,\mathrm{kN}$ [125, p. 39].

Surficial friction are subject of chemical and structural changes and so, their working environments have to be taken into account. For example, the adsorption of gas passivates dangling bonds, the friction of amorphous carbon thin films in vacuo is strongly increased over ambient air [132].

Wear phenomena and mechanisms on surfaces

Wear is traditionally defined as unwanted loss of material (or its properties) due to various causes, it is usually negatively connoted. [128, p. 273] It was studied in an observation-based

---

[9] After all, Hertz never intended this study for contact mechanics

manner in the past, early scientific studies on wear phenomena on coins observed that the quality of wear depends on the material pairing. [10] Early quantitative approaches were made by John Frederick Archard proposing the proportionality of wear debris volume to applied work in 1950s [11], which is fundamentally based on the energy dissipative hypothesis by Karl Theodore Reye in 1860 [12] and on the asperity model.

The two main objectives of discussion on wear revolve around the quality and quantity of generalised loading and of the tribo-system. For the **loading component**, the key contributing factors is contact stress; further factors like temperature, corrosion, and ageing are discussed later in section 2.3.4. Setting aside the loss of material due to melting or evaporation, a surface deteriorates by means of physical separation or chemical reactions. The four major wear mechanisms for those to occur are based on **adhesion**, **abrasion**, and **surface fatigue** for the former, and **tribochemical**/-physical **reactions** for the latter.

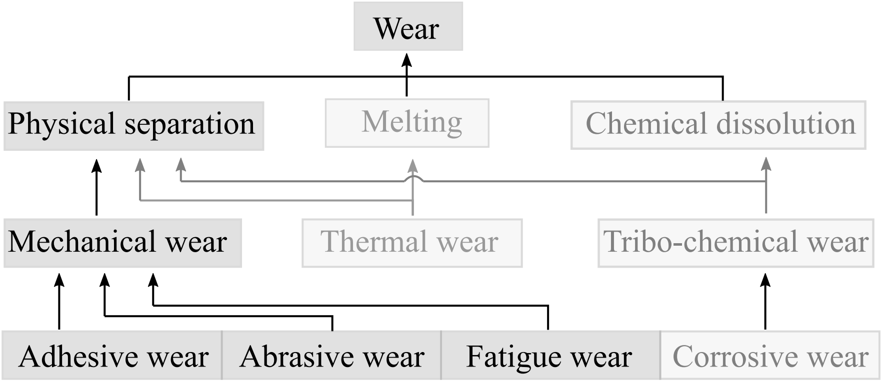

Figure 2.25: Categories of wear in thin film surfaces. Wear in other forms of contact is omitted. Adapted from textbook [128].

Mechanisms for physical separation require energy. In a simplified picture, energy of the tribo-system is *misguided* to take effect on the material. Adhesive wear is typical in *sliding* contact, the arising wear is captured in Archard's law

$$V_{\mathrm{adh}} = k_{\mathrm{adh}} \frac{F_N \cdot s}{H}, \tag{2.22}$$

which connects the wear debris volume V_{adh} to the normal force F_N and sliding distance s. Two parameters to control the volume V_{adh} is hardness H of the material and a dimensionless proportionality factor k_{adh} capturing tribo-system parameters. Abrasive wear at its core is *cutting* or *scratching*. It is most common in unlubricated contact in general, in intermittent contact like *hitting* or *splashing*, or accidentally by the presence of hard third bodies in the tribo-system. Rabinowicz's law connects the arising wear debris for abrasive wear

$$V_{\mathrm{abr}} = k_{\mathrm{abr}} \frac{F_N \cdot s}{H}, \tag{2.23}$$

in a strikingly similar fashion as Archard's law. Again, the two parameters to control the wear energy are the hardness H of the material and a proportionality factor k_{abr}. Surface fatigue is a more complex wear mechanism at periodical loading. It is fundamentally the initialisation of miniature cracks at the surface or even in the underlying material, which might be undetectable for a certain time. The expansion of those cracks leads over time to macroscopically visible delamination with characteristic phenomena like *pitting* in Figure 2.26, for example. These three mechanisms naturally generate **wear particles** by physical separation. One way to quantify wear is the measurement of wear particles volume as a function of friction work $F_N \cdot s$, wear rates span a huge range of $1 \times 10^{-15}\,\mathrm{mm}^3/\mathrm{Nm}$ to $1 \times 10^{-1}\,\mathrm{mm}^3/\mathrm{Nm}$. [128, p. 787] It is not uncommon for those wear particles to accelerate preceding or to initial further wear mechanisms, for example, wear particles generated slowly by adhesive wear over time then leads to abrasion with characteristic *ploughing* effects as in Figure 2.26 for reference.

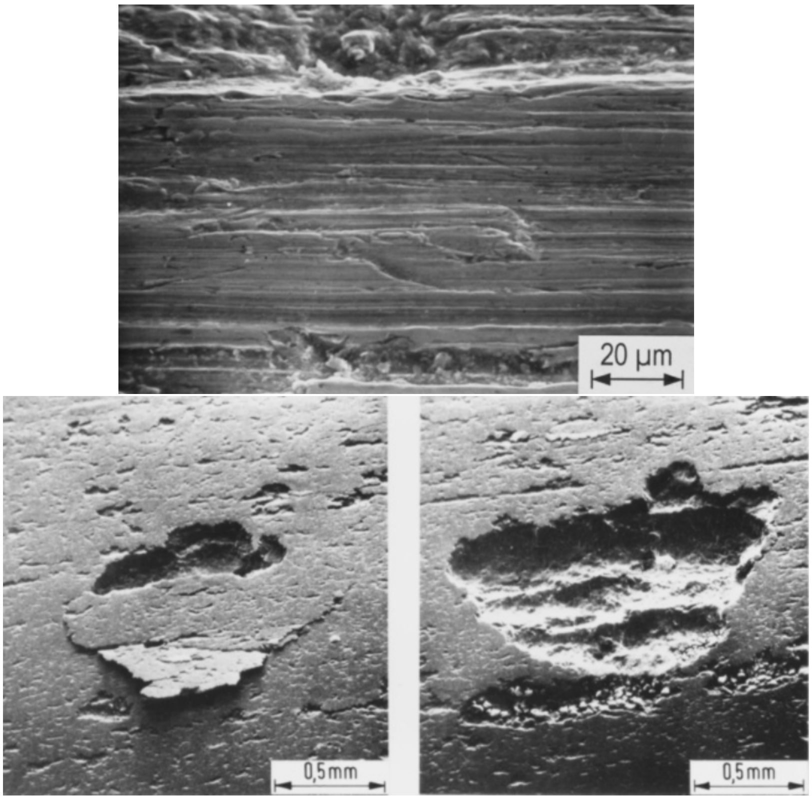

Figure 2.26: Example pictures for abrasive wear **(above)** and surface fatigue **(below)**, common picture for severely-worn rolling contacts. Taken from textbook [133], original pictures of surface fatigue in VDI guideline 3822 [134].

Chemical reactions impact the surface quality. In the simplest case, surface exposure to humidity and ambient oxygen results in naturally occurring oxide phase at the surface. If those oxides have identical or very similar properties in comparison to the unadulterated material, the wear situation would remain unchanged. [128, p. 295] Most oxides, however, differ considerably, for example, most oxides are harder than the bare metal and their adhesion to metal is typically weak. In a nutshell, the requirements for the generation of hard third-body wear particles are easily fulfilled.

On a final positive note on wear, the generation of wear particles for tribo-film formation play a crucial role [135, 136, 137, 138] but, of course, has to be kept in balance as excessive wear rates are obviously undesirable. Even in thin film systems which are known for high oxidative resistance and little wear, the absence of a certain degree of wear debris leads to an increase in oxygen-induced corrosion. [132, p. 214] In case of tribo-corrosion, oxides of a metal surface being harder than the metal may also become beneficial. As a part of the tribo-system, the task of lubrication is assigned to softer lubricants like MoS_2 powder, while the load carrying is assigned to the oxide of iron. [139]

2.3.3 Fluid-free lubrication: thin film lubricants of a-C and MoS_2

To fight against both friction and wear on bare contact interfaces, it is common to use fluid lubrication like oils and grease in technology and water-based compounds in nature. To its disadvantage, fluid lubrication is not fail-safe and bares a significant point of failure in machines. When such fluid lubricants are no option, for example in extreme conditions like very high or cryogenic temperatures, extreme contact pressure, or in vacuo, a modern approach is to apply fluid-free thin film lubricants. [128, p. 787] A recommended review on solid thin films is found in literature [140].

This work focusses on two classes of such thin films, namely amorphous carbons and molybdenum disulphide, both feature one of the lowest coefficients of friction within their designed working environment. [128, p. 793]

a-C and a-C:H thin film lubricants

Carbon is a unique element, whose most common allotropes span from one of the softest materials, graphite, to one of the hardest naturally occurring materials, diamonds. For being naturally occurring and (more or less) easily accessible, the dust of graphite might have been used for lubrication since ancient times. The usage of advanced carbon allotropes or -compounds in engineering gained momentum in the last few decades: In 1970s, artificial diamonds were of key interest in machining tools for their hardness, although being comparatively expensive. Diamond-like carbons, in fact, predated artificial diamonds by roughly 20 years, but scientific interest and systematic studies grew at first in 1970s to accommodate the efforts and poor scalability of diamonds. [128, pp. 871–874]

Amorphous carbon (a-C) are a metastable and short-range ordered structure of carbon with varying bonding lengths and -angles, the carbon atoms are mainly sp^2 or sp^3 hybridised and may be exposed to structural clustering and hydrogenation. [24, 141] The proportion of carbon hybridisation, which is closely linked to its spatial density, is tailored by deposition parameters of the growth technique specifying, in turn, the mechanical features of the a-C structure [42, 48, 141, 142, 143, 144]. Manufacturing even in moderate temperature environments on a manifold of material substrates is possible and beneficial for coating in cutting applications, because high temperature deposition of thin films, in contrast, might lead to thermal hardness loss of the substrate. [145, p. 466], Hydrogenated amorphous carbon (a-C:H) possesses a hybridised network similar to that of a-C, but with a few key differences: on the one hand, hydrogen stabilises the carbon sp^3 hybridisation by the formation of strong C-H bonds and, on the other hand, a high hydrogenation acts as barrier to the sp^2 clustering by defining carbon chains. [146] Both increase the mechanical resistance of the film and prevent its collapse into the thermodynamically stable phase of graphite. [128, p. 888] This variety opens up a broad spectrum for employing a-C thin films. As hard thin film, a-C is used for a manifold of scientific and technological purposes, which benefit from its rich electrical, optical, and mechanical properties [48, 147, 148]. Its intrinsic friction and wear behaviour [46, 65, 149, 14] is valued in sectors like automotive industry[10], aeronautics, or biomedical applications [150, 151, 152, 153, 154, 155] to name a few. Even when their intrinsic lubricating properties are not the primary objective, carbon and carbide thin films are used for conditioning of surfaces and finishes in general [156, 157, 158]. Chemical inertness and gas impermeability is used for storage of food and beverages. [159, 160]

The friction of a-C thin films show a broad range of COF, which is a staple of their versatility. Depending of their design and working environment, a value range in coefficient of friction μ of 0.003 to 0.6 are reported. For wear, the lack of standardised quantification renders a precise comparison of literature data difficult, but estimates give a lowest possible value in wear rate of $1 \times 10^{-8}\,\mathrm{mm^3/Nm}$. [128, p. 892] Self-forming films of carbon are found in machine parts after break-in. Direct comparison of such films and designed thin films of a-C revealed their similarity.

A key drawback of a-C and a-C:H structures, however, is their thermal instability potentially leading to (allotrope) conversion of the carbon network [24]. For this, carbon alone is not the limiting factor: applied as part of surface finish, thermal spraying an iron-carbon compound is used in cylinder bores of diesel engines for passenger vehicles (e.g. “Nanoslide” by Daimler AG, 2011). DLC is also used in internal combustion engines, but mostly restricted to areas without direct contact of the combustion, e.g. camshaft, piston ring /-pin, and valve lifter [161], which are traditionally coated with titanium or chromium nitride. By coating with hydrogen-free DLC, the Nissan Motor Corporation reports friction reduction of 40% for the involved parts and the friction reduction of 25% overall. Notably, however, the aimed friction reduction mechanism is to bind additive-modified engine oil to the surface, even though the inherent tribological performance of DLC is noted. [158] To accommodate such shortcomings or to modify the surface properties like specific applications like hydrophobic or bacterial inhibiting, a set of element-modification is applied to alter a-C and a-C:H thin films.

Molybdenum disulphide thin film lubricants

Transition-metal dichalcogenides (TMDCs) are comparatively old material class, which are well studied in the last 100 years. [16, p. ix] At its core, the friction reduction mechanism is based on the lamellar structure of TMDC, the weak interaction of individual layers allows for sliding with exceptionally low shearing forces. Of those, MoS_2 is one of the most investigated samples, albeit being of interest today for more complex purposes than simply lubrication.

The friction of MoS_2 thin films are well-esteemed in vacuum applications, in which they reach exceptionally low values in the range of $\mu = 0.002$ to 0.01. For this to function as intended, (mechanical) resistance against sliding shall remain the weak van der Waales-interaction between layers in a perfect basal orientation, see Figure 2.27. However, optimal friction values are often reported, on the contrary, for the concurring columnar structure, which wears out considerably faster and forms a tribo-film *in situ*, which ultimately reduces

---

[10] from classic internal combustion engines to new technologies like fuel cell- and battery-electric vehicles

friction and prevents (further) wear. Such a tribo-film builds up after wearing the top part of columnar structures and, by that, revealing the smeared out basal planes parallel to the sliding direction.

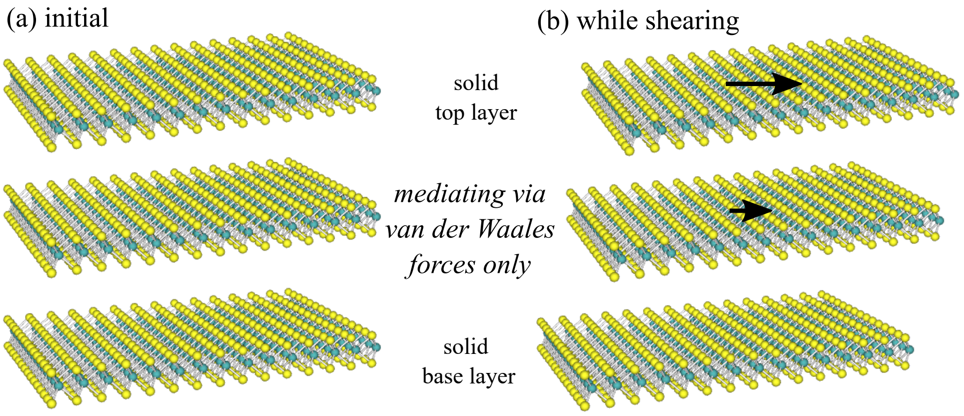

Figure 2.27: Layered structure **(a)** and the resulting friction mechanism **(b)** in MoS_2 thin film lubricants. The weak inter-layer van der Waales forces allow for easy shearing between layers. Picture adapted from textbook [162].

To some degree, the friction in MoS_2 is resilient against influences of temperature and weathers treatment in most acidic environments unlike oils and grease [128, pp. 794–795], but just as in a-C thin films, the applications are limited to low temperature and water-free applications. In more detail, moisture in ambient air diminishes the usage, temperatures above 375 °C lead to initial oxidation, and, at last, rapid oxidation is expected above 500 °C. [163][128, p. 794]

Again, to accomodate such shortcomings and to modify tribological properties, a selection of element-modification is reported. For example, metals or metal-compounds were studied from 1980s onwards and reported (one-sided) property improvements, which allow for application-specific tailoring, refer to textbook [128, p. 796] for an overview; for example, an amorphous structure in MoS_2 is reported to be beneficial if wear rate is the key concern.[128, p. 797]

2.3.4 The tribo-system at nano-scale: focus on tribo-film and working environment.

The tribo-system is comprised of a *tribo-pair*, the *intermediate* like lubricant in the contact (or lack thereof), and the *environment.* In dry sliding, the real contact is vastly smaller than the apparent contact area as discussed in Figure 2.24, wear phenomena lead to third-body material, which was formally a part of the tribo-pair and may now take a role - beneficial or noxious - in the intermediate. It shows that the situation is a multi-scale phenomenon, this work mostly enlightens the situation in nano- and micro-scale tribology, i.e. chemical/structural properties and transitions as well as the occurrence of wear phenomena. Of most importance are (a) formation of a tribo-film and (b) the impact on the working environment, onto which this work aims to set the focus.

Tribo-film, distinction from transfer films

Although being undoubtedly beneficial for friction reduction, a clear definition of a tribo-film with scientific rigour is still missing. The possibility to tap into the the mechanisms of the tribo-film formation and possibly to gain an understanding for its conditioning is still an object of research. The core difficulties lay in the obscure nature of the tribo-contact: it is usually not (optically) accessible, dependent on an overwhelming number of factors, and lack standardised testing environment or setup for *exact* replication of experiments. [30] Even on a more basic level, there are no predicting models for friction and wear derived from first principles.[30]

Extrinsic (extraneous) films appear on tribo-pair surfaces rather than being a element of the intermediate. For a simple phenomenological definition, a transfer film is the type of extrinsic film, which forms on one half of the tribo-pair and consists or is derived from material of the counter-part in the tribo-pair. The tribo-film, complementary, is formed on one tribo-pair and consists or is derived from material of itself. Observations in a-C thin films identify the formation of transfer films on counter-bodies, which places a intermediate sliding mechanism at the disposal.[128, p. 893] Similarly, the formation of MoS_2 tribo-film in a robust basal configuration, which differ from its initial structure in sputtered thin films (amorphous or columnar) is often observed - also in investigations of this work. This formation is always connected to loss of material from the tribo-pair (thin film), detached material is re-deposited onto the tribo-pair to from a extrinsic film. In this light, it raises the question whether the definition of wear needs a re-definition to distinguish between unusable material loss and material reuse as extrinsic film or as an intermediate.

Working environment in ambient air: Oxygen content, Humidity, Temperature

It is common knowledge in lubrication engineering that no substance works as universal lubricant for every conceivable application. Such conditions range from the environment's reactivity like content of oxygen, over radiation, vacuum, or extreme contact pressures to simply a range of temperatures. [128, p. 787]

For **humidity**, Figure 2.28 gives an impression on the importance of humidity in a-C and a-C:H thin films. The effect was first found in graphitic lubricants in vacuum and inert environments, in which accelerated wear and the generation of wear debris particles posed a problem termed “dusting”. [132, p. 208] In case of a-C and a-C:H, the friction behaviour is strongly dependent on relative humidity. For a-C, the absence of ambient moisture (and comparable passivating agents) lead to high friction, which is comparable to the dynamic friction between bare unlike metal pairings, that is $\mu = 0.4$ to 0.7. For increasing humidity, the initial high friction first remains high before dropping to the renown value range below $\mu = 0.2$. For a-C:H, the friction in dry atmosphere starts exceptionally low, in the super-low friction range $\mu = 0.001$ to 0.02, and worsens for increasing humidity. Likewise, the effect sets in after a barrier value of humidity is reached. The two opposing trends have two factors. In a-C, the dangling bonds remain unsaturated and yield a high interaction rendering bare a-C unsuitable for vacuum applications. With increasing humidity, the majority of dangling bonds are saturated, so the underlying mechanisms of friction reduction, e.g. incommensurable surfaces for *superlubricity* (structure-based ultra-low friction), become apparent. Eventually, a stable value is adapted for the high humidity range, in which

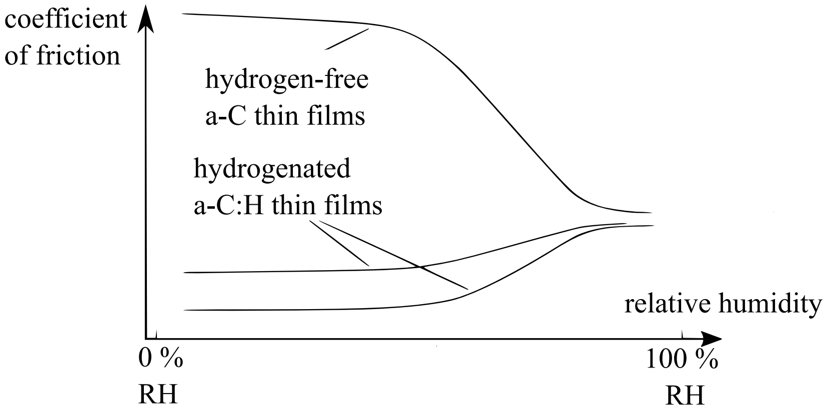

Figure 2.28: Environmental effects on the frictional performance of diamond-like carbons, coefficient of friction against humidity.

the friction reduction mechanisms are counteracted by capillary forces, that is, a water meniscus forming between the tribo-pair. For a-C:H, in the high humidity range, the same explanation is true, ergo, comparable values are found. Without the capillary forces of water, however, the full effect of incommensurate surfaces makes an impact without being hindered by highly interacting dangling bonds. Those dangling bonds in a-C:H are well saturated by the hydrogen content or likewise by comparable passivating agents. This shows that even within a material class of thin film lubricants, the effect of the environment can be diametric.
Upcoming capillary forces upon increasing humidity is essentially the same for other thin films lubricants, so by basic means, a similar effect is expected in MoS_2- as for hydrogenated a-C thin films. The comparison is made to a-C:H, because dangling bonds are not expected in sputtered MoS_2. While the general friction behaviour does, in fact, resemble that of a-C:H, both the friction reduction in dry environments and the friction increase in humid one arise from different friction mechanisms. The underlying mechanism for increasing friction is based on chemical reaction and wear particle build-up. In vacuo, MoS_2 reaches friction values in the super-low range. [164, 165] Contrarily in high humidity, water molecules adsorb on crystallite edges and hinder crystallite alignment or layer shearing, which impedes the basic friction-reduction mechanism in MoS_2 or leads to excessive wear in the extreme case. [164, 165] In ambient air, still, the performance of MoS_2 is satisfactory ($\mu = 0.15$ to 0.3) thanks to the formation of a MoS_2 tribo-film, which comes at a cost of (high initial) wear.

For **temperature**, solid lubricants excel the performance of its fluid trade rivals. Friction behaviour in solid lubricants like a-C and MoS_2 is athermal in low temperature ranges, while fluid lubricants rarely perform as intended, at last below 170 K. [164] Although a direct influence of temperature in MoS_2 friction is reported in literature, it was found to be “athermal” for temperatures above freezing point of water. [166] In this work, all effects of temperature on friction behaviour are indirect like initial oxidative processes. Much like in a-C, MoS_2 thin films are limited by their thermal stability, which in the present form is quantified to be 400 °C at least. [130, 163] Its tendency to chemical reactions imposes further problems like (premature) oxidation, chemical reactions, or restructuring. By comparison of chemical reactivity of crystalline bulk-MoS_2 to highly defected MoS_2 powders, it is apparent that chemical stability is connected to structure features like exposed crystalline edges, and indirectly linked to environment like oxidative agents or masking effects. [138] In short, temperatures up to 200 °C show the decrease in friction as water is leaving. This effect is enhanced by films properties inhibiting water adsorption, e.g. as in sub-stoichiometric films. Secondary, ordering processes set in, which is beneficial for tribo-film formation. Such ordering processes are discussed in detail in upcoming chapter, section 5.3. For higher temperatures, naturally, oxidation processes gain momentum, which ultimately leads to film loss at 400 °C. On the note of temperatures setting of chemical reactions, the same arguments are valid for **reactive environments** or for **catalysts** present, even in moderate temperatures. Thin films of a-C are notoriously inert, but MoS_2 thin films are reported to slowly corrode at ambient temperatures in pure oxygen environments. From the perspective of chemical reactions, some reactions require a protic solvent or an oxidising/reducing environment, for example, the reaction pathways (2.7) in the previous section.

The dependence on **contact pressures** is a curious case, a specialty in MoS_2 thin films. Best performance is reported (and repeatedly found in the publications or in the course of this study), for elevated contact pressures, while no clear dependence is found for a-C derivates. The (tribo-)contact pressure is essential for **tribo-film formation**. For this, a initial columnar structure and a strong generation of wear particles, which adhere to their surroundings in such a way that they do not leave the tribo-contact and are available for tribo-film formation, is the most desirable path. A dense microstructure with columnar growth, which is in fact a clear weak point for oxidation or humidity-related reaction as described above, leads to a quick generation of tribo-films. The friction of initially columnar structures and effective tribo-film formation exceeds the friction of initial basal orientation. [167]

Chapter 3

Experimental details and Methodology

In this chapter, experimental setup and methodology are presented. This work aims to subsume structural and chemical analysis via spatially-resolved Raman spectroscopy. Moreover, the nature of that concept shall allow for resolving enmeshed structural and chemical transitions, which occur as consequence of over-boarding tribological loading or excessive temperatures. This chapter is divided into sections for each broad topic - sample preparation, spectroscopy and data acquisition, optical temperature tuning and - measurement.

3.1 Sample preparation via Physical Vapour Deposition

Physical Vapour Deposition (PVD) is a manufacturing procedure of thin films. In 2001, the main processes for a-C thin film manufacturing are magnetron sputtering -, mass-selected ion beam -, cathodic arc -, and laser plasma deposition [168][128, p. 889] of which (pulsed) magnetron sputtering is still reported to be widely used in the industry [106], the situation for MoS_2 thin films is similar [169][128, p. 794].

In a simplified picture, the material of the desired thin film for a **substrate** is placed as **target** in vacuum and bombarded with highly energetic ions of a process gas, which knock out target material to be deposited on the substrate. In magnetron sputtering, the target is kept on a negative potential acting as a **cathode** and surrounded by a static magnetic field. This potential, the **bias voltage** U_{BV}, is often applied on the substrate to increase the film growth. The combination of both fields force the process gas ions in spirals towards the target for a considerably higher collision rate. While the exact involved mechanism is not thoroughly important for this thesis, some depositional parameters have a strong influence on film properties.[106, 170] As such, the **cathode power** P_{CP} is a measure of the bombardment of the target (cathode), which would ultimately heat up excessively. By pulsing, the thermal stress can be effectively reduced, because the sputtering yield is connected to the maximum peak power while the thermal load is connected to the average power equivalent.[171, 172]. The pulsing parameters like pulse length or frequency are omitted for this work, they were found to be subordinate in previous studies of the workgroups. [173]

As preparation steps, the PVD sample chamber is evacuated (below 1×10^{-4} mbar) and heated (above 100 °C) for humidity reduction. After roughly cleaning the raw steel substrates with alcohol, deeper cleaning is obtained by plasma-etching with highly ionised process gas, usually Argon and Krypton. During deposition, Argon is the only process gas with a pressure of $p = 300\,\mathrm{mPa}$ or 3×10^{-3} mbar.[146, 174]

Substrates

Samples are usually deposited on steel substrates, see Figure 3.1 for visual reference. The type of steel substrate varies over the samples of this thesis, but is assumed to be subordinately important. This assumption is based on the usual thickness of the film of roughly 1 µm (deviating thickness are larger), the laser penetration depth of at least one order of magnitude below even with “pessimistic” estimation.[42, p. 718]

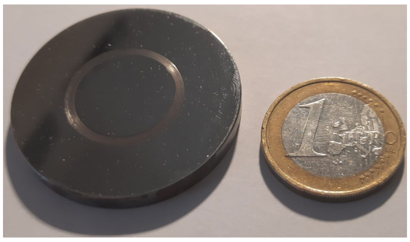

Figure 3.1: Picture of a representative sample of this work: a thin film deposited on metal substrate (40 mm diameter, 5 mm thickness). The surface is reflective, a concentric wear scar after ball-on-disk tribometer testing is visible.

Most **steel materials** for the substrate are commonly used **for tools**. [146] The samples are deposited on quenched and tempered *hot work-tool steel* [1] (for a-C:H with varying hydrogenation, a-C:Cu, a-C:Ag) [146, 175] and case-hardened *cold work-tool steel* [2] (for a-C(:H)(:X) with X ={Si, W} & for MoS_2 in different environments and MoS_2:X with X ={N, Cu}). For some studies in biomedical applications for a-C, a **titanium substrate** Ti6Al4V was chosen, which is commonly **used for protheses**. [176] The hardness of the raw substrate is known to impact the tribological performance of the final product, all steels have a hardness of (8.4 ± 0.4) GPa. An arithmetical mean roughness roughness of $R_\mathrm{a} = (3.1 \pm 0.6)$ nm for steel and $R_\mathrm{a} = (4.2 \pm 0.2)$ nm for titanium is usually obtained after grinding and polishing for all samples. [65, 138, 146, 174, 177] As preparation steps, e.g to remove impurities, steel substrates are usually either etched with in higher temperatures and bias voltage of about $U_\mathrm{BV} = -650$ V or treated with a special HiPIMS pretreatment. [177, 178]

Amorphous carbons and hydrogenated amorphous carbons

Thin films of a-C show a far improved film adhesion, when the sample layer is deposited on a mediating interlayer over the substrate. [176, 178] More specifically, the interlayer on steel substrates is a carbon-graded interlayer system of (a) CrN to CrCN to CrC or (b) Cr_xC_y only; interlayer on titanium substrates consists of carbon-graded Ti_xC_y. The interlayer is $2-3$ µm thick and provides a hardness of ≈ 13 GPa, refer to the respective publications [65, 146, 176, 178] for details.

For pure a-C thin films, purified graphite targets (purity at least 99.9%) are sputtered with cathode power $P_\mathrm{CP} \approx 2$ kW and a bias voltage $U_\mathrm{BV} = -100$ V [65]. The deposition time t_DT was set to achieve sample layer thickness d_layer of roughly 1 µm (usually 3h). For

---

[1] by DIN EN ISO 4957 standard: 1.2343/X37CrMoV5-1 - also: AISI H11

[2] by DIN EN ISO 4957 standard: 1.7131/16MnCr5 - also: AISI 5115/5117,

hydrogenated a-C:H thin films, additional injection of hydrocarbon (acetylene gas, C_2H_2) at a flow rate (FR) of 15 sccm (standard cubic centimetre) implements the hydrogenation. Additional heating along or after deposition ("annealing") is not discussed. By experience with deposition of a-C(:H) samples, a range of deposition parameters became the standard. These encompass cathode power $P_{\mathrm{CP}} = 2\,\mathrm{kW}$ to 2.1 kW and bias voltage $U_{\mathrm{BV}} = -83\,\mathrm{V}$ to −197 V. For a-C:H, the addition of hydrocarbon gas is influenced by the flow rate between 5.9 sccm and 3.4 sccm. [146] For element-modified a-C:X and a-C:H:X thin films with X={Si, W, Ag, Cu}, co-sputtering graphite targets with targets of the respective metal yielded the desired modification, refer to publications [65, 175, 179].

Molybdenum disulphide

Sputtering unmodified MoS_2 thin films is done by sputtering commerical MoS_2 targets with 99.95% purity with cathode power $P_{\mathrm{CP}} = 3\,\mathrm{kW}$, bias voltage $U_{\mathrm{BV}} = -100\,\mathrm{V}$ and additional heating power $P_{\mathrm{heat}} = 1\,\mathrm{kW}$ (yielding temperatures of 125 °C to 200 °C) for all samples. For nitrogen modification, the mere injection of nitrogen into the deposition chamber is sufficient, whose flow rate (FR) is controlled for graduated nitrogen content, qualitatively 20 to 120 sccm in steps of 20 sccm. For copper modification, copper targets are added to the target setup, the content of copper is controlled via the cathode power P_{CP} of 0.1 kW and from 0.5 to 2.5 kW in steps of 0.5 kW. Resulting sample characteristics are listed in Tables 3.1 and 3.2. Exact thickness of the sample is often left undetermined, but it is usually in the range of 1 µm to 5 µm. [174] Further details on manufacturing are found in publications [138, 177].

Cathode power P_{CP} (kW)	Cu content (at.-%)	Mo/S stoichiometry
0.1	3.1 ± 0.2	1.82
0.5	10.5 ± 0.1	2.05
1.0	19.5 ± 0.2	2.26
1.5	28.0 ± 0.1	2.20
2.0	30.0 ± 0.1	2.81
2.5	31.9 ± 0.1	2.57

Table 3.1: Sample list of copper-modified MoS_2:Cu thin films

N_2 flow rate (sccm)	N content (at.-%)	Mo/S stoichiometry	thickness (µm)
20	7.1 ± 0.3	1.77	3.0 ± 0.1
40	11.0 ± 0.4	1.61	3.1 ± 0.2
60	12.4 ± 0.2	1.54	2.8 ± 0.2
80	13.3 ± 0.3	1.49	2.4 ± 0.1
100	19.5 ± 0.5	1.4	2.1 ± 0.1

Table 3.2: Sample list of nitrogen-modified MoS_2:N thin films

3.2 Raman Spectroscopy and Data Acquisition

3.2.1 General Raman spectroscopy

Raman spectroscopy is well-suited for semiconductors as well as non-conducting materials, that is, materials with a considerable band gap E_g. Metals, in contrast, often do not fulfil the requirements. Raman spectroscopy requires three base instances: excitation, filtering, detection. [69] These instances are only loosely dependent from another, which allows for adjusting the setup for a given measurement aim.

For **excitation**, lasers provide photons with defined photon energy $E_{\mathrm{Ph}} = \hbar\omega_{\mathrm{Ph}} = hf_{\mathrm{Ph}}$. If the band gap E_g of a material is energetically overcome, the Raman signal is usually vastly overshadowed by fluorescence - roughly estimated, one photon by Raman scattering vs. millions photons by fluorescence relaxation [20][70, p. 3]. So, to an extent, the band gap E_g of the sample material is the upper bound on excitation energy E_{Ph}, up to which non-resonant Raman scattering is not hindered by fluorescence. The lower bound is not strictly set, however, the Raman scattering intensity is dependent on the fourth power of frequency f, which renders the aim of choosing the highest possible excitation frequency without fluorescence side effects. Raman spectroscopy was originally done by using delicately filtered sunlight. Modern lasers provide a range of different benefits and accelerated Raman spectroscopy usage. They provide sufficiently intense, (mostly) monochromatic, and (diffraction-limited) collimated light beams with a distinct polarisation and large coherence time. High coherence and polarisation do contribute to derivations of Raman spectroscopy, but are mostly disregarded in this work.

Filtering is divided into filtering by means of light intensity or by polarisation (other term: **analysing**). For one, the elastically scattered light is vastly more intense than Raman-related light emission. Yet, by nature of the Raman effect, the inelastically scattered light energy is directly related to the incident laser energy, rising the need to simultaneously measure elastically and inelastically scattered light. Not only would the lack of wavelength-specific damping overshadow the “true” signal, the sheer intensity would put detection equipment afterwards in danger. So, for filtering, a long-pass or notch filter are required for damping of laser light or Rayleigh-scattered light. Notch filter allow for measurement of both Stokes- and Anti-Stokes light, while long-pass filters usually have a higher transmission compared to notch filter. In this thesis, the Anti-Stokes signal is disregarded and elastically scattered light placed the outside the region of interest (ROI) of the detection. Because of the amorphous nature of the samples, polarisation-sensitive **analysing** the filtered light is less important and only conducted rarely in the underlying investigation to the thesis.

The requirements for light **detection** are shallow compared to regular equipment in scientific optical laboratories. The excitation usually lies in the ultraviolet- or visible range of light, thus, a Peltier- or liquid-nitrogen cooled charge-coupled device (CCD)- spectroscopy camera, is sufficient as detector. Nearly all regular Raman signatures are within the range of $-100\,\mathrm{cm}^{-1}$ to $3600\,\mathrm{cm}^{-1}$, the most interesting usually in the range of $30\,\mathrm{cm}^{-1}$ to $1700\,\mathrm{cm}^{-1}$. [70, pp. 76, 211]

A resolution of $1\,\mathrm{cm}^{-1}$ is said to be sufficient. [70] For the samples used in this thesis, broad peaks are expected, which renders any practical spectrometer resolution usable. The detector mostly defines the sensitivity and by this, the sampling duration. This is especially important on sensitive samples, which need excitation laser damping.

3.2.2 Confocal Raman microscopy, *MonoVista* setup

In the course of this thesis, the concept of Confocal Raman Microscopy is used. It presents immediate advantages over the coarser (macro-) Raman spectroscopy outline above, in short: (a) light is filtered except for scattered light out of the focus level for vastly improved signal-to-noise ratio, (b) a depth resolution is (more finely) defined for (semi-) transparent samples, (c) a considerably smaller region on the surface is investigated with at a time for a finer spatial resolution, and (d) setup is easily extendable by a microscopy camera for visual capture.

The working principle is depicted in Figure 3.2. Incoming light for excitation is coupled into a microscope setup and redirected through the focussing apparatus onto the focussing level, usually the sample surface.

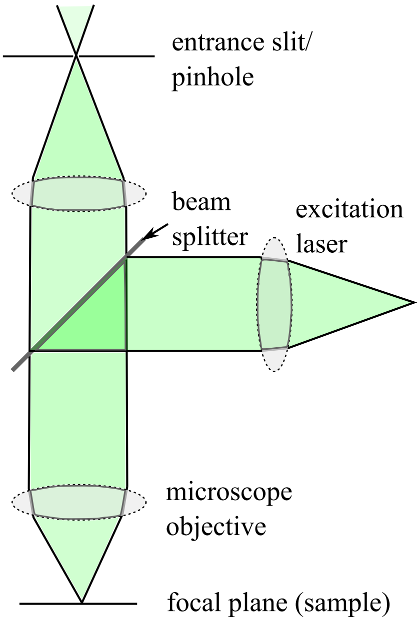

Figure 3.2: Schematic concept of confocal microscopy

Coupling may be done, for example by means of a beamsplitter for infinitely corrected microscopes as shown in the schematic 3.2 or of a smaller focussing mirror (not shown). At the focussing level, due to the nature of the beamsplitter, a fraction of the initial intensity is focussed onto a spot, whose size is dependent on regular optical considerations like beam waist and microscope objective parameters. After light scattering, the same microscope objective captures the light and focusses onto the optical path after the microscope. This backscattering geometry is reported to be the most efficient geometry, while a 90 degree geometry was applied in early studies, which yield roughly half of the intensity in backscattering. Only specific Raman measurement task are reported to be affected by scattering geometry. [180]

This latter optical path, in a nutshell, then filters and redirects the captured light in a similar manner as described for the non-confocal case with a difference of a critical component for confocality, the entrance slit or pinhole. Before entering the detection apparatus, confocality requires focussing the captured light onto a entrance slit, usually in the range of a few tens or hundreds of µms. This key component is responsible for filtering (stray) light at the entrance slit, which stems from other layers than the focus level. An alternative pathway of undesirable (stray) light from other sources does not pass the entrance slit. Raman microscopy on µm-scale, combined with a suitable fine-scale translation table, allows for automated mappings across a sample surface and to capture spatially diverse characteristics, e.g. on tribo-films and redeposited wear debris. For a-C, especially, a more refined spectrum for an in-depth investigation of the D-Raman peak is reported in comparison to macro-Raman setups. [181] For (semi-)transparent samples, a three dimensional focus volume has to be taken into consideration rather than a two-dimensional focus area. On that note, the penetration depth as in section 2.2.1 is key parameter for estimation.

In more detail, this work uses a commercial Confocal Raman Microscope as basis. This system - the 2005 MonoVista CRS+ (hereinafter referred to as “MonoVista”) by Spectroscopy & Imaging GmbH, Warstein, Germany - supplements the basic instances, the excitation by a microscope-based focussing and the filtering by confocality. A scheme of the used Raman setup is shown in Figure 3.3. Here, the setup is mainly used with 532 nm diode-pumped solid state laser (narrow natural bandwidth below 1 MHz), and a 633 nm HeNe gas laser with a narrow clean line filter for suppression of collateral laser modes. The linear polarisation of the laser is adjustable by an achromatic fresnel rhombus. Through the course of this work, the polarisation is set to the maximum intensity measured at the objective and unaltered upon. Excitation power is set to the upper bound of damage threshold for maximum signal-to-noise ratio. Although a laser power of 0.1 mW (equals power density of 400 W m^{-2}) is often assumed to be harmless for the sample [182], samples with micro- to nano-scale structures and high absorption rates are shown to degenerate.

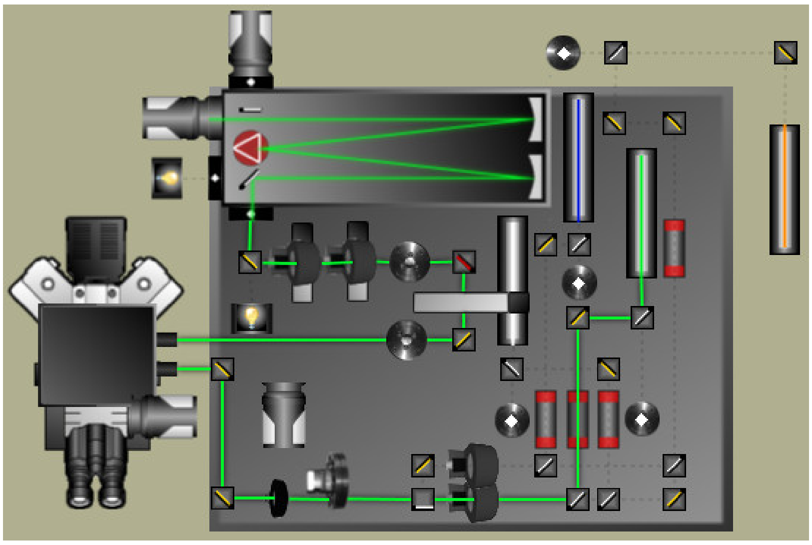

Figure 3.3: Schematic setup of the MonoVista CRS+ Raman Microscope, schematic by manufacturer’s software

3.3 Fit modelling in Raman spectroscopy

From the Raman spectroscopy setup, more precisely, from the analog-digital converter of the CCD, the raw spectrum contains an ordered list of calibrated spectral position and the accumulated intensity.

3.3.1 Fitting of a-C Raman spectra, standard fitting procedure

In fundamental works on Raman spectra of amorphous carbons, “no a priori reasons [exists] to choose a particular function to fit the spectrum” [101]. Graphitic samples like highly oriented pyrolytic graphite (HOPG) features purely Lorentzian-type Raman peaks, amorphous carbon are often assumed to have Gaussian-type Raman peaks. The later is problematic, because the origin of the D-Raman peak is not easily explained as for other Raman peaks, see details of double resonance Raman scattering and the peak-related sections 2.2.4 and 2.2.5. This means that the differentiation in Lorentzian- and Gaussian-type line profile is lacking for a-C, anyway. Furthermore, amorphous carbon should not be seen as fully disordered, glass-like network, but rather as short-range ordered network, which may contain ordered regions. Note, that another allotrope of carbon is glassy carbon - a fully sp^2 ordered, non-graphitising carbon network, which is not related to the amorphous carbons as discussed. To accommodate all these points, new aspects of Raman spectra fitting for carbons are proposed and published.[92] It is not the scope of this work to evaluate the exact choice of the model, but to chose an appropriate model for the investigation and deduce information cautiously. As such, the key feature of the upcoming investigations are the shift from a highly disordered case over a phase transition to the defected graphite case. From the Gaussian- to the Lorentzian-type Raman profile, the transition is best adopted by a Voigt or Pseudo-Voigt model, see equation (2.18).

As automated procedure, see truncated code in appendix 6.2.2,

- a raw data file from the spectrometer is cropped to the spectral range ($950\,\mathrm{cm}^{-1}$ to $1850\,\mathrm{cm}^{-1}$ for first-order and $2000\,\mathrm{cm}^{-1}$ to $3440\,\mathrm{cm}^{-1}$ for second-order peaks),
- a linear background is added to the fitting model,
- a pseudo-voigt peak models are added to the fitting model, two for first-order and four for second-order peaks.

The script works with and requires the *python3* libraries *numpy* for data processing, *matplotlib* for plotting, *uncertainties* for automated error propagation, *lmfit* for standard fitting routines and -modelling, and *os* for file handling. The model fitting details are found in the documentation online. For initialisation, the background fitting has a strongly detuned initial value for slope as 0.5, the peak modelling starts with a pseudo-voigt peak with width σ of $150\,\mathrm{cm}^{-1}$ at Raman shift ν of $1375\,\mathrm{cm}^{-1}$ and another with width σ of $50\,\mathrm{cm}^{-1}$of $1600\,\mathrm{cm}^{-1}$ for the D- and G-Raman peak, respectively. Optional value boundaries, see program code in appendix 6.2.2, ensure fitting stability.

Figure 3.4 shows the output of the fitting routine. As legitimation, the structural evolution in chapter 5 were also fitted with a pure Gaussian fit model and with a voigt model beforehand, yet, the trends in Raman shift, FWHM, and Intensity ratio remain.

3.3.2 Fitting of $\mathrm{MoS_2}$ Raman spectra

Molybdenum disulphide spectra are rarely fitted in this work, most statements refer to the visible occurrence/strengthening of $\mathrm{MoS_2}$ or its oxides signal intensity. In literature, the first-order $\mathrm{MoS_2}$ Raman features are fitted with Lorentzian line shapes. [119] In this work, the $\mathrm{MoS_2}$ Raman spectrum is fitted on occasion with the same routine by Pseudo-Voigt profiles as above.

3.3.3 Considerations on parameter uncertainties

Fit parameters above in Table 3.3 are reported from the algorithm with a standard deviation value. For better estimation, main sources of uncertainty in fit parameters are considered for error propagation.

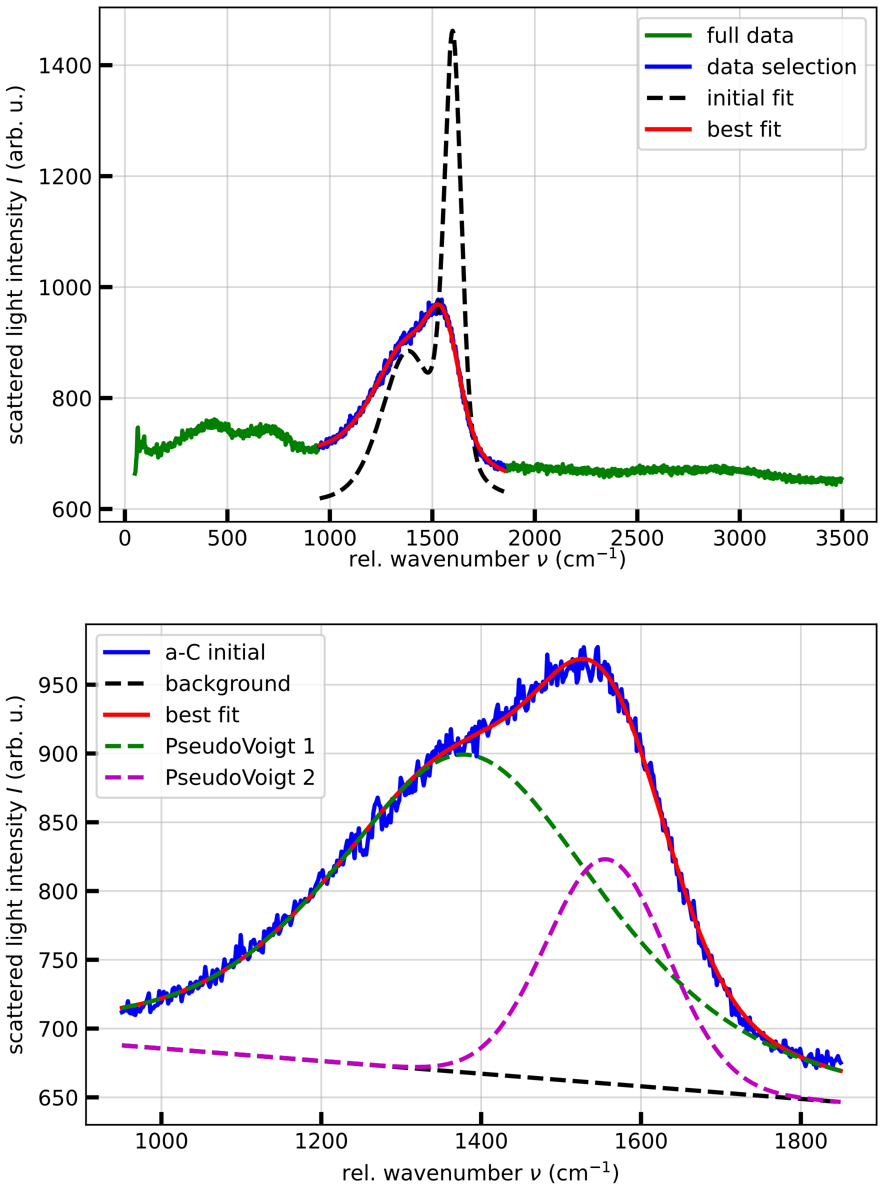

Figure 3.4: Exemplary output of the fitting routine: Raman spectrum of unmodified a-C thin films. Program code in appendix 6.2.2.

Raman peak	Raman shift ν/cm^{-1}	FWHM $/\mathrm{cm}^{-1}$	Height $I/\mathrm{arb.u.}$	Form factor $\alpha/\%$
D	1382 ± 11	409 ± 13	235 ± 7	70 ± 10
G	1556 ± 2	178 ± 8	160 ± 50	0 ± 0

Table 3.3: Exemplary fitting results of a standard a-C sample, the calculated intensity ratio reads $R_{\mathrm{Int}} = 1.44$.

For a start, the natural line width in general Raman spectroscopy is dependent on multiple factors, among which the internal temperature has a direct impact. This can be ruled out for this work, because such impact on line widths are mostly a considerable issue in gases and liquids, the line width of this work's sample are not affected by temperature in a direct manner. The Raman shift ν, which is linked to bonding characteristics and as such to the energetic landscape within the sample structure, underlies a natural distribution. For an rough estimate, this distribution of Raman shift ν was studied in Raman spectra of diamonds experimentally: Raman shift ν of diamond in a static experimental setup was measured. From this, a natural uncertainty in Raman shift ν is found to be below a tenths of cm^{-1}. [70] This is below the resolution of the MonoVista, which is estimated to be at least one pixel of the spectrum. This translates at the usual configuration to approximately $0.5\,\mathrm{cm}^{-1}$ for a $600\,\mathrm{mm}^{-1}$ grating and approximately $1.5\,\mathrm{cm}^{-1}$ to $2.1\,\mathrm{cm}^{-1}$ for a $300\,\mathrm{mm}^{-1}$ grating over the whole spectrum.

Uncertainty by deviations in by manufacturing parameters are hard to estimate a priori. So, the mean value and standard deviation in Raman shift ν and FWHM of a previous study on the impact on manufacturing parameters [173] was consulted. A statistical sample of a-C thin films was taken, which were deposited with different deposition parameters, namely a range of cathode power $P_{\mathrm{CP}} = 1500\,\mathrm{W}$ to $4000\,\mathrm{W}$, a mid-frequency $f_{\mathrm{mid}} = 20\,\mathrm{kHz}$ to $50\,\mathrm{kHz}$, and a bias voltage $U_{\mathrm{BV}} = 100\,\mathrm{V}$ to $200\,\mathrm{V}$. The sp^3/sp^2 ratio of this statistical sample spans roughly 4 % to 20 %. The fitting data revealed that the standard deviation of the (statistical) sample is considerably higher than the average of the reported standard deviations from the fitting routing. From this, it is estimated that uncertainty by manufacturing has a considerable impact. In summary, the fitting parameter uncertainty suffices as a lower bound; this work often discusses parameter values in comparison to other samples or value changes.

Raman peak	Fit parameter Raman shift ν			Fit parameter FWHM		
	Mean	Standard deviation	Mean of fit parameter uncertainty	Mean	Standard deviation	Mean of fit parameter uncertainty
G	$1556\,\mathrm{cm}^{-1}$	$7\,\mathrm{cm}^{-1}$	$2\,\mathrm{cm}^{-1}$	$220\,\mathrm{cm}^{-1}$	$23\,\mathrm{cm}^{-1}$	$6\,\mathrm{cm}^{-1}$
D	$1400\,\mathrm{cm}^{-1}$	$28\,\mathrm{cm}^{-1}$	$6\,\mathrm{cm}^{-1}$	$412\,\mathrm{cm}^{-1}$	$52\,\mathrm{cm}^{-1}$	$14\,\mathrm{cm}^{-1}$

Table 3.4: Mean value and standard deviation of fit parameters for uncertainty estimate. The values stem from 17 a-C thin films, which are manufactured with varying manufacturing parameters. Samples are the subject of a previous doctoral thesis [173] with similar equipment.

3.4 Optical temperature measurement and tuning

3.4.1 Methods for contact-free measurement of temperature

Special attention has to be paid to proper temperature measurement, because local heating is a main aspect in this work. Two general concepts are imaginable for this task: (a) a comparison of Stokes and Anti-Stokes signature intensity and (b) an external setup based on pyrometry. Further concepts, which indirectly probe the temperature via changes in Raman shift ν are reported, but related studies report a problematic reliability thereof. [183, 184]

Concept (a) relies on a difference between Stokes and Anti-Stokes signal intensity: the Anti-Stokes signal is attenuated by a factor proportional to $\exp(-{}^{E_\mathrm{j}}/_{k_\mathrm{B}T})$ with the phonon energy E_j, Boltzmann's constant k_B and absolute temperature T. As an example in Figure 2.14, the strongest Raman feature in a calibration silicon wafer at $520.5\,\mathrm{cm}^{-1}$ shows a Anti-Stokes counterpart. The phonon energy of the G-Raman peak in a-C is roughly four times higher, ergo, solely by the distance from the Rayleigh peak the attenuation factor is estimated to ${}^1/_{e^3} \approx 5\,\%$ over the case in silicon wafer. This concept, applied to amorphous carbons therefore requires a considerably more sensitive detection. Concept (b) exploits black-body radiation for contact-free temperature measurement. The natural approach of temperature measurement is the evaluation the energy E_λ of black body emission, in more detail

$$E_\lambda = \frac{\epsilon(\lambda) \cdot c_1 \lambda^{-5}}{\exp(\frac{c_2}{\lambda T}) - 1}, \qquad c_1, c_2 : \text{Planck's constants} \tag{3.24}$$

for a given wavelength λ at temperature T by Planck's radiation law. For this to function as intended using a single wavelength requires knowledge of the emissivity $\epsilon(\lambda)$, which is usually dependent on multiple factors, including temperature itself and individual properties like surface roughness, This quantity is a linear factor in E_λ, so by comparing radiation energy at two wavelengths and using their ratio, the emissivity is eliminated. This holds true with the assumption that the two chosen wavelength are close enough for $\epsilon(\lambda)$ to remain constant.

The measurement device is a scientific/ commercial-grade two-colour pyrometer *FIRE3* by *en2Aix GmbH*, Germany, which evaluates the radiation at wavelengths $1.7\,\mu\mathrm{m}$ and $2.0\,\mu\mathrm{m}$ via a fibre. Those two wavelengths are usually sufficiently close to meet the required constancy of emissivity, except for certain metals like aluminium [185]. The output of the system, a ratio between detector voltage values, is translated to absolute temperatures by prior calibration with a temperature-adjustable black-body radiation source. To measure within the pump spot, a $300\,\mu\mathrm{m}$ fibre is coupled with an achromatic fibre couple (curved metal mirror-based coupling rather than lens-based) and focussed onto the sample surface using an infrared microscope objective NIR x10 by Mitutoyo, Japan.

As a proof-of-concept, the pyrometer was used with a bare fibre with $300\,\mu\mathrm{m}$ diameter core with factory calibration. Data was collected by scanning the candle flame vertically within the flame, although a distance of $0.5\,\mathrm{cm}$ to $1.5\,\mathrm{cm}$ would not impede the results. Peak temperature was confirmed appropriately at roughly $1500\,°\mathrm{C}$, while peak temperature of a candle flame is expected at the main oxidative region (outer veil, non-luminous) with complete combustion at $1400\,°\mathrm{C}$. For temperature measurement on the sample surfaces, a MoS_2 sample was placed without vacuum on ambient air. Although continuous illumination with a infrared pulsed laser with cw-equivalent power of 175 mW, no valid temperature signature as in case of the candle flame was obtained. The only response of the system was obtained when an untouched surface of the sample was illuminated, which immediately results in oxidative reactions. For simplicity, the fibre was fixed onto the sample surface and the laser spot held steady, while the sample was moved. The measurement result translates to approximately 1000 °C with high uncertainty, although its uncertainty is mostly assigned to reaction enthalpy overshadowing the surface temperature at ambient air.

3.4.2 Optical temperature tuning

For thermal energy pumping, a Q-switched solid state laser *BL6S* by *SpectraPhysics*, Germany emits a pulsed laser beam with a maximum laser power of $P_{\text{pump}} = 2\,\text{W}$ with a pulse length τ_{pulse} in 6 ns to 20 ns range and a variable repetition rate f_{rep}. In preliminary studies [186], the (raw) laser power was taken as abscissa values for discussion. This is misleading, because laser power values shift when changing the repetition rate. To accommodate, the repetition rate f_{rep} is usually set to 10 000 Hz through the course of this thesis. The average laser power P_{pump} is converted to pulse energy E_{pulse} as $E_{\text{pulse}} = P_{\text{pump}}/f_{\text{rep}}$, so any direct impact of repetition rate f_{rep} is cancelled. For analysis, the (pulse) energy density over the illuminated area A_{spot} is regarded, which is simply $\rho_{\text{pulse}} = E_{\text{pulse}}/A_{\text{spot}}$. The maximum peak power of a pulse is disregarded for analysis; it is approximately 5 kW barring correlations between pulse length τ_{pulse} and repetition rate f_{rep}. The exact value of the pulse length τ_{pulse} is undetermined.

Over a Z-mirror configuration and spatial filter, the laser beam is directed to optical components. For a reduced divergence, the beam is widened with help of two lenses in telescope configuration. The raw laser power is attenuated by a rotatable $\lambda/2$ wave plate (HWP) and rotation-fixed Glan-Thompson prism (GTP) and spatially-filtered with a 150 µm pinhole (PH). The wave plate is set so that the unmodified laser beam remains unchanged in polarisation. From the Glan-Thompson prism, only the through-going beam (the so called extraordinary beam, s-polarised) is used. This beam is then focussed on a continuos intensity filter for finer scale intensity control (not shown in schematic) and collimated to a beam size of approximately 25 mm, which corresponds to the maximum aperture of the following optics. This is done for optimal focus, that is, to yield a 20 µm pump spot. To bring the beam to the sample chamber, a 100 mm achromatic lens is used. The laser power P_{pump} is measured in front of the sample chamber. The absorption loss by focussing through the measurement window (Suprasil) is neglected.

3.4.3 Prerequisite: sample chamber and vacuum

Besides the known trend to oxidise in ambient air in literature, preliminary studies with the optical temperature tuning setup found that the oxidation is critically limiting the measurement range. As hypothesis, a vacuum in the range of 1×10^{-6} mbar should slow down the rate of oxidation. For this, a simple vacuum chamber is constructed: a vacuum flange of size KF-DN40 and a standard Suprasil measurement window (approx. 1 mm thickness and diameter of 55 mm) residing on open flange facing towards the microscope objective. A Suprasil window was chosen for its optical transparency in the working range of the instrumentation, mostly for the wavelengths 532 nm and 1064 nm. As a vacuum pump, a combination of a mechanical pre-pump and a turbo-molecular pump reached a stable chamber pressure of below 6×10^{-6} mbar. The sample is placed into chamber in such a way that the sample keeps a certain distance to the Suprasil window to prevent ghosting effects due to reflections between the sample surface and the window.

3.5 Concluding summary of the measurement setup

The setup distinguishes between probe and pump lasers in distant relation to pump-probe-setups in semiconductor spectroscopy. Figure 3.5 illustrates the components of the setup, divided into components and *lines*:

(a) sample chamber: the sample is in a chamber at below 6×10^{-6} mbar, Suprasil measurement window.

(b) pump-line: a pulsed laser with fundamental wavelength of 1064 nm and the second-harmonic 532 nm are used. The raw laser power is attenuated by a variable $\lambda/2$ wave plate (HWP) and fixed Glan-Thompson prism (GTP) and spatially-filtered with a 150 µm pinhole (PH). A periscope and a free-mounted $f = 100$ mm achromatic lens focuses the pump laser onto the surface, yielding a 20 µm pump spot. The laser power P_{pump} is measured in front of the sample chamber.

(c) probe-line: a 532 nm spectroscopy laser is focused confocally through a microscope objective (MO) with 50x magnification onto the sample surface to yield a micrometer-sized spot. Scattered light is captured over the same MO, redirected over a beamsplitter (BS) and filtered through a Raman filter (RF) before entering a spectrometer and a CCD detector. The probe-line is actually a commercial Raman microscope, the *MonoVista*. The setup allows for visual microscopy to ensure the overlap of both pump and probe-spots. The probe spot is fixed, the pump-line allows for fine-scaled relative positioning, see master thesis [186] for detailed studies.

(d) pyrometer-line: via a 300 µm fibre, an achromatic fibre coupler, and an infrared microscope objective, the light of the pump spot is collected and directed into a calibrated two colour-pyrometer (CPM). For calibration, a precision black body radiation source is utilised beforehand.

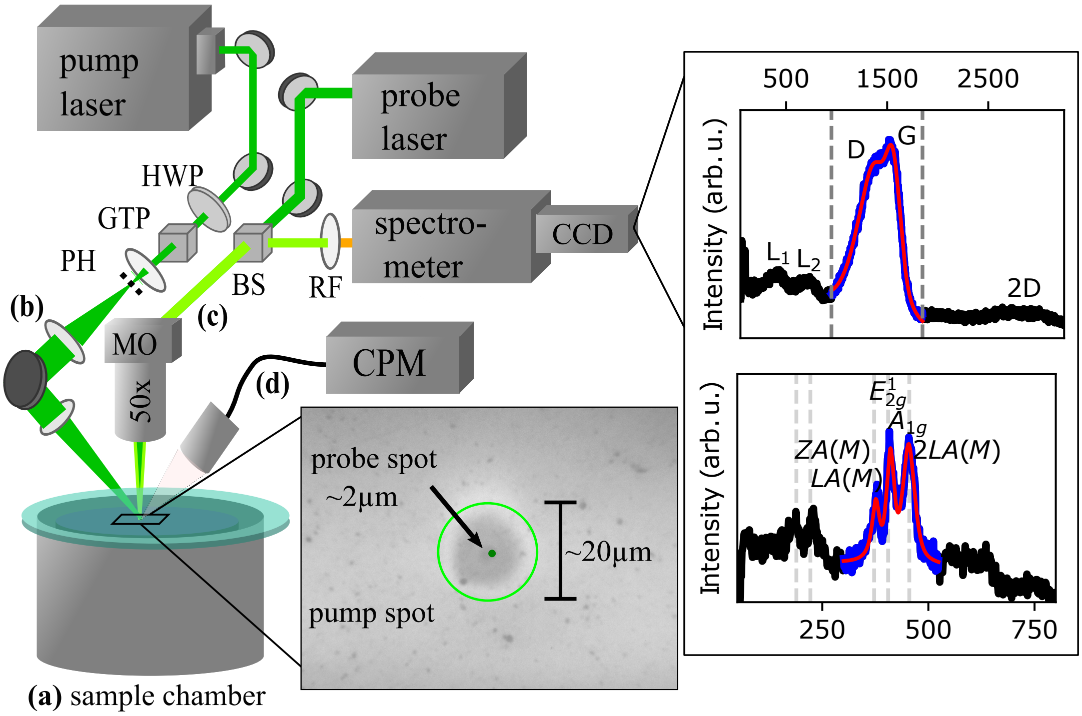

Figure 3.5: Concluding schematic of the experimental setup: **(a)** sample chamber, **(b)** *pump-line*, **(c)** *probe-line*, and **(d)** *pyrometer-line*.

Chapter 4

Tribological thin films and their structural and chemical properties - Raman analysis of initial and tribologically-loaded state

In this chapter, two fundamental classes of tribological thin films are studied exclusively via Raman microscopy: amorphous carbon (a-C) and molybdenum disulphide (MoS_2), both are deposited in magnetron sputtering PVD processes. Samples in this work were manufactured with the objective to optimise their tribological performance for a given application, and thus, these samples were externally examined for their tribological behaviour, i.e. coefficient of friction μ and wear rate. Such worn samples show characteristic tracks of wear, which span from mildly broken-in samples to loss of the thin film with substrate exposure. At the edge of the wear track, debris material is found. At first glance, such wear debris may be considered to be *disadvantageous*; in the tribological engineering perspective, however, wear debris is considered a part of the tribological system. Moreover, it is an essential requirement to attain a tribo-film or as transfer material, which are both considerably advantageous for friction reduction or chemical resistance.

Initial (i.e. as-deposited) characteristics regarding structure and chemistry of thin film lubricants are routinely investigated via Raman spectroscopy. A proficient theoretical basis and interpretation framework thereto are available, see the respective summaries in chapter 2, subsection 2.2.4 and subsection 2.2.5. If wear debris is present, Raman microscopy is used for spatially-resolved investigation on the wear track. Found material is expected to show an imprint of involved structural changes and chemical reactions. If used for modelling tribological conditioning or break-in processes, it opens the doors for a thorough investigation of and understanding for multi-scale tribology, i.e. the connection between nano-scale interaction to macro-scale phenomena. Scientific aim is to contribute to the understanding of such nano-scale processes in structural and chemical transitions. This chapter aims to evaluate usage of Raman spectroscopy by itself for (i) initial state characteristics on structure and chemistry, (ii) qualitative changes thereof via element-modification, and (iii) qualitative changes after tribological loading. Quantitative analysis of element-modification is done for selected samples.

Section 4.1 on a-C gives a short overview on the preceding efforts on the optimisation of manufacturing. This includes the deposition parameters and hydrogenation, and improving thin film adhesion via pretreatment or interstitial layers (inter-layers). Hereinafter, element-modification with silicon, tungsten, silver, copper is studied. **Section 4.2 on $\mathbf{MoS_2}$** likewise starts with preceding studies, the working environments of MoS_2 thin films are varied and a selection of element-modification are investigated.

4.1 Amorphous carbon and hydrogenated amorphous carbon thin films and their element-modified derivates

Both the inter-atomic bond characteristics and their interlinked structures give rise to a-C's properties. The former are, in principle, mostly accessible via Raman spectroscopy, a thorough discussion on basic a-C thin film Raman spectra is given in section 2.2, subsection 2.2.4; this chapter highlights the differences thereto in the interest of concise writing. The findings of this chapter is the fundamental work for an optical temperature tuning setup in the subsequent chapter, which aims to probe the thermal limits and structural and chemical changes for an organised in-field testing and deposition optimisation.

4.1.1 Objectives of a-C and a-C:H thin film manufacturing for general tribological application: sp^3 content, hardness, adhesion

Core ambition is the combination of low friction and adequate wear. In a-C thin films, the former is mainly reliant on avoidance of shearing forces and therefore vulnerable to presence of bonding vacancies (dangling bonds). In short, such dangling bonds may be saturated by ambient air components or deliberately by hydrogenation. Wear resistance is mostly related to hardness with sufficient thin film adhesion and cohesion. In a simplified picture, higher hardness of the resulting film is beneficial for general-purpose a-C thin films [42, p. 139], while the application-specific objective may differ. Film hardness is strongly correlated to sp^3 content and, in consequence, determined by the film manufacturing process and/or hydrogenation.

As an exemplary mechanism in PVD manufacturing, striking carbons with high kinetic energy penetrate the surface and cause a displacement of sp^2 carbon bonds in the existing film. [47, 144, 168, 187] These local sites of sp^3 hybridised carbons do not necessarily relax to their thermodynamically favourable sp^2 hybridisation, giving the carbon networks of a-C their metastable character. [141] Previous studies show that two deposition parameters, namely cathode power P_{CP} and bias voltage U_{BV}, are influential to this mechanism [106, 188, 189]. The effect on bonding and structure characteristics were visible in a-C's Raman spectra, although quantification of their sp^3 content required supplementary analysing methods. [106] However, the accompanying drawbacks are higher internal stress, which lead to brittleness or poor film adhesion, especially in the related thin film group of tetrahedral amorphous carbon (ta-C) with highest sp^3 content. In literature, ta-C does cope with higher critical loads in comparison to hydrogenated a-C thin films, but the superior wear resistance of the films is crucially limited to proper adhesion rather than hardness; adhesion, moreover, is dependent on the substrate material of choice. [190] The concept of hardness as measure for tribological performance is controversial [129, 191]. All this challenges the simplified picture above.

So, rather than hardness and sp^3 content by themselves, the adhesion is also of interest. In consequence, the inter-layers, substrate pretreatment, and hydrogenation are looked into [146, 176, 178].

Substrate pretreatment and inter-layers for chromium-steel substrates

Inter-layers mediate the discontinuous change in bonding type from metal bonding in the substrate to covalent bonding in a-C. [191, 192] Thermal properties like expansion coefficients, heat capacity, and heat transfer as well as intrinsic stress collide, all of which renders the transition between substrate and thin film a considerable point of failure. This, at its extreme, can be found in Figure 4.1, in which the cracked surface of a-C on polyether ether ketone (PEEK), a thermoplastic material substrate, is shown. Laser illumination of the sample leads to oxidation, see orange arrows in Figure 4.1, while the same laser power density for Raman measurements barely leaves a mark on the steel substrate equivalent. Among other material classes in hard coatings [195], carbide forming metals such as chromium (Cr) or titanium (Ti) are an intuitive choice and open the possibility to natively form gradient inter-layers [196][197, p. 131], which continuously mediate between metallic substrate and a-C top layer. To ensure the adhesion between the substrate and chromium carbide (CrC) inter-layer the substrate was pre-treated with the PVD process gas without any target (argon etching [198]) and with a combination of such argon etching and HiPIMS magnetron sputtering of chromium target (HiPIMS pre-treatment [178]) . Both processes are supposed to prepare the surface and to direct towards certain attributes for improved adhesion [199], like removal of surface contaminants and promotion of unsaturated bond vacancies [200]. The effect of pre-treatment and matching inter-layer is studied for a chromium-steel alloy substrate and for a titanium alloy substrate.

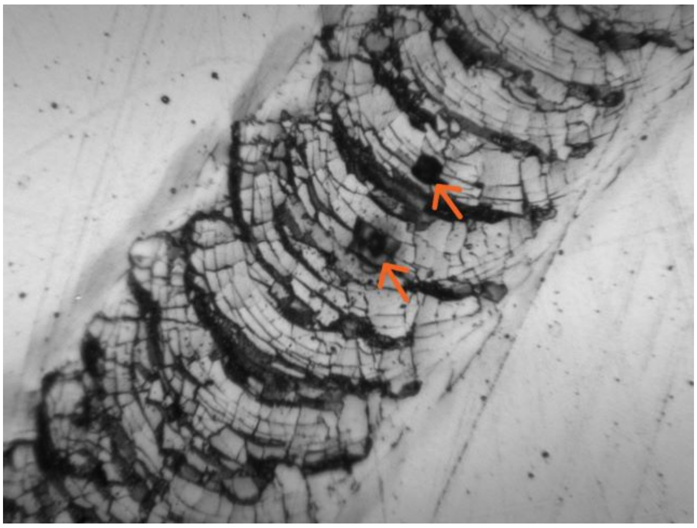

Figure 4.1: Delamination of a thin film as consequence of poor adhesion on polymer substrate (spalling failure). While the G-Raman peaks of some carbon compounds are sensitive for internal stresses by roughly a few cm^{-1} per GPa [193, 194, 98], a stress release of delaminated a-C was not measurable with certainty.

Figure 4.2(a)-(c) shows the Raman spectra of a-C thin films on a chromium-steel alloy substrate (16MnCr5) with graded CrC inter-layer; Raman spectra of bare CrC inter-layer without top-layer is shown in subfigure (a) and spectra of deposited a-C and a-C:H thin films in subfigures (b) and (c), respectively. For a-C and a-C:H top-layers, D- and G- Raman peaks are broad and overlapping with Raman shifts ν of roughly $1370\,\mathrm{cm}^{-1}$ and $1580\,\mathrm{cm}^{-1}$, characteristic widths, and intensity ratios. The Raman shift $\nu(\mathrm{D})$ of the D-Raman peak remains unchanged over all measurements, the G-Raman peak shifts down from its highest

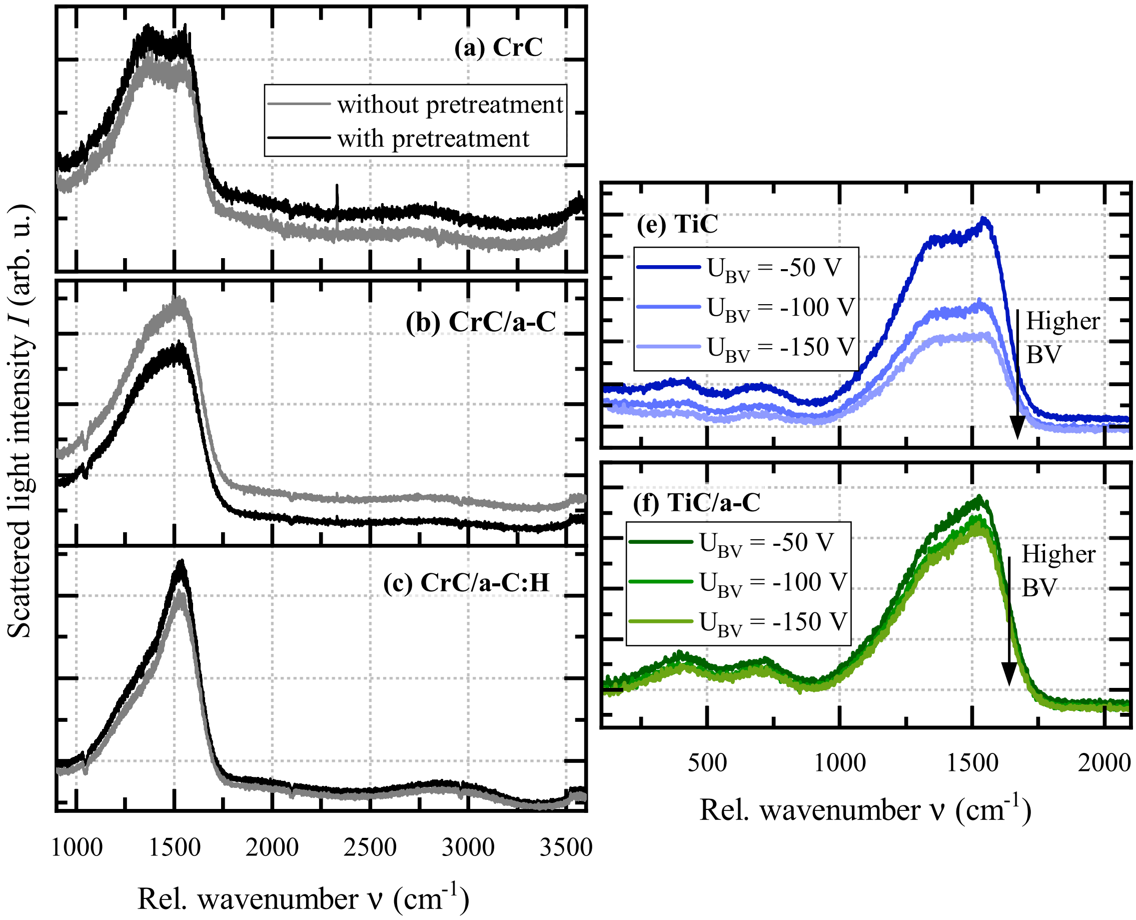

Figure 4.2: Effect of HiPIMS pretreatment on Raman spectrum of the interstitial layer (Inter-layer) and on the final thin film. **Left column:** steel substrates and CrC interlayers, comparison of Raman spectra of **(a)** carbon-gradient interlayer and **(b)+(c)** deposited a-C top-layers thereon. **Right column:** titanium substrates and TiC interlayers, Raman spectra of **(e)** graded TiC inter-layers and **(f)** the final a-C thin films. These samples are deposited on titanium alloy substrates at different bias voltages. Notice that the appearance of a-C signatures in subfigures **(a)** and **(e)** is also seen on CrC/TiC layers without any a-C top-layer.

value in inter-layer CrC of $1568\,\mathrm{cm^{-1}}$ to values of $1555\,\mathrm{cm^{-1}}$ and $1544\,\mathrm{cm^{-1}}$ in a-C and a-C:H top-layers, respectively. D- and G-Raman peaks in the inter-layer CrC are comparatively easy to distinguish, both peak intensity and peak width of Raman peaks in CrC are comparable to one another. In the range of roughly $2800\,\mathrm{cm^{-1}}$, the characteristic peaks of carbon-hydrogen stretching modes become visible. These modes are strongest in top-layer a-C:H in absolute terms, but appear as shallow as in CrC inter-layer and a-C top-layer measurements caused by the more pronounced Raman peaks of a-C:H. Further comparison of a-C and a-C:H is omitted, detailed discussion follows in the section for hydrogenation. Over all samples, the 2D-Raman peak was not found clearly. The comparison of pre-treatment methods yields negligible differences in general intensity.

All spectra show characteristic Raman peaks of a-C. For interpretation, the inter-layer spectra and differences to the top-layers are given special attention and the discussion on general properties of the top-layer films is subordinate. For the inter-layer CrC, the presence of Raman peaks similar to a-C modes is noteworthy. From the Raman spectra alone, one is not able to distinguish allotropes of carbon with certainty. With the expectancy that the spectra in CrC stem from a-C compound, the material is found to be rich in nano-crystalline graphite in an amorphous carbon matrix. The reduction of FWHM relative to a-C and a-C:H films shows the overall ordering in CrC. This view is challenged, however, when the Raman shifts ν are taken into consideration. The situation above is usually found with stronger distancing of both Raman modes, but here, only $\nu(\mathrm{G})$ is significantly elevated in CrC over a-C while D-Raman mode is unchanged. A similar spectrum is found in nano-sized CrC powder as synthesised in carbothermal reduction. [201] In short, CrC-related vibrational modes overshadow those in pure carbon, but still, the system is behaving like stressed, but sp^2 enriched a-C. For the present samples, the transition between the layers was found to be discontinuous by other measurements, the carbon content of the inter-layer was too low. With the sensitivity of Raman spectroscopy towards chemistry and structural changes in mind, one expects that the ideal transition between inter-layer and top-layer will be seamless, when the Raman spectra match. For mechanical endurance, it was found via *Rockwell indentation tests* and *scratch tests* that the adhesion in the substrate-film interface is important for avoiding spalling failures near the substrate, which eventually causes delamination of the entire film. It was further shown that the combination of etching and HiPIMS pre-treatment improved the adhesion. This effect does not show in Raman spectra, which shows the similarity of the top layers independent from the pre-treatment method.

In summary, Raman spectroscopy is not suitable for evaluating the adhesion to the substrate directly on the one hand. Reasons for this are based on the fact that the focus volume of this setup is assumed to be within 100 nm depth, so a direct assessment of underlying inter-layers through a micrometer-sized top layer is impossible. On the other hand, a badge of substrates with inter-layers only may be investigated in the beginning of manufacturing for structured quality assurance, Raman spectra of those inter-layers should be close to a-C thin films.

Inter-layers for titanium alloy substrates

Figure 4.2(d)-(e) is analogous to preceding discussion for a titanium carbide (TiC) inter-layer on titanium alloy substrate (Ti6Al4V): Raman spectra of bare TiC inter-layer without a-C top-layer are shown in subfigure (d) and spectra of final films system in (e). All samples are pre-treated in the same manner; in addition to the study before, the effect of bias voltage on the inter-layer only are taken into account. The bias voltage of the top-layer is always $-100\,\mathrm{V}$. [176]

Much like the situation for CrC inter-layers, the Raman spectra of the TiC inter-layers resemble the spectra of a-C, a strong correlation of the bias voltage to the Raman spectrum of TiC is found. The intensity of both Raman peaks decreases and the intensity ratio lifts significantly from 1.64 ± 0.05 to 1.98 ± 0.05 with increasing bias voltage. Both peaks also become broader, from $(373 \pm 4)\,\mathrm{cm}^{-1}$ to $(398 \pm 4)\,\mathrm{cm}^{-1}$ for the D-Raman peak and from $(140 \pm 1)\,\mathrm{cm}^{-1}$ to $(151 \pm 2)\,\mathrm{cm}^{-1}$ for the G-Raman peak. The Raman shifts ν are mostly constant within parameter uncertainty at $1372\,\mathrm{cm}^{-1}$ and $1563\,\mathrm{cm}^{-1}$. The most pronounced spectrum is yielded for the lowest bias voltage with slightly blue-shifted G-Raman peak at $1566\,\mathrm{cm}^{-1}$. In top-layer a-C, the effect of the inter-layer differences is vastly smaller. The intensity ratio does increase de jure, but the value spread from 1.43 ± 0.05 to 1.47 ± 0.04 is not significant. The FWHM of the top-layers show no clear broadening trend and stay close to $390\,\mathrm{cm}^{-1}$ and $175\,\mathrm{cm}^{-1}$, respectively; the Raman shifts $\nu(\mathrm{D})$ is unchanged from before, $\nu(\mathrm{G})$ is stable at $1553\,\mathrm{cm}^{-1}$.

The bias voltage has similar effects on TiC inter-layers as in a-C: higher bias voltages lead to higher density and hardness, heavily defected structure, and eventually higher stresses, which have to be avoided for proper film adhesion.[106] For different bias voltages, the broadening trend proves that higher bias voltage leads to higher disorder in inter-layers as expected. Although not quantifiable, the impact of bias voltage on inter-layer Raman spectra is measurable. The best match of inter-layer and top-layer is found for low bias voltages. The comparison of top-layer to inter-layer is mostly the same as in the study on CrC inter-layer: higher Raman shift $\nu(\mathrm{G})$ and generally higher intensity ratios in the inter-layer suggest a lower sp^3 content. Overall lower peak width in inter-layers may show a more ordered structure than in top-layers, the differences in peak width of the inter-layer to the top-layer are not as grave as before. Here, also, the inter-layer is behaving like stressed, but sp^2 enriched a-C.

In summary, Raman spectroscopy found that the structural impact of the inter-layer on the top-layer is minor. Spectral changes of the inter-layer may shine through the top-layer, which was not observed in the study on CrC inter-layers for different pre-treatment methods. More likely, however, a more defected inter-layer dictated the growth mechanism of the a-C top-layer. A stronger effect thereof is expected for thinner films of a-C, which renders a possibility for thickness measurement. This relies on the assumption that a-C growth remains an imprint of the underlying structure, but the effect washes out for thicker films.

Hydrogenation via presence of reactive hydro-carboneuous compound during manufacturing

Other than manufacturing parameter-driven increase of sp^3 content, and mechanical properties in turn [42, pp. 108 & 247 & 330], hydrogenation is commonly used to attain higher sp^3/sp^2 ratios. One possible way of hydrogenation is continuous addition of a gaseous hydrocarbon compound during the deposition process, among which acetylene (C_2H_2, systematic IUPAC name: ethyne) is high-yielding and "easier to handle" in comparison [47, p. 141]. Hydrogen stabilises sp^3 carbon hybridisation [54] due to the fact that hydrogen or hydrocarbon compounds split π-bonding in carbon double bonds in favour of single σ-bonding in an addition reaction. Hydrogen also saturates bonding vacancies (dangling bonds) close to the surface at lower concentrations [202] and terminates larger carbon structures like carbon chains in the amorphous network [146]. The effect of hydrogen on a-C is profound enough to classify a-C thin films on its hydrogen content besides sp^2 & sp^3 content and carbon clustering/cross-linking. [54, p. 14] Friction-wise, hydrogenation is beneficial in inert and dry environments over unmodified a-C, because a-C's unsaturated dangling bonds adhere to the tribo-contact counterpart; in wet atmospheres, in contrast, the adsorption of water is increased, which increases surface interaction and, consequently, friction. [203, p. 163]

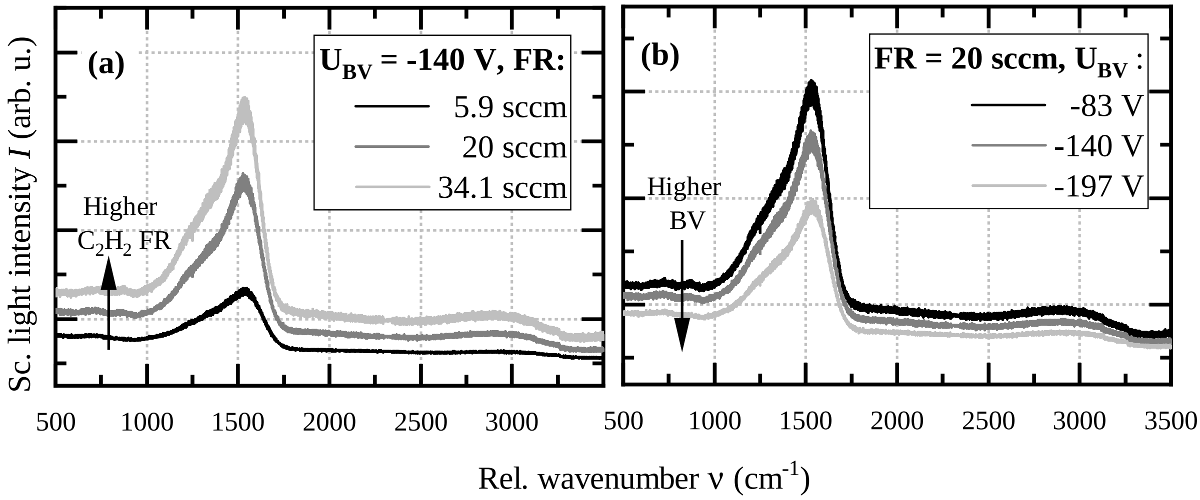

Figure 4.3: Raman spectra of hydrogenated a-C:H thin films, **(a)** deposited with different acetylene (C_2H_2) flow rates (FR) at a constant bias voltage U_{BV}, and **(b)** deposited at different bias voltages U_{BV} at a constant C_2H_2 flow rate.

Other than in a-C, the G-Raman mode in a-C:H is clearly distinguishable from the D-Raman mode, in other words, intensity ratio I(D)/I(G) is far below unity and both absolute peak intensities are higher than in a-C. The width of the G-Raman peak is comparable to the a-C counterpart, the D-Raman peak is narrower by roughly 25%. Although the Raman shifts ν appear comparable to a-C, peak fitting reveals significantly lower Raman shifts ν, but no more than $10\,\mathrm{cm}^{-1}$ each. As described before, the characteristic peaks of carbon-hydrogen stretching modes are visible in the range of roughly $2800\,\mathrm{cm}^{-1}$, no second-order peaks like 2D-Raman modes are visible clearly. Figure 4.3 shows samples, which are deposited for showing the effect of bias voltage and the effect of acetylene flow rate on the samples. In this study, multiple parameters are varied in framework of design of experiment setup [146]; only a few spectra are shown with constant bias voltage U_{BV} or flow rate (FR), the derived statements encompass all of the study. The mean point of the parameter variation are acetylene flow rate at 20 standard cubic centimetres (sccm) and bias voltage $U_{\mathrm{BV}} = -120\,\mathrm{V}$.

In subfigure (a), Raman spectra of increasing flow rate at constant bias voltage U_{BV} are shown. G-Raman peak is more pronounced than the D-Raman mode in comparison to a-C, the intensity ratio for all spectra is below unity. As a function of acetylene flow rate, the Raman shifts ν decrease from roughly $1350\,\mathrm{cm}^{-1}$ to $1340\,\mathrm{cm}^{-1}$ for the D-Raman peak ($1370\,\mathrm{cm}^{-1}$ for a-C) and increases vaguely around the mean value of $1555\,\mathrm{cm}^{-1}$ for the G-Raman peak ($1550\,\mathrm{cm}^{-1}$ for a-C). For increasing flow rates, both peak widths increase from roughly $330\,\mathrm{cm}^{-1}$ to $375\,\mathrm{cm}^{-1}$ and from roughly $190\,\mathrm{cm}^{-1}$ to $220\,\mathrm{cm}^{-1}$ for both modes (approx. $390\,\mathrm{cm}^{-1}$ and $200\,\mathrm{cm}^{-1}$ for a-C), respectively. Although the intensity ratio lies between 0.34 and 0.46 over all spectra of the study, at a constant bias voltage $U_{\mathrm{BV}} = -120\,\mathrm{V}$, the flow rate alone leads to a barely significant increase of 0.36 to 0.37, only. The intensity of the C-H stretching modes increase with flow rates at first, but reach a maximum intensity after approximately 20 sccm flow rate.

The two systems a-C and a-C:H are considered separate with own characteristics. Subsequently, a-C's interpretation framework may not be applied to a-C:H in general. For a-C:H thin films with hydrogen content below 20%, however, fundamental work suggests to interpret Raman spectra of a-C and a-C:H equivalently. [49] Direct measurement of hydrogen contents is not given in the underlying study, nevertheless, present films are assumed to have a hydrogen content well within that limit. The width of Raman peaks increase slightly for both modes, so increasing sp^2 bonding distortions and internal compressive stress are visible. [95, 204] Literature suggests that hydrogen has both ordering and disordering effects in balance. [49] This is seen here in FWHM(D): it lies below that of unmodified a-C, while FWHM(G) is the same for a-C and a-C:H. From this, the effect of hydrogen is observed to be more pronounced on sixfold-rings than sp^2 carbon pairs in general. The limited rise of C-H stretching modes, capped at 20 sccm, indicate a hydrogen saturation in the film. As literature suggests [141, p. 367], the effect is spatially restricted to the surface. Even so, the effect of hydrogen on the carbon network is visible beyond the found saturation flow rate. As an effect of higher flow rates at elevated bias voltage U_{BV}, increment of Raman shift $\nu(\mathrm{G})$ by $5\,\mathrm{cm}^{-1}$ only and shallow increment of intensity ratio suggest a mostly constant hybridisation mixture, but apparently with downward trend in sp^3 content. This is also seen in reduced hardness of questioned samples, which was measured by other means. This leads to the hypothesis that a higher flow rate leads to hydro-carbon saturated surfaces at first, whose deposition and re-sputtering rates are kept in balance at elevated bias voltages U_{BV}. The stronger re-sputtering than usual leads to minor annealing effect at the sub-surface carbon network, the generally higher surface bombardment leads to more diverse distortions. Finally, the most noticeable effect is the far higher scattering yield in a-C:H over a-C. The absolute intensity of the spectra are generally dependent of absorption behaviour [48, 205] and concentration of Raman scattering centres. While the later is not critical here, the former is a remarkably different from a-C to a-C:H. [206]

As secondary results in subfigure (b), increasing bias voltages U_{BV} at constant flow rate show an increase in both intensity ratio I(D)/I(G) and Raman shift $\nu(\mathrm{G})$ and, in turn, are interpreted as loss of sp^3 content. This is contrary to the situation in a-C, in which an increase of sp^3 content is d'accord with the mechanism of ion bombardment for higher energetic species. While the probability for re-sputtering of singular hydrogen atoms is low, because of both strong C-H bonding and small scattering cross-section for its size, it is also well known that hydrogen is emitted as hydro-carbon compounds of different molecular sizes [54]. So, the generally high re-sputtering for higher bias voltage U_{BV} in combination with hydrogen enrichment close to the surface may, in fact, lead to the loss of sp^3 sites in form of ejection of C-H compounds. For maximising the sp^3 content, a combination of high flow rate and high bias voltage U_{BV} is required. Besides this particular interaction, the behaviour of the spectra, e.g. FWHM versus bias voltage U_{BV}, is compliant with the discussion for subfigure (a). Friction-wise, the variation of flow rate and bias voltage U_{BV} in ranges 5.9 sccm to 34.1 sccm and −83 V to −197 V is mostly irrelevant. The coefficient of friction over all measurements is $\mu = 0.25 \pm 0.03$ with two outliers: higher flow rate with lower bias voltage (FR: 30 sccm & $U_{\mathrm{BV}} = -100\,\mathrm{V}$) with $\mu = 0.33$ and extreme flow rate (34.1 sccm & $U_{\mathrm{BV}} = -140\,\mathrm{V}$) with $\mu = 0.29$. By other measurements methods, the hardness of all samples are above 19 GPa and significantly lower for the outliers. Third-lowest hardness was found for the lowest bias voltage $U_{\mathrm{BV}} = -83\,\mathrm{V}$. Variation in friction behaviour may stem from water adsorption, which is expected to be visible in the hydro-carbon-related stretching modes and subordinately as water molecules per se. However, neither Raman modes of liquid water[1] nor an apparent change in hydro-carbon stretching modes were investigated.

In summary, Raman spectroscopy may be used to qualitatively distinguish between a-C and a-C:H by absolute intensity and it reveals a converse effect of bias voltage U_{BV} on both thin film systems. Usage of absolute intensity measures entails the risk of misinterpretation, other peak properties have to be taken into account. The reason of the converse effect of bias voltage U_{BV} is not explainable, a reason for the increased friction in a-C:H outliers (deposited at high acetylene flow rate FR) was also not identifiable.

4.1.2 Element-modification of a-C and a-C:H thin films with agents influencing hybridisation

Carbide forming metals serve another purpose in a-C and a-C:H film modification besides inter-layers. In the deposition process, targets of such metals can be co-sputtered leading to element-modification of thin films, for which the metals are assumed to become thoroughly incorporated into the carbon network. For this, silicon and tungsten are typical elements, which are thoroughly discussed in this thesis.

Silicon (Si), being isochemical to carbon, bonds to carbon as silicon carbide (SiC) via σ-bonding and is also able to form amorphous networks (a-Si) themselves as well. While more intricate bonding combinations of silicon and carbon are known, SiC are expected mostly. Because of the primary bonding via σ-bonds, they stabilise the sp^3 hybridisation of carbon in vicinity. Bonding strength in both a-Si and Si-C are weaker than their pure carbon counterpart. Low concentration silicon-addition to a-C leads to losses in elastic modulus and hardness, below 10 at.-% silicon content, sp^2 clusters are inhibited. [207] Residual sp^2 clusters change shape: silicon promotes the formation of sp^2 carbon chains [208], which in pure carbon networks is only seen for samples with very high sp^3 content as in ta-C.

---

[1] Over the course of study, such modes of liquid water were measured only in water-immersion microscopy for bioanalytical studies in vitro, which are not part of this work.

At elevated silicon concentrations, it affects the present carbon bondings in an amorphous network negatively, because silicon atoms are larger in size than carbon atoms. This leads to higher internal stresses and carbon bonding distortions, which, in turn, also stabilises present sp^3 hybridisation. Ultimately, too high internal stress critically limits the lifetime of a-C thin films. In total, a moderate silicon addition releases internal stresses as a-C weak point and hinders graphitisation as deterioration mechanism. So, silicon-modification is regularly used for increasing the thermal resistance of a-C; maximum thermal resistance up to 650 °C are reported. [26] Alternatively, the boost in thermal resistance may also stem from a competing a-Si network [209], which may act as a reduction of a-C network density or as sacrificial element. Besides stability, a key application for silicon in a-C:Si and a-C:H:Si is optimised friction behaviour, because silicon compounds promote the formation of a tribo-film. For this, a minimum content of silicon in a-C:X is required.

Tungsten (W), in contrast, forms stable bonds to carbon as tungsten carbides via π-bonding, namely sub-stoichiometric β-WC_{1-x} or W_2C, and thus, leads to stabilisation of sp^2 hybridisation of carbons. Unlike silicon and carbon pairing, tungsten does not form larger structures or amorphous networks, but remain nano-crystalline compounds in an amorphous matrix. The formation of tungsten-carbon compound and diffusion of tungsten into a-C requires temperatures above 700 °C [210], which exceeds a-C's natural thermal limit by far. From this, it is derived that tungsten acts as a barrier for structural processes in a-C. Low concentrations lead to drastic reduction of internal stress in a-C [211], which at elevated concentration becomes visible in weaker mechanical properties. Coincidently, the wear behaviour is reported to be improved for tungsten addition, unless too high concentrations are reached; the friction behaviour is usually not affected. [212] At highest concentration of tungsten, it's expected that the amorphous carbon structure vanishes in favour of tungsten-dominant carbide compounds, into which the carbon dissolves.

Both silicon and tungsten affect the hybridisation of the carbon network and limit sp^2 clusters in number and size, but with different approaches. For industrial applications, their benefit strongly depends on adjacently required qualities of the thin films. For scientific analysis, it permits the investigation of involved structural processes in nano-sphere and the effect thereof in the macro-sphere.

Investigation on as-deposited samples

Figure 4.4 shows exemplary Raman spectra of a-C:X and a-C:H:X thin films, in which the modifying element X is silicon or tungsten. Subfigure (a) presents the Raman spectra of a-C along with a-C:Si and a-C:W at concentration [2] of $\approx 11\,\%$ and $\approx 16\,\%$ for silicon and tungsten, respectively, subfigure (b) is analogous for the hydrogenated counterparts. The spectra gauge the as-deposited situation, the measurement process do not lead to changes in structure or chemistry.

The Raman shift $\nu(\mathrm{D})$ differs slightly, but mostly stays within fitting parameter uncertainty. a-C:Si and a-C:H:Si show the lowest Raman shifts $\nu(\mathrm{D})$ with downshift of approx. 20 and $30\,\mathrm{cm}^{-1}$ in comparison to pure a-C, a-C:W is not shifted, a-C:H:W is downshifted by $5\,\mathrm{cm}^{-1}$. FWHM(D) varies considerably: the highest value is found in a-C:W (FWHM $(395 \pm 13)\,\mathrm{cm}^{-1}$), which is slightly above the value for a-C (FWHM $(392 \pm 9)\,\mathrm{cm}^{-1}$), but

---

[2] These measures $X/(C + X)$ are strictly the atomic concentration with respect to carbon. The values differ only slightly from regular atom-percent (at.-%).

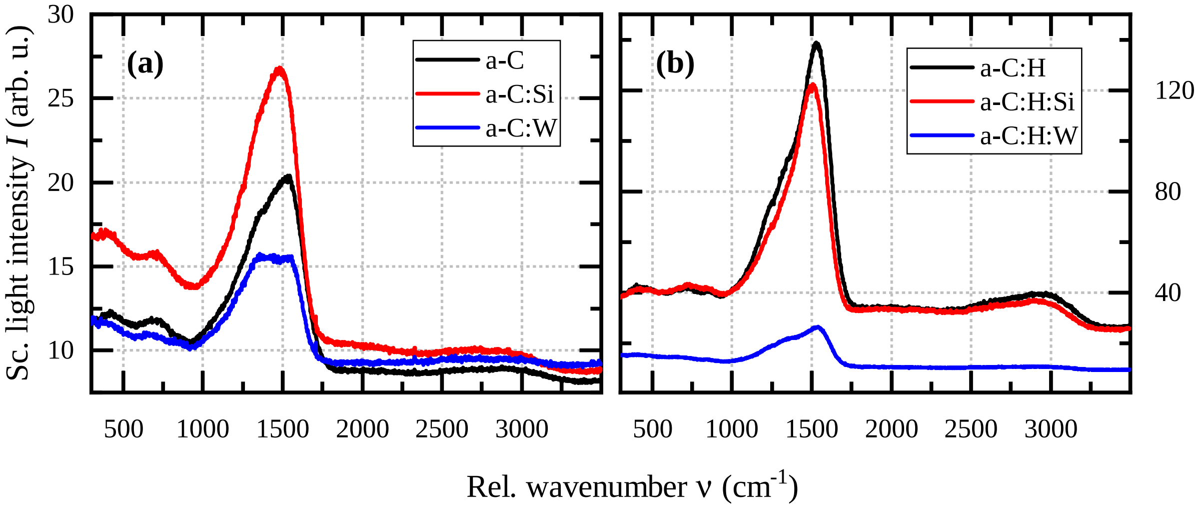

Figure 4.4: Raman spectra of element-modified **(a)** a-C and **(b)** a-C:H thin films with modification influencing hybridisation, namely silicon (Si) and tungsten (W).

also within the uncertainty. All other samples show significantly narrower D-Raman peak, with regards to a-C: a-C:H is narrower by $40\,\mathrm{cm}^{-1}$, a-C:Si and a-C:H:W by $50\,\mathrm{cm}^{-1}$ and a-C:H:Si by $65\,\mathrm{cm}^{-1}$. For the G-Raman mode, changes are already visible by eye. Raman shift $\nu(\mathrm{G})$ shows lower uncertainty and thus allow more precise inter-sample comparison: from highest to lowest,

$$\begin{array}{ll}
\text{a-C:W} & (1558 \pm 5)\,\mathrm{cm}^{-1}, \\
\text{a-C} & (1550 \pm 2)\,\mathrm{cm}^{-1}, \\
\text{a-C:H:W} & (1547 \pm 1)\,\mathrm{cm}^{-1}, \\
\text{a-C:H} & (1542 \pm 1)\,\mathrm{cm}^{-1}, \\
\text{a-C:Si} & (1518 \pm 2)\,\mathrm{cm}^{-1}, \\
\text{a-C:H:Si} & (1517 \pm 1)\,\mathrm{cm}^{-1}.
\end{array}$$

G-Raman peaks are broadest for a-C and a-C:Si, approx. $(193 \pm 8)\,\mathrm{cm}^{-1}$. By adding hydrogen to those, peaks narrow in a-C:H by $15\,\mathrm{cm}^{-1}$ and by $10\,\mathrm{cm}^{-1}$ in a-C:H:Si. Most narrow G-Raman peak is found in a-C:W at $(135 \pm 16)\,\mathrm{cm}^{-1}$ and second-most narrow in a-C:H:W at $(153 \pm 5)\,\mathrm{cm}^{-1}$. The intensity ratios in non-hydrogenated samples span 1.12 to 2.15 and 0.56 to 0.98 for hydrogenated samples. As already described in the discussion for hydrogenation, Raman modes of C-H stretching modes are prominently found for a-C:H and a-C:H:Si, less for a-C:H:W or non-hydrogenated samples. Second-order peaks, coinciding with features above, cannot be identified clearly.

The differences of a-C and a-C:H mostly resemble the situation already described before. In a-C:Si, the decrease in FWHM(D), but not in FWHM(G) indicates a structural process more pronounced in carbon rings rather than in general. Its a-C:H:Si counterpart has similarly reduced FWHM(D), but also mildly lowered FWHM(G), when FWHM(G) is mostly the same in a-C and a-C:H. From this it is found that the effect of hydrogen and silicon in a-C:H:Si is not independent from another. Both affect the carbon network by increasing the sp^3 content, but by different means. The smaller intensity ratio in a-C:H:Si indicates the large number of sp^3 carbon sites. The narrowing behaviour of tungsten and hydrogen, however do combine, FWHM(G) is lower in a-C:W than in a-C:H:W, indicating structural ordering by tungsten addition. It appears as if the possibility for tungsten to dictate ordering in a-C:H:W is hindered by the presence of hydrogen. On conceivable mechanism may lay in the stronger C-H bonds than C-C bonds. Also, a-C:W shows the highest intensity ratio and so includes the most prominent sp^2 carbon clusters in site and number. This effect, too, is hindered in a-C:H:W: The rise in I(D)/I(G) from a-C to a-C:W is twice as strong as in the hydrogenated sample pairing.

Analytical investigations in element-modified a-C:X thin films

Analytical investigations aim to qualify and quantify a substance, in this case, the content of element-modification in a-C via the effect thereof on its Raman spectra. As the qualitative observations were made before, the effect of silicon in a-C is now quantified via Raman spectroscopy. The appearance or exclusive intensity change of an otherwise absent or stable Raman peak is an overt approach in analytical chemistry. This taps into the correlation of intensity and substance concentration, it is used in *in-line* or *flow-through* Raman techniques [213, 214]. In bulk Raman spectroscopy also, the progress of an combustion reaction is commonly investigated via Raman spectroscopy, the intensity evolution in time follows a Avrami-type behaviour giving insights into. Here, the modifying element in a-C:X was rarely visible in the Raman spectra directly if the laser power density is low enough to not initiate chemical reactions. In preceding studies, deliberately chosen elevated laser power densities showed the oxides or other by-products of chemical reactions.

Figure 4.5 show the fitting parameters of silicon-modified a-C films of varying silicon content. The spectra were taken in as-deposited samples with laser power of 15.5 mW in a approx. 3 µm laser spot, yielding power densities in order of $200\,\mathrm{kW\,cm^{-2}}$. All plot symbols depict a sample of a larger set, which vary in deposition parameters. Because varying deposition parameters were proven to impact the Raman spectral features, any found correlation between fitting parameters and silicon content is subsequently reliably linked to silicon content. The peak parameters Raman shift ν and FWHM show a linear trend; linear fit parameters are found in Table 4.1. The intensity ratio I(D)/I(G) drops considerable for at lower silicon contents and reaches a stable minimum at roughly 1.6. The form factor α remains close to gaussian-type line shape in G-Raman peak, the D-Raman peak starts at high lorentzian-like values and furthermore show a slight trend towards lorentzian-type line shape. With increasing silicon content, the absolute intensity of both peaks increase non-linearly, the slope in the linear background follows suit.

Intensity ratio $R_{\mathrm{Int}} = \mathrm{I(D)/I(G)}$ and Raman shift ν(G) reveal the increase in sp^3 content with growing contribution of silicon. While the Raman shift ν(G) does not give any further clues, the intensity ratio suggests a saturation effect at approximately 11 at.-% silicon content, which was the chosen content for studies in silicon-modified a-C:Si in the previous subsection. From FWHM(D) and form factor α(D), ordering processes with dominant effect in six-fold aromatic ring clusters, i.e. the structures giving rise to the D-Raman peak, take place. This may stem from the capability of silicon to displace sp^2 rings in exchange for chains, which do not contribute. This effect does not seem to approach a limit as before, the decrease in FWHM(D) continues over the silicon content limit from before. The in-

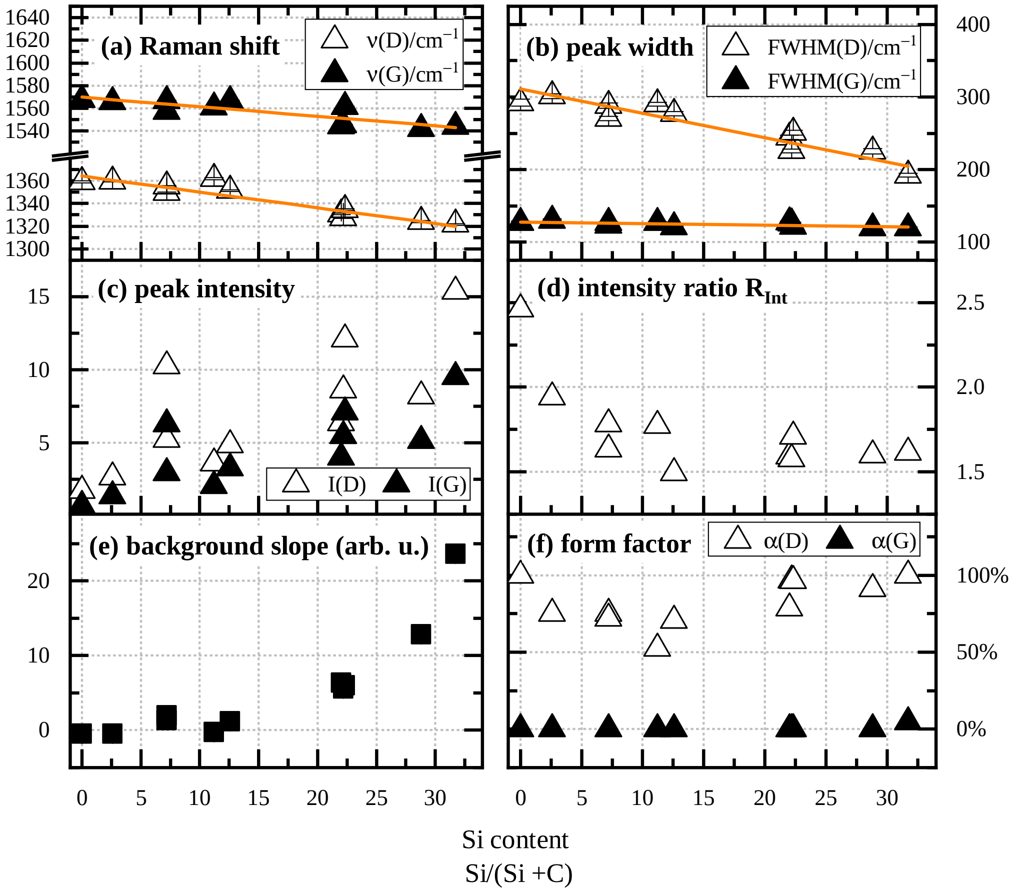

Figure 4.5: Raman fit parameters as a function of silicon content for quantitative analysis. The deposition parameters of the samples vary, so any systematic trend is mostly linked to silicon content. Intensity ratio symbol R_{Int} refers to I(D)/I(G).

terpretation of the intensity is omitted, the background slope behaviour suggests stronger contributions to broad, unspecific spectral features spanning the entire spectral range. Although Raman spectra of a-Si are in fact characteristically broad and feature-less, they are not eligible for explanation. From this, a competing amorphous network could not be identified. The rise in background slope most likely stems from general light scattering or weak fluorescence effects, which gain momentum with stronger silicon content.

It appears that Raman spectroscopy, especially the analysis of the D-Raman mode in Raman shift ν and FWHM with dependable coefficient of determination R^2, is in fact fitting for the quantitative analysis of silicon content. The maximum value in R^2 has to be considered in the light of samples with varying manufacturing parameters, whose effect was estimated to be significant in subsection 3.3.3. These observations are compliant with the previous investigation in behaviour, but all values differ. Other than before, the measurements were done at elevated laser power densities, a microscopically visible imprint is found after laser illumination. In a similar manner, the behaviour in a-C:W and a-C:Ag was investigated, but no comparable significant trends are found. Their fit parameters are found in the backmatter, see Appendix Figure S2 and Figure S3.

Investigation on samples after tribological loading

Two types of tribological loading are investigated in this work, both ex-operando and ex-situ: First, the wear track after a film adhesion test (*scratch test*), in which a steel ball was dragged once along a straight line with increasing normal force, and second, the wear track after measurements for friction and wear coefficients (ball-on-disc *tribometer test*), in which a steel ball is run periodically in rotary manner with a constant normal force. Both test encompass two vastly different situations from tribological perspective, see section 3.1 for details. For a start, scratch test purposefully exceed the film's maximum design capacity of normal force loading until failure, the scar is depicted in Figure 4.6 for reference. For such conditions, only initial and intrinsic properties of the thin film provide tribological aspects, no fully-developed tribo- or transfer-film is expected in such short-lived tribo-contacts. Other than sub-prime lubrication without tribo- and transfer-film contribution, the high contact pressures constitutes external strain and yields plastic deformation.

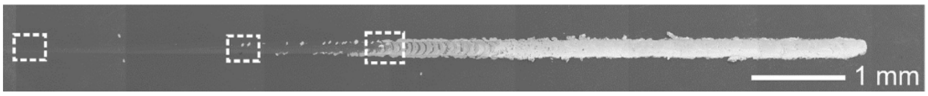

Figure 4.6: Microscope picture of a wear scar after scratch-testing an a-C thin film sample. In such tests, the occurrence of certain wear phenomena are measured for an empirical quantification of thin film adhesion. The first occurrence of the wear phenomena (*cracks*, *spalling*, and *delamination*) are marked as white boxes. Picture taken from publication [215].

Figure 4.7 shows the fit parameters of the Raman modes in a-C:Si and a-C:W after **scratch testing**. Horizontal axis depicts the measurement position along the scratch track and therefore acts as a simple measure for contact pressure. In film adhesion testing, visible cues on wear-related phenomena (like *spalling* failure in Figure 4.1) give the endurance of the testing sample, which is measured in hardness classes. The onset-point of the measurement starts in the worn area, the mapping exceeds the points of spalling failure. The geometry of the measurement only allowed for a fixed focus, so special attention is required for correct allocation of spectral features related to intensity. **In a-C:Si**, the absolute peak intensity is increasing towards the mapping centre, which was chosen to be in ideal focus. From this point on, roughly 20 units, the intensity decreases in a comparable rate until the intensity plummets. Raman shift ν in both modes decrease uniformly and approach a lower limit, that is, ν(G) lowers from 1550 cm^{-1} to 1510 cm^{-1} and ν(D) from 1380 cm^{-1} to 1330 cm^{-1}.

Peak parameter	slope m	intercept b/cm^{-1}	R^2
Raman shift ν(D)	-1.4 ± 0.2	1364 ± 3	0.895
Raman shift ν(G)	-0.8 ± 0.2	1570 ± 4	0.64
FWHM(D)	-3.3 ± 0.4	310 ± 8	0.88
FWHM(G)	-0.2 ± 0.1	128 ± 2	0.32

Table 4.1: Linear fit parameters in Raman shift ν and peak width for D- and G-Raman peak for quantitative analysis with coefficient of determination R^2 value.

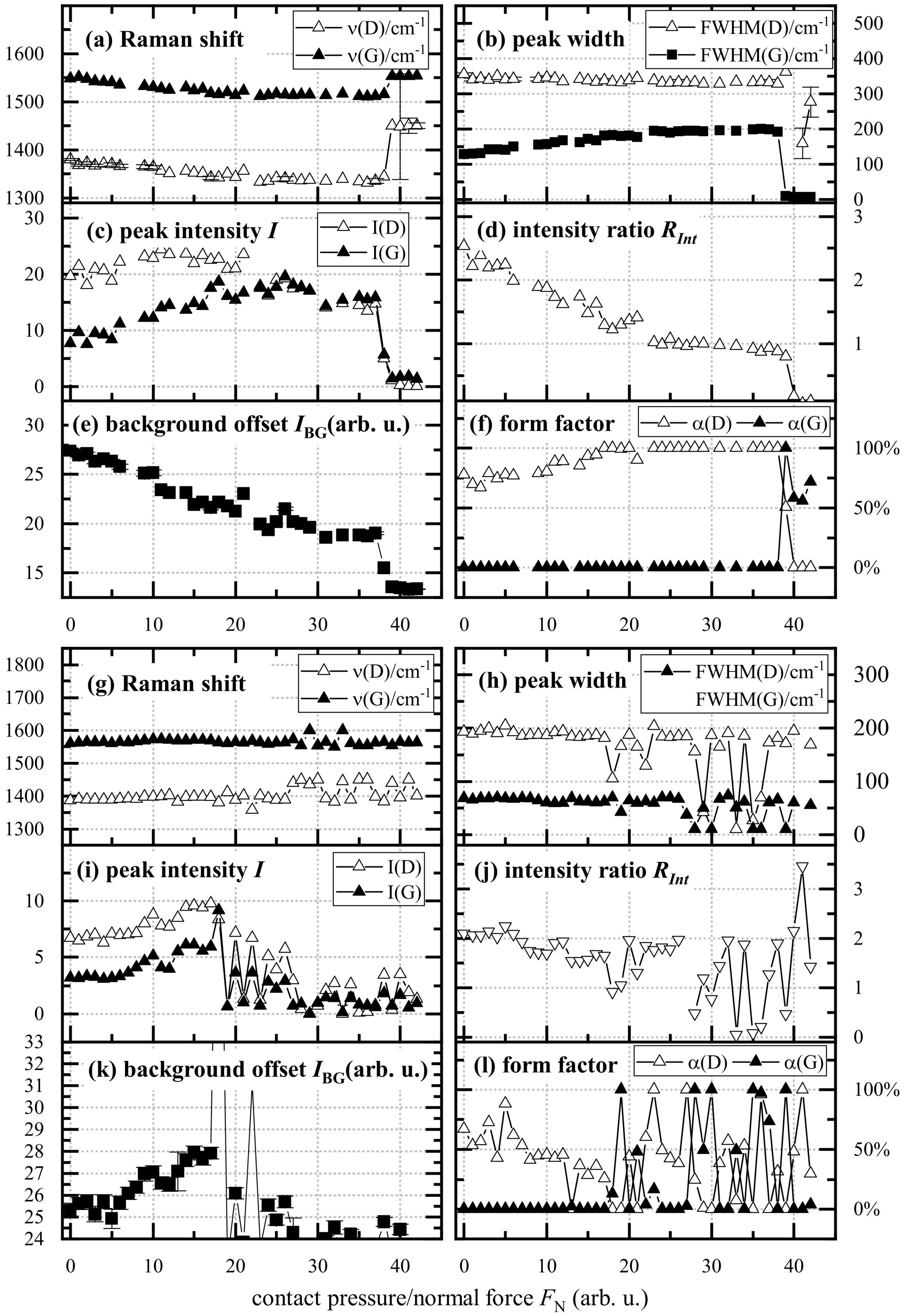

Figure 4.7: Raman fit parameters, when the underlying sample was used for a film adhesion test (scratch test).**(a)-(f)**: Fit parameters for a-C:Si, **(g)-(l)** fit parameters for a-C:W. Intensity ratio symbol R_{Int} refers to I(D)/I(G). Horizontal axis depicts the measurement position along the scratch track and therefore acts as a simple measure for contact pressure. At the horizontal value at roughly 20 units, the underlying sample starts to show spalling failures, which leaves an imprint on the spectra and their fit parameters.

The FWHM is mostly stable for the D-Raman mode, while the G-Raman peak continuously widens from 128 cm^{-1} to 198 cm^{-1}. The intensity ratio is unusually high in comparison to the intensity ratios in the previous section and continuously decreases towards unity. Form factor α(D) shows an increasing contribution of Lorentzian-type modes, the G-Raman peak remains fully gaussian-like. **In a-C:W**, the core peak parameters are mostly unchanging until the middle of the mapping, when it becomes less stable. The lack of stability is clearly seen in peak height, in which an up-and-down between mapping points are detected. Continuing beyond this point, the intensity decreases until the last quarter of the mapping. Beyond this point, deviating and unstable behaviour is found in all peak parameters. The Raman shift ν is weakly affected by the contact pressure, Raman shift ν(G) vaguely increases by the end of the first half. Peak widths show no clear dependence, the intensity ratio appears to have a vague downwards trend. Form factor α of the G-Raman mode remains fully gaussian-like; the D-Raman mode becomes more gaussian-like, but a reliable statement is spared because of high fluctuations and uncertainty.

In both systems, the initial values are deviating from all discussed values above. For clarification, one has to consider the different circumstances, under which these measurements are taken, in short, at elevated laser powers and at tribologically worn sites. As the theoretical framework for a-C is intended for use in undamaged a-C thin films, estimations of sp^3 content or nano-crystalline particle size via intensity ratio/ν(G) is purely qualitative. For quantitative reassurance, other means of measurements have to be supplemented. **In a-C:Si**, a much stronger correlation between the fit parameters and the contact pressure is found. Both intensity ratio and Raman shift ν(G) suggest an increase in sp^3 content as reaction to the intense loading; internal stress is measurable as upshift in ν(G) in literature, but no competing effect thereof was clearly found here. Bonding distortions in all sp^2 carbon sites give rise to the increment in FWHM, apparently the ordering in D-Raman mode-structures are mostly unchallenged. With the results in chapter 5, the defect mechanism in this tribological loading is not graphitisation. There, an increase in FWHM was never observed. Here, initial graphitisation is expected in a limited fashion, as the elevated laser power does leave a visible imprint on the samples after measurement. This, agrees well with the deviating initial peak parameter values. The dominant structural process is the enrichment of sp^3. **In a-C:W**, on the contrary, the very shallow dynamics give little insight about structural changes upon mechanical loading. The formation of sp^3 does not noticeably take place as in a-C:Si, their formation appears to be sufficiently suppressed by tungsten.

The other type of tribological loading, **ball-on-disc tribometer** testing, is a common and first-principle approach for quantitative measurements for the coefficient of friction and wear rate for tribological thin films. For service-life simulation, the testing sample is periodically brought in sliding contact at a fixed normal force and at a constant sliding velocity. In harsh contrast to the scratch test before, the sample stays in conditions and environment for which they are technically designed. Foremost, tribo-material is worn out of the film material's original configuration and has the opportunity to re-deposit on the sample and to become part of the tribo- and transfer-film. In such tribo-meter tests, the coefficient of friction and wear rate are usually averaged after a break-in period. The microscopy pictures of the sample show smooth wear tracks with mostly shallow depth. At the edge of the wear track a non-continuous transition between contact-area and untouched thin film is distinguishable by eye. By the tribological testing, although only small values

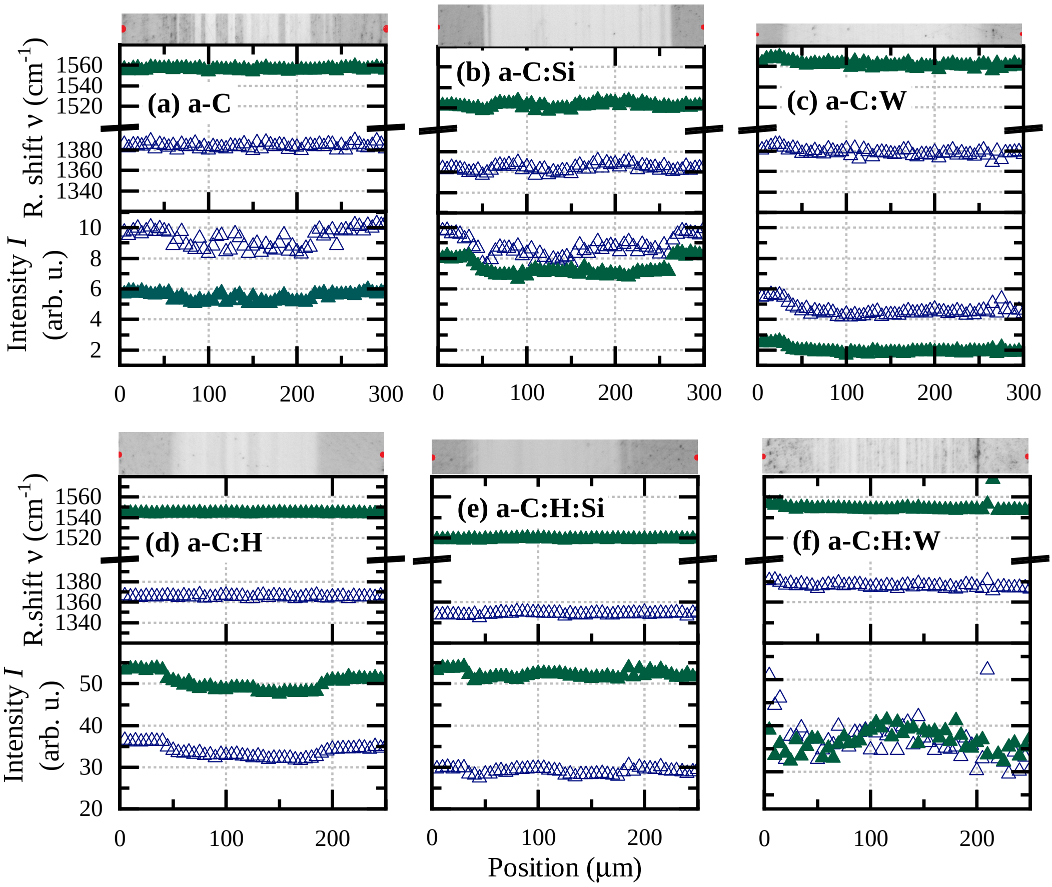

Figure 4.8: Raman fit parameters, when the underlying sample was used for a friction and wear-test, in which a steel ball was periodically dragged on the sample with constant normal force (ball-on-disk tribometer test). The vertical scale the same for each row **(a)-(c)** and **(d)-(f)** with the exception of subfigure **(f)**.

are found, the wear rates are non-negligible. Clearly, wear debris was formed, yet no hints on a formed tribo-film was found here other than in literature. Two situations are conceivable: (i) the wear debris left the tribo-contact and the averaged wear rates mostly capture the material loss, and (ii) the wear debris was (partially) re-deposited onto the film, for example in the wear tracks. By means of a mapping of Raman spectra across a wear track, changes in structure and chemistry in the thin film are detectable.

Figure 4.8 gives an overview on the microscope pictures of the wear tracks and found fitting parameters at each position. Across all samples, the relevant fit parameters are mostly unchanging. For representation, the Raman shift ν of D- and G-Raman mode plus the absolute intensity are chosen, the other fitting parameters evolutions are mostly flat and the averaged values are mostly resembling the discussing of the as-deposited situation described earlier. For some combinations, the spread of peak parameters becomes larger, as soon as the wear track is captured. This can be seen in Figure 4.8 in Raman shifts ν(G) in a-C:Si and a-C:W. This is the closest significant change in (relevant) Raman peak properties, the uncertainty in Raman shift ν are low. Yet, this is deemed as sub-ordinate effect and further discussion is omitted. The absolute intensity does significantly show a spatial correlation. All spectra within the wear tracks have a lower signal-to-noise/absolute intensity ratio or are at level of the wear track exterior. The value spread in absolute intensity seem to be larger within the wear tracks than outside, the uncertainty through the fitting routine is unchanged.

The found constancy in peak parameters rejects the hypothesis of higher-tiered structural or chemical changes during tribo-meter testing in the present extent. As wear debris material is expected to be distinct form the initial state, the absence of wear debris in the wear track suggests that the wear debris was not re-deposited and the wear material left the tribo-contact. As said before, the wear rates in a-C and modified a-C films are low in comparison to MoS_2 thin films, for example. The behaviour of the absolute intensity may stem from a deviating surface within the wear track, for example, random ridges by contact sliding. The general drop in intensity may furthermore have a technical background, because the set focus of the microscope is fixed along the Raman mapping. With a spatial resolution in order of micro-metres and working distance of the microscope objective of in order of millimetres, the shallow depth of the wear tracks may be a significant contribution. It is surprising to find unchanging parameters here, after a visible correlation between peak parameter and contact pressure in scratch test were identified.

4.1.3 Element-modification of a-C thin films with catalysing agents

Silver and copper are neither forming carbides nor bonding to carbon in other ways. Unlike carbide-forming metals, the insertion leads to nano-crystalline metals within a amorphous matrix. Apart from such nano-composite structure, silver in low concentration fully dissolve in a-C [216, 217]; higher concentration leads to growing metallic inclusions. Their effect on carbon is, in contrast to silicon and tungsten, not bound to hybridisation, but on catalytic effects.

Figure 4.9(a)-(d) encompasses the deposition of a-C:Ag on a steel- and on a titanium-based substrate. On **steel-substrates** [215] , the effect of bias voltage U_{BV} is co-measured, it shows a strong correlation with the over-all scattering yield. This behaviour was not observed in the studies of bias voltage U_{BV} on a-C deposition. On the contrary, the background zero-level of the Raman spectra was mostly unchanged and an increasing bias voltage U_{BV} worsens the signal-to-noise level. In fact, fitting reveals that the peak intensity of D- and G-Raman modes are actually decreasing slightly with rising bias voltage U_{BV}. With that revelation, the behaviour of the Raman modes, but not the zero-level, agree more with the bias voltage U_{BV} study above. On the relevant peak parameters, most prominent behaviour are up-shift and narrowing of the G-Raman mode, so called phonon mode hardening, with increasing silver content. The D-Raman peak remains constant over the course of this study, a trend in intensity ratio was not found clearly. On **titanium-substrates** [219] , the silver content is varied at constant bias voltage U_{BV}. The zero-level is affected by the silver content alone, the outcome however is miniscule against the previous case. The behaviour of the D-Raman peak and intensity ratio is analogous to the steel-substrate counterpart, but the Raman shift $\nu(G)$ is unchanged for the G-Raman peak as well. Its FWHM narrows in a comparable fashion from $161\,\mathrm{cm}^{-1}$ to $153\,\mathrm{cm}^{-1}$ for increasing silver content. At the highest amount of silver and therein especially at lowest bias voltages, the D- and G-Raman peaks start to separate and become similar to graphitising carbons. Second-order peaks are not

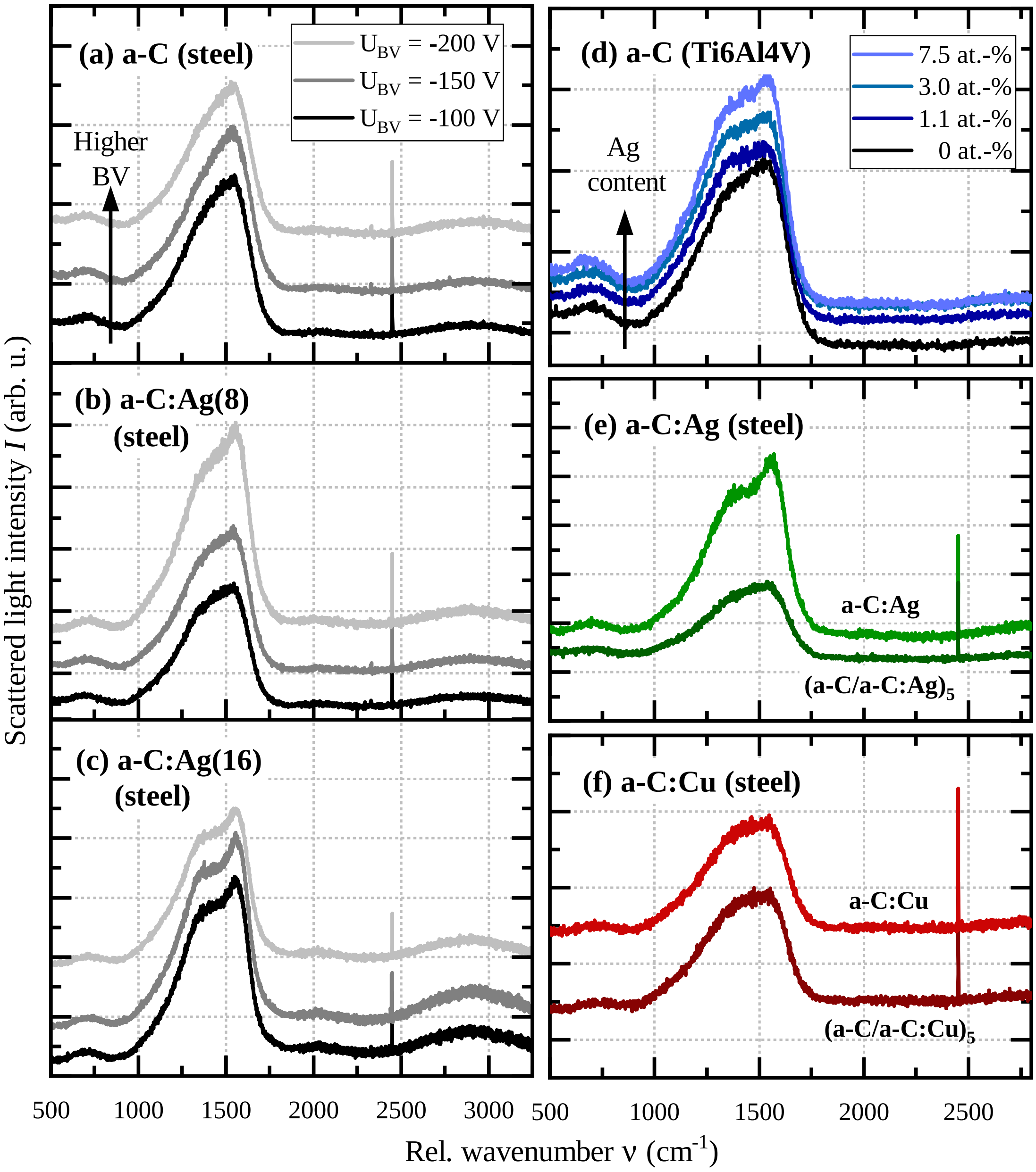

Figure 4.9: Raman spectra of silver-modified a-C:Ag **(a)-(c)** on steel substrates or **(d)** on titanium-based substrates, each with different degree of silver-modification. Subfigure **(e)** compares Raman spectra of a singular a-C:Ag to a multi-layer system of a-C/a-C:Ag, subfigure **(f)** is analogous for copper-modified a-C:Cu. Spectral feature near 2330 cm^{-1} is ascribed to atmospheric nitrogen [218].

found clearly, although a pronounced bulge in the corresponding spectral range is found for highest silver content.

The increase in zero-level likely stems from altered (optical) absorption behaviour of the thin film. By other means, the re-sputtering rate of silver sites was found, so an increased bias voltage U_{BV} The behaviour of the G-Raman peak suggests a general structural ordering process, i.e. proliferation sp^2 carbon clusters in six-fold rings at the expense of sp^3, and reduction in defects. This seems plausible, because catalytic agents shift a mixture of thermodynamically and kinetically stable species towards thermodynamic stable products. [215] Internal stresses might be a co-factor in the Raman mode upshift, but this would suggest an increase in FWHM(G). Such internal stresses are assumed by other means in the underlying study, in this case, poor adhesion. Increasing the intensity ratio along with the upshift in ν(G) naturally suggest a decrease in sp^3 content, which was complementary found in X-ray spectroscopy. A 10 % decrease in intensity ratio translates to a drop in sp^3 content by a few percent. In the highest silver content, approx. 9 and 12 at.-% the onset of graphitisation is found by its characteristic peak narrowing and distinguition. For silver content up to 7.5 %, however, no graphitisation process was found.

Figure 4.9(e)-(f) shows the Raman spectra of a-C:Ag and a-C:Cu thin films and their multi-layer counterparts. Multi-layer film structure feature improved tribological performance over regular a-C:X thin films. The individual layers have a thickness of 100 nm and are comparable to the penetration depth of the laser. The top layer consists of modified a-C:X. The single-layer a-C:Ag thin film in subfigure (e) suffers from initial graphitisation (not shown), which was previously found to set of at silver content above 7.5 at.-%. Surprisingly, the thermal stability is increased, i.e. graphitisation is suppressed, in the multi-layer film system. Avoidance of graphitisation is linked to increased hardness, which is indirectly verifiable via Raman spectroscopy in the case of a-C:Ag being prone to graphitisation. Additionally, the effect of copper-modification is described as well. D- and G-Raman mode show directly comparable spectral features with minor differences. The behaviour of copper is closely related to the behaviour of silver, but no graphitisation is found. By other means of investigation, the frictional behaviour of a-C:Cu differs from the situation in a-C:Ag. The amount of nano-crystalline particles of copper has a self-lubrication effect, but no evidence thereof is measurable by Raman spectroscopy.

In summary, Raman spectroscopy shows the onset of thin film failure due to graphitisation and shows its usage in quality assessment. The addition of silver to a-C, especially, may lead to reduced stability, which is circumvented by multi-layer thin film systems. Reactions of catalytically-modified a-C thin film towards thermal heat is studied in the upcoming chapter.

4.2 Molybdenum disulphide thin films and their element-modified derivates

Key advantages of molybdenum disulphide are based on high tolerance towards surface pressures in comparison to other lubricant compounds and, foremost, on its tribo-film formation in operando and in situ. Their nano-scale mechanisms or possible conditioning, however, are still object of research. While a general understanding for a complete picture on the tribo-film formation suffers from it taking place *in situ* and *in operando*, and thus making direct probing mostly infeasable, the *ex situ* situation is far easier accessible. Measurements of wear rates and coefficient of friction are done as a ball-on-disc *tribometer test*, in which a steel ball is run periodically in rotary manner with a constant normal force. The resulting scar after measurements show characteristic wear track, debris particles, and baked-on tribo-film material, see Figure 4.15 for reference.

A thorough discussion on basic MoS_2 thin film Raman spectra is given in chapter 2.2, subsection 2.2.5. This chapter highlights the differences thereto in the interest of concise writing. Rather than structural changes alone, the evolution in MoS_2 thin films is often detectable via the presence of oxidation products, which have a unique Raman signature.

4.2.1 Objectives of MoS_2 film manufacturing for general tribological application: improving friction by balancing stability

For tribological applications of MoS_2 thin films, core objective is the reduction of friction. As apparent later, the objective in designing MoS_2 thin films is mostly avoidance of chemical or structural weak points. In more detail, the friction is directly and indirectly dependent on a manifold of parameters. For this work, those are grouped in (i) properties of the film and (ii) conditions in the tribo-contact, both of which are also relevant for (iii) tribo-film formation and stability. Wear[3] is considered secondary, because the tribological benefit of MoS_2 thin film is based on tribo-film formation, which requires third body particles to some degree. In literature, the majority of a deposited MoS_2 thin film is reported to wear out in the break-in process. [136]

Properties of the film encompass physical and chemical aspects, of which a selection is considered in this work, namely crystallinity and growth direction, defect type and - density. By other means of investigation, influence on friction is known for e.g. general density, elastic modulus, hardness, and ductility [130], but they are disregarded here. Chemical properties are reaction- and interaction-related like reactivity towards environment. On the one hand, properties of the film are chosen to counteract the shortcomings of the film, namely chemical sensitivity of crystallite edges towards water or oxygen, and a preferable orientation with low shearing. On the other hand, low friction is known to be found when the deposited films are rich in small crystallites [130], which translates to a dense microstructure, and basal orientation. [220] The deposited thin films in this work are polycrystalline with diverse growth orientation in nature. The diversity in growth orientation also encompasses competitive growth processes, which could ultimately induce internal stresses. Another origin of stress in thin films stem from sub-surface implantation of highly energetic species, which may be thermalised onwards.

---

[3] Wear as defined as material removal from its initial location

The majority of properties are related to structure or chemistry and may therefore be accessible via the Raman spectroscopy. Influencing elements of those three groups take effect in different circumstances. For a start, influences **during deposition or during annealing** are of interest.

Influences on film properties during deposition manufacturing

Present thin films in this work are deposited via high-power impulse magnetron sputtering (HiPIMS), which naturally provides thin films with better quality in morphology, suitable wear-limiting hardness, and oxidation resistance by comparison to e.g. compressed powders, which do not cohere well. [130, 221, 222, 223] Present thin films show the best friction behaviour with higher sulphur vacancies (sub-stoichiometry) and basal growth direction with respect to the substrate. [63] The deposition temperature influences diffusion and/or relaxation processes of adatoms on a surface, which result in larger crystallite sizes in preferable orientation and lower density structural defects, while sub-stoichiometry may be maintained. [224] Previous studies also show the influence of bias voltage U_{BV} on growth direction and structural defect relaxation. [63] This, however, does not show in Raman spectroscopy. The combination of bias voltage and deposition temperature gives rise to defect-rich thin films, even amorphous samples in extreme cases, which increase hardness due to altered bonding characteristics and resulting stresses. In Raman spectra, this is found in higher Raman shifts ν in more defect-rich samples.

Post-deposition processes include **annealing**, which acts on residual stress or defects in the film. By the possible ejection of sulphur compounds, annealing at 300 °C near the thermal stability limit generates sub-stoichiometry of $x \approx 1.7$. [225] Annealing at 600 °C, strain is relaxed, structural diversity is reduced, and basal growth direction is favoured over columnar. Such high-temperature annealing generates films similar to bulk-like $\mathrm{MoS_2}$ crystals. In annealed samples, an overall better signal in Raman spectra is achieved, which is associated to reducing amorphous regions that don't contribute to the signal. When Raman spectra become measurable, the involved line widths narrow - a clear sign for defect relaxation, structural ordering and diversity reduction. On bonding level, strain reduction is measured in general Raman shift ν like for substrate temperatures. Although reduction of stoichiometry acting in favour of lower friction, in total, increasing annealing temperature impedes friction reduction as structural homogenesis and ordering counteract stronger.

4.2.2 Influences of environments on tribological performance and tribo-film formation

The effect of humidity on the properties of present films is known to be vital. Benefit and disadvantage thereof are in balance [226]; the former revolves around the desired tribo-film, the latter focusses on higher (initial) friction by higher shearing forces. **Inert environments** are required when both friction and wear have to be kept low. [164] This is the core argument for using $\mathrm{MoS_2}$ lubricants in vacuum or space applications over e.g. a-C thin films. Nitrogen (N), in fact, is known for its self-absorbent behaviour acting as a masking agent for chemical weak points. [227]. In **humid environments**, contrarily, water adsorbs and even partially diffuses into the film, so oxidation occurs. [163, 228] Naturally, the initial wear rates in ambient air and in inert atmospheres are diametric. The friction behaviour, however, shows a more intricate behaviour. Initial friction is higher in air than in argon and nitrogen, but particle generation for tribo-film formation is vastly accelerated. Although the friction start higher, the benefit of tribo-film formation counteracts the initial higher friction. This is true under the premise of having a sufficiently high contact pressure, in a nutshell, the mechanical prerequisite for a stable tribo-film. [136, 137, 138] A high contact pressure attenuates the impact of environment on wear in the long run, which is mostly independent on sliding velocity, and therefore also mostly independent on friction power at constant normal force. It may even prevent the rupture of the thin film. Although friction benefits from tribo-film formation in humid air, the friction is not as low as in inert environments. The difference, however, is an increase of < 0.2 in coefficient of friction, only. Again, for a constant normal force, friction is mostly independent on sliding velocity and thus on friction power.

For Raman studies, both initial and tribo-film material are of interest, which make surface oxidation and ordering processes apparent. Figure 4.10 gives a summary on all relevant Raman spectra; subfigure (a) shows **initial material** spectra, (b) the various **tribo-film material**.

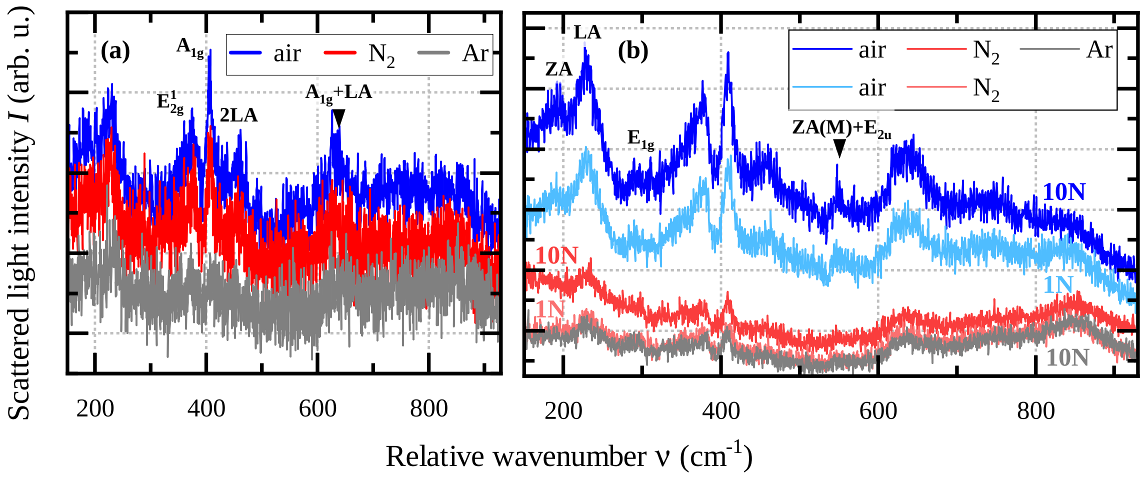

Figure 4.10: Raman spectra of unmodified MoS_2 thin films, which were worn in a ball-on-disk examination with different environments, namely, dry argon (Ar), dry nitrogen (N_2), and humid air. Subfigure **(a)** depicts untouched sample locations for the as-deposited situation, subfigure **(b)** captures wear debris near the wear scar edges. Indicated force values indicate the used contact force in the ball-on-disk tribometer.

The **initial material** shows no relevant differences in Raman spectra with respect to environment other than deviating scattering yield, all spectra are similar to the basic spectrum in chapter 2, section 2.2.5. Absolute intensity of Raman peaks is linked to the concentration of scattering centres and on optical properties of the surface. The latter often has a negative impact, especially when newly-forming or -ordered material is more optically absorbent or structurally Raman-inactive. Literature suggests that little oxidation starts immediately, even at ambient temperatures and ambient partial pressures of oxygen, and only gains momentum for elevated ambient temperatures. [163] Only the ambient air is suspected to show any effect even if minor. The laser power is purposefully chosen to not initiate any chemical reactions. For all this to play a crucial role, the background is expected to remain basically unchanged. So, the present spectrum-wide gain in intensity is most likely not linked to relevant structural changes, but on reducing Raman-inactive material like amorphous thin film material. Of note, all samples are transported through and stored in ambient air, so related effects are expected on all samples. An unaccounted contribution, regarding the higher friction and wear, may be a higher local temperature of the material close to the wear track, which is not sufficiently verifiable via the present measurement.

Wear particles are generally found at the edge of wear tracks forming the **tribo-film**, see Figure 4.15 for reference. For nitrogen and humid environments (at higher surface pressures), the wear particles yield a visibly more pronounced tribo-film than in argon atmosphere, which agrees with the expectation as described above. For humid environments and high contact pressures, the tribo-film even covers most of the wear track. For low contact pressures, the found tribo-film is comparatively lean, but the friction is reduced over bare steel contact, even although the film material is visibly lost. The Raman spectra show no chemical reaction of the film, the spectra is still mostly allocated to MoS_2. The Raman bands of MoS_2 which were also found in the initial material, show much clearer signals and strongly improved thermal resistance. In more detail, the thermal resistance is sufficient to withstand a laser power, which is known to initiate oxidation otherwise, as in the initial material in subfigure (a). Any other changes like change in FWHM or Raman shift ν are not apparent, but clearer peaks are found at roughly 630, 750 and $845\,\mathrm{cm}^{-1}$.

The higher scattering yield is linked to the formation particle sizes, which elevates the scattering yield. The mechanism for reduced heat transfer is two-fold: first, the particle size participates in a different type of scattering with lower energy transfer in general, presumably Mie scattering. In such, the particle sizes are in the same order of magnitude as the wavelength of the photon. This seems plausible, because the initial state do show the same Raman modes, but much fainter. Highly defected or amorphous MoS_2 thin film structures do not give clear bulk-like MoS_2 signatures. The new peaks at 630, 750 cm^{-1} are attributed to second-order scattering processes and latter at 845 cm^{-1} to secondary molybdenum compounds. Oxides of the thin film material or of the substrate are not found. This result suggests that either flash temperatures in the tribo-contact are not sufficient for relevant oxidation or the thermal stability is increased, i.e. the tribo-film is sufficiently protecting the wear track. Such relevant oxidation is distinguished from surface oxidation in general, as oxidation is known to set in immediately. [163] Relevant oxidation should have an impact on the friction behaviour, however, even sliding in 250 °C in ambient air is found to be within tolerance; of note, oxidation rates in similar films are lower than the regular wear rate, [228] so superficial oxidation is worn out along with film material removal and tribo-film generation. While the adaption of basal orientation is not measurable in Raman spectroscopy directly, it was shown via other means like X-ray spectroscopy directly and through the reduction in friction. In contrast, reduction of strain or ordering processes, should become visible in altered Raman shifts ν or FWHM, as described above. Both peak parameter are changing negligibly, only.

In total, the structural changes are not directly visible in Raman spectroscopy, but the implications of such are. The only measurable structural change, the particle size, leaves a mark in the spectrum as general intensity. More interestingly, the thermal stability increased, which may be studied in future in more detail.

4.2.3 Copper-modification: MoS_2:Cu thin films

Besides increasing friction performance by mildening the short-comings of MoS_2 thin films or by promoting the formation of tribo- and transfer-films, the combination of MoS_2 with other types of solid lubricants are conceivable, for example, as part of a film system or as composite film. Within the scope of this study, a selection of metals were incorporated into MoS_2 thin films, among which copper stood out for being a solid lubricant itself.

Copper (Cu) is a comparatively soft metal, it features a both self-lubricating and catalytic behaviour. Its friction behaviour is based on lower shearing forces and, possibly, by formation of tribo-films in MoS_2; copper provides impact on lubrication and on structure of MoS_2 of salience. Incorporated into MoS_2 thin films, copper replaces molybdenum atoms leaving them unbound in the solid and increasing Mo/S stoichiometry. [229, 230] At lower copper contents the basal-plane growth direction is preferred over the others, copper content above certain levels induces amorphous structures in MoS_2 thin films. Incorporation of other transition metals usually just results in densification and preferred basal-plane growth, copper additionally acts as an amorphising agent. Unmodified MoS_2 thin films usually show a mixture of different growth directions. Densification and preference in basal growth direction were previously described to improve intrinsic tribological performance. Friction reduction is impeded at higher contents, however, because amorphous thin film is more likely to be irrecoverably removed with substrate exposure. The friction in this situation is still lower than the non-lubricated material pairings. The wear is lowest for amorphous MoS_2 thin films, i.e. with highest copper content. So, the formation of transfer-films with its tribological improvement is likely.

Figure 4.11 presents the Raman spectra of the film in their **initial state** and the situation at **bare wear track locations** without pronounced wear particles. Figure 4.12 features worn samples, specifically a **selection of wear particles**. The former covers a study of various copper contents, the later the effect of post-deposition annealing on wear debris.

Initial state after deposition, wear track after a ball-on-disk tribometer testing

Raman spectra of the film in their **initial state** in subfigure 4.11(a) show regular MoS_2 signatures. Most interesting, above a certain copper content, all Raman modes decrease and eventually yield an empty spectrum. Prominent spectral features, the Raman modes $E^1_{2g}, A_{1g}, 2LA(M)$, drop in intensity at comparable rate; the acoustic mode $LA(M)$ has a stronger decline at low concentration. Peak widths are mostly unchanged, additional peaks are not found. From Raman spectra alone, the absence of features may stem coverage of copper, which is not Raman-active, or from amorphous MoS_2, whose features are very faint.

The situation in particle-free **wear track** in subfigure 4.11(b) also shows the absence of spectral features at highest copper content. The panels of lowest copper content show oxides of the substrate; further analysis thereon is omitted. In the intermediate range, usual MoS_2 Raman peaks are found, namely the Raman modes $LA(M), E^1_{2g}, A_{1g}, 2LA(M)$. Unlike before, the intensity does not decline in lock-step and an empty spectrum is postponed to the sample of highest copper content. Also, the $LA(M)$ mode is changing in its own pace again. The general background appears to increase at copper contents above 28 at.-%.

The exposure of the substrate indicates the loss of the thin film directly, the presence of MoS_2 signatures upon copper content of 30 at.-% prove structural changes in the wear track.

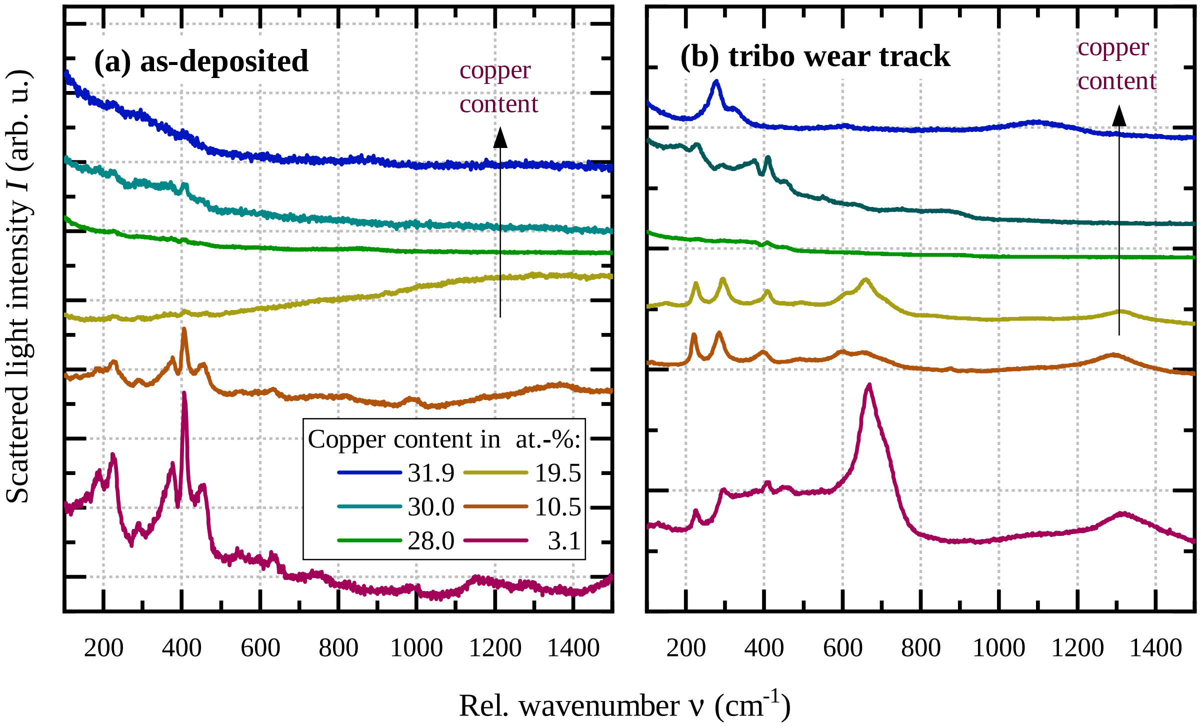

Figure 4.11: Raman spectra of copper-modified MoS_2 thin films in **(a)** the as-deposited state and **(b)** worn state, situation in wear track without pronounced debris.

Chemical changes can be neglected, because no signs of oxidation are found. The lack of attenuation as above, which was connected to be related to coverage of copper, indirectly shows a precipitation effect of copper in MoS_2 at higher contents. This was verified in the underlying study by other means.

Effect of annealing

The previous investigation concluded that MoS_2:Cu with copper content of 28.0 at.-% is on the brink of amorphisation, the wear scar has full MoS_2 character. This sample is chosen for studying the effect of annealing. Figure 4.12 shows Raman spectra of distinct locations in the wear scar of the sample. It is divided into three subfigures, for annealing temperatures of 100 °C, 200 °C, and 300 °C each. The colours of the spectra are matched for a type of wear debris or sample location. For clarity, two Groups of sample locations are defined: Group 1 features bare white locations in the tribo-track or white plateaus on top of debris, Group 2 features gray debris, side debris, or locations in bare gray tribo-tracks. For a visual orientation, refer to the upper and middle row in Figure 4.15.

More pronounced Raman signatures are found for Group 2: gray debris (dark gray spectra), side debris (red spectra), or in bare gray tribo-tracks (yellow ochre spectrum). The **behaviour of annealing** with temperatures of 100 and 200 °C yields an mostly empty or very shallow Raman signatures for Group 1, specifically bare white tribo-track (mint green spectra) or white plateaus on top of debris (violet spectra). More pronounced Raman signatures are found for Group 2: gray debris (dark gray spectra), side debris (red spectra), or in bare gray tribo-tracks (yellow ochre spectrum). MoS_2 signatures are most pronounced in gray debris, all other spectra have a lower signal-to-noise ratio, if any. Direct comparison of annealing with temperatures of 100 °C and 200 °C shows that all MoS_2 signatures decline for higher annealing temperatures, even the most distinct particle type, the gray debris. In spectra of Group 2, a well pronounced spectral feature around $800\,\mathrm{cm}^{-1}$ appears with vastly higher peak widths and asymmetry. This features appears more strongly in 200 °C annealing, the peak is generally upshifted. In some places in the tribo-track, the surface appears tarnished, which is only visible in colour microscopy pictures. The Raman spectra of those location fall in between the two groups above. The behaviour of annealing of 300 °C stands out, only Raman signatures of substrate oxides are found, independently of sample locations.

The strong MoS_2 signatures in gray debris are conform with the behaviour of wear particles in different environments, in short: the thermal stability towards laser heating, which is based on particle sizes of a certain size (presumably resulting in Mie scattering), and the Raman scattering yield are increased. Annealing is expected to reduce amorphous regions and to reduce stresses. The wear phenomena are comparable in 100 °C and 200 °C annealing, so no fundamentally different processes in tribo-film take place. However, from the generally weaker MoS_2 signals in higher temperature annealing, it is deduced that MoS_2 sites form in lower extent. Apparently, the reduction of amorphous regions or stresses inhibited the formation of ordered MoS_2 site in the tribo-film, although the opposite is expected. To explain this apparent contradictory, one has to distinguish the natural formation of MoS_2 via temperature annealing and the forced formation *in situ* for the tribo-film formation. If those processes were equivalent, the 200 °C annealing should present clearer MoS_2 signatures, which it does not. For the feature around $800\,\mathrm{cm}^{-1}$, no singular mode is assumed, because singular Raman modes of size and asymmetry like are vastly uncommon. Here, it stems from multiple Raman modes of molybdenum oxides and more complex structures of iron and molybdenum oxides. In more detail, simpler molybdenum oxides like MoO_3 at $778\,\mathrm{cm}^{-1}$ and complex oxides like Mo_4O_{11} at $849\,\mathrm{cm}^{-1}$ and $907\,\mathrm{cm}^{-1}$ [231] are assumed to give rise to the feature. Adjacently, Raman mode of $Fe_2(MoO_4)_3$ at $942\,\mathrm{cm}^{-1}$ may contribute in border cases. All involved Raman modes are expected to be broad and overlapping, as the material is most likely strongly disordered or amorphous. From this, it appears that 200 °C annealing dictated the wear debris towards oxides, which are more complex or bordering to iron-molybdenum oxide compounds.

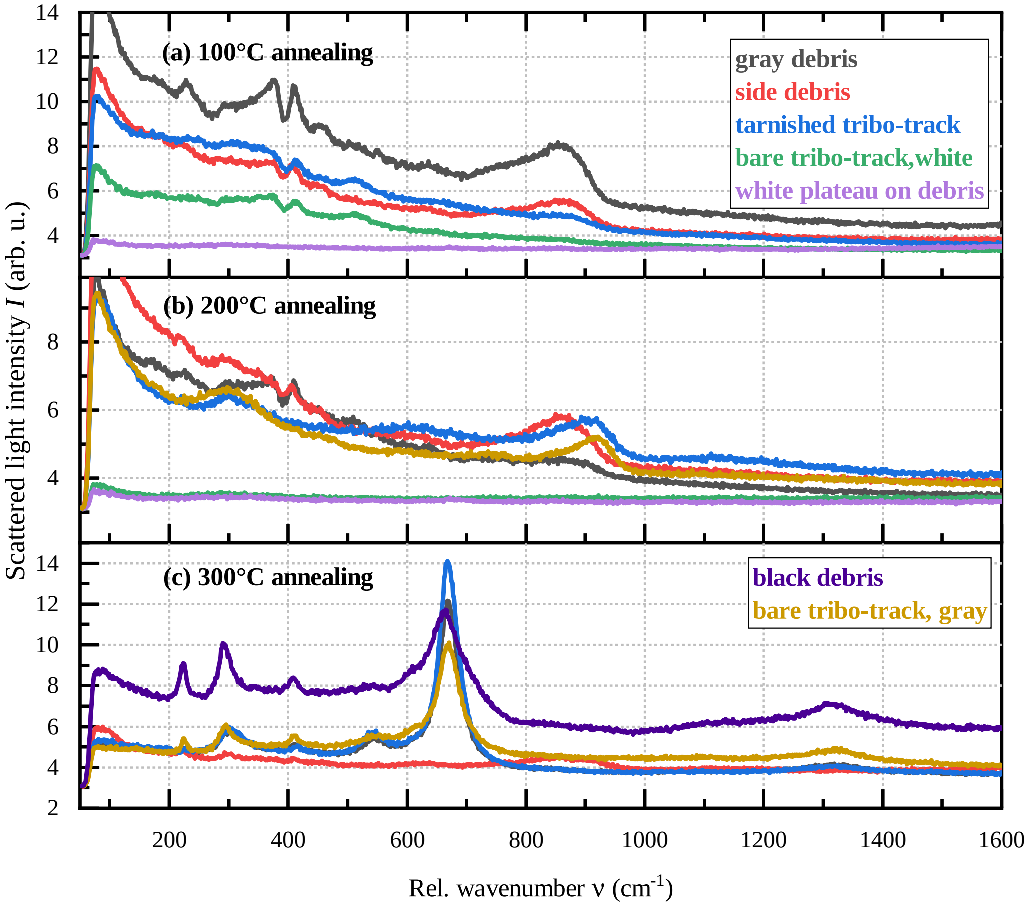

Figure 4.12: Raman spectra of copper-modified MoS_2 thin films, effect of annealing at various probing locations and different types of pronounced wear particles. For probing locations, refer to Figure 4.15.

4.2.4 Nitrogen-modification: MoS_2:N thin films

Nitrogen modification in MoS_2 is comparatively simple to achieve by injection of nitrogen gas (N_2) in the deposition chamber during manufacturing. Naturally occurring nitrogen is infamous for its strong intrinsic bonds. On that note, it is surprising that the mere presence of nitrogen gas leads to atomically bonded nitrogen-modification rather than nitrous compounds or solution into the thin films.

In MoS_2 thin films, nitrogen is used for increase of load bearing capacity. It counteracts short-comings of an unmodified MoS_2 thin film like its preference for columnar rather than basal growth direction and preference for porous rather than dense micro-structures. Those lead to poor hardness and adhesion, so excessively high wear rate may remove MoS_2 material from the tribo-system before being re-deposited and re-structured to form a tribo-film. At lower concentrations, the effect in adhesion behaviour is already measurable by other means in the underlying study. [177] Structurally, nitrogen contents of (7 to 20) at.-% induce a transformation from crystalline to amorphous as determined via X-ray diffraction spectroscopy. Polycrystalline or amorphous thin films show considerable tougher mechanical properties, which is directly linked to wear. As mechanism, the effect of nitrogen sets in at one of the weak point in MoS_2, the adsorption of water at particle edges. Their presence has a essential role for chemical reactions (*metasomatosis*), as well as direct impact on tribological properties, because shearing of planes are impeded. Chemically, mixture compounds such as amorphous Mo-S-N films are reported, which form during re-orientation. This *in situ* reorientation from columnar to basal orientation, as discussed earlier, improves frictional properties over initial basal-forced thin films.

The key friction reduction mechanism in MoS_2 arises from the formation of tribo-films, which, in turn, requires a certain degree of (initial) wear particle generation. The long-term wear coefficient in MoS_2:N, in contrast, is significantly reduced over the standard situation (unmodified thin film in humid ambient air), while friction performance remains steady. In essence, a previously amorphous MoS_2:N thin film is still able to form MoS_2-based tribo-films. For this, of course, wear particle formation may not be overlooked: the combination of wear particles not leaving the contact and still being available for tribo-films settlement, concludes improvement in wear behaviour. The break-down of thin films, which are a considerable factor in thin film modification, is comparable to the unmodified situation with amorphous and/or porous microstructure, because nitrogen compounds evaporate upon activation. As shown later, this is shown for thermal curing in this work and for tribological activation as well in literature for related films. [177]

Figure 4.13 presents the Raman spectra of the film in their initial state and the situation at bare wear track locations without pronounced wear particles. Figure 4.14 features worn samples, specifically a selection of wear particles. The former covers a study of various nitrogen contents, the later the effect of post-deposition annealing on wear debris on one sample with highest nitrogen content, MoS_2:N with nitrogen flow of 120 sccm.

Initial state after deposition

Raman spectra of the initial state show MoS_2 signatures for nitrogen content (7.1 ± 0.3), (11.0 ± 0.4), and (12.4 ± 0.2) at.-%, only. The signatures are the usual prominent spectral features, the Raman modes $E^1_{2g}, A_{1g}, 2LA(M)$ along with poorly resolved acoustical modes

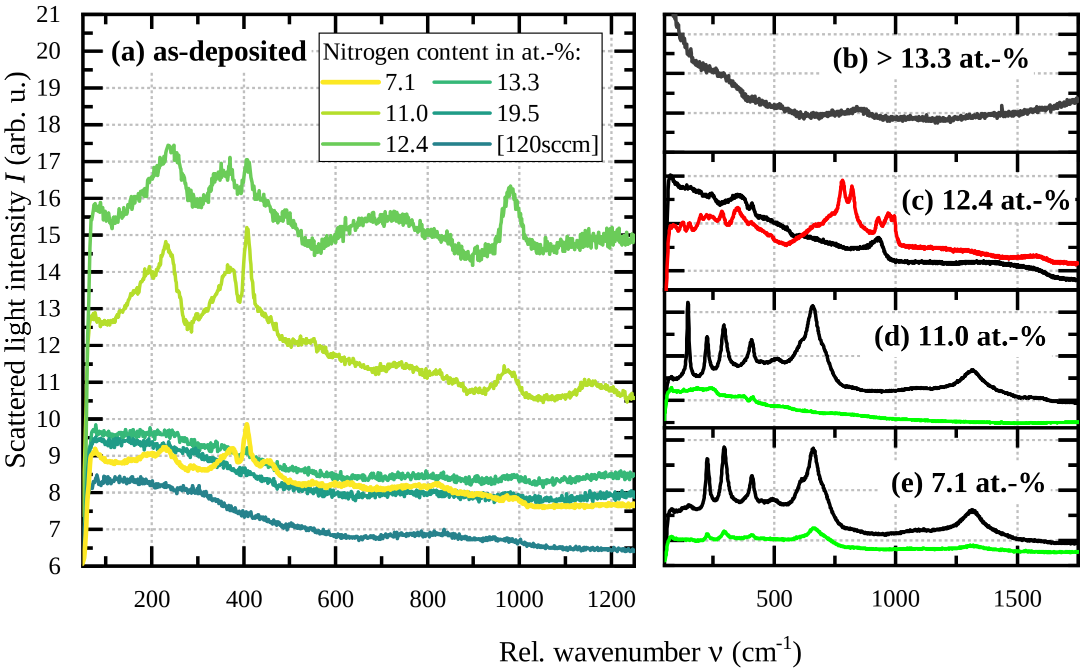

Figure 4.13: Raman spectra of nitrogen-modified MoS_2 thin films in **(a)** the as-deposited state and **(b)-(e)** worn state, situation in wear track without pronounced wear particles. In subfigures **(b)-(e)** black plot colour denotes gray or white debris, green plot colour dark debris. In subfigure **(c)**, the red plot colour denotes a flake, which was only found in this sample.

in the 200 cm^{-1} range, which form a hump. The sample with (11.0 ± 0.4) at.-% nitrogen content shows the clearest signals with strongly elevated background. In comparison to the preceding content, it appears that the $2LA(M)$ mode stays mostly the same and does not increase in lock-step with the other Raman peaks; it is only detectable as shoulder. The ratio between A_{1g} and E^1_{2g} mode, although better pronounced, appears to decrease. The acoustical modes in front are as intense as the highest optical mode A_{1g}, an additional peak in the range 950 cm^{-1} arises. The next highest content is a smaller increment at (12.4 ± 0.2) at.-% nitrogen, but still shows the trends from before: a considerably elevated background, a declining A_{1g} mode in comparison to the E^1_{2g} mode and further increasing peak in the range 950 cm^{-1}. The acoustical modes are similarly pronounced as before. Nitrogen contents above 12.4 at.-% prompt empty spectra with drastically reduced background over the previous spectra, which further drop in intensity with increasing nitrogen content.

Smaller content of nitrogen give rise to more pronounced peaks as it was observed before. It raises the hypothesis that the disordering character of nitrogen first yields a polycrystalline structure or structures of similar size, which was previously found in re-depositioned wear debris contributing to Mie scattering, presumably. When signal intensity was the objective, a flow rate of 40 sccm would be ideal. Declining A_{1g} modes as well as the strong acoustical modes in rising nitrogen content gauge the density of defects. The behaviour of the second-order $2LA(M)$ would suggest otherwise, the reason was not resolved.

Wear track after a ball-on-disk tribometer testing

The situation in particle-free wear track of MoS_2:N for higher nitrogen content shows empty spectra in agreement with the findings in the initial state and in case of copper-modified MoS_2 thin films at high copper content. The green spectra in the two lowest contents represent sample locations within the wear track in gray, the black spectra represent the usual dark spots, see Figure 4.15 for sample images. The green spectra are both mostly empty, the sample with 11 at.-% nitrogen shows faint signatures of MoS_2, while the black spectra show the characteristic spectrum of substrate oxides. The situation in the sample with medium-strength modification is like the green spectra and the higher-modified samples mostly empty. Only a flake-type wear debris (red spectrum) shows Raman signatures of MoS_2 and oxides. Such oxides were not found elsewhere and in no other samples of this series.

Empty spectra for the higher-modified samples was also found previously in copper-modified MoS_2 thin films at high copper content. There, two explanations revolve around amorphous MoS_2 material and around copper smearing, both yield no or very weak Raman signatures. In MoS_2:N, the possibility of a shielding effect is excluded for nitrogen, so, the empty spectra in MoS_2:N are attributed to amorphous MoS_2:N. It is noteworthy that amorphous MoS_2 appears to be more laser-resistant than the initial, as-deposited state, which was previously only found for wear debris with strong MoS_2 Raman signatures. It appears that the re-structuring mechanisms in nitrogen-modified MoS_2 also increase the thermal resistance, but does not solely rely on structure. Amorphous and re-deposited MoS_2 can withstand the impact of the laser energy.

Effect of annealing

For investigation on annealing effects, the highest content of nitrogen was chosen. In previous investigations, such high content of nitrogen prompts empty spectra, which was linked to strong amorphisation. Like for MoS_2:Cu, Figure 4.14 is divided into three subfigures for each annealing temperature, colours of the spectra are matched for a type of wear debris or sample location. For a visual orientation, refer to the lower row in Figure 4.15.

When annealing amorphous MoS_2:N with temperature of 100 °C, the usual locations in the wear track yield weak Raman signatures of MoS_2, namely gray debris (dark gray), side debris (red) or bare white tribo-track (mint green). Unlike in MoS_2, all locations with MoS_2 signature are comparatively weak. White plateau on debris (violet spectrum) is mostly empty. For temperatures of 200 °C, every position yielded MoS_2 signatures. The spectra appear stacked, i.e. the relative intensity of the peaks are comparable, but the background deviates. In comparison to the annealing temperature of 100 °C, all spectra in subfigure (b) are lower than the most pronounced spectra before. It appears that the higher annealing temperature assimilates the spectra. In high-temperature annealing, only gray debris shows faint MoS_2 signatures, the other locations are empty or stem from substrate oxides. In all spectra, the spectral feature between 800 and 900 cm^{-1} found in MoS_2:Cu is absent.

Annealing appears to undo the amorphisation of nitrogen-modification at least partially. In 100 °C annealing, white plateaus on debris is featureless, which in accordance to the discussion above stem from amorphous MoS_2. Gray and side debris has the strongest MoS_2

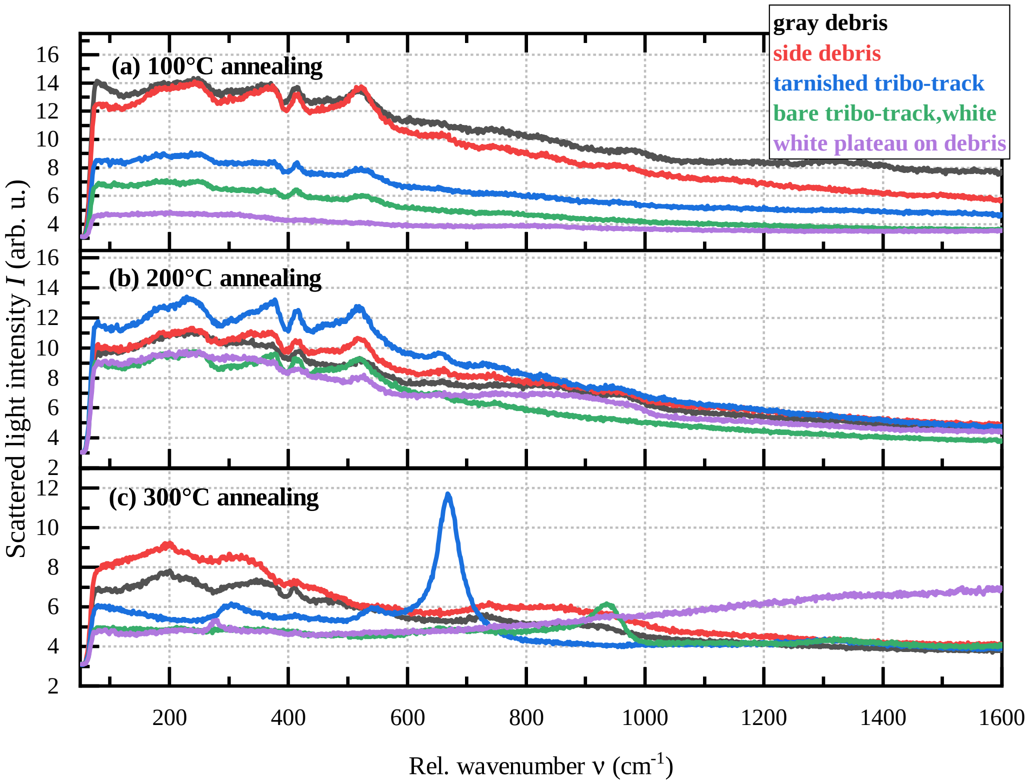

Figure 4.14: Raman spectra of nitrogen-modified MoS_2 thin films, effect of annealing at various probing locations and different types of pronounced wear particles. For probing locations, refer to Figure 4.15.

signature, while in non-annealed samples no MoS_2 signature was found. Like before, the intensity increase may stem from partial re-crystallisation during tribo-film formation. This, most notably, was made possible by annealing. Stronger annealing as for temperature of 200 °C lead to the assimilation, the effect of nitrogen was completely counteracted. The mechanism here is assumed to be the relief of bonded nitrogen out of the thin films. Temperatures of 300 °C, which yielded only substrate oxides independently of sample locations for MoS_2:Cu, seem to be less diminishing in MoS_2:N. From this, the oxidative sensitivity of MoS_2:N is found to be lower in comparison to MoS_2:Cu. The formation of crystalline MoS_2 in gray debris, a presumed main feature of tribo-film, is hindered, however.

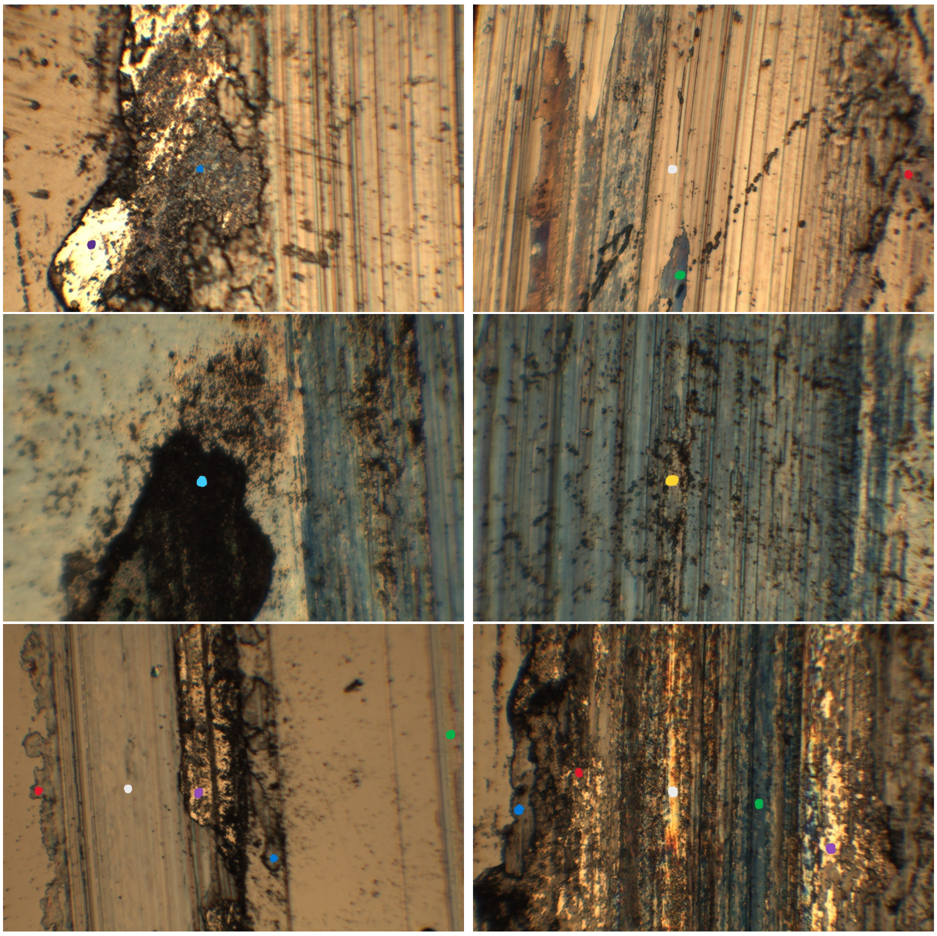

Figure 4.15: Exemplary microscopy images of wear debris in MoS_2:N and MoS_2:Cu thin films. Measurement locations: black debris (light blue), gray debris (dark blue), side debris (red), tarnished tribo-track (green), bare white tribo-track (white), bare gray tribo-track (yellow) and white plateau on debris (violet)
Above: MoS_2:Cu with highest copper content, 100 °C annealing and, after ball-on-disk tribometer testing.
Middle: MoS_2:Cu with highest copper content, 300 °C annealing and, after ball-on-disk tribometer testing.
Below: MoS_2:N with highest nitrogen content (flow rate 120 sccm N_2 during deposition) after ball-on-disk tribometer testing. Left: 100 °C annealing, Right: 100 °C annealing.

Chapter 5

Optical temperature tuning in solid thin film lubricants

In this chapter, the thermal stability and structural evolution of a-C and sputtered MoS_2 thin films plus a selection of their element-modified derivates are investigated. Such thin films can be tailored for a given application, no known thin film is appropriate for all conceivable working conditions. So, all uses of solid lubricants are designed for given working conditions, especially temperatures (see subsection 2.3.4). A deviation from their design working environment may cause film loss, because of thermally-initialised phase transitions or chemical reaction like oxidations. This chapter specifically probes the behaviour of thin films towards localised heating, in which the temperatures reach from room temperature up to thermal film loss to vaporisation. It is done to simulate the reaction to frictional heat or flash temperatures in a tribo-contact, the latter of which can easily reach temperatures of a few hundreds or over 1000 °C. [125, p. 79] Also, peak temperatures are distributed in a smaller area than the apparent contact (see subsection 2.3.1) and are known to provide sufficient energy for structural changes or chemical reactions. [125, p. 87]

Here, a method of probing structural changes via Raman spectroscopy like in the preceding chapter is combined with a pulsed optical laser for fine-tuned local heating. For temperature measurement, a calibrated infrared pyrometer was shown to be a viable option over anti-Stokes measurements or thermography (see subsection 3.4.1 for details). This pump&probe-style testing environment points towards in-field testing, which helps to customise the films for temperature-sensitive and/or chemically reactive applications and to scientifically explore the tribo-contact. The acquired knowledge of the film's behaviour under certain conditions is used for explanation.

5.1 Amorphous carbon and hydrogenated amorphous carbon thin films

Solid-to-solid phase transitions are known to occur in various carbon allotropes and organic compounds. [20, 21, 22, 23, 27] When carbon nano-phases with high sp^3 content are the objective, engineering is challenged by the fact that the conversion of sp^3 to sp^2 hybridisation is energetically beneficial and only kinetically hindered. Moreover, some carbon allotropes e.g. nano-tubes, -onions, -diamond, or carbon black are ideally absorbing with low thermal diffusivity and high laser absorption close to the surface. [182, 232] The thermal stability of various sp^3-rich carbons strongly varies, so the stability is not connected to the hybridisation alone. Besides diamond, the most stable sp^3-rich carbons are found in detonation products, which gives a hint on strong non-equilibrium and pressure effects. [233]

For amorphous carbons networks being metastable in nature, (exuberant) laser processing leads to both local amorphisation and (re-)crystallisation, but eventually to full-sp^2 graphitisation. [234] Other processes by nanosecond laser pulses include evaporation of compounds or impurities [25], surface smoothing, ablation, swelling, or delamination; even ablation without restructuring is possible when single pulses are used. [235] These processes are also very well possible by other forms of energy if they eventually generate local heating. As such, other known methods are joule heating, microwave heating, ultraviolet and x-ray pulses, spanning far along the electromagnetic spectrum. [236, 237, 238, 239, 240, 241] Heating hydrogenated amorphous carbon additionally leads to the evaporation of hydrogen and hydrocarbons, which is partially independent from the other structural processes [242, p. 191]. With those being near the surface, the evaporation of hydrogen induces dramatic changes in optical properties, e.g. the increase of extinction with rising temperature in a-C:H [243], and to a porous structure, which wears fast. [46] Heat energy during the deposition process also makes a strong impact: temperatures of 50 °C to 450 °C create mostly featureless sp^2-rich carbons with increasing ordering processes like formation of aromatic rings and graphitic clustering. Minding the influence of the sp^3/sp^2 ratio on sample properties (see Figure 2.8), high deposition temperatures lead to lower hardness and Young's modulus [244], which is generally undesired for tribological applications. In case of HiPIMS magnetron sputtering, the plasma alone produces deposition temperatures of roughly 160 °C per se (experience value). Annealing with temperatures up to 300 °C after deposition typically causes lattice defect and non-sixfold ring reduction without graphitic fragments. Higher temperatures lead to the conversion from amorphous carbon to nanocrystalline graphite, paraphrasing reduction of sp^3 bonded carbon in favour of sp^2. [242, p. 191] Extreme temperatures "[allow] a thorough rearrangement" [245], i.e. full graphitisation, which is largely independent of precursor species (like graphitisation in pitch-bonded coke [132, p. 209]), and eventually sublimation [246].

In all studies above, mechanisms including structural transitions in various carbon allotropes are often investigated piecewise or in limited temperature ranges, only. Also, a-C structures and their element modifications explicitly for tribological purposes are rarely taken into account. Despite the fact that limitations of Raman spectroscopy analysis is mainly challenged by the fitting model and supporting physical explanation thereof [20], all structural changes are proven to be sufficiently analysable with Raman spectroscopy [27, 170]. In this thesis also, no new fitting model is proposed, but a robust fitting routine with enough flexibility is applied. Subsequently, all considerations are always in view of amorphous carbons and their possible defective derivates. Main focus lies on the validation of the dominant structural evolution mechanism and on the effect of chemical modification.

The evolution of Raman scattering intensity in both a-C and a-C:H arrayed by the pump laser pump power density ρ_{pump} is presented in Figure 5.1. Three ranges are detectable by eye: The first **range (i)** shows typical spectra of amorphous carbon without visible evolutionary processes. Both D- and G-Raman peaks are the broadest and closest in this stage, the spectra are close to the exemplary single spectra in subfigure (c) with little dynamics. This gives a hint at energetic barriers for structural processes already. Subfigure 5.1(c) shows two key differences between a-C and a-C:H: firstly, general Raman scattering intensity of a-C:H is considerably higher than that of a-C, and secondly, the intensity ratio of D- and G-Raman peak R_{Int} starts at a different value. In **range (ii)**, changes in D- and G-Raman peak are most pronounced, i.e. peaks narrow and separate. For a-

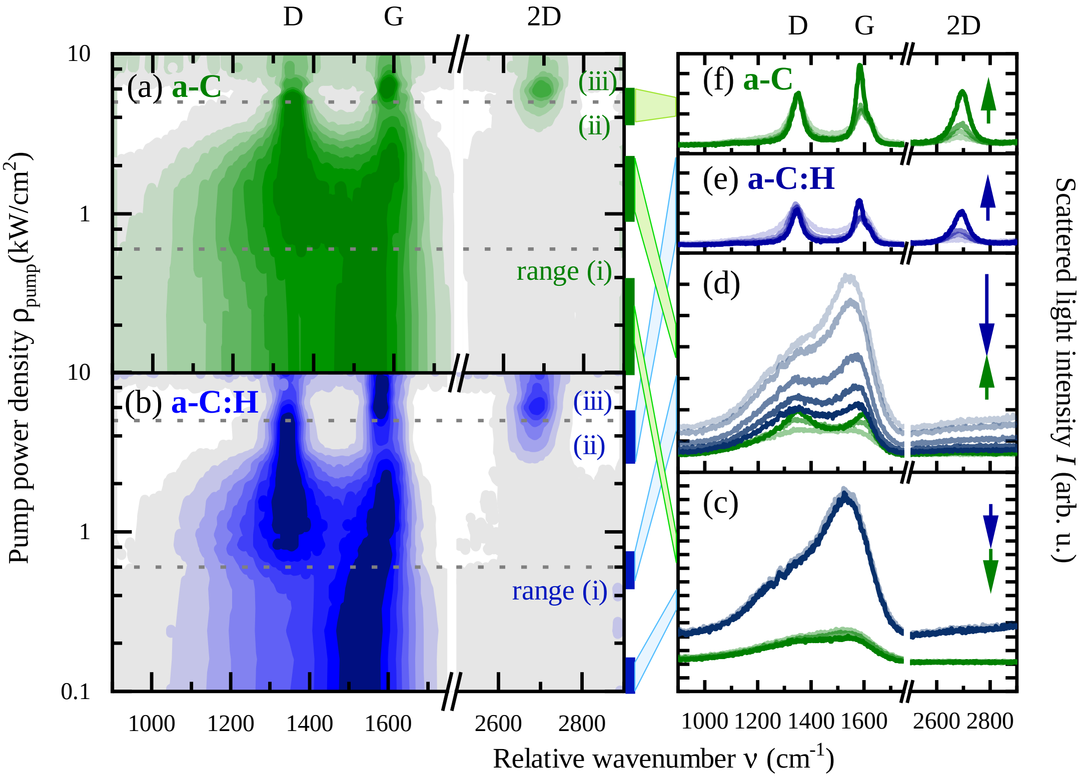

Figure 5.1: Raman spectra of a-C(:H) against laser power density: **(a)-(b)** contour plots of Raman spectra for a-C and a-C:H (green, blue) against laser power density and **(c)-(e)** exemplary single spectra thereof in the inscribed ranges. Evolution is indicated by colour-coded arrows in the exemplary spectra, from transparent to opaque in spectra.The intensity within the contour plot is normalised in **(a)-(b)** for clarity, but a measure of raw intensities is given in the exemplary Raman spectra **(c)-(e)**.

C:H especially, the general intensity and the G-Raman peak intensity start prevalent in subfigure (d), but become subordinate during heavy structural evolution and continuously approach a-C (blue spectra in subfigure (d)). The 2D-Raman peak becomes measurable with comparatively shallow dynamics by the end of range (ii). The latter is a clear indication for the beginning graphitisation. Hereinafter, both samples behave similar, which hints towards phase transition. The third **range (iii)** shows peaks of (defective) graphite under full graphitisation, in which D- and G-Raman peaks become clearly distinct from one another and the 2D-Raman peak reaches its intensity maximum.

By fitting the spectra, a more intricate picture arises, Figure 5.2 presents the relevant fit parameters for analysis.

5.1.1 Stage (I) - short-ranged ordered amorphous carbon

Stage (I) represents the as-deposited situation, which is stable for power densities up to a few tenths of kW cm^{-2}, the maximum surface temperature T_{surf} reaches approximately

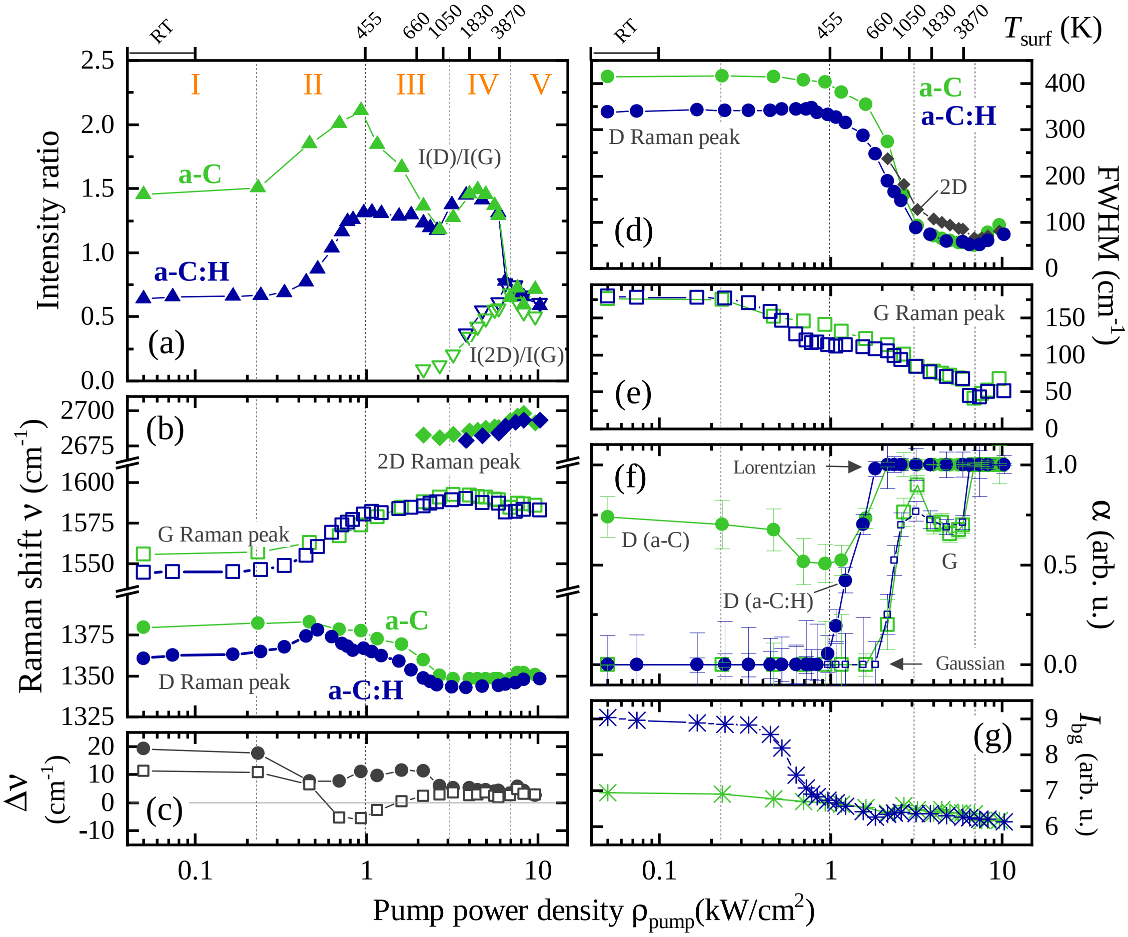

Figure 5.2: Raman fit parameters of a-C and a-C:H (green, blue) against laser power density ρ_{pump} and measured surface temperature T_{surf}: **(a)** intensity ratios (full symbols: $R_{\text{Int}} = I(\text{D})/I(\text{G})$, open: $I(\text{2D})/I(\text{G})$) **(b)** Raman shift ν of D-, G-, 2D- Raman peak (circle, square, diamond) **(c)** inter-sample difference of ν between a-C and a-C:H **(d)** FWHM of D- and 2D-Raman peaks **(e)** FWHM of G-Raman peaks **(f)** form factor α of D- and G-Raman peak **(g)** axis intercept value of background I_{bg} as measure of general intensity. Identified stages are inscribed as orange roman numerals in **(a)** with dotted separation lines throughout. Some plots lack error bars for clarity, further discussion in section 5.1.5. Raman shift ν and FWHM have uncertainties covered by the symbol sizes.

350 K. Unsurprisingly, the found fit parameters are congruent to the findings in the previous chapter 4.

The a-C sample shows its characteristic spectral features. The intensity ratio R_{Int} in a-C is near 1.45 at low ρ_{pump}. Likewise, Raman shift ν of the D- and G-Raman peak remain steady at $1380\,\mathrm{cm}^{-1}$ ($1550\,\mathrm{cm}^{-1}$) with FWHM near $410\,\mathrm{cm}^{-1}$ ($175\,\mathrm{cm}^{-1}$). G-Raman peak is completely Gaussian-like at first, $\alpha(\mathrm{G}) = 0$, while the D-Raman peak shows a distinct combination of Lorentzian- and Gaussian-like contributions, $\alpha(\mathrm{D}) = 0.75$. Over all, both peaks of a-C are the broadest and closest in this stage. Fit parameters of a-C:H are mostly follows suit to a-C with key difference in general downshift of $\sim 20\,\mathrm{cm}^{-1}$, a more narrow, completely Gaussian-like D-Raman peak and an intensity ratio $R_{\mathrm{Int}} = 0.7$. Investigations on closely related samples suggest a saturation of dangling carbon bonds by hydrogen on the surface of a-C:H, which condenses the possible effect of hydrogen close to the surface, where heat is diffused into. [247, 248]

The intensity ratio R_{Int} of a-C yields an sp^3 content of approximately 12 %, a density of $\approx 2\,\mathrm{g\,cm}^{-3}$, an optical density and extinction of $n = 2.5 \pm 0.5, k_{\mathrm{min}} = 0.7$, and an equivalent graphitic cluster size $\sim 15\,\text{Å}$. [48, 101, 175, 249, 250] Heat is rapidly diffused into a region in order of magnitude of 100 nm [251], so no interaction with the substrate is assumed. The main inter-sample difference between a-C and a-C:H is mostly attributed to more diverse bonding in a-C:H in comparison to a-C. For the present a-C:H sample with a low hydrogen content ($< 20\%$), a-C and a-C:H may be read and interpreted equally. [252] Besides generally higher sp^3 content to C-H bonding, investigations on closely related samples to a-C:H suggests a hydrogen saturation of dangling carbon bonds on the surface, which confines the effect of hydrogen close to the surface [141, 168], into which heat diffuses. The higher scattering intensity is also linked to surfaces properties [65], because the general scattering yield is a function of scattering centre density and, subsequently, absorption and penetration depth. [48, 205] Absorption is known to differ from a-C to a-C:H. [206]

The lack of dynamics in this stage indicates that all mechanisms yet to be clarified feature low-level energetic barriers, which are not overcome for now.

5.1.2 Stage (II) - progressive aromatic enrichment

Stage (II) ranges from $0.2\,\mathrm{kW\,cm}^{-2}$ to $0.9\,\mathrm{kW\,cm}^{-2}$ with a maximum surface temperature T_{Surf} of approximately 455 K. In a-C, the intensity ratio R_{Int} linearly increases with a maximum of over 2.1. The Raman peaks start to separate continuously and to narrow, in figures, D-Raman peak at $1375\,\mathrm{cm}^{-1}$ with FWHM of $400\,\mathrm{cm}^{-1}$ and G-Raman peak at $1570\,\mathrm{cm}^{-1}$ with FWHM of $140\,\mathrm{cm}^{-1}$, eventually. FWHM(D) is preserved, while FWHM(G) starts to decrease uniformly until the global end. While the form factor $\alpha(\mathrm{G})$ of Gaussian-like G-Raman peak remains unchanged, D-Raman form factor $\alpha(\mathrm{D})$ becomes more Gaussian-like monotonously and reaches its extreme by the end of this stage. This detail will be important shortly. In a-C:H, the intensity ratio R_{Int} shifts up logistically from the initial plateau value to a local maximum at 1.25 by the end. At the onset of its rise, a-C:H equals the Raman shift ν of the a-C counterpart, which is also the global maximum of the D-Raman peak shift $\nu_{\text{a-C:H}}(D)$. The inter-sample difference of both intensity ratios R_{Int} is at maximum. FWHM of both peaks in a-C:H follow suit of a-C. Both peaks of a-C:H remain a constant Gaussian-like form factor, $\alpha = 0$.

a-C starts as amorphous carbon matrix with nano-crystalline graphitic (ncg) structures (stage 2 in Three Stage Model [101]). The rise of intensity ratio R_{Int} stems from a slight reduction of absolute intensity of the G-Raman peak I(G) and consistency of I(D) in Figure 5.3. This behaviour is unexpected, the reduction of I(G) lacks a profound explanation. In combination with a (shallow) reduction in general intensity I_{bg} in Figure 5.3(g), however, it is assumed that the scattering intensity decreases and appearance of constant D-Raman peak intensity is in fact a slight increase.[1]

This increase can be properly interpreted via the activation mechanism of D-Raman peak: edges of the sixfold ring clusters contribute to the D-Raman peak; thus, intensity I(D) is among others probing the cluster density and their area-circumference ratio, that is, cluster size. [73, 254] While sixfold rings themselves (benzene-type sp^2 bonded carbon rings) contribute negligibly to the D-Raman peak, clusters of size 15 Å do considerably. [101] Up to here, the increment of intensity ratio can stem from both expansion of existing clusters (to a limited extent) and from enrichment of ordered regions (graphitic *seeds*) in an unordered a-C matrix. In fact, literature finds the same upshift of the G Raman peak and the increase of intensity ratio and relates is to the increment of graphitic cluster size. [255] Here, however, the dominant mechanism can be now identified by considering FWHM and form factor α. FWHM is inversely proportional to the lifetime of involved (quasi-) particles in the scattering process and, subsequently probes micro- and nano-structural

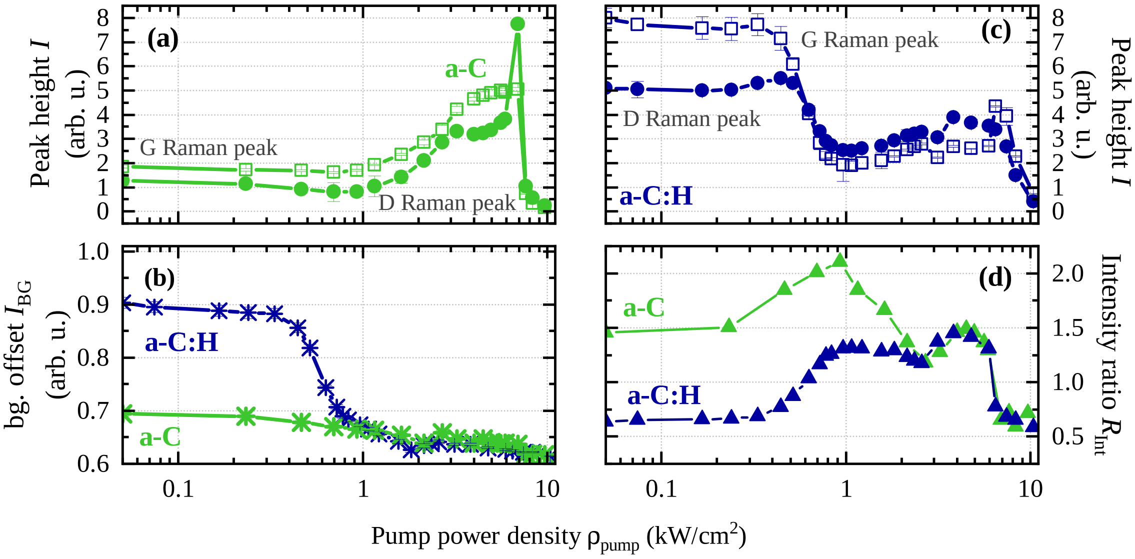

Figure 5.3: Absolute intensity of D- and G-Raman peak in a-C and a-C:H for additional analysis, respectively. Although considerations of absolute Raman intensity are discouraged, this helps to distinguish various mechanisms, which yields the increment of the intensity ratio. Note that the intensity ratio increment in stage (II) and in stage (IV) stem from different behaviour of D- and G-Raman peak individually. Lower panels show intensity ratio and background offset I_{bg} for reference.

---

[1] In fact, in related pioneering studies [186] the expected behaviour, increasing I(D), was found and published [253].

sizes. A distribution of Raman modes with similar, but different Raman shifts ν would also gives rise to a broad spectral feature, which is discussed for some carbon allotropes explicitly [21, 256], but is disregarded for this work. Like the form factor α, FWHM probes different structures individually, that is, FWHM(D) probes order in sp^2 carbons in aromatic ring structures, while FWHM(G) gauges sp^2 carbon pairs in general. On the one hand, expansion of clusters would imply a significant effect in FWHM(D). Its constancy indicates minuscule changes in bonding energy landscape at the cluster edges. On the other hand, enrichment of clusters increases independent scattering centres of similar properties and, in turn, the Gaussian-like contributions, which give the D-Raman peak its shape. Additionally, the behaviour of G-Raman peak indicates an over-all ordering progress [100]. This seems plausible, because arising nano-crystalline graphitic structures are more ordered than the predecessor a-C matrix. The continuous decent in FWHM(G) may stem from compositional purification (reduction of sp^3 content), the blueshift from structural ordering (homogeneous bonding lengths and angles).

The situation in a-C:H is similar. Low-level hydrogen introduction into mainly sp^2 amorphous carbons have balanced ordering and disordering effects. [252] It is known that the effusion of hydrogen and hydrocarbons does not take place below a temperature of 700 K. [255] Most noteworthy process in a-C:H, additionally, is the drastic reduction in absolute intensity - Raman intensity I and background I_{bg}, which may stem from changing absorption coefficient - and the upshift of the D-Raman peak. The first process is gauged in background, which is fitted as linear function with (disregarded) slope and intercept I_{bg}. Aromatic enrichment in the samples upmost surface regions is therefore likely impeded by C-H-terminal bonds, yet absorption coefficients react to this dominant process. The Raman shift of the D-Raman peak ν(D) is rarely considered in literature. Solely, Raman shift ν(D) is reported to reach higher values than usual. [101] In conclusion, no standard interpretation for Raman shift ν(D) exists in literature. Subordinately, the form factor α of the D-Raman peak in a-C:H is also over-saturated, like the G-Raman peak in a-C, which suggests an energetically diverse landscape in sixfold ring structures near C-H-terminal bonds.

It indicates that the dominant mechanism in stage (II) is enrichment of ordered seeds over expansion of graphitic regions. In more detail, lattice defect- and non-sixfold ring reduction is dominant in stage (II), that is, aromatic enrichment in a (still) amorphous carbon matrix. As such, the G-Raman peak is still fully Gaussian-like with $\alpha(\mathrm{G}) = 0$. The dominance of this mechanism was also experimentally verified in recent studies. [27]

5.1.3 Stage (III) - solid-to-solid phase transition from amorphous to ordered structures

In stage (III), more drastic changes in core fit parameters appear. It ranges from $1\,\mathrm{kW\,cm^{-2}}$ to $3\,\mathrm{kW\,cm^{-2}}$ with surface temperatures of 455 K to 1100 K. In a-C, D- and G-Raman peak gain distance, eventually reaching a stable maximum distance, and losing the major part of their peak width while gaining intensity. The intensity ratio R_{Int} changes sharply from linearly increasing to linearly decreasing, and finally reaches a local minimum of 1.2. Peeking into the raw intensities for reference, both peak intensities start to rise at different rates. Peak separation reaches its global unchanging maximum, while the narrowing of the D-Raman peak accelerates, having its inflection point at the end of the stage. Meanwhile, the G-Raman peak steadily narrows (as stated before). Up to the centre of the stage, the

D-Raman peak form factor $\alpha(D)$ becomes more Lorentzian-like and reaches a stable full Lorentzian-like shape at $2.3\,\mathrm{kW\,cm^{-2}}$. Immediately before the D-Raman peak reach the full Lorentzian-like shape $\alpha(D) = 1$, the G-Raman peak form factor begins to change, reaching a local maximum of $\alpha(\mathrm{G}) = 0.9$. 2D-Raman signatures with a width comparable to the D-Raman peak becomes measurable. The processes in a-C:H mostly resemble that of a-C.

The narrowing indicates major structural and topological changes in contrast to stages (I) and (II). Vast ordering appears in all structures, the spectral bandwidth of contributing phonon modes narrows. This is especially true for the D-Raman peak, which is becoming four-times narrower. The intensity increase is likely to stem from formation of hexagonal lattice regions, which are known to be efficient scattering processes. In more detail, the Raman relaxation length between hexagonal lattice regions and defects is reduced for the electrons. The concept of Raman relaxation length, however, are discussed for graphitic materials with considerably higher lattice area in literature. [257, 258, 259, 260, 261] One can also identify a turning point in form factor $\alpha(D)$: in the first half of stage (III), changes are visible only in D-Raman peak form factor $\alpha(D)$, while the G-Raman peak remains fully Gaussian-like. But when the sixfold-ring cluster edges become the mostly homogeneous and thus the D-Raman peak has a stable Lorentzian-like shape $\alpha(D) = 1$ (roughly in this stage's centre), the G-Raman peak form factor $\alpha(G)$ changes as well, it reaches for a local maximum until the end of the stage. This finding indicates that introduced heat is first and dominantly used for the graphitic structures rather than sp^2 carbon pairs in general. This seems plausible, because sp^2 carbon bonding in aromatic configurations is stronger and shorter compared to the olefinic counterpart. Also, at the point of fully Lorentzian-like D-Raman peak, the second-order 2D-Raman peak becomes detectable in the Raman spectrum, which is a clear proof of the long-ranged graphitic structures formed, that is, the onset of graphitisation. For a-C:H, especially, the effusion of hydrogen and hydrocarbons are expected to begin. Still present hydrogen in the first half of the stage inhibits the formation of hexagonal structures in the same manner as in a-C, but on-going effusion reduces the effect along the stage. After completion, the hydrogenated sample is hardly distinguishable from its counterpart.

This all leads to the conclusion that the sample undergoes a solid-to-solid phase transition. It is now referred to as defective graphitic mixture, in which lattice defects are mostly non-hexagonal lattice arrangements. Viewed from another perspective, sp^2 bound sides (planar) and sp^3-bound sides (tetrahedral) directly compete [48], sp^2 sides now taking over. The reduction of sp^3 carbon sides may have been finished in stage (II) already. When the dominant ordering mechanism was centred around enrichment of ordered seeds before, it is now assumed to be leaning towards the expansion of hexagonal structures.

5.1.4 Stages (IV) and (V) - evolution in the defected graphite phase

By the end of stage IV, temperatures of $T_{\mathrm{Surf}} \sim 3800\,\mathrm{K}$ are reached, which is the limit of sublimation for graphite-like carbons. [262] The Raman shift $\nu(2\mathrm{D})$ weakly increases from $2680\,\mathrm{cm^{-1}}$ to $2690\,\mathrm{cm^{-1}}$, while both first order peaks are fixed. FWHM of D- and 2D-Raman peaks merge and descend to their global minimum, eventually, with values from $40\,\mathrm{cm^{-1}}$ to $65\,\mathrm{cm^{-1}}$. Most notably, however, the intensity ratio R_{Int} undergoes a comparable progress as in stages (II) and (III) with a local maximum in intensity ratio $R_{\mathrm{Int}} = 1.5$ at the stage's centre. Also noteworthy, the form factor $\alpha(G)$ of the G-Raman peak continuously drops

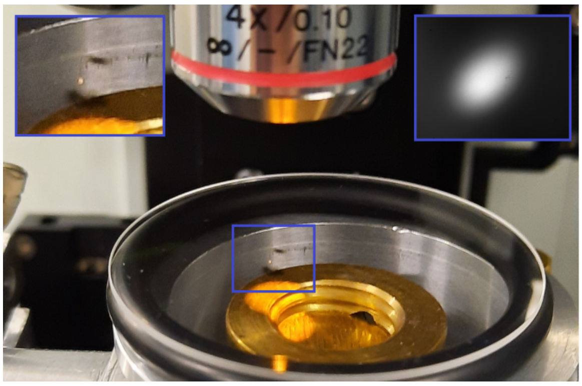

Figure 5.4: Re-deposition of carbons after laser ablation in stage (V), insets show the magnified picture **(left)** and capture of the microscope camera **(right)**, in which the re-deposition of carbons onto the chamber window is overexposed.

into a local minimum when the maximum of intensity ratio R_{Int} is reached, yet becomes fully Lorentzian-like by the end. This resembles the progress of the D-Raman peak form factor α(D) in stages (II) and (III) in a-C. As for the 2D-Raman peak, the intensity ratio I(2D)/I(G) linearly increases to its global maximum of 0.7 at the stage's end. The 2D-Raman peak is highly Lorentzian-like and remains its shape (not shown).

Raman scattering events do not face significant changes any more, but residual ordering is still detectable in intensity ratio R_{Int}, FWHM(G), and α(G): the rise of the G-Raman peak intensity comes to a halt, which yields the the second hump in intensity ratio R_{Int}. This indicates the upcoming completion of the over-all ordering process, that is all available carbon sides are paired up sp^2 carbons. Expansion (and hypothetically fusion) of graphitic clusters contributes to larger ordered structures, as seen in the 2D-Raman peak intensity ratio and the still on-going reduction in FWHM(G). The reduction in α(G) is interpreted as inhibition of lattice enlargement; in other words, clusters interfere and thus are naturally limited at first. If clusters were free to expand indefinitely, the Tuinstra-Koenig model for nano-crystalline graphite, which links the "graphite crystal size" L_A inversely to the intensity ratio R_{Int} (I_{1355}/I_{1575} in publication [91]). It suggests a continuous decrease in intensity ratio, which is only observed from this stage's centre onwards. [91]

All in all, the dominant mechanism in stage (IV) is (progressive) graphitisation. Long-reaching hexagonal structures agree with the IUPAC definition of graphite in distinction to nano-crystalline or defective graphite. [36] In literature, the corresponding temperatures in the onset of stage (IV) are reported to yield a more ordered structure of a-C, but not graphite by definition yet: microcrystalline particles and lamellar structures [27, 263], which agrees well with the growth in lattice size.

In the final stage (V), no further dynamics in all peaks are visible and the signal is lost eventually. The sample is lost to laser ablation as the estimated temperature of 3800 K is reached, which is the sublimation limit of carbon. This was further proven by placing glass close to the sample, which was then covered in laser-sputtered carbon thin film, see Figure 5.4. The sample's surfaces is heavily defected, the signal-to-noise ratio of the Raman signal is too weak for further analysis.

5.1.5 Uncertainty estimation for intensity ratios

Error bars in Figure 5.2 of fit parameters are omitted for the parameters Raman shift ν, FWHM, intensity ratios, and background offset I_{bg}. The former two have uncertainties in size of the plot markers, the latter is only mildly of interest. On a technical basis, a previous study [186] has shown that the exact overlap of pumping- and probing spot are not obligatory and would still remain a recognisable shape of fit parameter plot, but possibly introduce a shift in horizontal direction. Furthermore, problems arise for the intensity ratios. When the moderately uncertain peak intensities (as in Figure 5.3) are calculated as ratio, it will yield excessively high fit parameter uncertainty mathematically.

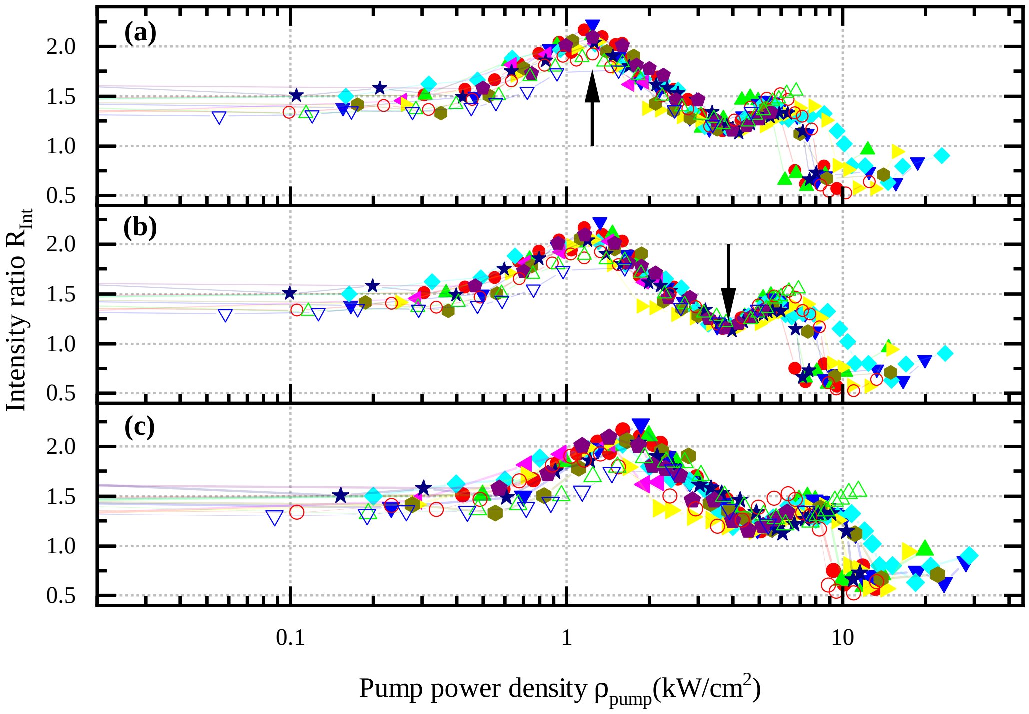

Figure 5.5: Multiple intensity ratio measurements for uncertainty estimation. Subfigures **(a)** and **(b)** show a selection of R_{Int} evolutions, which are horizontally aligned on the stage transition (II)-(III) and (III)-(IV), respectively, for uncertainty estimation of R_{Int} value. Subfigure **(c)** shows R_{Int} evolutions unshifted for uncertainty estimation of all considerable errors.

To face all these possible uncertainties, Figure 5.5 plots multiple intensity ratio R_{Int} measurements in one. Two additional subfigures (a)+(b) are duplicates of the former (c), in which all plots are horizontally shifted to be matched at the transition between stages. These point are chosen arbitrarily. Alignment on the transition (II)-(III) in (a) is less sharp than on (III)-(IV) in (b), which suggests a well-defined point. The highest uncertainty is found in the onset point of stage (V) and in the behaviour of the stage (V) itself, which matches the expectation. This convergence tube gives a natural estimate of involved parameter uncertainty. The uncertainty are estimated by eye be roughly 0.25 in value. Subfigure (c) gives an estimate for the horizontal uncertainty, by eye, a factor of 15 %.

5.2 Element-modified amorphous carbon

Chemical element-modification of a few atom percent (at. %) is regularly applied for tailoring a-C thin films for a given application. For example, silicon often used for enhancement of thermal stability [26, 264], while the hydrogenation of a-C (among others) makes the usage in vacuum applications possible. Silicon and tungsten are able to form carbides, silver and copper have catalytic effects. Thus, their influence on the hybridisation equilibrium [265] render them prime candidates for probing the mechanism in the structural evolution. Element modification with silicon (8.6 at.-% & 11 at.-% Si), copper (9.7 at.-% Cu), silver (5.6 at.-% Ag), and tungsten (16 at.-% W) affects all parameters, which are mainly represented by Raman shift ν and intensity ratio R_{Int}.

5.2.1 Silicon- and copper-modification in a-C:Si and a-C:Cu

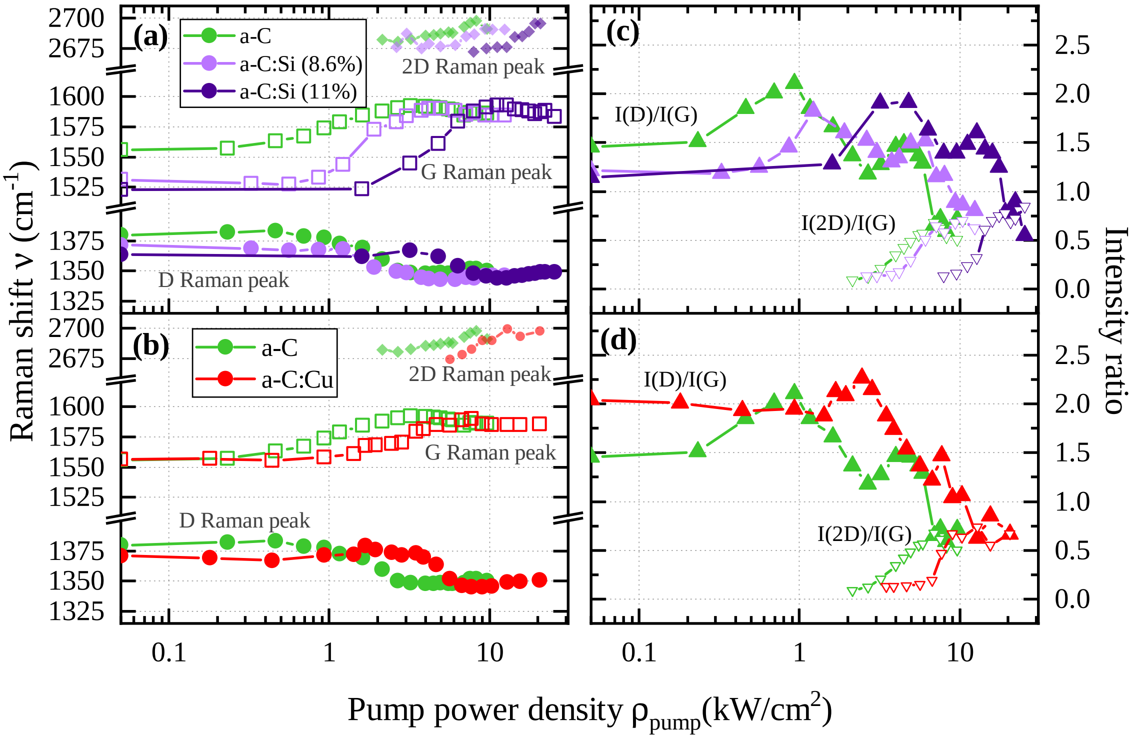

Figure 5.6: Intensity ratio R_{Int} and Raman shift ν of silicon- and copper-modified a-C:X. Element modification contents are 8.6 at.-% & 11 at.-% for a-C:Si and 9.7 at.-% for a-C:Cu.

At the start of the structural evolution in a-C:Si, the fit parameters deviate from pure a-C slightly: Raman shift $\nu(G)$ is notably downshifted, reduction of Raman shift $\nu(D)$ is more mild. This effect is correlated to the quantity of silicon content. Other parameters (not shown) are only weakly correlated to the silicon content, if at all. Most striking effect in a-C:Si is the staggered arrangement of Raman shift ν and intensity ratio R_{Int}. The addition of silicon causes 1.36- and 3-fold stretching, respectively, which appears as shift in logarithmic scale. By hypothesis, this translates to a substantial elevation of thermal stability of a-C, which is originally estimated to be 300 °C. [209, 266] Apart from minor differences in stage (I) and stage (II) in terms of exact evolution path, the silicon-containing samples mimic the a-C counterpart in stage (III) and onwards. This leads to the assumption that silicon addition does not impede formation of large graphitic structures.

All these effects are consistently explained by stabilising sp^3 hybridised carbon single bonds over the sp^2 hybridised carbon double bonds, which promotes the reduction of sp^2 clusters in size and number. [65, 179, 207, 208, 264] The narrowing of the D-Raman peak is the result of a more homogeneous distribution of carbon ring-topologies (bonding lengths and angles), e.g. by reduction of strain. [52, 252, 267] The thermal stability upgrade may also stem from the fact that silicon forms a competing network of amorphous silicon (a-Si) [209], which may act as a reduction of a-C network density or as sacrificial element. In contact point of the two networks, Si-C bonds form with stress reducing and sp^3-stabilising effect. Expected Si-C and Si/O bonds [268, 269], however, show a recognisable signature in Raman spectra [270], which were not observed. Raman signatures of a-Si are broad and comparatively weak [271], also undetected.

The effect of copper is comparable to silicon. The catalytic effect on sp^2 structures are found in the elevated intensity ratio R_{Int}, which mimics the catalytic effect on sp^2 structures of tungsten or silver. [65, 175] The shift along the abscissa may, again, be attributed to the reduction of carbon network density and of internal stress. The lack of stage (IV), however, coincides with the loss of the sample via laser-ablation. This supports the hypothesis of sacrificial a-Si network in a-C:Si, which lacks in copper-modification.

5.2.2 Tungsten- and silver-modification in a-C:W and a-C:Ag

Tungsten-doped samples deviate from their pure a-C counterpart, because tungsten modification favours sp^2 hybridisation in a-C.[65, 265] D- and G-Raman signatures narrow and separate slightly, but fully remain their a-C nature. Most notable difference to a-C is the elevated intensity ratio R_{Int}, starts at 1.8, which is its overall maximum.

The two most important effects are the lack of stages (II) and (IV) in intensity ratio R_{Int} and more shallow in the second-order signatures. For the first effect, tungsten addition is known to strengthen the sp^2 clusters in number and size. This explains the plateau to the start of structural evolution, as the magnitude of sp^2 clusters remain in their maximum from start to the onset of stage (III). Any thermal stabilisation or weakening like in a-C:Si is ruled out, because the distinctive points of intensity ratio R_{Int} remain on the spot. Tungsten is the only modifying element, that does not shift the evolution along the power density axis. For the second effect, tungsten is known to not diffuse in a amorphous carbon network at lower temperatures and therefore may act as a barrier to growing graphitic structures [210, 272]. Also, lacking the possibility to evaporate, these barriers remain through the destruction of any carbon network. The lack or heavy suppression of stage (IV) may therefore be seen as approaching the maximum cluster size barrier. The second-order Raman signatures are similar to a-C in Raman shift ν, but the intensity ratio I(2D)/I(G) is horizontally shifted towards lower power densities. From this, it is seen that the requirements for the shift of large area-ordering mechanism take place earlier than in a-C. In detail, both enrichment of carbon clusters is saturated and graphitisation starts earlier.

Using silver as a *doping* material, that is at fractions of at.-%, silver is known to fully

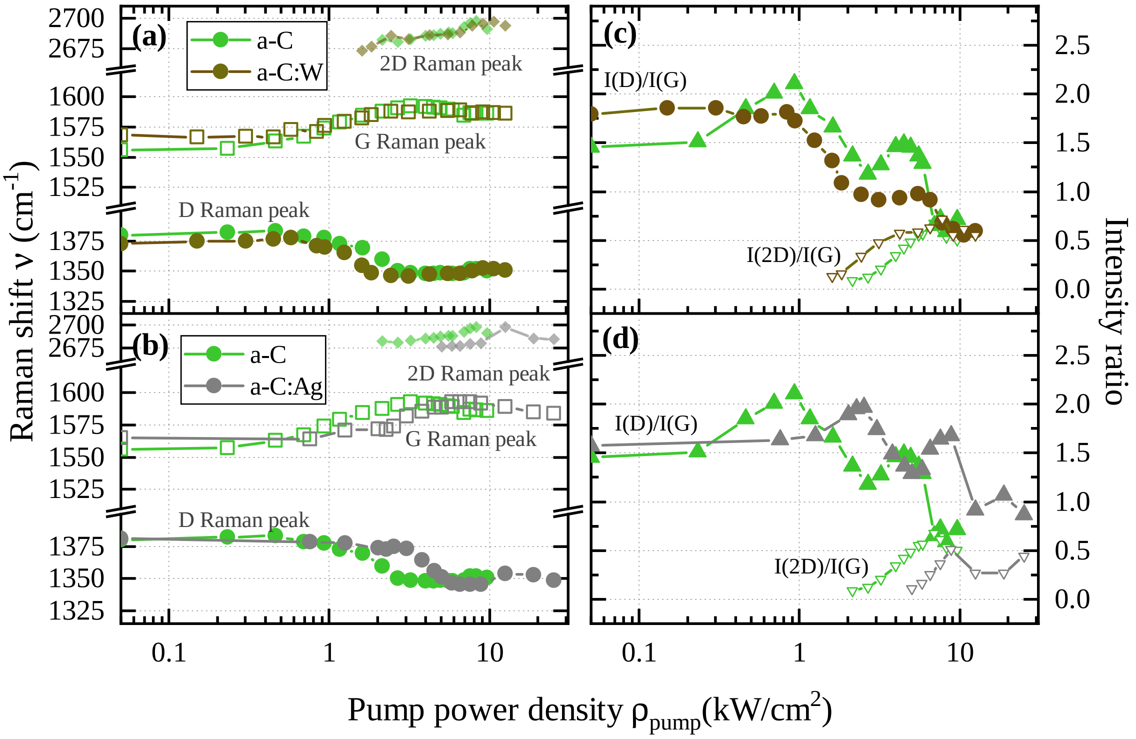

Figure 5.7: Intensity ratio R_{Int} and Raman shift ν of tungsten and silver modified a-C:X. Element modification contents are 5.6 at.-% for a-C:Ag and 16 at.-% for a-C:W.

dissolve in the amorphous carbon matrix without the formation of phases or crystallites. At elevated concentration between 1.7 at.-% and 6.8 at.-%, crystalline silver particles are expected to be found within the a-C matrix. [266] Similar results like in a-C:Si and a-C:Cu are assumed, which are, in short, density reduction and elevation of thermal resistance. In fact, the addition of silver closely resembles a mixture of a-C:Si and a-C:Cu: (i) no strong impact on the sp^2/sp^3-ratio, as seen in similar Raman shifts ν and, (ii) horizontal shift towards higher pump power densities ρ_{pump}, which is (iii) aborted in the middle of the secondary hump in intensity ratio R_{Int}. From that, an elevated thermal stability is assumed, which is not as high as in a-C:Si, but considerably higher than in a-C:Cu.

5.3 Molybdenum disulphide thin films

Molybdenum compounds feature a variety of structures and phase transitions between those. In molybdenum disulphide (MoS_2) monolayers, two phases are stable under normal conditions, (regular and usually more stable) trigonal prismatic and distorted octahedral; their stability is subject to chemical altering, e.g. by lithium, and heating or ageing. [273] In pristine MoS_2 crystals, additionally, weak bonding between layers yields some degree of structural possibilities, which are linked to varying stacking order, hexagonal or rhombohedral, and molybdenum coordination, octahedral or trigonal prismatic [37, p. 2][274], like for monolayers. Powders and sputtered thin films naturally have a plurality of lattice boundaries. Structurally, sputtered MoS_2 may be considered as micro- or nano-crystalline MoS_2 with varying degree of domain size, growth orientation (basal or columnar) and defect density. Some element-modifications like nitrogen or copper lead to amorphous films for the extreme case. Chemically, disulphides of molybdenum are prone to oxidation. [275, 276]

The properties of molybdenum oxides are largely dependent on their structures and stoichiometry. [277] The two prevalent oxidation states of molybdenum in this work are Mo^{IV}- and Mo^{VI}-oxides as molybdenum dioxide MoO_2 and - trioxide MoO_3, respectively. On the one hand, crystalline MoO_2 is monoclinic with a rutile-type structure of MoO_6 octahedra units and metal-metal bonds [278, p. 150], which give “molybdenum dioxide [...] metal-like properties”[277]. On the other hand, crystalline MoO_3 has two main crystalline phases plus multiple hydrates: (regular and thermodynamically stable) orthorhombic α-MoO_3 and monoclinic β-MoO_3[124], of which only the orthorhombic phase is regarded in this work.

Bare molybdenum synthesised in industrial scale via hydrogen-aided reduction of starting materials, MoO_3 powder among others, in two steps.[279] The first reduction of MoO_3 powder to MoO_2 is possible at 600 °C and gives off reaction heat (exothermic reaction), the second reduction of MoO_2 to Mo requires an operational temperature of 1050 °C. [279] In absence of oxidative agents, molybdenum thin films can reach temperatures of 9000 K upon femto-second pulsed laser irradiation, which is far above the melting point (700 °C to 800 °C) at equilibrium. [280] Synthesis of crystalline molybdenum oxides and their phases (in laboratory scale) is conventionally done by (global) heating in oxidative environments [281] or alternatively by (local) laser annealing [277], in which the yield of MoO_3 with pure Mo pre-cursor is linked to the oxidation potential of the environment. [280] The oxidation of Mo to MoO_2 is reported to require temperatures of 500 °C in water vapour. [280, 282] MoO_3 forms from MoO_2 precursor in temperature range of 650 °C to 750 °C, but at those temperatures, MoO_3 also evaporates in a competing simultaneous process.[280]

The oxidation of monoclinic MoO_2 to orthorhombic MoO_3 starts with desorption of water at 306 °C followed by gradual endothermic oxidation to MoO_3 in a temperature range of 306 °C to 600 °C (“zone I” in publication). [277]. For those temperatures, phases of sub-stoichiometric β-MoO_{3-x} and sub-stoichiometric α-MoO_{3-x} are present, while higher temperatures of 600 °C to 765 °C are attributed to the synthesis completion of α-MoO_3 (“zone II” in publication).[277] MoO_3 melts at 800 °C as powder [279] or in temperature range of 800 °C to 900 °C as thin film (“zone III” in publication) [277]. MoS_2 as used in tribological applications oxidise with a rate dependent on temperature: Bulk-heated[2] MoS_2 thin films oxidise above 660 K and at increased rate above 830 K [283][284, as cited in Windom

---

[2] Both studies published before or shortly after invention of Maiman laser in 1960

et al. (2011)], while local heating via laser irradiation leads to finely detectable oxidation from room-temperature to 575 °C in oxidative environments [163]. In that study, MoO_3 is also formed slightly at ambient temperatures when MoS_2 is exposed to pure oxygen, but increased oxidation rates require bulk temperatures above 375 K. Likewise, non-thermal oxidation by O_2 plasma leads to partial oxidation to nanometre-scale molybdenum oxysulphides MoS_xO_y clusters within seconds of exposure, which act as passivating layer, and sub-oxide defects MoS_xO_{1-x}.[276] In that study, XPS analysis proved the conversion from (intermittently present) Mo^{IV} to Mo^{VI}; Raman and AFM analysis showed the proceeding oxidation from the top layer downwards with decelerating passivating effect. In absence of oxidative agents, MoS_2 thermally decomposes at 1873 K in sulphuric gases and molybdenum residue [285], without any oxides.

The oxides of a metal are usually harder than the bare metal, which enables the oxide layer of a technical surface to carry load. Molybdenum, in contrast, is one notable exception, which loses 65% of hardness when oxidising to molybdenum trioxide [125, p. 33]. Low friction of MoS_2 thin films is kept in oxidation under the premise of "a [remaining] effective subfilm of [MoS_2]", although MoO_3 itself yields considerably higher friction. [283] In such studies, MoO_2 is usually not found, because MoO_2 is unstable in ambient air with introduction of heat [277]. Previous studies show that the laser stability of MoS_2 is connected to its macroscopic structure; as such microcrystalline powder oxidises considerably more likely than crystals due to particle edges as points of attack.[18, 163] In these studies, laser stability of sputtered MoS_2 is shown to be significantly enhanced, when wear debris of MoS_2 are re-deposited at the edge of a wear scar.[18] This is shown in own studies as well, as described in the previous chapter, section 4.2.2.

Raman spectroscopy proved to be a versatile tool for capturing both chemical transitions and structural changes.[163, 277, 280] This even includes features of a field-tested tribo-film formed from organic precursor molybdenum compounds (e.g. MoDTC) like amorphous carbon traces in a MoS_2 main film. [18] When a sample of MoS_2 is investigated in laser spectroscopy, a clear indication of high heat introduction by the laser is the occurrence of MoO_3 Raman signatures.[18] Starting from nano-crystalline MoS_2, within tens of seconds upon laser irradiation the nano-crystalline phase of MoS_2 disappears in favour of a complete oxidation of the top layers, which become measurable as mixture of pristine MoS_2 and the oxide top layers in Raman investigations. [276] The oxides, however, "are far from α-MoO_3 and more likely to be amorphous and isotropic"[276]. Higher laser power densities leads to film loss; in MoS_2, the depleted energy leads to both phase changes and to evaporation [280]. In this work, the Raman intensity is plotted for different laser power density ρ_{pump}. Multiple phases can be separated by eye, which are identified by their Raman peaks. Although peak fitting is conducted and parameter behaviour is discussed in publications, here, general trends of MoS_2 peaks suffice for discussion, although being fitted for data integrity.

Main focus lies on the onset of chemical and structural phases and the effect of chemical modification on occurring phases. Raman spectra of sputtered MoS_2 arrayed by the pump laser power density ρ_{pump} is presented in Figure 5.8.

In Figure 5.8, the probe spot is placed in the centre of the pump spot in subfigure (a), while it is off-centred in (b) and leaning to the outside edge in (c); labels indicate the involved vibrational mode. The first spectrum of each series, dark gray line by convention,

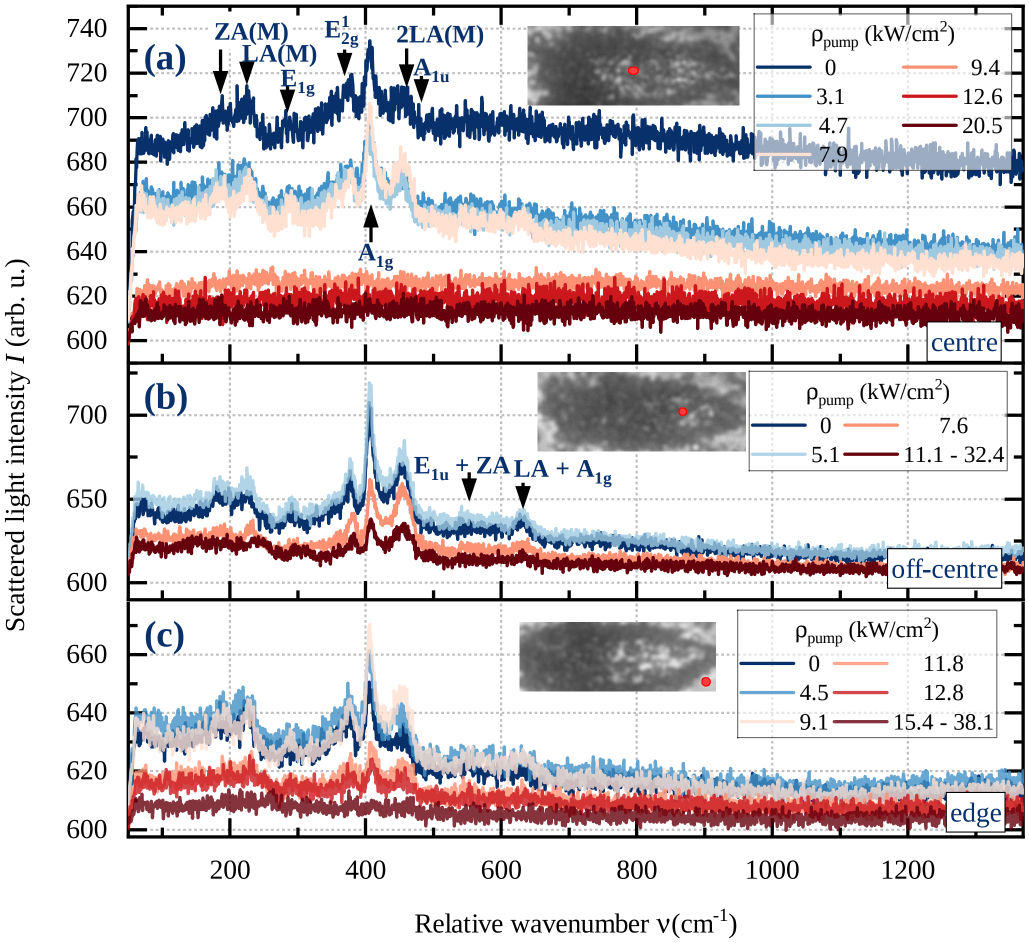

Figure 5.8: Raman spectra of MoS_2 at different laser power density in vacuo, labels indicate the underlying vibrational mode: **(a)** Probe spot in centre of pump spot: after general drop in general scattering intensity, a typical Raman signal of sputtered MoS_2 is recorded for power densities up to 8 kW cm^{-2}. Increasing the power density leads to loss of signal. No oxides or recurring phases are found. **(b)** Probe spot off-centred from the pump spot, in which no oxides or change of phases are found. **(c)** Probe spot at the (outside) edge of the pump spot: two-fold spectral cluster appear as in inset of panel (a).

shows the as-deposited situation. In the centre of the pump spot, a typical Raman signal of sputtered MoS_2 is found up to power densities of 8 kW cm^{-2}. The first reaction of the sample is the general reduction of scattering intensity, but peaks are apparently unchanged. In more detail, fitting the modes E^1_{2g}, A_{1g}, 2LA(M) reveal a shallow, but monotonous upshift of all peaks (E^1_{2g}: 366 cm^{-1} to 379 cm^{-1}, A_{1g}: 406 cm^{-1} to 412 cm^{-1}, 2LA(M): 450 cm^{-1} to 454 cm^{-1}) and intensity gain in A_{1g} mode until signal collapse (not shown). Furthermore, a noticeable change is the separation and detailed presentation of acoustic modes ZA(M) and LA(M), which originally start as broader, overlapping peaks. Increasing the power density leads to loss of signal eventually and no oxides or prominent phases changes are found. In subfigure (b), no loss of MoS_2 signal is found at the end of the series, although the power densities near the edge of the pump spot are sufficient to have a visible impact on the sample surface. In contrast, signal loss is found at the edge in subfigure (c), the fit parameters are presented in Figure 5.9. At the edge, the Raman spectra show a slight gain compared to the as-deposited situation, which is strongest at $9.1\,\mathrm{kW\,cm^{-2}}$. In the first power density range up to $9.1\,\mathrm{kW\,cm^{-2}}$, Raman shift ν and FWHM are remain mostly unchanged, although the FWHM value in E^1_{2g} mode is fluctuating. In terms of intensity, the A_{1g} mode shows the strongest net gain, yet the intensity ratios with respect to both adjacent peaks E^1_{2g} and 2LA(M) reveal that the other peaks rise in lock-step. In that second power range of $9.1\,\mathrm{kW\,cm^{-2}}$ to $14.5\,\mathrm{kW\,cm^{-2}}$, the spectra cluster with reduced intensity. In this range, intensity ratios show a intricate behaviour, in which the modes A_{1g} and 2LA(M) stay equally pronounced, while the E^1_{2g} mode does not hold step. The peak behaviour in the power density range $4.5\,\mathrm{kW\,cm^{-2}}$ to $12.8\,\mathrm{kW\,cm^{-2}}$ is directly comparable to the situation in subfigure (a) with an exception of FWHM. The value of FWHM for the A_{1g} mode in the pump spot centre is left unchanged, while the other two modes are narrowing (not shown). The peaks at the pump spot edge show a opposite behaviour: A_{1g} and 2LA(M) modes are stable within parameter uncertainty, only E^1_{2g} mode narrows.

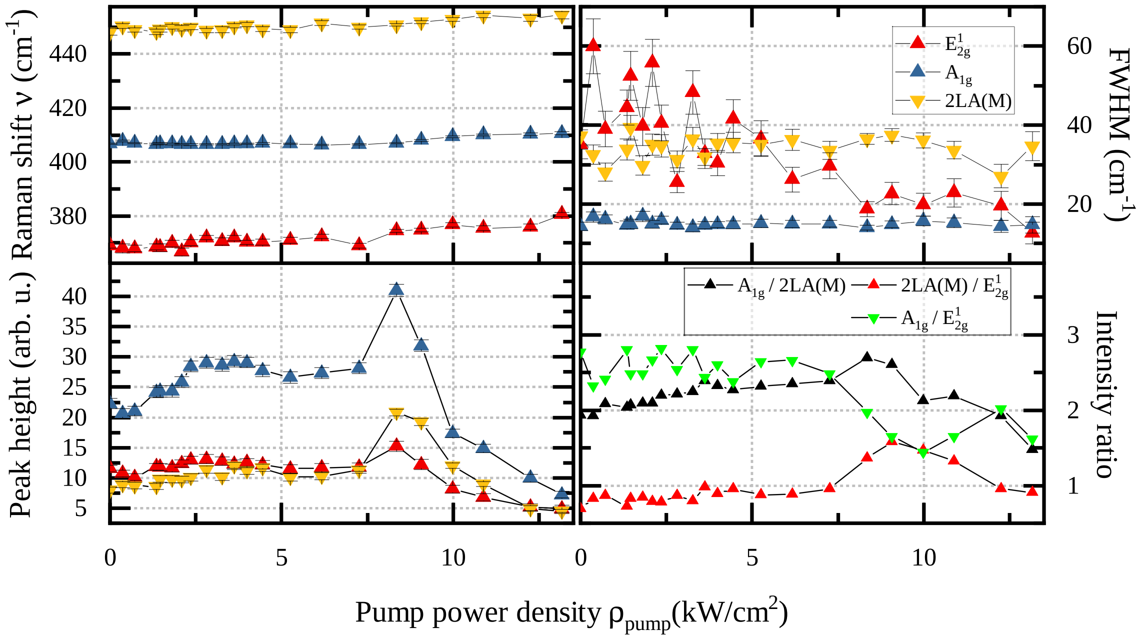

Figure 5.9: Fit parameters of MoS_2 spectra as captured at a pump spot edge, spectra in subfigure 5.8(c).

The upshift in the three main Raman peaks correspond to mode hardening, so a structural ordering process may take place. Unfortunately, the fit parameter FWHM, which is usually consulted for such estimations, is scored as unreliable. The relative position of probe spot to the pump spot has a more intricate impact on the spectra in comparison to the case in amorphous carbon. The stable MoS$_2$ signal within the pump spot, but not necessarily at the edge, raises the hypothesis of non-uniform evaporation and re-deposition without (further) chemical transitions. Also, MoS$_2$ decomposition at temperatures of at 1873 K is unlikely. Measurement off-centred and near the edge are found to be beneficial, that is, provide the clearest Raman signals.

Figure 5.10 presents spectra in a similar configuration, but all irradiation is done in ambient air. The unstacked spectra in the inset overlap, so representing spectra are vertically shifted for readability. Signals of MoS$_2$ are maintained for power densities up to 2.2 kW cm^{-2} (spectrum not shown). Over the course of five measurement steps within that limit, the modes E^1_{2g}, A_{1g}, 2LA(M) gain intensity in a linear fashion with laser power and E^1_{2g}, 2LA(M) broaden slightly while A_{1g} remains at unchanged width. Shortly before the MoS$_2$ signal declines, the E^1_{2g} mode narrows. All three main peaks are at a constant Raman shift ν. Laser power densities in the medium range, i.e. 2.8 kW cm^{-2} and 4 kW cm^{-2}, show new, but weakly pronounced peaks at 820 cm^{-1} and 995 cm^{-1} and from 4.6 kW cm^{-2} on-

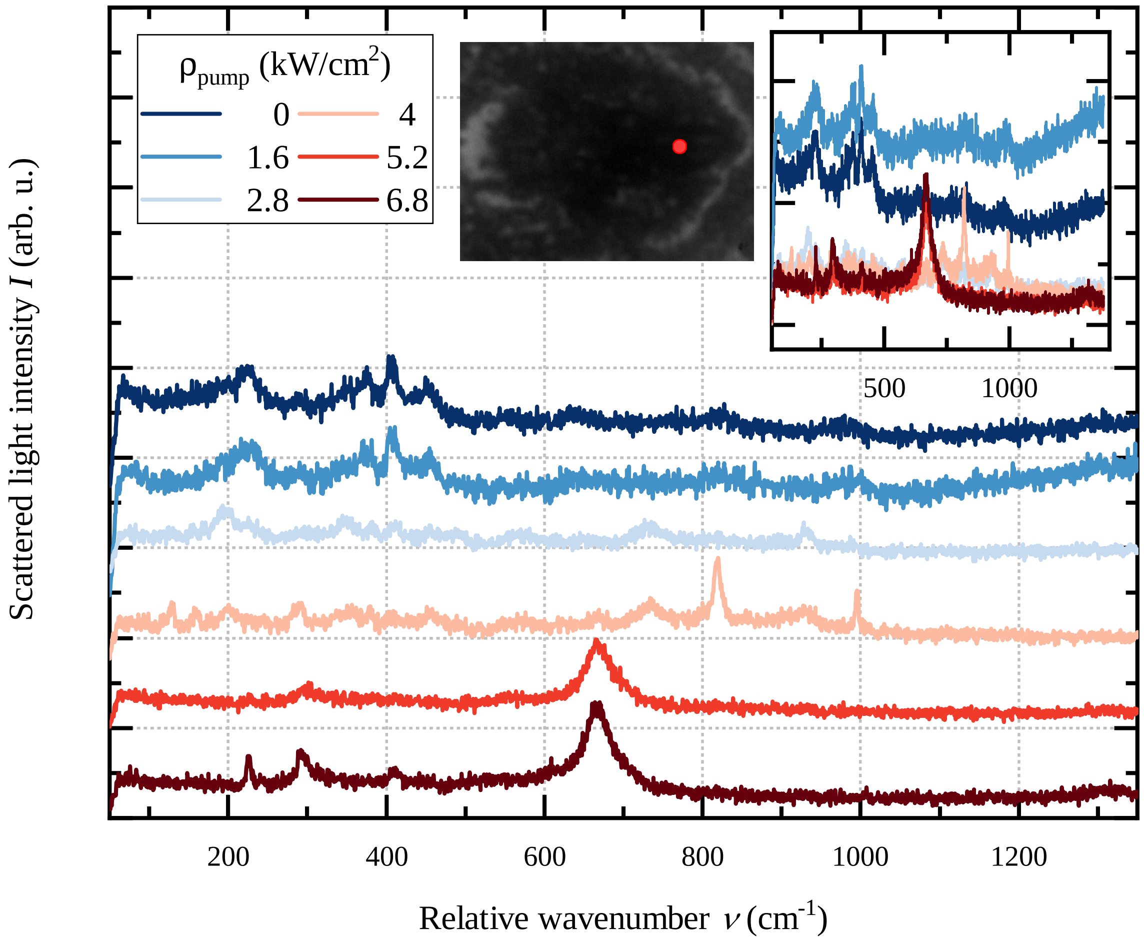

Figure 5.10: Raman spectra of MoS$_2$ at different laser power density in ambient air, probe spot off-centred in the pump spot.

wards, a stable configuration is set with a well pronounced peak at 670 cm^{-1}. In comparison to the situation in vacuo, reactions on laser power sets in far earlier: the maximum power density in vacuo with still measurable MoS_2 signal of 8 kW cm^{-2} leads to complete film loss in ambient air. The maximum measured power density with still measurable MoS_2 signal in ambient air is 2.2 kW cm^{-2} (spectrum not shown). The peaks in the medium range stem from MoO_3 and therefore show the process of oxidation. Because of the poor resolution of the spectral range 100 cm^{-1} to 600 cm^{-1} in the medium power density range, no reliable information is further extracted here. As speculation based on the known transitions listed in the introduction, a mixture of MoO_2 and MoO_3 may be present. The higher power densities of more than 4.6 kW cm^{-2} show the oxides of the substrate material, which indicates the loss of the thin film in total.

Finding film ablation and re-deposition in MoS_2 before, the pump spot after the last measurement series in ambient air is spatially resolved in Figure 5.11. The measurement point in the map indicated with pink symbol is close to the measurement spot in the preceding series, for comparison. At the outside edge of the pump spot, typical MoS_2 signals are found, which agrees with the findings before. In more detail, the spectrum taken at 70 µm and 60 µm (brown and blue in inset (i)) differ from general scattering intensity and in background slope. On the other side, spectra at −100 µm and −90 µm (dark and light blue in inset (iv)) are far more similar to one another, the inner spectra is showing a weakly pronounced peak at roughly 930 cm^{-1}, which becomes far stronger pronounced as the pump spot centre is approached. In subfigure (iv), the spectra at −70 µm and −60 µm (blue and green) show more or less unclear signals of MoS_2 and show a intricate behaviour in the second half spectral range, i.e. 500 cm^{-1} to 1000 cm^{-1}. Further towards the centre, the spectrum −40 µm (dark blue in subfigure (iii), orientation marker) is the strongest Raman scattering in this series overall. The strongest peaks at 767 cm^{-1}, 818 cm^{-1}, and 995 cm^{-1}, which presented previously, are partially clipped. In the first half spectral range, spectrum at −40 µm gives clear Raman signals, which were poorly resolved before. Finally, subfigure (ii) covers the spatial region 0 µm to 30 µm, which also includes the pump centre. There, in spectra 0 µm and 10 µm (dark and light blue in subfigure (ii)), the only well-pronounced peak at 670 cm^{-1} is accompanied by shallow low-frequency contributions in the spectral range around 250 cm^{-1}. These become clearer in the blue adjacent spectrum 20 µm with elevated general scattering intensity and unclear again in the green spectrum 30 µm.

As already described above, the involved materials are MoS_2 (see spectrum at −100 µm or at 70 µm), MoO_3 (see spectrum at −40 µm or at −30 µm), and substrate oxides (see spectrum at 0 µm) or mixtures thereof. Involved Raman peaks are often broader than their literature reference data, and a more complex background in the vicinity of strongly pronounced peaks is found. Both observations are linked to the disordered and inhomogeneous structures, which are expected in sputtered thin films and in re-depositioned phases. Ambient air humidity was present during irradiation, so the less stable MoO_2 phase was neither clearly found nor expected. In literature, microscope pictures of the laser spot after irradiation is observed, which exploits the different morphology and colours of occurring oxides and phases. [280, 286, 287] In comparison, such studies find a fine-distributed selection of structural phases and different oxides. Here, a simpler picture arises, in which the local power density of the pump spot gives rise to (I) a uplift in MoS_2 intensity, (II) signal conversion/loss, (III) molybdenum oxide phase and substrate oxides at last.

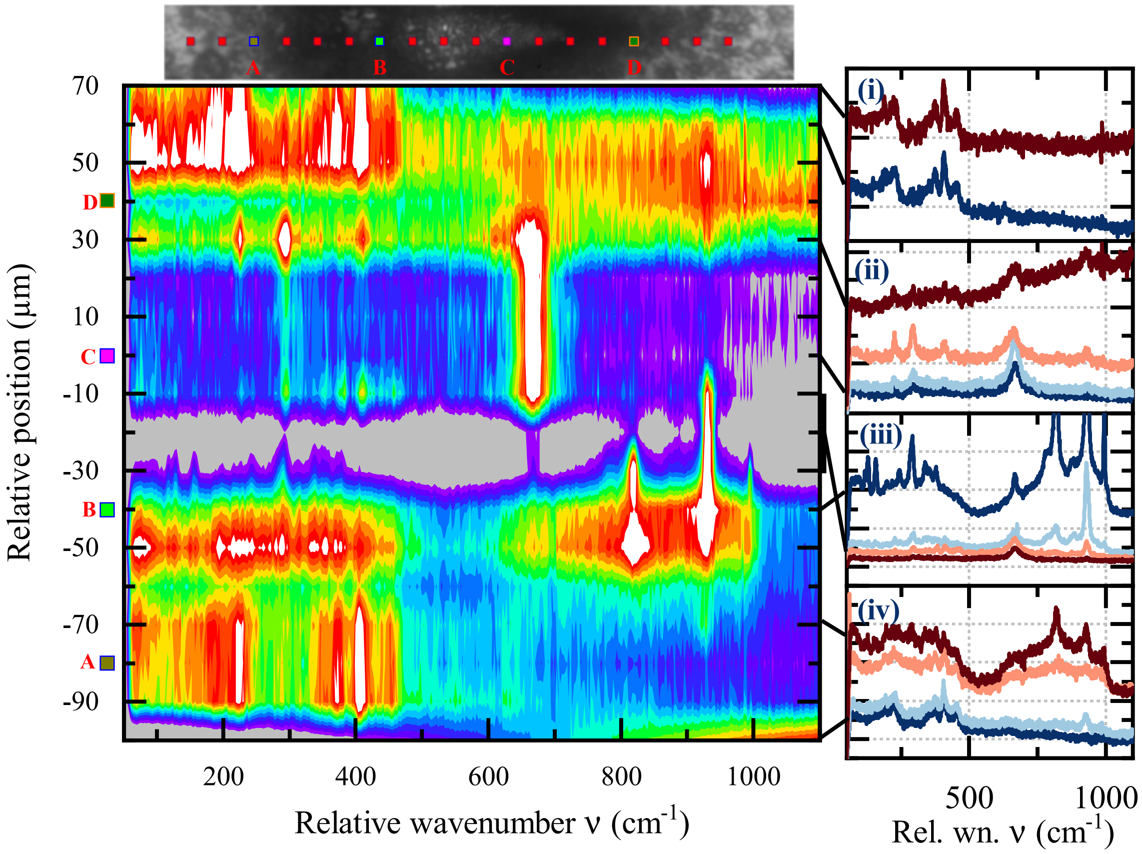

Figure 5.11: Mapping of Raman spectra along a laser irradiation spot to show redeposition effect. The main window show individually-normalised spectra, but a impression of the natural intensities is given in the side panels (i)-(iv). Colours from violet to red in natural order cover a intensity percentage in range 30 % to 80 %, lower values are light gray to clip background signals and higher values are white for highlighting the strongest features of any spectrum. See appendix S1 for microscope pictures before and after laser irradiation.

5.4 Nitrogen-modification in MoS_2:N, five phase model

As MoS_2 quintessentially suffers the same limited thermal stability as amorphous carbon, one motivation for chemical modifications is the increase of usable maximum operation temperature of thin films. Another motive for optimisation is the push towards more appropriate material - or tribological properties like hardness adjustment or basal orientation microstructure over a columnar structure, respectively. Like in a-C, element-modification allow for optimising or parameter adjustment under a given premise.[165] Here, nitrogen modification in MoS_2:N for enhanced thermal stability is studied, which gives rise to additional phases compared to the unmodified MoS_2thin films above.

For a film with at least 17.6 at.-% nitrogen content, an increment from 320 °C to 650 °C, which translates to increasing the effective service temperature of MoS_2 thin films to 400 °C. [165] Figure 5.12 presents measurement series of nitrogen-modified MoS_2:N thin films, which are annealed at 100 °C (moderately) or at 300 °C (strongly). The behaviour of both MoS_2:N thin films deviate significantly from the behaviour of MoS_2, which, in combination, suggests the differentiation of five phases. Three parameter sets are considered, see Table 5.1.

Phases (I) and (II) - restructuring of MoS_2 from the amorphous start

The first phase covers the as-deposited situation. MoS_2:N thin films prominently show the absence of distinctive Raman peaks, which are visible in unmodified MoS_2 thin films from the start. In MoS_2:N samples, the spectra show a roughly linear background in the spectral range $200\,\mathrm{cm}^{-1}$ to $1000\,\mathrm{cm}^{-1}$ with weak and broad features in the vicinity of acoustical phonon peaks and near the A_{1g} mode. This mode in particular is the only pronounced peak in phase (I) for MoS_2:N. Increasing the laser power density leads to a decline in background and the detailed presentation of the expected peaks in MoS_2 samples. By the end of phase (I), a stable Raman signal of MoS_2 is achieved. This situation is similar in unmodified MoS_2 samples. To collect multiple influencing factors like the excitation wavelength, annealing temperature, or relative probe position, the following is structured in a design of experiment-style manner, that is, three sets of varying factors are compared to each other. The required power density range in case of non-resonant irradiation with 1064 nm is (0-5) $\mathrm{kW\,cm}^{-2}$ for non- and moderately annealed samples with relative probe positions near pump spot centre (set 1) and (0-8) $\mathrm{kW\,cm}^{-2}$ for moderately and strongly annealed samples with off-centred probe positions (set 2). For 532 nm pumping, moderately annealed samples, and centred

	Pumping wavelength	annealing temp.	probe position
set 1	1064 nm	100 °C 100 °C	centre
set 2	1064 nm	100 °C 300 °C	off-centre
set 3	532 nm	100 °C 100 °C	centre

Table 5.1: Set of parameters in MoS_2:N series for comparison

relative probe positions (set 3), value range of (0-1.4) kW cm^{-2} was found. After those power ranges, phase (II) is distinguished by mostly stable MoS$_2$ signal with shallow peak evolution as discussed above. Power density range are (5 - 6) kW cm^{-2} or (8-12) kW cm^{-2} for set 1 and 2, respectively, or (1.4-2.1) kW cm^{-2} for set 3.

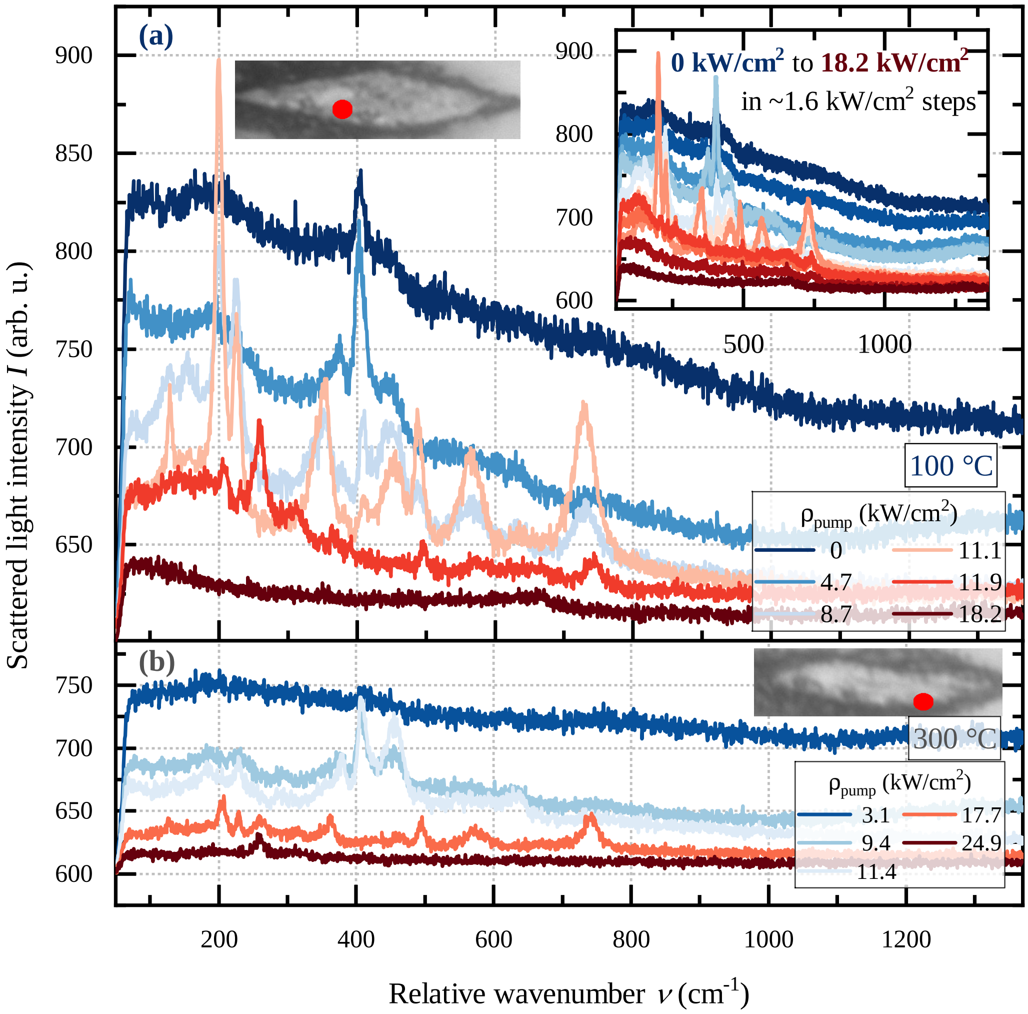

Figure 5.12: Raman spectra of MoS$_2$:N at different laser power densities, both for 1064 nm pumping: **(a)** MoS$_2$:N sample with 100 °C heat treatment for annealing, probe spot in centre of pump spot (in set 1), **(b)** MoS$_2$:N sample with 300 °C heat treatment for annealing, probe spot in off-centre of pump spot (in set 2).

Phase (I) does not provide clear signals in MoS$_2$:N thin films at start. The uniform background may suggest acoustical phonons or boson peak-like artefacts as underlying contributions. Increasing the power leads to clear MoS$_2$ signals in phase (II) and reduction of the background signal. Microscopically, the impact of the laser is sufficient to change the optical appearance by shallow brightening with disappearing dark freckles in and around the laser spot. As processes, two concepts are assumed to be conjointly taking place: firstly, changes in microscope picture suggests that a surface adsorption layer exists and is removed within the first step of investigation. In that regard, supplementary comparisons between lightly scratched surfaces and unadulterated samples show no significant differences in Raman spectra. The severity of those scratches is comparable to handling the samples and cleaning them with a dry tissue and light pressure by hand. As result, the samples change their macroscopical optical appearance only, the spectra are mostly left unchanged. Secondly and more profoundly, the structural ordering and crystallisation is expected. This relies on the previous results of chapter 4.2, in which MoS_2:N thin films are discussed, whose amorphism was independently shown by XPS spectroscopy. Amorphous thin films of MoS_2 do provide Raman spectra, but they are comparatively weak and extensively broad. [288] By own investigations, samples do not give a clear Raman signal in their amorphous state. Literature suggests that nitrogen-free MoS_2 thin films also consists of amorphous and crystalline phases in mixture [165], which explains in part the behaviour in MoS_2 for some relative probing spots.

Phase (III) - (a) formation and (b) stable range of MoO_2

After phase (II), the spectra change drastically; first and foremost, the signatures of MoS_2 are decreasing. Like described for the MoS_2 figures above, strongest changes are the decline of the A_{1g} mode and the uplift of 2LA(M) mode with the separation and narrowing of both low-frequency acoustical modes ZA(M) and LA(M). Simultaneously to the signal loss of MoS_2, a stable Raman signal is obtained with previously unobserved peaks at $130\,\mathrm{cm^{-1}}$, $199\,\mathrm{cm^{-1}}$, $226\,\mathrm{cm^{-1}}$, $352\,\mathrm{cm^{-1}}$, $489\,\mathrm{cm^{-1}}$, $564\,\mathrm{cm^{-1}}$, $733\,\mathrm{cm^{-1}}$. The phase $(\mathrm{III})_a$, the signal loss of the previous phase, takes place for power densities of (5-6.5) $\mathrm{kW\,cm^{-2}}$ for set 1, (12-16) $\mathrm{kW\,cm^{-2}}$ for set 2, and (2.1-2.7) $\mathrm{kW\,cm^{-2}}$ for set 3. After the decline, a stable phase $(\mathrm{III})_b$ of the new peaks appears with power density maxima of $10\,\mathrm{kW\,cm^{-2}}$ for set 1, $21\,\mathrm{kW\,cm^{-2}}$ for set 2, and $6\,\mathrm{kW\,cm^{-2}}$ for set 3.

These new signatures stem from MoO_2. The transition is not isochemical and requires the exchange of sulphur and oxygen atoms. With respect to their crystalline counterpart, the enthalpy of formation $\Delta_f H^0$ is $-65.999\,\mathrm{kcal\,mol^{-1}}$ and $-140.50\,\mathrm{kcal\,mol^{-1}}$, the standard entropy S^0 is $14.95\,\mathrm{cal\,mol^{-1}\,K^{-1}}$ and $11.10\,\mathrm{cal\,mol^{-1}\,K^{-1}}$ for MoS_2 and MoO_2, respectively. [289] So, by considering the enthalpy of the bonding alone, the formation of molybdenum dioxide is energetically beneficial, although entropically (= kinetically) hindered. The reaction product is stable, because the change in enthalpy is vastly larger than the change in entropy. In more detail, a negative Gibbs enthalpy $\Delta G = \Delta H - T \cdot \Delta S$ is required. Comparing to MoO_3, however, the potential differences are larger: $\Delta_f H^0 = -178.10\,\mathrm{kcal\,mol^{-1}}$ and $S^0 = 18.59\,\mathrm{cal\,mol^{-1}\,K^{-1}}$. [289] As result of the Bell-Evans-Polanyi principle, the energetically more favourable product features a lower activation barrier and is therefore more likely formed. By these considerations, with no other restrictions, the formation of MoO_2 is hindered in favour of MoO_3. Furthermore, the transition requires a structural reordering breaking present structures and bonds. MoS_2 may be present as disordered or even amorphous when deposited, but still phase (II) and the rise of MoS_2 Raman signature hints to the crystalline configuration. Also, the hexagonal symmetry is known to be more stable than the rhombohedral counterpart, which transforms to hexagonal symmetry upon heating. [37, p. 55] Although not impossible at all, this would lead to stress or lattice mismatching, which, in turn, is likely to be seen in Raman signatures. Finally, the sample is heated in vacuum with residual pressure in order of nbar. Oxygen is still present, but in considerably reduced quantity, which suggests the hindering of oxidative processes. The oxidative reaction of MoS_2 to MoO_3 in ambient air requires a comparatively large amounts of oxygen, see chemical equation (2.5), and is therefore hindered. The reaction pathway to MoO_2 was not resolved in the scope of this study; complex oxysulphides of molybdenum are known to be intermittently present.[276] As reducing conditions are required for the formation of MoO_2 from MoS_2, one might assume the presence of adsorbed water to be a key component. This hypothesis, however, does not hold, because water vapour are expected to be (mostly) desorbed at the temperatures above 308 °C, which are present in phase (III). An alternative might be the reduction of MoS_2 to (metallic) Mo and subsequent oxidation like in net chemical equation (2.7). For this, the oxide layer on an as-deposited thin film as part of a technical surface would be sufficient.

Phases (IV) and (V) - unclear nitrogen-specific phase and film ablation

When the samples are chemically altered with nitrogen, new peaks arise as additional phases. In Figure 5.12, pronounced peaks at $208\,\mathrm{cm^{-1}}$, $260\,\mathrm{cm^{-1}}$, and $313\,\mathrm{cm^{-1}}$ are found along with weakly pronounced peaks, which are assumed to be residuals of the previous phase. Phase (IV) is stable for power densities up to $12\,\mathrm{kW\,cm^{-2}}$ in set 1 or $25\,\mathrm{kW\,cm^{-2}}$ in set 2. It was not found in set 3, i.e. with 532 nm pumping. The only peak remaining in the final phase (V) is a rather unspecific, highly asymmetric peak near $670\,\mathrm{cm^{-1}}$. This phase appears in samples, which are oxidised in ambient air.

The peaks in phase (IV) are not allocatable with sufficient confidence and only occur in nitrogen-containing samples. So, the assumption is a (final) reaction with molybdenum dioxide with nitrogen or with substrate material. Molybdenum is a known catalyst for reducing nitrate to nitrite species [290], so a mixture of residual MoO_2 and nitrous compounds of molybdenum may play a role. Molybdenum nitride MoN and its reaction products with ambient oxygen are excluded, although they are believed to be present in related research. [165] Also of interest is the appearance for 1064 nm pumping, only. This suggests that compounds in phase (IV) are more absorbent for 532 nm light, which leads to their demise. The one characteristic peak in phase (V) is also found, when be substrate material is oxidised in ambient air. Therefore, the thin film is lost regardless of the last oxidation state to laser ablation. The surface of the sample is highly irregular, so unsteady signals are connoted to unspecified residuals peeking in-and-out of focus of the microscope. A comparable situation is also found at the last stage of amorphous carbons (not shown).

Chapter 6

Summary and Outlook

6.1 Usage of Raman spectroscopy for thin film analysis

Raman microscopy proved to be a versatile tool in investigation of a-C thin films. In this work, its exclusive use in investigation of thin films was conduced with satisfactory results. The effect of element-modification of D- and G-Raman peak are summarised in Table 6.1, second-order peaks are disregarded.

	Raman shift ν/cm^{-1}		Peak width $/\mathrm{cm}^{-1}$		Intensity ratio
	G	D	G	D	R_{Int}
a-C	1556 ± 2	1382 ± 11	178 ± 8	409 ± 13	1.44(*)
a-C:Si	↓	↓	↓	↑	↓
a-C:W	→	↑	↑	↓↓	↑
a-C:Ag	↑	→	↓	→	→
CrC	→	↑	↓	↓	↑
TiC	→	↑	↓	↓	↑
a-C:H	1542 ± 1	1361 ± 11	180 ± 4	351 ± 13	0.65(*)
a-C:H:Si	↓	↓↓	↓	↓	↓↓
a-C:H:W	↓	↓	↑	↓	↑↓

Table 6.1: Trends in element-modified a-C thin films. The interlayers CrC and TiC are not considered as proper a-C thin films but are listed for completeness.
(*) Uncertainty in R_{Int} estimated conservatively to ± 0.25, not as fitting parameter uncertainty (see subsection 5.1.5 for details).

The effect of silicon- and tungsten-modification in a-C resembles the preceding literature work, competing and complementary effects thereof in a-C:H were qualitatively described. Modification with silver and copper have similar effects in a-C thin films, multi-layer structures differ in thermal resistance.

Measurands in Raman spectroscopy for a-C thin films

Raman spectroscopy was already treated as analysing method of choice. Its usage as singular method in this work gives mostly positive results.

On the *positive side*, the structural impact of inter-layers, which are applied to relief the short-coming of poor adhesion, on the top-layer a-C is minor. In the **study of CrC interlayers** for different pre-treatment methods, no effect in the top-layer arising from different inter-layer properties are found at all. For **manufacturing of hydrogenated a-C:H**, the setup can be used for qualitative analysis: a set of optimal deposition parameters was found. Differences in Raman spectra between a-C and a-C:H are most striking in absolute intensity. A converse effect of bias voltage on both thin film systems was revealed, but its underlying mechanism remains unknown. For **manufacturing of element-modified a-C(:H):X**, the setup can likewise be used for qualitative analysis. Agents acting on $sp^2 - sp^3$ hybridisation balance like silicon and tungsten show their impact on the Raman spectra in a-C. The same situation for a-C:H allows for discussion whether the hybridisation effect of modifying elements or hydrogen compensate or cooperate. Agents acting as catalysts, ergo breaking energetically unfavourable bondings like those under stress or sp^3 hybridised carbons, also show their impact on the Raman spectra in a-C. Both elements in this study, silver and copper, lead to thin films, which are leaning towards graphitisation, therefore reduction thermal stability. This effect increases with silver content, the effect of copper was omitted in this thesis. The reduction of thermal stability in a-C:Ag is successfully circumvented by the concept of multi-layers. In case of **silicon-modified a-C:Si**, quantitative analysis was rudimentarily possible. For this, especially the analysis of the D-Raman mode in Raman shift and FWHM with dependable coefficient of determination R^2, is in fact adequate for the quantitative analysis of silicon content. In a similar manner, the behaviour in a-C:W and a-C:Ag was investigated, but no comparable significant trends are found. **After tribological loading**, the Raman spectra reveal an imprint of the thin film usage. The usage of thin films in adhesion tests (scratch tests), i.e. a steel ball being dragged once along a straight line with increasing normal force, which ultimately leads to spalling failures due to delamination, shows clear trends. In a-C:Si, Raman shifts ν of both D- and G- Raman peaks declined significantly by $50\,\mathrm{cm}^{-1}$, while the intensity ratio R_{Int} drops; in a-C:W, no comparably clear trends appeared in Raman shift ν, peak width or intensity ratio R_{Int}. The behaviour in a-C:Si is not reproducible by optical temperature tuning, so the impact of scratch tests onto thin films is **not exclusively thermal**. The onset of thin film failure due to graphitisation may be further developed for usage in quality assessment: as concept, a machine part features a thin film lubricant, whose internal stress or the release thereof acts as a hint to excessive loading. When combined with fluid lubricants as main lubricant, the thin film may be tailored for proper fluid film adhesion and as a witnessing agent of improper usage or wear. On that note, the absence of significant changes in the ball-on-disk tribometer testing proved the resilience of the thin films against this form of tribological loading, although a stronger impact on structure and chemistry was anticipated for study. **Future studies** shall measure the whole range of scratched wear scar and compare the evolution of the fit parameters between samples with different silicon content; for ball-on-disk tribometer testing, severely worn samples or *in situ* measurements are promising for resolving detrimental or transient structural impact, respectively.

On the *negative side*, Raman spectroscopy is not suitable for evaluating the adhesion to the substrate directly. Reasons for this are based on the fact that the focus volume of this setup is assumed to be in order of 100 nm, so a direct assessment of underlying inter-layers through a micrometer-sized top layer is impossible. On the other side, a badge of substrates with inter-layers only may be investigated in the beginning of manufacturing for structured quality assurance, Raman spectra of those inter-layers are supposed be close to a-C thin films for ideal adhesion. The reduction of thermal stability in a-C:Ag is successfully circumvented by the concept of multi-layers, however, the current setup does not capture a difference in spectra. In other words, thin film parameters like thermal conductivity are not directly accessible via Raman spectroscopy.

Raman spectroscopy for MoS_2 thin film analysis

Evaluating Raman spectroscopy in MoS_2 as singular tool yields mixed results.

On the *positive side*, structural aspects, the qualitative degree of crystallinity and especially the lack thereof in amorphous structures, were identified clearly as well as finely analysis on occurring oxides. The effect of annealing was partially resolved in this manner. Due to the complex nature of tribo- and transfer-films in MoS_2 thin films, the spatial resolution in confocal Raman spectroscopy helped to identify a structural transition from initial MoS_2 thin film material to wear debris. Also, the increase in thermal stability was measurable qualitatively in Raman microscopy, which would be easily transferred to quantitative studies via temperature tuning. Furthermore, a detailed analysis of the Raman peak behaviour is unhindered: the occurrence of forbidden Raman peaks were exploited to identify stacking faults in previous related studies. [174] By comparison of **Raman spectra of annealed wear debris**, weaker MoS_2 signals in annealed MoS_2:Cu and MoS_2:N relative to MoS_2 wear debris gave a strong clue that ordering MoS_2 by heat or by pressure is not equivalent. If those processes were equivalent, the 200 °C-annealing should present clearer MoS_2 signatures, which it does not. The formation of MoS_2 tribo-films in MoS_2:Cu and MoS_2:N are assumed to differ. Wear debris in MoS_2:Cu show less clear MoS_2 signal relative to MoS_2:N; apparently, something inhibited the formation of ordered MoS_2 sites for the tribo-film in MoS_2:Cu. As hypothesis, catalysing effects of copper remain, when nitrogen in the same configuration evaporates. **Future studies** should include actual contact pressures, for example via constant pressure glass lenses or rather via *in situ* measurements. Element-modification with copper and nitrogen are still promising samples to further study the formation of MoS_2 tribo-films in general.

On the *negative side*, a core property in use for thin film engineering, the growth direction of MoS_2 thin films in magnetron sputtering, is inaccessible and remains to be measured by X-ray spectroscopy methods. Like in a-C, mechanical properties like hardness are also not measurable.

Outlook on future studies

For further study, mechanical properties of thin films like elastic modulus or hardness need to be measurable. Brillouin spectroscopy is conceptually similar to Raman spectroscopy, but sets the focus on acoustical phonon modes. From those phonon modes, related material properties like speed of sound, heat conductivity and mechanical properties like elastic modulus can be derived. If the speed of sound is anisotropic in MoS_2, this setup is a promising approach to access the growth direction without the usage of X-ray equipment. Methodologically, the setup may be expanded by a secondary probe line for Brillouin spectroscopy: on the same probe spot, collimated light could be split for two spectroscopy pathways - one for the Raman spectrometer as is and one for a Brillouin interferometer. Depending on the required laser intensity for the two detectors, this maybe even possible using the same excitation laser.

All worn samples in this thesis were measured *ex situ*. Future investigations shall take place *in situ*, which is assumed to be critical for an understanding on the tribo-film formation mechanism. Typical rotation speed in ball-on-disk tribometer does not match with the required measurement time of this work's setup, usually multiple accumulations of 30 s for a-C and multiple accumulations of 300 s for MoS_2. For reduction of detection time other Raman-based spectroscopy methods like stimulated Raman spectroscopy are advantageous.

6.2 Optical temperature tuning in solid lubricant thin films

6.2.1 Optical temperature tuning in a-C thin films and derivates

In a-C thin films and their derivates, Raman spectroscopy is sensitive for structural and topological defect dynamics in (hydrogenated) amorphous carbon and allows the identification of dominant ordering processes by interpretation in Pseudo-Voigt fitting models. This allows for identification of two dominant ordering mechanisms and for a clear distinction of (hydrogenated) amorphous carbon with nano-crystalline components and heavily defected graphitic lining mixtures, which both occur in thermal impact in thin films of a-C and a-C:H. Only in their initial stage, a-C and a-C:H vastly differ in key properties on both macroscopic (i.e. optical) and microscopic scale (i.e. compositional and structural). Amorphous carbon remains a short-range ordered network in the low-temperature range and transitions continuously to defected carbon via thermal energy deposition. In the contest of structures, which reacts first, the hexagonal nano-crystalline clusters within the amorphous network surpass

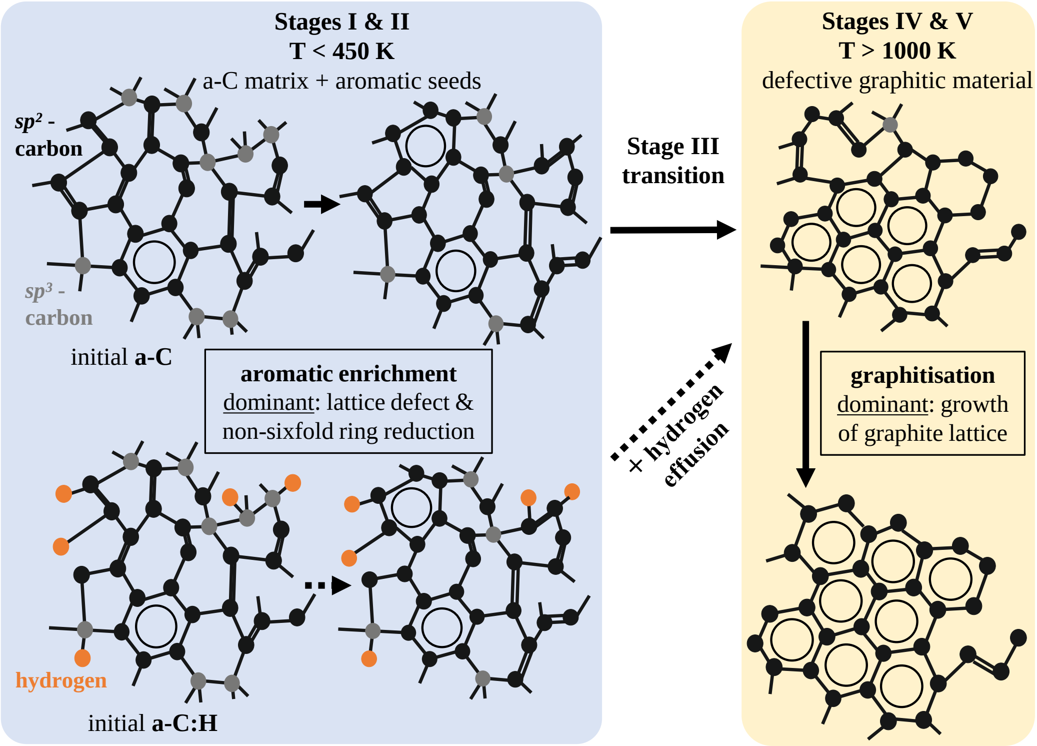

Figure 6.1: Depiction of key ordering mechanisms in the Five Stage model, structure of a-C is based on an early depiction of Galli et al. [51].

the general sp^2 hybridised carbon pairs in stability. For this reason, ordered graphitic seeds in an amorphous matrix are formed first. As sixfold rings are able to be enchanted with aromatic character by delocalised π-electrons, that stabilise the system by energetic relaxation, the system seeks to become more aromatic first to face against the high distortions and stresses found in sputtered a-C and a-C:H alike. So, the dominant mechanism is the aromatic enrichment of the a-C matrix. **When the enrichment is saturated**, changes in graphitic structures are gauged by the second order Raman scattering event, the $2D$-Raman peak. As two-phonon scattering event, it requires a minimum coherence length, which is first met after the transition to defected graphite stages. Hydrogen and hydrocarbons have left the matrix, co-joining a-C and a-C:H precursor networks at the common ending point. This is the moment, in which the transition from amorphous carbon to defected graphite is completed. Energy depletion in defected graphite is further used for the growth of graphitic area, so the dominant mechanism in the high-temperature regime is graphitisation, before the carbon network is lost to laser ablation. **Addition of silicon and copper** shifts the evolution towards higher laser power densities. Both modifications are assumed to protect the samples temperature related evolution by thinning of the carbon network and/or by release of internal stress. Although affecting thermal stability comparably, a-C:Cu is still limited to laser ablation, which is considerably postponed in a-C:Si.

In summary, this work immediately gives an adequate, yet simple analysing method for checking the constitution and “health status” of amorphous carbon thin film. Also, it provides an ordered course for in field-testing of thermal stability in search of stability-enhancing modification by probing structural internals in simple ways without the need of any advanced X-ray spectroscopy.

6.2.2 Optical temperature tuning in MoS_2 thin films

In studies of optical temperature tuning in MoS_2, initial ordering process of amorphous MoS_2 and subsequent reaction to distinct oxides of molybdenum was found. Onset points of chemical and structural phases and the effect of chemical modification on occurring phases are identified. In more detail, five phases are found in MoS_2:N, which were partially found in unmodified MoS_2 thin films. The occurrence of such oxides with deviating hardness values in an otherwise intact MoS_2 thin film hints to a possible abrasive-style wear mechanism. An exact temperature measurement is drastically more complex in MoS_2 in comparison to a-C, because the involved chemical transitions are exothermic. Although a local and transient temperature is detectable as expected, the reading gives a false impression, most readings are vastly to high.

Oxides of molybdenum were found in section 5.3 when heated excessively. It reacts abundantly to MoO_3 and substrate oxides in ambient air, and entirely to MoO_2 (or oxide mixtures) in vacuo. Figure S4 shows rare Raman spectra, which were found at different locations in the tribo-film for copper-modified MoS_2:Cu thin films in ambient air. In the same manner, Figure S5 shows all Raman spectra for nitrogen-modified MoS_2 thin films. The red spectra in the background are reference spectra of Mo compounds, the foreground spectra are numerated and discussed individually. The occurrence of MoO_2 in these situations was not reliably resolved in this work. As stated in the theoretical chapters, the oxides could play a key role for a wear mechanism in MoS_2 thin films. What role do the rarely appearing oxides mixtures in MoS_2 thin films play in tribo-film formation?

Oxides of copper-modified MoS_2:Cu thin films

All spectra consist mostly of **signatures from molybdenum oxides MoO_2 and MoO_3, and disulphide MoS_2**, although usually only MoO_3 is found in this case. In chapter 5.3, a clear contribution of MoO_2 was rarely found for samples other than for nitrogen-modified MoS_2 thin films. ID 1 (outside the tribo track, 3.1 at.-%) shows the most diverse mixture; all three contributions are visible. The spectrum in ID 2 (edge of the tribo-track without pronounced debris, 10.5 at.-%) is comparatively weak and only features faint MoO_3 signatures and the copper oxides. A pronounced feature at Raman shift 926 cm^{-1} will be discussed later. At a comparable probing position in ID 3-4 (copper content of 19.5 at.-% and 28 at.-%, respectively), mixtures of oxides are visible, like in ID 1. Finally in ID 5-6 (as-deposited situation, highest copper content of 30 at.-% and 31.9 at.-%, respectively), MoO_3 contribution is found, only. Traces of MoS_2 and MoO_2 are close to negligible.

Although the change in copper content is less than ten percent between ID 5 and ID 6, the **general scattering intensity drops**. This effect was found in chapter 4.2 as screening effect of surficial copper precipitation. A new peak arises well pronounced at 926 cm^{-1} in ID2, which is only vaguely found in ID1 and ID5 as shoulders. In the region of acoustical phonon modes, new peaks at 220 cm^{-1} and 285 cm^{-1} arise sporadically, which stem from **copper oxides**.

Oxides of nitrogen-modified MoS_2:N thin films

All peaks in ID 1+2 (7.1 at.-%), ID 3+4 (11 at.-%), ID 6 (12.4 at.-%), ID 7 (13.3 at.-%), and ID 9 (19.5 at.-%) **are ascribed to MoO_3**. Remnant **MoS_2 signatures are rarely** found on wear debris, like in ID 4 and ID5 (12.4 at.-%). The extent of MoO_3 in ID 3 far exceeds that of ID1, although the nitrogen content is only slightly elevated. Directly comparing the reference data and with ID 1-3, the acoustical phonons are far more elaborate. In ID 9, the signatures of MoO_3 are more finely resolved in the as-deposited probing location than in wear debris.

The peak at 926 cm^{-1} shows in ID 5 (gray) in the thin film sample with nitrogen content (12.4 at.-%), but not in ID 6. It is also found in the highest clarity in ID 8, besides weak signatures of MoO_3. Between those nitrogen contents in the sample ID 7 (13.3 at.-%), it was found at no point.

Conclusion

The unknown Raman peak at 926 cm^{-1} was never found in previous chapter, for which the measurement data are required to be repeatable. It may stem from an alloy of iron and molybdenum as a evidence of interaction between the counter-body and the thin film. Alternatively, molybdenum minerals like Lindgraynite, Markascherite, Obradovicite feature Raman peaks close to the unidentified peak. A similar peak was found for sulphur dioxide in aqueous solution, namely in surface-enhanced Raman studies for sulphur dioxide in wine. [291] However, the cited publications of this work do not provide a clear proof that the statement is still true for *regular* Raman spectroscopy: in the original publication, the peak is only visible in surface-enhanced Raman spectroscopy or in silver sulphate $AgSO_4$. [292] In *regular* Raman spectroscopy, on the contrary, the vibrational mode is found with a Raman shift in the range 950 cm^{-1} to 990 cm^{-1}, which is coherent with other reports for various sample categories [293, 294, 295].

For future studies on the interaction of main-body and counter-body, it is advisable to keep sharp lookout on deviating metal oxide peaks and to vary the materials of counter-bodies in chemical inertness and hardness, for example, soft polymer counter-bodies. From this, any hypothetical interaction between molybdenum and the counter-body material may be resolved in finely-resolved Raman mappings. The acoustical phonons in these samples are more detailed than in reference mineral spectra. Future studies are advised to resolve the acoustical phonons and to find any correlation to the measurement position in spatially-resolved Raman mappings. Previous studies [174] of the workgroup already showed that the occurrence of acoustical phonon modes are step stones for resolving ordering/restructuring processes in MoS_2. Ideally, ordering mechanisms as identified for a-C thin films in this work, should be resolved for MoS_2 thin films. For conception of tribo-film formation, *in situ* investigations in MoS_2 thin films are a promising approach.

Appendix A: Supplementary figures

This appendix holds all supplementary figures, which were mentioned in the main matter of this work. Those are

1. Microscope pictures of the MoS_2 sample surface in Figure S1,
2. Raman fit parameters in tungsten-modified a-C:W thin films for quantitative analysis in Figure S2,
3. Raman fit parameters in silver-modified a-C:Ag thin films for quantitative analysis in Figure S3.
4. Rarely appearing oxides oxides in copper-modified MoS_2:Cu thin films with different copper content in Figure S4.
5. Rarely appearing oxides oxides in nitrogen-modified MoS_2:N thin films with different nitrogen content in Figure S5.

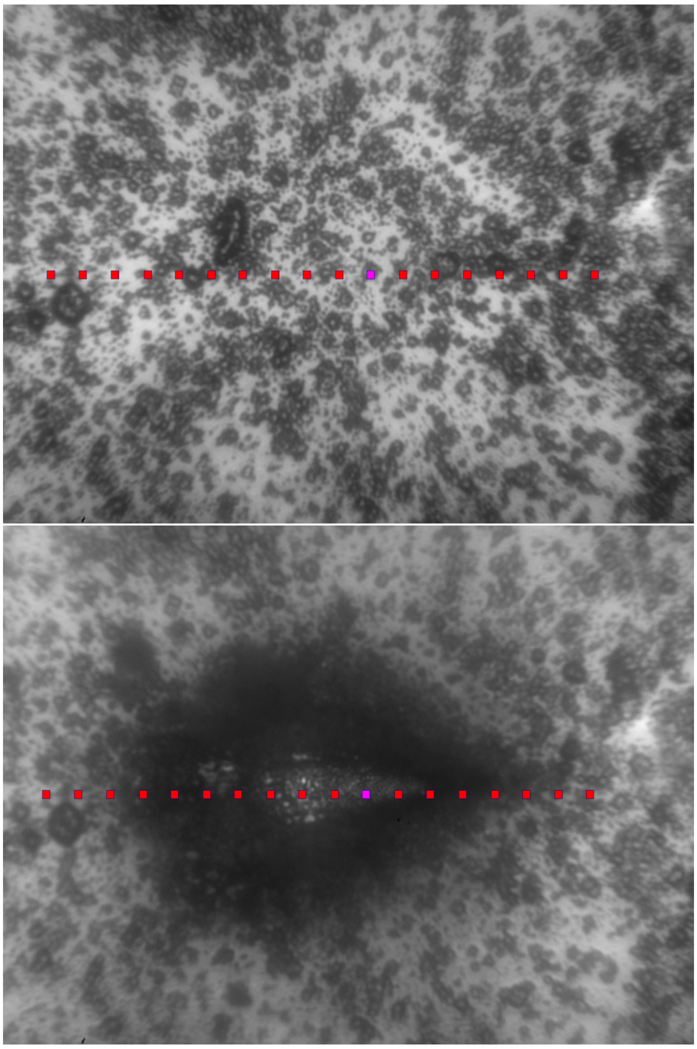

Figure S1: Microscope gray-scale pictures of the MoS_2 sample surface with inscribed measurement points, sample surface before laser irradiation **(upper)** and after laser irradiation **(lower)**. The morphology is typically rough for sputtered MoS_2 in comparison to some chemically modified derivates. The purple symbol denotes the spot, which was used in measurement in Figure 5.8.

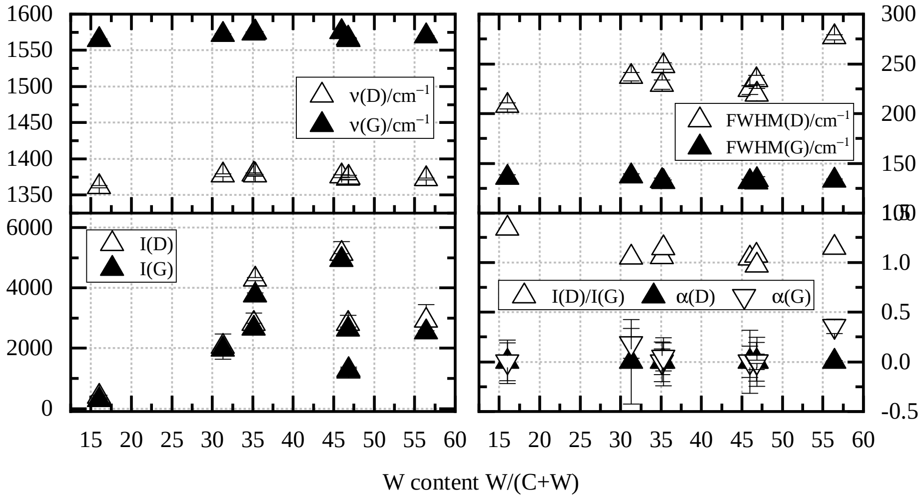

Figure S2: Raman fit parameters in tungsten-modified a-C:W thin films for quantitative analysis. No clear trends are visible.

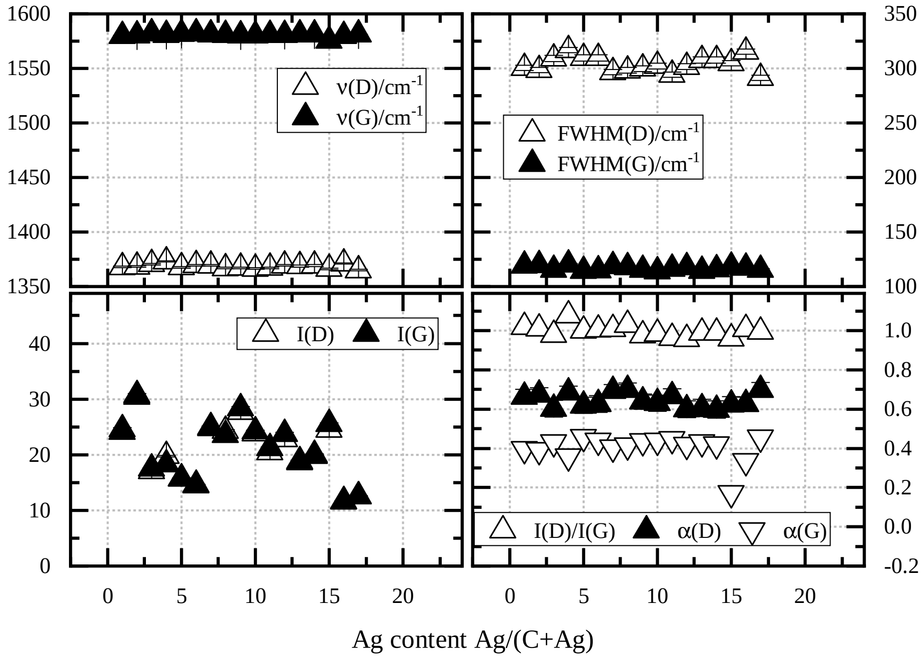

Figure S3: Raman fit parameters in silver-modified a-C:Ag thin films for quantitative analysis. No clear trends are visible.

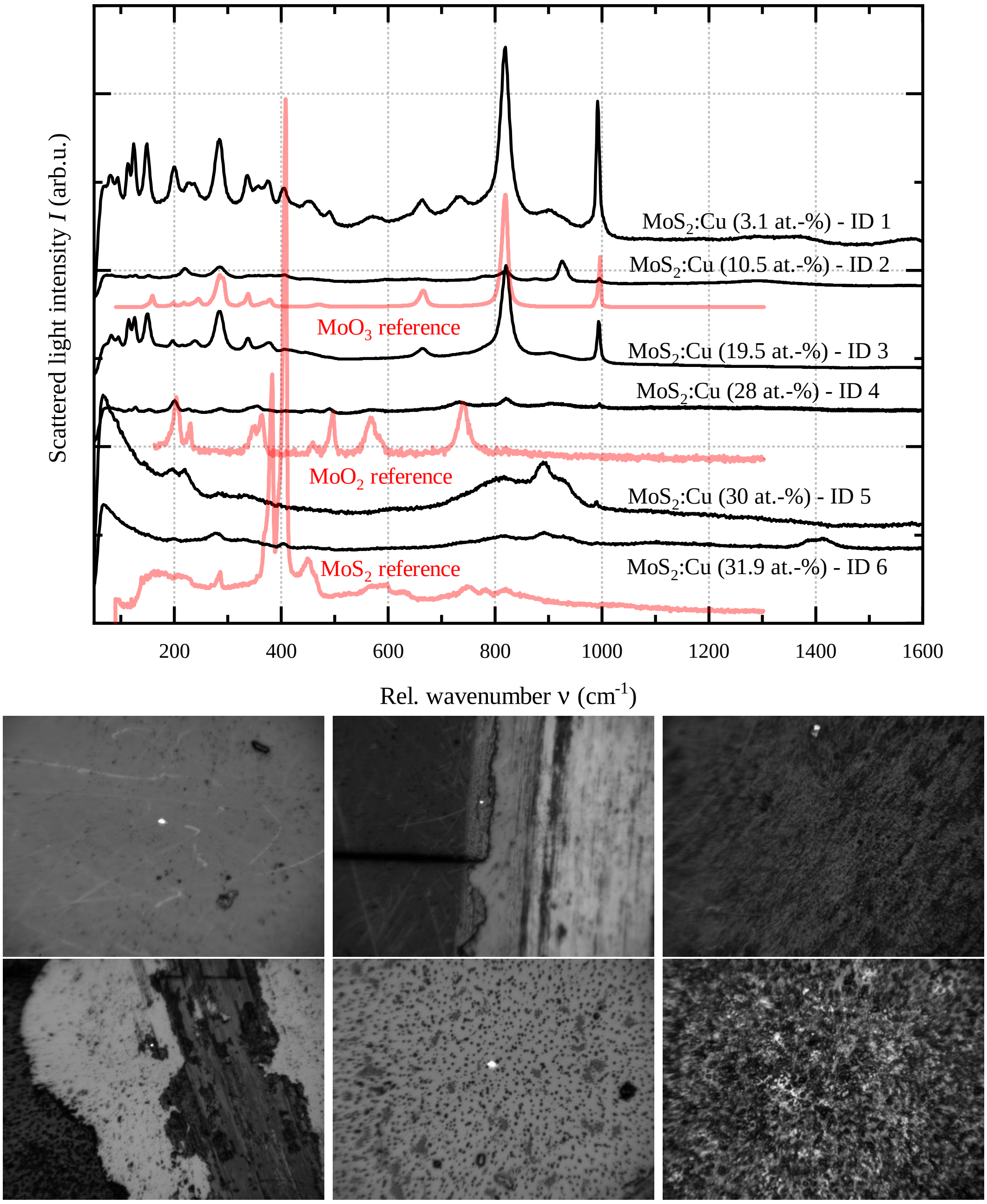

Figure S4: Raman spectra of rarely appearing oxides in copper-modified MoS$_2$:Cu thin films with different copper content **(above)**, microscope image of the sample surface for ID1-ID6 in reading direction **(below)**.

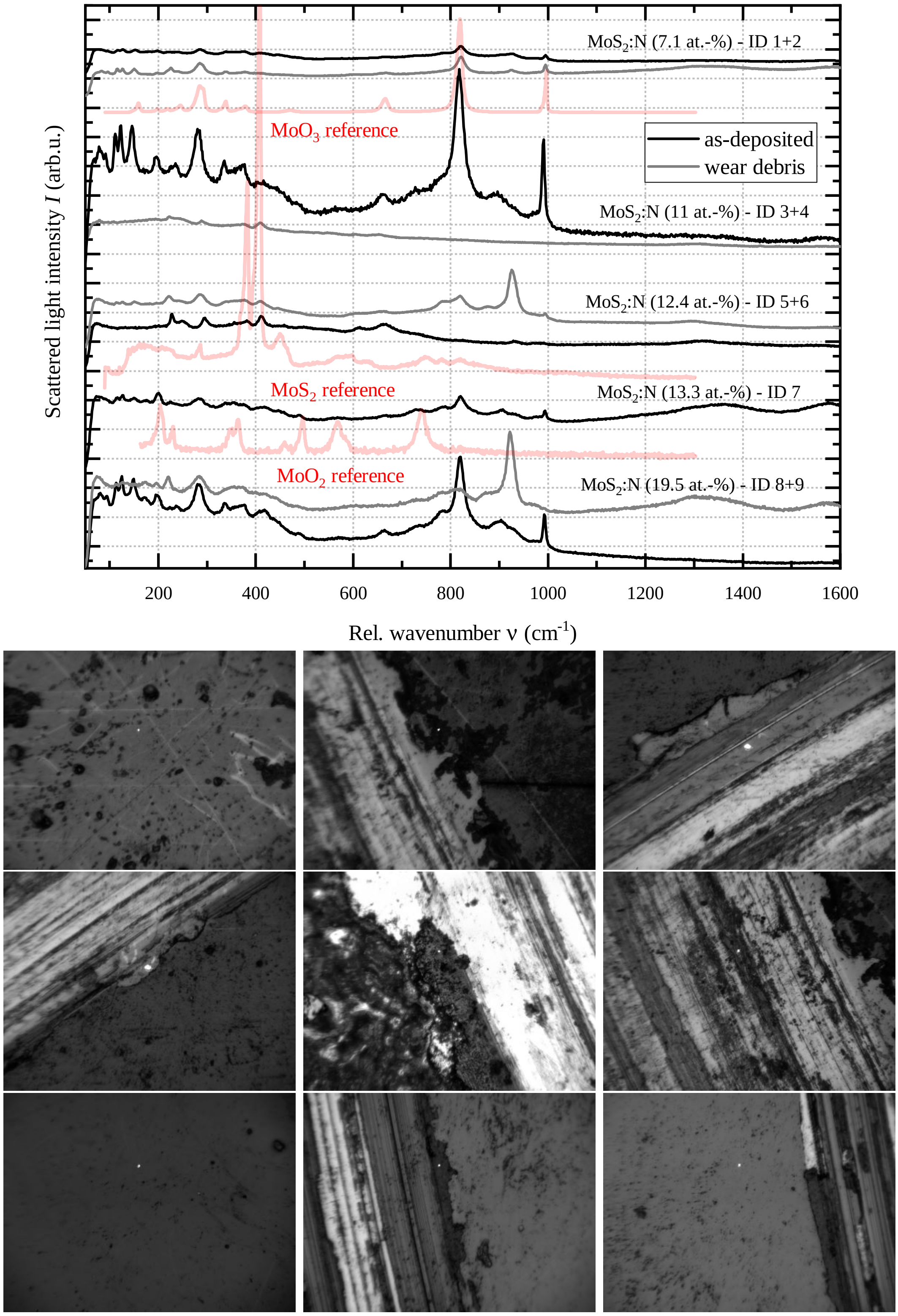

Figure S5: Raman spectra of rarely appearing oxides in nitrogen-modified MoS$_2$:N thin films with different nitrogen content **(above)**, microscope image of the sample surface for ID1-ID9 in reading direction **(below)**.

Appendix B: Python code for automated spectra fitting

This python script works with (and requires) the libraries *numpy* for data processing, *matplotlib* for plotting, *uncertainties* for automated error propagation, *lmfit* for standard fitting routines and -modeling, and *os* for file handling. The model fitting details are found in the documentation online, see `https://lmfit.github.io/lmfit-py/builtin_models.html`.

```
import numpy as np
import matplotlib.pyplot as plt
from uncertainties import ufloat
from lmfit.models import VoigtModel,PseudoVoigtModel,GaussianModel,LinearModel
import os
```

(1) The background fitting has a strongly detuned initial value for slope as 0.5:

```
background_model = LinearModel(prefix='bg_')
pars = background_model.make_params(intercept=50000)
pars['bg_slope'].set(value=0.5)
```

(2a) The peak modelling starts with a Pseudo-Voigt peak with width σ of $150\,\mathrm{cm}^{-1}$ at Raman shift ν of $1375\,\mathrm{cm}^{-1}$ for the D-Raman peak and another with width σ of $50\,\mathrm{cm}^{-1}$ at Raman shift ν of $1600\,\mathrm{cm}^{-1}$ for the G-Raman peak; optional value boundaries ensure fitting stability:

```
pv1_model = PseudoVoigtModel(prefix='pv1_')
pars.update(pv1_model.make_params())
pars['pv1_sigma'].set(value=150, min=10)
pars['pv1_center'].set(value=1375, min=1200, max=1450)
pars['pv1_amplitude'].set(value=1e7, min=10)

pv2_model = PseudoVoigtModel(prefix='pv2_')
pars.update(pv2_model.make_params())
pars['pv2_sigma'].set(value=50, min=10)
pars['pv2_center'].set(value=1600, min=1400, max=1800)
pars['pv2_amplitude'].set(value=1e8, min=10)

peak_model = pv1_model + pv2_model
```

(2b) For second-order Raman peaks in carbons, the peak modelling captures four Pseudo-Voigt peaks in the range 2470 cm^{-1} to 3250 cm^{-1} for the D+D”, 2D, D+D’, 2D’ Raman modes at Raman shift ν of roughly 2470 cm^{-1}, 2680 cm^{-1}, 2940 cm^{-1}, and 3150 cm^{-1}:

```
# for the D+D'' Raman peak at 2470icm
pv1_model = PseudoVoigtModel(prefix='pv1_')
pars.update(pv1_model.make_params())
pars['pv1_sigma'].set(value=40, min=20, max=80)
pars['pv1_center'].set(value=2507, min=2350, max=2520)
pars['pv1_amplitude'].set(value=250, min=10)

# for the 2D Raman peak at (2670-2690)icm
pv2_model = PseudoVoigtModel(prefix='pv2_')
pars.update(pv2_model.make_params())
pars['pv2_sigma'].set(value=50, min=0)
pars['pv2_center'].set(value=2680, min=2650, max=2800)
pars['pv2_amplitude'].set(value=10000, min=10)

# for the D+D' Raman peak at (2930-2950)icm
pv3_model = PseudoVoigtModel(prefix='pv3_')
pars.update(pv3_model.make_params())
pars['pv3_sigma'].set(value=50, min=0, max =150)
pars['pv3_center'].set(value=2900, min=2800, max=3100)
pars['pv3_amplitude'].set(value=8000,)

# for the 2D' Raman peak at (3100-3250)icm
pv4_model = PseudoVoigtModel(prefix='pv4_')
pars.update(pv4_model.make_params())
pars['pv4_sigma'].set(value=50, min=20)
pars['pv4_center'].set(value=3170, min=3100, max=3300)
pars['pv4_amplitude'].set(value=2500, min=10)

peak_model = pv1_model + pv2_model + pv3_model + pv4_model
```

(3) Fitting execution and value parsing finally:

```
model = background_model + peak_model
init = model.eval(pars, x=dataX_truncated)
out = model.fit(dataY_truncated, pars, x=dataX_truncated)
print(out.fit_report(min_correl=0.5))
for names, params in out.params.items():
    print(names)
    print(ufloat(params.value, params.stderr))
```

Bibliography

[1] H. A. Harris. “Lubrication in Antiquity.” In: *Greece & Rome* 21.1 (1974), pp. 32–36. ISSN: 0017-3835. DOI: `10.1017/S0017383500021665`.

[2] K. J. Anderson. “A History of Lubricants.” In: *MRS Bulletin* 16.10 (Oct. 1991), pp. 69–69. ISSN: 0883-7694, 1938-1425. DOI: `10.1557/S0883769400055895`.

[3] *Encyclopedia of Lubricants and Lubrication*. Berlin, Heidelberg: Springer Berlin Heidelberg, 2014. ISBN: 978-3-642-22646-5. DOI: `10.1007/978-3-642-22647-2`.

[4] I. M. Hutchings. “Leonardo da Vinci’s studies of friction.” In: *Wear* 360–361 (Aug. 2016), pp. 51–66. ISSN: 0043-1648. DOI: `10.1016/j.wear.2016.04.019`.

[5] H. Hertz. “Ueber die Berührung fester elastischer Körper.” In: *Journal für die reine und angewandte Mathematik* 1882.92 (Jan. 1882), pp. 156–171. ISSN: 1435-5345. DOI: `10.1515/crll.1882.92.156`.

[6] K. L. Johnson, K. Kendall, A. D. Roberts, and D. Tabor. “Surface energy and the contact of elastic solids.” In: *Proceedings of the Royal Society of London. A. Mathematical and Physical Sciences* 324.1558 (Jan. 1997), pp. 301–313. DOI: `10.1098/rspa.1971.0141`.

[7] B. V. Derjaguin, V. M. Muller, and Y. P. Toporov. “Effect of contact deformations on the adhesion of particles.” In: *Journal of Colloid and Interface Science* 53.2 (Nov. 1975), pp. 314–326. ISSN: 0021-9797. DOI: `10.1016/0021-9797(75)90018-1`.

[8] J. A. Greenwood and J. B. P. Williamson. “Contact of Nominally Flat Surfaces.” In: *Proceedings of the Royal Society of London. Series A, Mathematical and Physical Sciences* 295.1442 (1966), pp. 300–319. ISSN: 0080-4630.

[9] J. A. Greenwood, J. B. P. Williamson, and F. P. Bowden. “Contact of nominally flat surfaces.” In: *Proceedings of the Royal Society of London. Series A. Mathematical and Physical Sciences* 295.1442 (Jan. 1997), pp. 300–319. DOI: `10.1098/rspa.1966.0242`.

[10] J. C. Chaston. “Wear resistance of gold alloys for coinage.” In: *Gold Bulletin* 7.4 (Dec. 1974), pp. 108–112. ISSN: 2190-7579. DOI: `10.1007/BF03215051`.

[11] J. F. Archard. “Contact and Rubbing of Flat Surfaces.” In: *Journal of Applied Physics* 24.8 (Aug. 1953), pp. 981–988. ISSN: 0021-8979, 1089-7550. DOI: `10.1063/1.1721448`.

[12] K. T. Reye. “Zur Theorie der Zapfenreibung.” In: *Der Civilingenieur: Zeitschrift für das Ingenieurwesen. 6.* (1860), pp. 235–255.

[13] M. Urbakh, J. Klafter, D. Gourdon, and J. Israelachvili. “The nonlinear nature of friction.” In: *Nature* 430.6999 (July 2004), pp. 525–528. ISSN: 0028-0836, 1476-4687. DOI: `10.1038/nature02750`.

[14] C. Donnet. “Recent progress on the tribology of doped diamond-like and carbon alloy coatings: a review.” In: *Surface and Coatings Technology* 100–101 (1998), pp. 180–186. ISSN: 02578972. DOI: `10.1016/S0257-8972(97)00611-7`.

[15] B. Kohlhauser, M. Ripoll, H. Riedl, C. Koller, N. Koutna, A. Amsüss, H. Hutter, G. Ramirez, C. Gachot, A. Erdemir, and P. Mayrhofer. “How to get noWear? – A new take on the design of in-situ formed high performing low-friction tribofilms.” In: *Materials & Design* 190 (May 2020), p. 108519. ISSN: 02641275. DOI: `10.1016/j.matdes.2020.108519`.

[16] A. V. Kolobov and J. Tominaga. *Two-Dimensional Transition-Metal Dichalcogenides*. Vol. 239. Springer Series in Materials Science. Cham: Springer International Publishing, 2016. ISBN: 978-3-319-31449-5. DOI: `10.1007/978-3-319-31450-1`.

[17] L. Yan, W. Yue, C. Wang, D. Wei, and B. Xu. “Comparing tribological behaviors of sulfur- and phosphorus-free organomolybdenum additive with ZDDP and MoDTC.” In: *Tribology International* 53 (Sept. 2012), pp. 150–158. ISSN: 0301679X. DOI: `10.1016/j.triboint.2012.04.002`.

[18] D. N. Khaemba, A. Neville, and A. Morina. “A methodology for Raman characterisation of MoDTC tribofilms and its application in investigating the influence of surface chemistry on friction performance of MoDTC lubricants.” In: *Tribology Letters* 59.3 (Sept. 2015), p. 38. ISSN: 1023-8883, 1573-2711. DOI: `10.1007/s11249-015-0566-6`.

[19] D. N. Khaemba, A. Neville, and A. Morina. “New insights on the decomposition mechanism of Molybdenum DialkyldiThioCarbamate (MoDTC): a Raman spectroscopic study.” In: *RSC Advances* 6.45 (Apr. 2016), pp. 38637–38646. ISSN: 2046-2069. DOI: `10.1039/C6RA00652C`.

[20] A. Orlando, F. Franceschini, C. Muscas, S. Pidkova, M. Bartoli, M. Rovere, and A. Tagliaferro. “A Comprehensive Review on Raman Spectroscopy Applications.” In: *Chemosensors* 9.9 (2021), p. 262. ISSN: 2227-9040. DOI: `10.3390/chemosensors9090262`.

[21] J. Xu, Q. He, Z. Xiong, Y. Yu, S. Zhang, X. Hu, L. Jiang, S. Su, S. Hu, Y. Wang, and J. Xiang. “Raman Spectroscopy as a Versatile Tool for Investigating Thermochemical Processing of Coal, Biomass, and Wastes: Recent Advances and Future Perspectives.” In: *Energy & Fuels* 35.4 (Feb. 2021), pp. 2870–2913. ISSN: 0887-0624, 1520-5029. DOI: `10.1021/acs.energyfuels.0c03298`.

[22] J. Tu, J. Wang, S. Li, W.-L. Song, M. Wang, H. Zhu, and S. Jiao. “High-efficiency transformation of amorphous carbon into graphite nanoflakes for stable aluminum-ion battery cathodes.” In: *Nanoscale* 11.26 (2019), pp. 12537–12546. DOI: `10.1039/C9NR03112J`.

[23] H. Okubo, C. Tadokoro, Y. Hirata, and S. Sasaki. “In Situ Raman Observation of the Graphitization Process of Tetrahedral Amorphous Carbon Diamond-Like Carbon under Boundary Lubrication in Poly-Alpha-Olefin with an Organic Friction Modifier.” In: *Tribology Online* 12.5 (2017), pp. 229–237. DOI: `10.2474/trol.12.229`.

[24] J. Robertson. “Amorphous carbon.” In: *Advances in Physics* 35.4 (1986), pp. 317–374. ISSN: 0001-8732, 1460-6976. DOI: `10.1080/00018738600101911`.

[25] H. Akasaka, S. Kawaguchi, S. Ohshio, and H. Saitoh. “Estimation of Thermal Decomposition on Amorphous Carbon Films.” In: *Transactions of the Materials Research Society of Japan* 36.3 (2011), pp. 505–508. ISSN: 1382-3469, 2188-1650. DOI: `10.14723/tmrsj.36.505`.

[26] M. Rouhani, J. Hobley, F. Chau-Nan Hong, and Y.-R. Jeng. “In-situ thermal stability analysis of amorphous Si-doped carbon films.” In: *Carbon* 184 (Oct. 2021), pp. 772–785. ISSN: 00086223. DOI: `10.1016/j.carbon.2021.08.075`.

[27] D. B. Schuepfer, F. Badaczewski, J. M. Guerra-Castro, D. M. Hofmann, C. Heiliger, B. Smarsly, and P. J. Klar. “Assessing the structural properties of graphitic and non-graphitic carbons by Raman spectroscopy.” In: *Carbon* 161 (May 1, 2020), pp. 359–372. ISSN: 0008-6223. DOI: `10.1016/j.carbon.2019.12.094`.

[28] D. B. Schüpfer, F. Badaczewski, J. Peilstöcker, J. M. Guerra-Castro, H. Shim, S. Firoozabadi, A. Beyer, K. Volz, V. Presser, C. Heiliger, B. Smarsly, and P. J. Klar. “Monitoring the thermally induced transition from sp^3-hybridized into sp^2-hybridized carbons.” In: *Carbon* 172 (Feb. 1, 2021), pp. 214–227. ISSN: 0008-6223. DOI: `10.1016/j.carbon.2020.09.063`.

[29] S. S. Perry and W. T. Tysoe. “Frontiers of fundamental tribological research.” In: *Tribology Letters* 19.3 (July 2005), pp. 151–161. ISSN: 1023-8883, 1573-2711. DOI: `10.1007/s11249-005-6142-8`.

[30] W. G. Sawyer and K. J. Wahl. “Accessing Inaccessible Interfaces: In Situ Approaches to Materials Tribology.” In: *MRS Bulletin* 33.12 (Dec. 2008), pp. 1145–1150. ISSN: 0883-7694, 1938-1425. DOI: `10.1557/mrs2008.244`.

[31] D. Lyubimov, K. Dolgopolov, and L. Pinchuk. *Micromechanisms of Friction and Wear: Introduction to Relativistic Tribology.* Vol. 176. Springer Series in Materials Science. Berlin, Heidelberg: Springer Berlin Heidelberg, 2013. ISBN: 978-3-642-35147-1. DOI: `10.1007/978-3-642-35148-8`.

[32] C. Kittel. *Einführung in die Festkörperphysik.* 15th ed. Munich: Oldenbourg Verlag, 2013. ISBN: 978-3-486-59755-4.

[33] G. Czycholl. *Theoretische Festkörperphysik Band 1.* 4th ed. Springer Spektrum, 2016. ISBN: 978-3-662-47140-1.

[34] F. J. Owens and C. P. Poole Jr. *The Physics and Chemistry of Nanosolids.* Wiley, 2008. ISBN: 978-0-470-06740-6.

[35] M. Roy. “Nanocrystalline and Disordered Carbon Materials.” In: *Functional Materials.* Elsevier, 2012, pp. 675–706. ISBN: 978-0-12-385142-0. DOI: `10.1016/B978-0-12-385142-0.00017-9`.

[36] E. Fitzer, K.-H. Kochling, H. P. Boehm, and H. Marsh. “Recommended terminology for the description of carbon as a solid (IUPAC Recommendations 1995).” In: *Pure and Applied Chemistry* 67.3 (1995), pp. 473–506. ISSN: 1365-3075. DOI: `10.1351/pac199567030473`.

[37] *MoS_2: Materials, Physics, and Devices.* Vol. 21. Lecture Notes in Nanoscale Science and Technology. Cham: Springer International Publishing, 2014. ISBN: 978-3-319-02849-1. DOI: `10.1007/978-3-319-02850-7`.

[38] E. Riedel and C. Janiak. “Anorganische Chemie.” In: *Anorganische Chemie*. De Gruyter, Feb. 2011. ISBN: 978-3-11-022567-9. DOI: `10.1515/9783110225679`.

[39] G. Gouadec and P. Colomban. “Raman Spectroscopy of nanomaterials: How spectra relate to disorder, particle size and mechanical properties.” In: *Progress in Crystal Growth and Characterization of Materials* 53.1 (2007), pp. 1–56. ISSN: 09608974. DOI: `10.1016/j.pcrysgrow.2007.01.001`.

[40] O. Durand-Drouhin and M. Benlahsen. “Internal stress of sputtered amorphous carbon nitride thin films.” In: *Solid State Communications* 131.7 (2004), pp. 425–429. ISSN: 0038-1098. DOI: `10.1016/j.ssc.2004.06.013`.

[41] G. Galli, R. M. Martin, R. Car, and M. Parrinello. “Carbon: The nature of the liquid state.” In: *Physical Review Letters* 63.9 (1989), pp. 988–991. ISSN: 0031-9007. DOI: `10.1103/PhysRevLett.63.988`.

[42] B. Schultrich. *Tetrahedrally Bonded Amorphous Carbon Films I*. Vol. 263. Springer Series in Materials Science. Berlin, Heidelberg: Springer Berlin Heidelberg, 2018. ISBN: 978-3-662-55925-3. DOI: `10.1007/978-3-662-55927-7`.

[43] L. Zhang, X. Wei, Y. Lin, and F. Wang. “A ternary phase diagram for amorphous carbon.” In: *Carbon* 94 (2015), pp. 202–213. ISSN: 0008-6223. DOI: `10.1016/j.carbon.2015.06.055`.

[44] Z. Zeng, L. Yang, Q. Zeng, H. Lou, H. Sheng, J. Wen, D. J. Miller, Y. Meng, W. Yang, W. L. Mao, and H.-k. Mao. “Synthesis of quenchable amorphous diamond.” In: *Nature Communications* 8.1 (2017), p. 322. ISSN: 2041-1723. DOI: `10.1038/s41467-017-00395-w`.

[45] R. E. Franklin and J. T. Randall. “Crystallite growth in graphitizing and non-graphitizing carbons.” In: *Proceedings of the Royal Society of London. Series A. Mathematical and Physical Sciences* 209.1097 (Oct. 1951), pp. 196–218. DOI: `10.1098/rspa.1951.0197`.

[46] A. Erdemir and C. Donnet. “Tribology of diamond-like carbon films: recent progress and future prospects.” In: *J. Phys. D: Appl. Phys* 39 (2006), pp. 311–327. DOI: `10.1088/0022-3727/39/18/R01`.

[47] J. Robertson. “Diamond-like amorphous carbon.” In: *Materials Science and Engineering: R: Reports* 37.4–6 (May 2002), pp. 129–281. ISSN: 0927796X. DOI: `10.1016/S0927-796X(02)00005-0`.

[48] L. Liu, F. Lu, J. Tian, S. Xia, and Y. Diao. “Electronic and optical properties of amorphous carbon with different sp^3/sp^2 hybridization ratio.” In: *Applied Physics A* 125.5 (May 2019), p. 366. ISSN: 0947-8396, 1432-0630. DOI: `10.1007/s00339-019-2660-3`.

[49] C. Casiraghi, A. Ferrari, and J. Robertson. “Raman spectroscopy of hydrogenated amorphous carbons.” In: *Physical Review B* 72.8 (2005), p. 085401. ISSN: 1098-0121, 1550-235X. DOI: `10.1103/PhysRevB.72.085401`.

[50] X.-W. Li, M.-W. Joe, A.-Y. Wang, and K.-R. Lee. "Stress reduction of diamond-like carbon by Si incorporation: A molecular dynamics study." In: *Surface and Coatings Technology* 228 (2013), S190–S193. ISSN: 02578972. DOI: `10.1016/j.surfcoat.2012.06.031`.

[51] G. Galli, R. M. Martin, R. Car, and M. Parrinello. "Structural and Electronic Properties of Amorphous Carbon." In: *Physical Review Letters* 62.5 (Jan. 1989), pp. 555–558. ISSN: 0031-9007. DOI: `10.1103/PhysRevLett.62.555`.

[52] A. C. Ferrari and J. Robertson. "Raman spectroscopy of amorphous, nanostructured, diamond–like carbon, and nanodiamond." In: *Philosophical Transactions of the Royal Society of London. Series A: Mathematical, Physical and Engineering Sciences* 362.1824 (Nov. 2004). Ed. by A. C. Ferrari and J. Robertson, pp. 2477–2512. ISSN: 1364-503X, 1471-2962. DOI: `10.1098/rsta.2004.1452`.

[53] W. Jacob and W. Möller. "On the structure of thin hydrocarbon films." In: *Applied Physics Letters* 63.13 (1993), pp. 1771–1773. ISSN: 0003-6951, 1077-3118. DOI: `10.1063/1.110683`.

[54] J. Robertson. "Classification of Diamond-like Carbons." In: *Tribology of Diamond-Like Carbon Films: Fundamentals and Applications*. Ed. by C. Donnet and A. Erdemir. Boston, MA: Springer US, 2008, pp. 13–24. ISBN: 978-0-387-49891-1. DOI: `10.1007/978-0-387-49891-1_1`.

[55] C. Casiraghi, F. Piazza, A. C. Ferrari, D. Grambole, and J. Robertson. "Bonding in hydrogenated diamond-like carbon by Raman spectroscopy." In: *Diamond and Related Materials* 14.3–7 (2005), pp. 1098–1102. ISSN: 09259635. DOI: `10.1016/j.diamond.2004.10.030`.

[56] M. Ramsteiner and J. Wagner. "Resonant Raman scattering of hydrogenated amorphous carbon: Evidence for π-bonded carbon clusters." In: *Applied Physics Letters* 51.17 (1987), pp. 1355–1357. ISSN: 0003-6951. DOI: `10.1063/1.98677`.

[57] A. Magnéli. "The Crystal Structure of Mo_4O_{11} (gamma-Molybdenum Oxide)." In: *Acta Chemica Scandinavica* 2 (1948).

[58] R. F. Sebenik, A. R. Burkin, R. R. Dorfler, J. M. Laferty, G. Leichtfried, H. Meyer-Grünow, P. C. H. Mitchell, M. S. Vukasovich, D. A. Church, G. G. Van Riper, J. C. Gilliland, and S. A. Thielke. "Molybdenum and Molybdenum Compounds." In: *Ullmann's Encyclopedia of Industrial Chemistry*. John Wiley & Sons, Ltd, 2000. ISBN: 978-3-527-30673-2. DOI: `10.1002/14356007.a16_655`.

[59] L. M. S. Alves, F. S. Oliveira, B. S. de Lima, M. S. da Luz, A. Rebello, S. H. Masunaga, J. J. Neumeier, C. Giles, J. B. Leão, and C. A. M. dos Santos. "Evidence of phase transitions in MoO_2 single crystals." In: *Journal of Alloys and Compounds* 705 (May 2017), pp. 764–768. ISSN: 0925-8388. DOI: `10.1016/j.jallcom.2017.02.148`.

[60] M. Camacho-López, L. Escobar-Alarcón, M. Picquart, R. Arroyo, G. Córdoba, and E. Haro-Poniatowski. "Micro-Raman study of the m-MoO_2 to -MoO_3 transformation induced by cw-laser irradiation." In: *Optical Materials* 33.3 (2011), pp. 480–484. ISSN: 09253467. DOI: `10.1016/j.optmat.2010.10.028`.

[61] S. Kumbhar, G. Pizzi, T. Sohier, and H. Miranda. *Interactive phonon visualizer.* accessed: 15-09-2023. 2018. URL: `https://interactivephonon.materialscloud.io/`.

[62] *Creative Common Attribution License, CC BY 4.0.* accessed: 15-09-2023. Creative Commons Corporation, 2020. URL: `https://creativecommons.org/licenses/by/4.0/`.

[63] H. Moldenhauer, A. Wittig, D. Kokalj, D. Stangier, A. Brümmer, W. Tillmann, and J. Debus. "Resonant Raman scattering characterization of thermally annealed HiPIMS deposited MoS_x coatings." In: *Surface and Coatings Technology* 377 (2019), p. 124891. ISSN: 0257-8972. DOI: `10.1016/j.surfcoat.2019.124891`.

[64] M. S. Ullah, A. H. B. Yousuf, A. D. Es-Sakhi, and M. H. Chowdhury. "Analysis of optical and electronic properties of MoS_2 for optoelectronics and FET applications." In: *AIP Conference Proceedings* 1957.1 (Apr. 2018), p. 020001. ISSN: 0094-243X. DOI: `10.1063/1.5034320`.

[65] W. Tillmann, A. Wittig, N. F. L. Dias, D. Stangier, C. A. Thomann, H. Moldenhauer, and J. Debus. "Silicon- and tungsten-containing hydrogen-free and hydrogenated amorphous carbon films for friction-reducing applications." In: *Diamond and Related Materials* 123 (Mar. 2022), p. 108866. ISSN: 0925-9635. DOI: `10.1016/j.diamond.2022.108866`.

[66] *Broadband Dielectric Spectroscopy.* Berlin, Heidelberg: Springer Berlin Heidelberg, 2003. ISBN: 978-3-642-62809-2. DOI: `10.1007/978-3-642-56120-7`.

[67] A. Smekal. "Zur Quantentheorie der Dispersion." In: *Naturwissenschaften* 11.43 (1923), pp. 873–875. ISSN: 1432-1904. DOI: `10.1007/BF01576902`.

[68] C. V. Raman and K. S. Krishnan. "A New Type of Secondary Radiation." In: *Nature* 121 (1928), pp. 501–502.

[69] P. Vandenabeele. *Practical Raman spectroscopy: an introduction.* The Atrium, Southern Gate, Chichester, West Sussex, United Kingdom: Wiley, 2013. ISBN: 978-0-470-68319-4.

[70] *Confocal Raman Microscopy.* Vol. 66. Springer Series in Surface Sciences. Cham: Springer International Publishing, 2018. ISBN: 978-3-319-75378-2. DOI: `10.1007/978-3-319-75380-5`.

[71] G. Landsberg. "Molekulare Lichtzerstreuung in festen Körpern. I." In: *Zeitschrift für Physik* 43 (1927), pages 773–778.

[72] G. Landsberg and L. Mandelstam. "Eine neue Erscheinung bei der Lichtzerstreuung in Krystallen." In: *Naturwissenschaften* 16 (1928), pp. 557–558.

[73] S. Reich and C. Thomsen. "Raman spectroscopy of graphite." In: *Philosophical Transactions of the Royal Society of London. Series A: Mathematical, Physical and Engineering Sciences* 362.1824 (Nov. 2004). Ed. by A. Ferrari and J. Robertson, pp. 2271–2288. ISSN: 1364-503X, 1471-2962. DOI: `10.1098/rsta.2004.1454`.

[74] K.-i. Sasaki, Y. Tokura, and T. Sogawa. "The Origin of Raman D Band: Bonding and Antibonding Orbitals in Graphene." In: *Crystals* 3.1 (Feb. 2013), pp. 120–140. ISSN: 2073-4352. DOI: `10.3390/cryst3010120`.

[75] D. A. Long. "Early history of the Raman effect." In: *International Reviews in Physical Chemistry* 7.4 (1988), pp. 317–349. ISSN: 0144-235X, 1366-591X. DOI: `10.1080/01442358809353216`.

[76] M. Cardona. "Resonance phenomena." In: *Light Scattering in Solids II: Basic Concepts and Instrumentation.* Ed. by M. Cardona and G. Güntherodt. Topics in Applied Physics. Berlin, Heidelberg: Springer, 1982, pp. 19–178. ISBN: 978-3-540-39075-6. DOI: `10.1007/3-540-11380-0_14`.

[77] R. J. Meier. "On art and science in curve-fitting vibrational spectra." In: *Vibrational Spectroscopy* 39.2 (2005), pp. 266–269. ISSN: 09242031. DOI: `10.1016/j.vibspec.2005.03.003`.

[78] A. Tagliaferro, M. Rovere, E. Padovano, M. Bartoli, and M. Giorcelli. "Introducing the Novel Mixed Gaussian-Lorentzian Lineshape in the Analysis of the Raman Signal of Biochar." In: *Nanomaterials* 10.9 (2020), p. 1748. ISSN: 2079-4991. DOI: `10.3390/nano10091748`.

[79] T. Jawhari, P. J. Hendra, H. A. Willis, and M. Judkins. "Quantitative analysis using Raman methods." In: *Spectrochimica Acta Part A: Molecular Spectroscopy.* Applications of Fourier Transform Raman Spectroscopy 46.2 (1990), pp. 161–170. ISSN: 0584-8539. DOI: `10.1016/0584-8539(90)80086-E`.

[80] R. P. Vidano, D. B. Fischbach, L. J. Willis, and T. M. Loehr. "Observation of Raman band shifting with excitation wavelength for carbons and graphites." In: *Solid State Communications* 39.2 (July 1981), pp. 341–344. ISSN: 0038-1098. DOI: `10.1016/0038-1098(81)90686-4`.

[81] G. Adamopoulos, J. Robertson, N. A. Morrison, and C. Godet. "Hydrogen content estimation of hydrogenated amorphous carbon by visible Raman spectroscopy." In: *Journal of Applied Physics* 96.11 (Dec. 2004), pp. 6348–6352. ISSN: 0021-8979. DOI: `10.1063/1.1811397`.

[82] D. Tuschel. "Why Are the Raman Spectra of Crystalline and Amorphous Solids Different?" In: *Spectroscopy.* Spectroscopy-03-01-2017 32.3 (Mar. 2017), pp. 26–33.

[83] V. K. Malinovsky and A. P. Sokolov. "The nature of boson peak in Raman scattering in glasses." In: *Solid State Communications* 57.9 (Mar. 1986), pp. 757–761. ISSN: 0038-1098. DOI: `10.1016/0038-1098(86)90854-9`.

[84] M. Ivanda, I. Hartmann, F. Duschek, and W. Kiefer. "Raman Study of "Boson Peak" in Amorphous Silicon: Dependence on Hydrogen and Carbon Content." In: *Materials Science Forum* 173–174 (Sept. 1994), pp. 243–248. ISSN: 1662-9752. DOI: `10.4028/www.scientific.net/MSF.173-174.243`.

[85] F. Finkemeier and W. von Niessen. "Boson peak in amorphous silicon: A numerical study." In: *Physical Review B* 63.23 (May 2001), p. 235204. ISSN: 0163-1829, 1095-3795. DOI: `10.1103/PhysRevB.63.235204`.

[86] J. Schroeder, W. Wu, J. L. Apkarian, M. Lee, L.-G. Hwa, and C. T. Moynihan. "Raman scattering and Boson peaks in glasses: temperature and pressure effects." In: *Journal of Non-Crystalline Solids* 349 (Dec. 2004), pp. 88–97. ISSN: 00223093. DOI: `10.1016/j.jnoncrysol.2004.08.265`.

[87] R. Zorn. “The boson peak demystified?” In: *Physics* 4 (May 2011), p. 44. ISSN: 1943-2879. DOI: `10.1103/Physics.4.44`.

[88] C. V. Raman. “The vibration spectrum of a crystal lattice.” In: *Proceedings of the Indian Academy of Sciences - Section A* 18.5 (Nov. 1943), pp. 237–250. ISSN: 0370-0089. DOI: `10.1007/BF03046531`.

[89] R. S. Krishnan. “Raman Spectrum of Diamond.” In: *Nature* 155.39283928 (Feb. 1945), pp. 171–171. ISSN: 1476-4687. DOI: `10.1038/155171a0`.

[90] R. S. Krishnan. “Temperature variations of the Raman frequencies in diamond.” In: *Proceedings of the Indian Academy of Sciences - Section A* 24.1 (July 1946), p. 45. ISSN: 0370-0089. DOI: `10.1007/BF03170739`.

[91] F. Tuinstra and J. L. Koenig. “Raman Spectrum of Graphite.” In: *The Journal of Chemical Physics* 53.3 (Aug. 1970), pp. 1126–1130. ISSN: 0021-9606, 1089-7690. DOI: `10.1063/1.1674108`.

[92] A. Tagliaferro, M. Rovere, E. Padovano, M. Bartoli, and M. Giorcelli. “Introducing the Novel Mixed Gaussian-Lorentzian Lineshape in the Analysis of the Raman Signal of Biochar.” In: *Nanomaterials* 10.9 (2020), p. 1748. ISSN: 2079-4991. DOI: `10.3390/nano10091748`.

[93] M. S. Dresselhaus and G. Dresselhaus. “Intercalation compounds of graphite.” In: *Advances in Physics* 30.2 (Apr. 1981), pp. 139–326. ISSN: 0001-8732, 1460-6976. DOI: `10.1080/00018738100101367`.

[94] P. Lespade, A. Marchand, M. Couzi, and F. Cruege. “Caracterisation de materiaux carbones par microspectrometrie Raman.” In: *Carbon* 22.4 (Jan. 1984), pp. 375–385. ISSN: 0008-6223. DOI: `10.1016/0008-6223(84)90009-5`.

[95] M. A. Tamor and W. C. Vassell. “Raman ‘fingerprinting’ of amorphous carbon films.” In: *Journal of Applied Physics* 76.6 (Sept. 1994), pp. 3823–3830. ISSN: 0021-8979, 1089-7550. DOI: `10.1063/1.357385`.

[96] J. Schwan, S. Ulrich, V. Batori, H. Ehrhardt, and S. R. P. Silva. “Raman spectroscopy on amorphous carbon films.” In: *Journal of Applied Physics* 80.1 (1996), pp. 440–447. ISSN: 0021-8979, 1089-7550. DOI: `10.1063/1.362745`.

[97] A. C. Ferrari and J. Robertson. “Resonant Raman spectroscopy of disordered, amorphous, and diamondlike carbon.” In: *Physical Review B* 64.7 (July 2001), p. 075414. ISSN: 0163-1829, 1095-3795. DOI: `10.1103/PhysRevB.64.075414`.

[98] X. X. Yang, J. W. Li, Z. F. Zhou, Y. Wang, L. W. Yang, W. T. Zheng, and C. Q. Sun. “Raman spectroscopic determination of the length, strength, compressibility, Debye temperature, elasticity, and force constant of the C–C bond in graphene.” In: *Nanoscale* 4.2 (2012), pp. 502–510. ISSN: 2040-3364, 2040-3372. DOI: `10.1039/C1NR11280E`.

[99] M. Couzi, J.-L. Bruneel, D. Talaga, and L. Bokobza. “A multi wavelength Raman scattering study of defective graphitic carbon materials: The first order Raman spectra revisited.” In: *Carbon* 107 (Oct. 2016), pp. 388–394. ISSN: 0008-6223. DOI: `10.1016/j.carbon.2016.06.017`.

[100] A. Merlen, J. G. Buijnsters, and C. Pardanaud. “A Guide to and Review of the Use of Multiwavelength Raman Spectroscopy for Characterizing Defective Aromatic Carbon Solids: from Graphene to Amorphous Carbons.” In: *Coatings* 7.10 (2017). ISSN: 2079-6412. DOI: `10.3390/coatings7100153`.

[101] A. C. Ferrari and J. Robertson. “Interpretation of Raman spectra of disordered and amorphous carbon.” In: *Physical Review B* 61.20 (May 2000), pp. 14095–14107. ISSN: 0163-1829, 1095-3795. DOI: `10.1103/PhysRevB.61.14095`.

[102] W. Kohn. “Image of the Fermi Surface in the Vibration Spectrum of a Metal.” In: *Physical Review Letters* 2.9 (May 1959), pp. 393–394. DOI: `10.1103/PhysRevLett.2.393`.

[103] S. Piscanec, M. Lazzeri, F. Mauri, A. C. Ferrari, and J. Robertson. “Kohn Anomalies and Electron-Phonon Interactions in Graphite.” In: *Physical Review Letters* 93.18 (Oct. 2004), p. 185503. DOI: `10.1103/PhysRevLett.93.185503`.

[104] I. Milošević, N. Kepčija, E. Dobardžić, M. Damnjanović, M. Mohr, J. Maultzsch, and C. Thomsen. “Kohn anomaly in graphene.” In: *Materials Science and Engineering: B* 176.6 (Apr. 2011), pp. 510–511. ISSN: 09215107. DOI: `10.1016/j.mseb.2010.11.004`.

[105] A. C. Ferrari, A. Libassi, B. K. Tanner, V. Stolojan, J. Yuan, L. M. Brown, S. E. Rodil, B. Kleinsorge, and J. Robertson. “Density, sp^3 fraction, and cross-sectional structure of amorphous carbon films determined by x-ray reflectivity and electron energy-loss spectroscopy.” In: *Physical Review B* 62.16 (Oct. 2000), pp. 11089–11103. DOI: `10.1103/PhysRevB.62.11089`.

[106] W. Tillmann, N. F. Lopes Dias, D. Stangier, M. Bayer, H. Moldenhauer, J. Debus, M. Schmitz, U. Berges, and C. Westphal. “Interaction effects of cathode power, bias voltage, and mid-frequency on the structural and mechanical properties of sputtered amorphous carbon films.” In: *Applied Surface Science* 487 (Sept. 2019), pp. 857–867. ISSN: 01694332. DOI: `10.1016/j.apsusc.2019.05.131`.

[107] C. S. Casari, A. Li Bassi, A. Baserga, L. Ravagnan, P. Piseri, C. Lenardi, M. Tommasini, A. Milani, D. Fazzi, C. E. Bottani, and P. Milani. “Low-frequency modes in the Raman spectrum of $sp - sp^2$ nanostructured carbon.” In: *Physical Review B* 77.19 (May 2008), p. 195444. ISSN: 1098-0121, 1550-235X. DOI: `10.1103/PhysRevB.77.195444`.

[108] W. S. Bacsa, J. S. Lannin, D. L. Pappas, and J. J. Cuomo. “Raman scattering of laser-deposited amorphous carbon.” In: *Physical Review B* 47.16 (Apr. 1993), pp. 10931–10934. ISSN: 0163-1829, 1095-3795. DOI: `10.1103/PhysRevB.47.10931`.

[109] R. Faiman and K. Larsson. “Assignment of the C-H stretching vibrational frequencies in the Raman spectra of lipids.” In: *Journal of Raman Spectroscopy* 4.4 (1976), pp. 387–394. ISSN: 1097-4555. DOI: `10.1002/jrs.1250040406`.

[110] J. Šebek, R. Knaanie, B. Albee, E. O. Potma, and R. B. Gerber. “Spectroscopy of the C–H Stretching Vibrational Band in Selected Organic Molecules.” In: *The Journal of Physical Chemistry A* 117.32 (Aug. 2013), pp. 7442–7452. ISSN: 1089-5639. DOI: `10.1021/jp4014674`.

[111] Y. Liu and L. Ojamäe. “CH-Stretching Vibrational Trends in Natural Gas Hydrates Studied by Quantum-Chemical Computations.” In: *The Journal of Physical Chemistry C* 119.30 (July 2015), pp. 17084–17091. ISSN: 1932-7447. DOI: `10.1021/acs.jpcc.5b01903`.

[112] G. Fuseya, S. Takeya, and A. Hachikubo. “Temperature effects on the C–H symmetric stretching vibrational frequencies of guest hydrocarbon molecules in 5^{12}, $5^{12}6^{2}$ and $5^{12}6^{4}$ cages of sI and sII clathrate hydrates.” In: *RSC Advances* 10.61 (Oct. 2020), pp. 37582–37587. ISSN: 2046-2069. DOI: `10.1039/D0RA06668K`.

[113] N. Kuhar, S. Sil, and S. Umapathy. “Potential of Raman spectroscopic techniques to study proteins.” In: *Spectrochimica Acta Part A: Molecular and Biomolecular Spectroscopy* 258 (Sept. 2021), p. 119712. ISSN: 1386-1425. DOI: `10.1016/j.saa.2021.119712`.

[114] T. J. Wieting and J. L. Verble. “Infrared and Raman Studies of Long-Wavelength Optical Phonons in Hexagonal MoS_2.” In: *Physical Review B* 3.12 (June 1971), pp. 4286–4292. ISSN: 0556-2805. DOI: `10.1103/PhysRevB.3.4286`.

[115] A. Molina-Sánchez, K. Hummer, and L. Wirtz. “Vibrational and optical properties of MoS_2: From monolayer to bulk.” In: *Surface Science Reports* 70.4 (Dec. 2015), pp. 554–586. ISSN: 01675729. DOI: `10.1016/j.surfrep.2015.10.001`.

[116] J. M. Chen and C. S. Wang. “Second order Raman spectrum of MoS_2.” In: *Solid State Communications* 14.9 (May 1974), pp. 857–860. ISSN: 0038-1098. DOI: `10.1016/0038-1098(74)90150-1`.

[117] B. L. Evans, P. A. Young, and R. W. Ditchburn. “Optical absorption and dispersion in molybdenum disulphide.” In: *Proceedings of the Royal Society of London. Series A. Mathematical and Physical Sciences* 284.1398 (Mar. 1965), pp. 402–422. ISSN: 0080-4630, 2053-9169. DOI: `10.1098/rspa.1965.0071`.

[118] A. M. Stacy and D. T. Hodul. “Raman spectra of IVB and VIB transition metal disulfides using laser energies near the absorption edges.” In: *Journal of Physics and Chemistry of Solids* 46.4 (Jan. 1985), pp. 405–409. ISSN: 0022-3697. DOI: `10.1016/0022-3697(85)90103-9`.

[119] B. R. Carvalho, Y. Wang, S. Mignuzzi, D. Roy, M. Terrones, C. Fantini, V. H. Crespi, L. M. Malard, and M. A. Pimenta. “Intervalley scattering by acoustic phonons in two-dimensional MoS_2 revealed by double-resonance Raman spectroscopy.” In: *Nature Communications* 8.11 (Mar. 2017), p. 14670. ISSN: 2041-1723. DOI: `10.1038/ncomms14670`.

[120] *RRUFF database.* RRUFF project. URL: `https://rruff.info/`. last accessed: 27.08.2023.

[121] I. R. Beattie and T. R. Gilson. “Oxide phonon spectra.” In: *Journal of the Chemical Society A: Inorganic, Physical, Theoretical* 0 (Jan. 1969), pp. 2322–2327. ISSN: 0022-4944. DOI: `10.1039/J19690002322`.

[122] A. Moulahi. “Controlled Hydrothermal Synthesis of Nano-MoO_2 as Anode for Lithium Ion Battery.” In: *Indian Journal of Science and Technology* 13.3 (Jan. 2020), pp. 277–285. ISSN: 09746846, 09745645. DOI: `10.17485/ijst/2020/v13i03/149476`.

[123] P. A. Spevack and N. S. McIntyre. “Thermal reduction of molybdenum trioxide.” In: *The Journal of Physical Chemistry* 96.22 (Oct. 1992), pp. 9029–9035. ISSN: 0022-3654, 1541-5740. DOI: `10.1021/j100201a062`.

[124] L. Seguin, M. Figlarz, R. Cavagnat, and J.-C. Lassègues. “Infrared and Raman spectra of MoO_3 molybdenum trioxides and $MoO_3 \cdot xH_2O$ molybdenum trioxide hydrates.” In: *Spectrochimica Acta Part A: Molecular and Biomolecular Spectroscopy* 51.8 (July 1995), pp. 1323–1344. ISSN: 1386-1425. DOI: `10.1016/0584-8539(94)00247-9`.

[125] *Tribologie-Handbuch.* Wiesbaden: Springer Fachmedien Wiesbaden, 2015. ISBN: 978-3-8348-1810-2. DOI: `10.1007/978-3-8348-2236-9`.

[126] V. L. Popov. *Kontaktmechanik und Reibung.* Berlin, Heidelberg: Springer Berlin Heidelberg, 2009. ISBN: 978-3-540-88836-9. DOI: `10.1007/978-3-540-88837-6`.

[127] *Technische Universität Berlin - Friction Physics.* accessed: 15-09-2023. TU Berlin, 2013. URL: `https://www.youtube.com/@Friction_Physics`.

[128] *Modern tribology handbook.* Mechanics and materials science series. Boca Raton, FL: CRC Press, 2001. ISBN: 978-0-8493-8403-5.

[129] G. Pintaude. “Hardness as an indicator of material strength: a critical review.” In: *Critical Reviews in Solid State and Materials Sciences* 0.0 (June 2022), pp. 1–19. ISSN: 1040-8436. DOI: `10.1080/10408436.2022.2085659`.

[130] D. Kokalj, J. Debus, D. Stangier, H. Moldenhauer, A. Nikolov, A. Wittig, A. Brümmer, and W. Tillmann. “Controlling the Structural, Mechanical and Frictional Properties of MoS_x Coatings by High-Power Impulse Magnetron Sputtering.” In: *Coatings* 10.8 (Aug. 2020), p. 755. ISSN: 2079-6412. DOI: `10.3390/coatings10080755`.

[131] *Tribology for Scientists and Engineers: From Basics to Advanced Concepts.* New York, NY: Springer New York, 2013. ISBN: 978-1-4614-1944-0. DOI: `10.1007/978-1-4614-1945-7`.

[132] B. K. Yen. “Influence of water vapor and oxygen on the tribology of carbon materials with sp^2 valence configuration.” In: *Wear* 192.1–2 (Mar. 1996), pp. 208–215. ISSN: 00431648. DOI: `10.1016/0043-1648(95)06807-4`.

[133] K. Sommer, R. Heinz, and J. Schöfer. “Tribologische Grundlagen.” In: *Verschleiß metallischer Werkstoffe.* Wiesbaden: Springer Fachmedien Wiesbaden, 2014, pp. 3–34. ISBN: 978-3-8348-2463-9. DOI: `10.1007/978-3-8348-2464-6_2`.

[134] *Failure analysis - Fundamentals and performance of failure analysis.* Nov. 2011. URL: `https://www.vdi.de/richtlinien/details/vdi-3822-schadensanalyse-grundlagen-und-durchfuehrung-einer-schadensanalyse-1`. last accessed: 2023-09-14.

[135] I. L. Singer, S. D. Dvorak, K. J. Wahl, and T. W. Scharf. “Role of third bodies in friction and wear of protective coatings.” In: *Journal of Vacuum Science & Technology A* 21.5 (Sept. 2003), S232–S240. ISSN: 0734-2101. DOI: `10.1116/1.1599869`.

[136] I. L. Singer, S. Fayeulle, and P. D. Ehni. “Wear behavior of triode-sputtered MoS_2 coatings in dry sliding contact with steel and ceramics.” In: *Wear* 195.1 (July 1996), pp. 7–20. ISSN: 0043-1648. DOI: `10.1016/0043-1648(95)06661-6`.

[137] I. L. Singer, R. N. Bolster, J. Wegand, S. Fayeulle, and B. C. Stupp. “Hertzian stress contribution to low friction behavior of thin MoS_2 coatings.” In: *Applied Physics Letters* 57.10 (Sept. 1990), pp. 995–997. ISSN: 0003-6951. DOI: `10.1063/1.104276`.

[138] W. Tillmann, A. Wittig, D. Stangier, C.-A. Thomann, H. Moldenhauer, J. Debus, D. Aurich, and A. Brümmer. “Investigation of the Tribofilm Formation of HiPIMS Sputtered MoS_x Thin Films in Different Environments by Raman Scattering.” In: *Lubricants* 7.11 (2019), p. 100. ISSN: 2075-4442. DOI: `10.3390/lubricants7110100`.

[139] Z. Cao, S.-q. Wang, K.-z. Huang, B. Zhang, G.-h. Wen, Q.-y. Zhang, and L. Wang. “Effect of artificial tribological layer on sliding wear behavior of H13 steel.” In: *Journal of Iron and Steel Research International* 24.9 (Sept. 2017), pp. 943–949. ISSN: 1006-706X, 2210-3988. DOI: `10.1016/S1006-706X(17)30137-1`.

[140] T. W. Scharf and S. V. Prasad. “Solid lubricants: a review.” In: *Journal of Materials Science* 48.2 (Jan. 2013), pp. 511–531. ISSN: 0022-2461, 1573-4803. DOI: `10.1007/s10853-012-7038-2`.

[141] J. Robertson. “The deposition mechanism of diamond-like a-C and a-C: H.” In: *Diamond and Related Materials* 3.4–6 (1994), pp. 361–368. ISSN: 09259635. DOI: `10.1016/0925-9635(94)90186-4`.

[142] J. C. Angus. “Empirical categorization and naming of “diamond-like” carbon films.” In: *Thin Solid Films* 142.1 (1986), pp. 145–151. ISSN: 00406090. DOI: `10.1016/0040-6090(86)90310-X`.

[143] S. Wang and K. Komvopoulos. “Structure evolution during deposition and thermal annealing of amorphous carbon ultrathin films investigated by molecular dynamics simulations.” In: *Scientific Reports* 10.1 (2020), p. 8089. ISSN: 2045-2322. DOI: `10.1038/s41598-020-64625-w`.

[144] S. Logothetidis, M. Gioti, P. Patsalas, and C. Charitidis. “Insights on the deposition mechanism of sputtered amorphous carbon films.” In: *Carbon* 37.5 (Apr. 1999), pp. 765–769. ISSN: 0008-6223. DOI: `10.1016/S0008-6223(98)00268-1`.

[145] H.-G. Fuß and M. Frank. “Industrial Production of DLC Coatings.” In: *Tribology of Diamond-Like Carbon Films: Fundamentals and Applications*. Ed. by C. Donnet and A. Erdemir. Boston, MA: Springer US, 2008, pp. 457–468. ISBN: 978-0-387-49891-1. DOI: `10.1007/978-0-387-49891-1_6`.

[146] W. Tillmann, H. Ulitzka, N. F. Lopes Dias, D. Stangier, C. A. Thomann, H. Moldenhauer, and J. Debus. “Effects of acetylene flow rate and bias voltage on the structural and tribo-mechanical properties of sputtered a-C:H films.” In: *Thin Solid Films* 693 (Jan. 2020), p. 137691. ISSN: 00406090. DOI: `10.1016/j.tsf.2019.137691`.

[147] G. A. J. Amaratunga and S. R. P. Silva. “Field emission from a-C:H and a-C:H:N.” In: *Journal of Non-Crystalline Solids*. Amorphous Semiconductors-Science and Technology 198–200 (1996), pp. 611–614. ISSN: 0022-3093. DOI: `10.1016/0022-3093(95)00774-1`.

[148] J. Robertson. “Comparison of diamond-like carbon to diamond for applications.” In: *physica status solidi (a)* 205.9 (2008), pp. 2233–2244. ISSN: 18626300, 18626319. DOI: `10.1002/pssa.200879720`.

[149] C. Donnet and A. Erdemir, eds. *Tribology of diamond-like carbon films: fundamentals and applications*. New York: Springer, 2008. ISBN: 978-0-387-30264-5. DOI: `10.1007/978-0-387-49891-1`.

[150] R. Cruz, J. Rao, T. Rose, K. Lawson, and J. R. Nicholls. "DLC–ceramic multilayers for automotive applications." In: *Diamond and Related Materials*. Proceedings of the joint 11th International Conference on New Diamond Science and Technology and the 9th Applied Diamond Conference 2006 15.11 (2006), pp. 2055–2060. ISSN: 0925-9635. DOI: `10.1016/j.diamond.2006.07.006`.

[151] W. Shao, Z. Shi, L. Rao, S. Zhang, X. Xing, Y. Zhou, and Q. Yang. "High-Temperature Sliding Friction Behavior of Amorphous Carbon Films: Molecular Dynamics Simulation." In: *Langmuir: the ACS journal of surfaces and colloids* 36.50 (Dec. 2020), pp. 15319–15330. ISSN: 1520-5827. DOI: `10.1021/acs.langmuir.0c02765`.

[152] Y. Qing, L. Cheng, R. Li, G. Liu, Y. Zhang, X. Tang, J. Wang, H. Liu, and Y. Qin. "Potential antibacterial mechanism of silver nanoparticles and the optimization of orthopedic implants by advanced modification technologies." In: *International Journal of Nanomedicine* Volume 13 (2018), pp. 3311–3327. ISSN: 1178-2013. DOI: `10.2147/IJN.S165125`.

[153] F. Bi, X. Li, P. Yi, K. Hou, L. Peng, and X. Lai. "Characteristics of amorphous carbon films to resist high potential impact in PEMFCs bipolar plates for automotive application." In: *International Journal of Hydrogen Energy* 42.20 (May 2017), pp. 14279–14289. ISSN: 0360-3199. DOI: `10.1016/j.ijhydene.2017.04.113`.

[154] W. Wang, H. Huang, B. Wang, C. Qian, P. Li, J. Zhou, Z. Liang, C. Yang, and S. Guo. "A new dual-ion battery based on amorphous carbon." In: *Science Bulletin* 64.21 (Nov. 2019), pp. 1634–1642. ISSN: 2095-9273. DOI: `10.1016/j.scib.2019.08.021`.

[155] J. Nai, X. Zhao, H. Yuan, X. Tao, and L. Guo. "Amorphous carbon-based materials as platform for advanced high-performance anodes in lithium secondary batteries." In: *Nano Research* 14.7 (July 2021), pp. 2053–2066. ISSN: 1998-0000. DOI: `10.1007/s12274-021-3506-9`.

[156] S. J. Henley, S. R. P. Silva, and J. D. Carey. "Surface morphology and evolution of amorphous carbon thin films." In: *Diamond and Related Materials*. Proceedings of the 6th Specialists Meeting in Amorphous Carbon 16.10 (Oct. 2007), pp. 1777–1781. ISSN: 0925-9635. DOI: `10.1016/j.diamond.2007.07.005`.

[157] X. Zhou, Y. Zheng, T. Shimizu, C. Euaruksakul, S. Tunmee, T. Wang, H. Saitoh, and Y. Tang. "Colorful Diamond-Like Carbon Films from Different Micro/Nanostructures." In: *Advanced Optical Materials* 8 (2020), p. 1902064. DOI: `10.1002/adom.201902064`.

[158] *Nano-technology based ultra-low friction technology*. URL: `https://www.nissan-global.com/EN/INNOVATION/TECHNOLOGY/ARCHIVE/DLC/`. last accessed: 02.11.2022.

[159] C. Casiraghi, J. Robertson, and A. C. Ferrari. "Diamond-like carbon for data and beer storage." In: *Materials Today* 10.1–2 (2007), pp. 44–53. ISSN: 13697021. DOI: `10.1016/S1369-7021(06)71791-6`.

[160] N. Boutroy, Y. Pernel, J. M. Rius, F. Auger, H. J. von Bardeleben, J. L. Cantin, F. Abel, A. Zeinert, C. Casiraghi, A. C. Ferrari, and J. Robertson. “Hydrogenated amorphous carbon film coating of PET bottles for gas diffusion barriers.” In: *Diamond and Related Materials* 15.4–8 (Apr. 2006), pp. 921–927. ISSN: 09259635. DOI: `10.1016/j.diamond.2005.10.049`.

[161] D. Hofmann, S. Kunkel, K. Bewilogua, and R. Wittorf. “From DLC to Si-DLC based layer systems with optimized properties for tribological applications.” In: *Surface and Coatings Technology* 215 (Jan. 2013), pp. 357–363. ISSN: 02578972. DOI: `10.1016/j.surfcoat.2012.06.094`.

[162] *Protective Thin Coatings Technology.* Boca Raton: CRC Press, Aug. 2021. ISBN: 978-1-00-308834-9. DOI: `10.1201/9781003088349`.

[163] B. C. Windom, W. G. Sawyer, and D. W. Hahn. “A Raman Spectroscopic Study of MoS_2 and MoO_3: Applications to Tribological Systems.” In: *Tribology Letters* 42.3 (2011), pp. 301–310. ISSN: 1023-8883, 1573-2711. DOI: `10.1007/s11249-011-9774-x`.

[164] T. Gradt and T. Schneider. “Tribological Performance of MoS_2 Coatings in Various Environments.” In: *Lubricants* 4.3 (Sept. 2016), p. 32. ISSN: 2075-4442. DOI: `10.3390/lubricants4030032`.

[165] H. Ju, R. Wang, N. Ding, L. Yu, J. Xu, F. Ahmed, B. Zuo, and Y. Geng. “Improvement on the oxidation resistance and tribological properties of molybdenum disulfide film by doping nitrogen.” In: *Materials & Design* 186 (Jan. 2020), p. 108300. ISSN: 0264-1275. DOI: `10.1016/j.matdes.2019.108300`.

[166] T. F. Babuska, A. A. Pitenis, M. R. Jones, B. L. Nation, W. G. Sawyer, and N. Argibay. “Temperature-Dependent Friction and Wear Behavior of PTFE and MoS_2.” In: *Tribology Letters* 63.2 (June 2016), p. 15. ISSN: 1573-2711. DOI: `10.1007/s11249-016-0702-y`.

[167] X. Zhang, R. G. Vitchev, W. Lauwerens, L. Stals, J. He, and J.-P. Celis. “Effect of crystallographic orientation on fretting wear behaviour of MoS_x coatings in dry and humid air.” In: *Thin Solid Films* 396.1 (Sept. 2001), pp. 69–77. ISSN: 0040-6090. DOI: `10.1016/S0040-6090(01)01141-5`.

[168] Y. Catherine. “Preparation Techniques for Diamond-Like Carbon.” In: *Diamond and Diamond-like Films and Coatings.* Ed. by R. E. Clausing, L. L. Horton, J. C. Angus, and P. Koidl. Vol. 266. NATO ASI Series. Boston, MA: Springer US, 1991, pp. 193–227. ISBN: 978-1-4684-5969-2. DOI: `10.1007/978-1-4684-5967-8_10`.

[169] P. J. Kelly and R. D. Arnell. “Magnetron sputtering: a review of recent developments and applications.” In: *Vacuum* 56.3 (Mar. 2000), pp. 159–172. ISSN: 0042-207X. DOI: `10.1016/S0042-207X(99)00189-X`.

[170] F. Rose, N. Wang, R. Smith, Q.-F. Xiao, H. Inaba, T. Matsumura, Y. Saito, H. Matsumoto, Q. Dai, B. Marchon, F. Mangolini, and R. W. Carpick. “Complete characterization by Raman spectroscopy of the structural properties of thin hydrogenated diamond-like carbon films exposed to rapid thermal annealing.” In: *Journal of Applied Physics* 116.12 (2014), p. 123516. ISSN: 0021-8979, 1089-7550. DOI: `10.1063/1.4896838`.

[171] K. Sarakinos, J. Alami, and S. Konstantinidis. “High power pulsed magnetron sputtering: A review on scientific and engineering state of the art.” In: *Surface and Coatings Technology* 204.11 (2010), pp. 1661–1684. ISSN: 0257-8972. DOI: `10.1016/j.surfcoat.2009.11.013`.

[172] J. Alami, S. Bolz, and K. Sarakinos. “High power pulsed magnetron sputtering: Fundamentals and applications.” In: *Journal of Alloys and Compounds* 483.1–2 (2009), pp. 530–534. ISSN: 09258388. DOI: `10.1016/j.jallcom.2008.08.104`.

[173] H. Moldenhauer. “Correlating Raman scattering signatures with microstructural properties of tribological surfaces.” Dissertation. TU Dortmund university, 2021. DOI: `10.17877/DE290R-22371`.

[174] H. Moldenhauer, A. Wittig, D. Kokalj, D. Stangier, A. Brümmer, W. Tillmann, and J. Debus. “Resonant Raman scattering characterization of thermally annealed HiPIMS deposited MoS_x coatings.” In: *Surface and Coatings Technology* 377 (2019), p. 124891. ISSN: 0257-8972. DOI: `10.1016/j.surfcoat.2019.124891`.

[175] W. Tillmann, N. F. Lopes Dias, D. Stangier, S. Matveev, C. A. Thomann, and J. Debus. “Design of Cu- and Ag-containing amorphous carbon multilayers with improved tribo-mechanical properties.” In: *Materials Letters* 284 (Feb. 2021), p. 128905. ISSN: 0167577X. DOI: `10.1016/j.matlet.2020.128905`.

[176] W. Tillmann, N. F. Lopes Dias, C. Franke, D. Kokalj, D. Stangier, C. A. Thomann, and J. Debus. “Mechanical properties and adhesion behavior of amorphous carbon films with bias voltage controlled Ti_xC_y interlayers on Ti6Al4V.” In: *Diamond and Related Materials* 115 (May 2021), p. 108361. ISSN: 09259635. DOI: `10.1016/j.diamond.2021.108361`.

[177] W. Tillmann, A. Wittig, H. Moldenhauer, C.-A. Thomann, J. Debus, D. Aurich, and A. Bruemmer. “Nitrogen doping of MoS_x thin films sputtered by reactive High Power Impulse Magnetron Sputtering.” In: *Thin Solid Films* 713 (Nov. 2020), p. 138267. ISSN: 00406090. DOI: `10.1016/j.tsf.2020.138267`.

[178] W. Tillmann, N. F. Lopes Dias, D. Stangier, W. Maus-Friedrichs, R. Gustus, C. A. Thomann, H. Moldenhauer, and J. Debus. “Improved adhesion of a-C and a-C:H films with a CrC interlayer on 16MnCr5 by HiPIMS-pretreatment.” In: *Surface and Coatings Technology* 375 (Oct. 2019), pp. 877–887. ISSN: 02578972. DOI: `10.1016/j.surfcoat.2019.07.076`.

[179] W. Tillmann, N. F. Lopes Dias, D. Stangier, S. Matveev, C.-A. Thomann, and J. Debus. “Structure and tribo-mechanical properties of Si- and W-containing amorphous carbon based multilayers.” In: *Applied Surface Science Advances* 5 (Sept. 2021), p. 100105. ISSN: 26665239. DOI: `10.1016/j.apsadv.2021.100105`.

[180] M. R. Perrone, V. Piccinno, G. de Nunzio, and V. Nassisi. “Dependence of rotational and vibrational Raman scattering on focusing geometry.” In: *IEEE Journal of Quantum Electronics* 33.6 (June 1997), pp. 938–944. ISSN: 00189197. DOI: `10.1109/3.585480`.

[181] G. Amato, G. Milano, U. Vignolo, and E. Vittone. “Kinetics of defect formation in chemically vapor deposited (CVD) graphene during laser irradiation: The case of Raman investigation.” In: *Nano Research* 8.12 (Dec. 2015), pp. 3972–3981. ISSN: 1998-0124, 1998-0000. DOI: `10.1007/s12274-015-0900-1`.

[182] S. Osswald, K. Behler, and Y. Gogotsi. “Laser-induced light emission from carbon nanoparticles.” In: *Journal of Applied Physics* 104.7 (2008), p. 074308. ISSN: 0021-8979. DOI: `10.1063/1.2980321`.

[183] S. Kouteva-Arguirova, T. Arguirov, D. Wolfframm, and J. Reif. “Influence of local heating on micro-Raman spectroscopy of silicon.” In: *Journal of Applied Physics* 94.8 (2003), p. 4946. ISSN: 00218979. DOI: `10.1063/1.1611282`.

[184] S. J. Tinnemans, M. H. F. Kox, M. W. Sletering, T. A. (Nijhuis, T. Visser, and B. M. Weckhuysen. “Dealing with a local heating effect when measuring catalytic solids in a reactor with Raman spectroscopy.” In: *Physical Chemistry Chemical Physics* 8.20 (2006), p. 2413. ISSN: 1463-9076, 1463-9084. DOI: `10.1039/b602311h`.

[185] J. Bartl and M. Baranek. “Emissivity of aluminium and its importance for radiometric measurement.” In: *MEASUREMENT SCIENCE REVIEW* 4 (2004), p. 6.

[186] A. Wittrock. “Raman-spektroskopische Untersuchungen von tribologischen Dünnschichten unter laserinduzierten Energieeinträgen.” Master thesis. TU Dortmund university, 2020.

[187] Y. Lifshitz, S. R. Kasi, and J. W. Rabalais. “Subplantation model for film growth from hyperthermal species: Application to diamond.” In: *Physical Review Letters* 62.11 (1989), pp. 1290–1293. DOI: `10.1103/PhysRevLett.62.1290`.

[188] P. Koidl, C. Wild, B. Dischler, J. Wagner, and M. Ramsteiner. “Plasma Deposition, Properties and Structure of Amorphous Hydrogenated Carbon Films.” In: *Materials Science Forum* 52–53 (Jan. 1991), pp. 41–70. ISSN: 1662-9752. DOI: `10.4028/www.scientific.net/MSF.52-53.41`.

[189] P. Koidl, C. Wild, R. Locher, and R. E. Sah. “Amorphous, Hydrogenated Carbon Films and Related Materials: Plasma Deposition and Film Properties.” In: *Diamond and Diamond-like Films and Coatings*. Ed. by R. E. Clausing, L. L. Horton, J. C. Angus, and P. Koidl. NATO ASI Series. Boston, MA: Springer US, 1991, pp. 243–265. ISBN: 978-1-4684-5967-8. DOI: `10.1007/978-1-4684-5967-8_12`.

[190] P. Lemoine, J. P. Quinn, P. Maguire, and J. A. McLaughlin. “Comparing hardness and wear data for tetrahedral amorphous carbon and hydrogenated amorphous carbon thin films.” In: *Wear* 257.5 (Sept. 2004), pp. 509–522. ISSN: 0043-1648. DOI: `10.1016/j.wear.2004.01.010`.

[191] A. Leyland and A. Matthews. “On the significance of the H/E ratio in wear control: a nanocomposite coating approach to optimised tribological behaviour.” In: *Wear* 246.1 (Nov. 2000), pp. 1–11. ISSN: 0043-1648. DOI: `10.1016/S0043-1648(00)00488-9`.

[192] S. Neuville and A. Matthews. “A perspective on the optimisation of hard carbon and related coatings for engineering applications.” In: *Thin Solid Films* 515.17 (June 2007), pp. 6619–6653. ISSN: 00406090. DOI: `10.1016/j.tsf.2007.02.011`.

[193] J.-K. Shin, C. S. Lee, K.-R. Lee, and K. Y. Eun. “Effect of residual stress on the Raman-spectrum analysis of tetrahedral amorphous carbon films.” In: *Applied Physics Letters* 78.5 (Jan. 2001), pp. 631–633. ISSN: 0003-6951, 1077-3118. DOI: `10.1063/1.1343840`.

[194] J. E. Lee, G. Ahn, J. Shim, Y. S. Lee, and S. Ryu. “Optical separation of mechanical strain from charge doping in graphene.” In: *Nature Communications* 3.11 (Aug. 2012), p. 1024. ISSN: 2041-1723. DOI: `10.1038/ncomms2022`.

[195] H. Holleck. “Material selection for hard coatings.” In: *Journal of Vacuum Science & Technology A* 4.6 (Nov. 1986), pp. 2661–2669. ISSN: 0734-2101. DOI: `10.1116/1.573700`.

[196] C. C. Chen and F. C. N. Hong. “Interfacial studies for improving the adhesion of diamond-like carbon films on steel.” In: *Applied Surface Science* 243.1–4 (Apr. 2005), pp. 296–303. ISSN: 0169-4332. DOI: `10.1016/j.apsusc.2004.09.085`.

[197] Y. Pauleau. “Residual Stresses in DLC Films and Adhesion to Various Substrates.” In: *Tribology of Diamond-Like Carbon Films: Fundamentals and Applications*. Ed. by C. Donnet and A. Erdemir. Boston, MA: Springer US, 2008, pp. 102–136. ISBN: 978-0-387-49891-1. DOI: `10.1007/978-0-387-49891-1_4`.

[198] K. Koski, J. Hölsä, J. Ernoult, and A. Rouzaud. “The connection between sputter cleaning and adhesion of thin solid films.” In: *Surface and Coatings Technology* 80.1 (Mar. 1996), pp. 195–199. ISSN: 0257-8972. DOI: `10.1016/0257-8972(95)02710-6`.

[199] J. E. E. Baglin. “Thin film adhesion: New possibilities for interface engineering.” In: *Materials Science and Engineering: B* 1.1 (Aug. 1988), pp. 1–7. ISSN: 0921-5107. DOI: `10.1016/0921-5107(88)90024-4`.

[200] J. E. E. Baglin. “Interface tailoring for adhesion using ion beams.” In: *Nuclear Instruments and Methods in Physics Research Section B: Beam Interactions with Materials and Atoms* 39.1 (Mar. 1989), pp. 764–768. ISSN: 0168-583X. DOI: `10.1016/0168-583X(89)90892-6`.

[201] H.-T. Lin, P. K. Nayak, S.-C. Wang, S.-Y. Chang, and J.-L. Huang. “Electron-energy loss spectroscopy and Raman studies of nanosized chromium carbide synthesized during carbothermal reduction process from precursor Cr(CO)6.” In: *Journal of the European Ceramic Society* 31.14 (Nov. 2011), pp. 2481–2487. ISSN: 09552219. DOI: `10.1016/j.jeurceramsoc.2010.12.005`.

[202] J. Fontaine, C. Donnet, A. Grill, and T. LeMogne. “Tribochemistry between hydrogen and diamond-like carbon films.” In: *Surface and Coatings Technology*. Proceedings of the 28th International Conference on Metallurgic Coatings and Thin Films 146–147 (Sept. 2001), pp. 286–291. ISSN: 0257-8972. DOI: `10.1016/S0257-8972(01)01398-6`.

[203] H. Ronkainen and K. Holmberg. “Environmental and Thermal Effects on the Tribological Performance of DLC Coatings.” In: *Tribology of Diamond-Like Carbon Films: Fundamentals and Applications*. Ed. by C. Donnet and A. Erdemir. Boston, MA: Springer US, 2008, pp. 155–200. ISBN: 978-0-387-49891-1. DOI: `10.1007/978-0-387-49891-1_6`.

[204] J. Robertson. “Properties and prospects for non-crystalline carbons.” In: *Journal of Non-Crystalline Solids* 299–302 (Apr. 2002), pp. 798–804. ISSN: 00223093. DOI: `10.1016/S0022-3093(01)00985-1`.

[205] C. Casiraghi, A. C. Ferrari, and J. Robertson. “The smoothness of tetrahedral amorphous carbon.” In: *Diamond and Related Materials* 14.3 (2005), pp. 913–920. ISSN: 0925-9635. DOI: `10.1016/j.diamond.2005.01.023`.

[206] X. Zhou, T. Suzuki, H. Nakajima, K. Komatsu, K. Kanda, H. Ito, and H. Saitoh. “Structural analysis of amorphous carbon films by spectroscopic ellipsometry, RBS/ERDA, and NEXAFS.” In: *Applied Physics Letters* 110.20 (May 2017), p. 201902. ISSN: 0003-6951, 1077-3118. DOI: `10.1063/1.4983643`.

[207] H. Jung. “Determination of local bonding configuration and structural modification in amorphous carbon with silicon incorporation.” In: *Diamond and Related Materials* 12.8 (2003), pp. 1373–1377. ISSN: 09259635. DOI: `10.1016/S0925-9635(03)00110-9`.

[208] M. Veres, M. Koós, N. Orsós, S. Tóth, M. Füle, M. Mohai, and I. Bertóti. “Incorporation of Si in a-C:Si:H films monitored by infrared excited Raman scattering.” In: *Diamond and Related Materials* 15.4–8 (Apr. 2006), pp. 932–935. ISSN: 09259635. DOI: `10.1016/j.diamond.2005.10.051`.

[209] D. Zhang, S. Li, X. Zuo, P. Guo, P. Ke, and A. Wang. “Structural and mechanism study on enhanced thermal stability of hydrogenated diamond-like carbon films doped with Si/O.” In: *Diamond and Related Materials* 108 (Oct. 2020), p. 107923. ISSN: 09259635. DOI: `10.1016/j.diamond.2020.107923`.

[210] Y. Hatano, M. Takamori, K. Matsuda, S. Ikeno, K. Fujii, and K. Watanabe. “Solid state reaction between tungsten and amorphous carbon.” In: *Journal of Nuclear Materials* 307–311 (2002), pp. 1339–1343. ISSN: 00223115. DOI: `10.1016/S0022-3115(02)00986-8`.

[211] A.-Y. Wang, H.-S. Ahn, K.-R. Lee, and J.-P. Ahn. “Unusual stress behavior in W-incorporated hydrogenated amorphous carbon films.” In: *Applied Physics Letters* 86.11 (2005), p. 111902. ISSN: 0003-6951, 1077-3118. DOI: `10.1063/1.1883328`.

[212] Q. Yong, G. Ma, H. Wang, S. Chen, and B. Xu. “Influence of tungsten content on microstructure and properties of tungsten-doped graphite-like carbon films.” In: *Journal of Materials Research* 31.23 (2016), pp. 3766–3776. ISSN: 0884-2914, 2044-5326. DOI: `10.1557/jmr.2016.433`.

[213] B. Hansson, C. H. Allen, S. Qutob, B. Behr, B. Nyiri, V. Chauhan, and S. Murugkar. “Development of a flow cell based Raman spectroscopy technique to overcome photodegradation in human blood.” In: *Biomedical Optics Express* 10.5 (Apr. 2019), pp. 2275–2288. ISSN: 2156-7085. DOI: `10.1364/BOE.10.002275`.

[214] M. Karimi-Jafari, R. Soto, A. B. Albadarin, D. Croker, and G. Walker. “In-line Raman spectroscopy and chemometrics for monitoring cocrystallisation using hot melt extrusion.” In: *International Journal of Pharmaceutics* 601 (May 2021), p. 120555. ISSN: 0378-5173. DOI: `10.1016/j.ijpharm.2021.120555`.

[215] W. Tillmann, N. F. Lopes Dias, D. Stangier, A. Nienhaus, C. A. Thomann, A. Wittrock, H. Moldenhauer, and J. Debus. "Effect of the bias voltage on the structural and tribo-mechanical properties of Ag-containing amorphous carbon films." In: *Diamond and Related Materials* 105 (May 2020), p. 107803. ISSN: 09259635. DOI: `10.1016/j.diamond.2020.107803`.

[216] H. W. Choi, J.-H. Choi, K.-R. Lee, J.-P. Ahn, and K. H. Oh. "Structure and mechanical properties of Ag-incorporated DLC films prepared by a hybrid ion beam deposition system." In: *Thin Solid Films* 516.2 (Dec. 2007), pp. 248–251. ISSN: 0040-6090. DOI: `10.1016/j.tsf.2007.06.154`.

[217] X. Yu, M. Hua, and C. Wang. "Influence of Ag Content and Nanograin Size on Microstructure, Mechanical and Sliding Tribological Behaviors of Ag-DLC Films." In: *Journal of Nanoscience and Nanotechnology* 9.11 (Nov. 2009), pp. 6366–6371. DOI: `10.1166/jnn.2009.1304`.

[218] R. N. Compton, N. I. Hammer, E. C. Lambert, and J. S. Hager. "Fundamentals of Raman Spectroscopy and Raman Under Nitrogen (RUN)." In: *Raman Spectroscopy Under Liquid Nitrogen (RUN)*. Ed. by R. N. Compton, N. I. Hammer, E. C. Lambert, and J. S. Hager. Springer Series on Atomic, Optical, and Plasma Physics. Cham: Springer International Publishing, 2022, pp. 7–20. ISBN: 978-3-030-99395-5. DOI: `10.1007/978-3-030-99395-5_2`.

[219] W. Tillmann, N. F. Lopes Dias, C. Franke, D. Kokalj, D. Stangier, V. Filor, R. H. Mateus-Vargas, H. Oltmanns, M. Kietzmann, J. Meißner, M. Hein, S. Pramanik, K.-P. Hoyer, M. Schaper, A. Nienhaus, C. A. Thomann, and J. Debus. "Tribo-mechanical properties and biocompatibility of Ag-containing amorphous carbon films deposited onto Ti6Al4V." In: *Surface and Coatings Technology* 421 (Sept. 2021), p. 127384. ISSN: 02578972. DOI: `10.1016/j.surfcoat.2021.127384`.

[220] P. D. Fleischauer, M. R. Hilton, and R. Bauer. "Paper V (i) Effects of microstructure and adhesion on performance of sputter-deposited MoS_2 solid lubricant coatings." In: *Tribology Series*. Ed. by D. Dowson, C. M. Taylor, and M. Godet. Vol. 17. Mechanics of Coatings. Elsevier, Jan. 1990, pp. 121–128. DOI: `10.1016/S0167-8922(08)70248-7`.

[221] A. P. Ehiasarian, A. Vetushka, A. Hecimovic, and S. Konstantinidis. "Ion composition produced by high power impulse magnetron sputtering discharges near the substrate." In: *Journal of Applied Physics* 104.8 (Oct. 2008), p. 083305. ISSN: 0021-8979. DOI: `10.1063/1.3000446`.

[222] E. Lewin, D. Loch, A. Montagne, A. P. Ehiasarian, and J. Patscheider. "Comparison of Al–Si–N nanocomposite coatings deposited by HIPIMS and DC magnetron sputtering." In: *Surface and Coatings Technology* 232 (Oct. 2013), pp. 680–689. ISSN: 0257-8972. DOI: `10.1016/j.surfcoat.2013.06.076`.

[223] G. Kamath, A. P. Ehiasarian, Y. Purandare, and P. E. Hovsepian. "Tribological and oxidation behaviour of TiAlCN/VCN nanoscale multilayer coating deposited by the combined HIPIMS/(HIPIMS-UBM) technique." In: *Surface and Coatings Technology* 205.8 (Jan. 2011), pp. 2823–2829. ISSN: 0257-8972. DOI: `10.1016/j.surfcoat.2010.10.049`.

[224] T. Spalvins. “Structure of Sputtered Molybdenum Disulfide Films at Various Substrate Temperatures.” In: *A S L E Transactions* 17.1 (Jan. 1974), pp. 1–7. ISSN: 0569-8197. DOI: `10.1080/05698197408981432`.

[225] A. Aubert, J. P. Nabot, J. Ernoult, and P. Renaux. “Preparation and properties of MoS_x films grown by d.c. magnetron sputtering.” In: *Surface and Coatings Technology* 41.1 (Feb. 1990), pp. 127–134. ISSN: 0257-8972. DOI: `10.1016/0257-8972(90)90136-Z`.

[226] C. Donnet, J. M. Martin, T. Le Mogne, and M. Belin. “Super-low friction of MoS_2 coatings in various environments.” In: *Tribology International* 29.2 (Feb. 1996), pp. 123–128. ISSN: 0301-679X. DOI: `10.1016/0301-679X(95)00094-K`.

[227] G. Colas, A. Saulot, N. Bouscharain, C. Godeau, Y. Michel, and Y. Berthier. “How far does contamination help dry lubrication efficiency?” In: *Tribology International.* 39th LEEDS-LYON SYMPOSIUM ON TRIBOLOGY Special Issue: Great Challenges in Tribology 65 (Sept. 2013), pp. 177–189. ISSN: 0301-679X. DOI: `10.1016/j.triboint.2012.12.011`.

[228] H. S. Khare and D. L. Burris. “The Effects of Environmental Water and Oxygen on the Temperature-Dependent Friction of Sputtered Molybdenum Disulfide.” In: *Tribology Letters* 52.3 (Dec. 2013), pp. 485–493. ISSN: 1573-2711. DOI: `10.1007/s11249-013-0233-8`.

[229] T. Wang, C. Xue, S. Yu, W. Chen, and G. Zhang. “The effect of S/Mo ratio on structure and properties of MoS_x-Ti composite coatings deposited by magnetron sputtering.” In: *Materials Research Express* 7.10 (Oct. 2020), p. 106401. ISSN: 2053-1591. DOI: `10.1088/2053-1591/abbd5f`.

[230] W. D. Sun, J. Wang, K. W. Wang, J. J. Pan, R. Wang, M. Wen, and K. Zhang. “Turbulence-like Cu/MoS_2 films: Structure, mechanical and tribological properties.” In: *Surface and Coatings Technology* 422 (Sept. 2021), p. 127490. ISSN: 0257-8972. DOI: `10.1016/j.surfcoat.2021.127490`.

[231] M. S. Mihalev. “TRANSITION METAL OXIDES AS MATERIALS FOR ADDITIVE LASER MARKING ON STAINLESS STEEL.” In: *Acta Polytechnica* 57.44 (Sept. 2017), pp. 252–262. ISSN: 1805-2363. DOI: `10.14311/AP.2017.57.0252`.

[232] T. Seto, A. Inoue, H. Higashi, Y. Otani, M. Kohno, and M. Hirasawa. “Phase transition and restructuring of carbon nanoparticles induced by aerosol laser irradiation.” In: *Carbon* 70 (2014), pp. 224–232. ISSN: 00086223. DOI: `10.1016/j.carbon.2013.12.111`.

[233] I. Bydzovska, E. Shagieva, I. Gordeev, O. Romanyuk, Z. Nemeckova, J. Henych, L. Ondic, A. Kromka, and S. Stehlik. “Laser-Induced Modification of Hydrogenated Detonation Nanodiamonds in Ethanol.” In: *Nanomaterials* 11.9 (2021), p. 2251. ISSN: 2079-4991. DOI: `10.3390/nano11092251`.

[234] E. Cappelli, C. Scilletta, S. Orlando, V. Valentini, and M. Servidori. “Laser annealing of amorphous carbon films.” In: *Applied Surface Science* 255.10 (2009), pp. 5620–5625. ISSN: 01694332. DOI: `10.1016/j.apsusc.2008.10.062`.

[235] L. Marcinauskas, A. Grigonis, P. Valatkevicius, and A. Medvid. “Irradiation of the graphite-like carbon films by ns-laser pulse.” In: *Applied Surface Science* 261 (2012), pp. 488–492. ISSN: 01694332. DOI: `10.1016/j.apsusc.2012.08.042`.

[236] A. Barreiro, F. Börrnert, S. M. Avdoshenko, B. Rellinghaus, G. Cuniberti, M. H. Rümmeli, and L. M. K. Vandersypen. “Understanding the catalyst-free transformation of amorphous carbon into graphene by current-induced annealing.” In: *Scientific Reports* 3.1 (Jan. 23, 2013), p. 1115. ISSN: 2045-2322. DOI: `10.1038/srep01115`.

[237] T. Kim, J. Lee, and K.-H. Lee. “Full graphitization of amorphous carbon by microwave heating.” In: *RSC Advances* 6.29 (2016), pp. 24667–24674. ISSN: 2046-2069. DOI: `10.1039/C6RA01989G`.

[238] T. Roch, A. Lasagni, and E. Beyer. “Nanosecond UV laser graphitization and delamination of thin tetrahedral amorphous carbon films with different sp^3/sp^2 content.” In: *Thin Solid Films* 519.11 (Mar. 2011), pp. 3756–3761. ISSN: 00406090. DOI: `10.1016/j.tsf.2011.01.338`.

[239] T. Seto, A. Inoue, H. Higashi, Y. Otani, M. Kohno, and M. Hirasawa. “Phase transition and restructuring of carbon nanoparticles induced by aerosol laser irradiation.” In: *Carbon* 70 (Apr. 2014), pp. 224–232. ISSN: 00086223. DOI: `10.1016/j.carbon.2013.12.111`.

[240] A. Grigonis, L. Marcinauskas, V. Vinciunaite, and G. Raciukaitis. “Modification of the amorphous carbon films by the ns-laser irradiation.” In: *Open Physics* 9.5 (Jan. 1, 2011). ISSN: 2391-5471. DOI: `10.2478/s11534-011-0037-0`.

[241] J. Gaudin, O. Peyrusse, J. Chalupský, M. Toufarová, L. Vyšín, V. Hájková, R. Sobierajski, T. Burian, S. Dastjani-Farahani, A. Graf, M. Amati, L. Gregoratti, S. P. Hau-Riege, G. Hoffmann, L. Juha, J. Krzywinski, R. A. London, S. Moeller, H. Sinn, S. Schorb, M. Störmer, T. Tschentscher, V. Vorlíček, H. Vu, J. Bozek, and C. Bostedt. “Amorphous to crystalline phase transition in carbon induced by intense femtosecond x-ray free-electron laser pulses.” In: *Physical Review B* 86.2 (July 11, 2012), p. 024103. ISSN: 1098-0121, 1550-235X. DOI: `10.1103/PhysRevB.86.024103`.

[242] D. R. Tallant, J. E. Parmeter, M. P. Siegal, and R. L. Simpson. “The thermal stability of diamond-like carbon.” In: *Diamond and Related Materials* 4.3 (1995), pp. 191–199. ISSN: 09259635. DOI: `10.1016/0925-9635(94)00243-6`.

[243] C. Hopf, T. Angot, E. Aréou, T. Dürbeck, W. Jacob, C. Martin, C. Pardanaud, P. Roubin, and T. Schwarz-Selinger. “Characterization of temperature-induced changes in amorphous hydrogenated carbon thin films.” In: *Diamond and Related Materials* 37 (2013), pp. 97–103. ISSN: 09259635. DOI: `10.1016/j.diamond.2013.05.004`.

[244] A. A. Onoprienko and I. B. Yanchuk. “Temperature dependence of the mechanical properties of amorphous carbon films deposited by magnetron sputtering.” In: *Powder Metallurgy and Metal Ceramics* 45.3–4 (2006), pp. 190–195. ISSN: 1068-1302, 1573-9066. DOI: `10.1007/s11106-006-0062-5`.

[245] G. C. Loh and D. Baillargeat. “Graphitization of amorphous carbon and its transformation pathways.” In: *Journal of Applied Physics* 114.3 (2013), p. 033534. ISSN: 0021-8979, 1089-7550. DOI: `10.1063/1.4816313`.

[246] M. Joseph, N. Sivakumar, and P. Manoravi. “High temperature vapour pressure studies on graphite using laser pulse heating.” In: *Carbon* 40.11 (2002), pp. 2031–2034. ISSN: 00086223. DOI: `10.1016/S0008-6223(02)00158-6`.

[247] Y. Catherine. “Preparation Techniques for Diamond-Like Carbon.” In: *Diamond and Diamond-like Films and Coatings.* Ed. by R. E. Clausing, L. L. Horton, J. C. Angus, and P. Koidl. Vol. 266. Series Title: NATO ASI Series. Boston, MA: Springer US, 1991, pp. 193–227. DOI: `10.1007/978-1-4684-5967-8_10`.

[248] J. Robertson. “The deposition mechanism of diamond-like a-C and a-C: H.” In: *Diamond and Related Materials* 3.4-6 (Apr. 1994), pp. 361–368. ISSN: 09259635. DOI: `10.1016/0925-9635(94)90186-4`.

[249] M. Hiratsuka, H. Nakamori, Y. Kogo, M. Sakurai, N. Ohtake, and H. Saithoh. “Correlation between Optical Properties and Hardness of Diamond-Like Carbon Films.” In: *Journal of Solid Mechanics and Materials Engineering* 7.2 (2013), pp. 187–198. DOI: `10.1299/jmmp.7.187`.

[250] W. Tillmann, A. Wittig, D. Stangier, H. Moldenhauer, C.-A. Thomann, J. Debus, D. Aurich, and A. Bruemmer. “Influence of the bias-voltage, the argon pressure and the heating power on the structure and the tribological properties of HiPIMS sputtered MoS_x films.” In: *Surface and Coatings Technology* 385 (Mar. 2020), p. 125358. ISSN: 02578972. DOI: `10.1016/j.surfcoat.2020.125358`.

[251] E. Cappelli, C. Scilletta, S. Orlando, V. Valentini, and M. Servidori. “Laser annealing of amorphous carbon films.” In: *Applied Surface Science* 255.10 (Mar. 2009), pp. 5620–5625. ISSN: 01694332. DOI: `10.1016/j.apsusc.2008.10.062`.

[252] C. Casiraghi, A. C. Ferrari, and J. Robertson. “Raman spectroscopy of hydrogenated amorphous carbons.” In: *Physical Review B* 72.8 (Aug. 2005), p. 085401. ISSN: 1098-0121, 1550-235X. DOI: `10.1103/PhysRevB.72.085401`.

[253] C. A. Thomann, A. Wittrock, A. Wittig, N. F. Lopes Dias, D. Stangier, W. Tillmann, and J. Debus. “Tuning of solid-to-solid structural transitions in amorphous carbon films by optical pumping and chemical modification.” In: *APL Materials* 11.3 (2023), p. 031106. ISSN: 2166-532X. DOI: `10.1063/5.0138362`.

[254] C. Castiglioni, F. Negri, M. Rigolio, and G. Zerbi. “Raman activation in disordered graphites of the A1’ symmetry forbidden $k \neq 0$ phonon: The origin of the D line.” In: *The Journal of Chemical Physics* 115.8 (Aug. 2001), pp. 3769–3778. ISSN: 0021-9606. DOI: `10.1063/1.1381529`.

[255] C. Hopf, T. Angot, E. Aréou, T. Dürbeck, W. Jacob, C. Martin, C. Pardanaud, P. Roubin, and T. Schwarz-Selinger. “Characterization of temperature-induced changes in amorphous hydrogenated carbon thin films.” In: *Diamond and Related Materials* 37 (2013), pp. 97–103. ISSN: 09259635. DOI: `10.1016/j.diamond.2013.05.004`.

[256] J. Guerrero-Contreras and F. Caballero-Briones. “Graphene oxide powders with different oxidation degree, prepared by synthesis variations of the Hummers method.” In: *Materials Chemistry and Physics* 153 (Mar. 2015), pp. 209–220. ISSN: 0254-0584. DOI: `10.1016/j.matchemphys.2015.01.005`.

[257] D. M. Basko. “Boundary problems for Dirac electrons and edge-assisted Raman scattering in graphene.” In: *Physical Review B* 79.20 (May 2009), p. 205428. ISSN: 1098-0121, 1550-235X. DOI: `10.1103/PhysRevB.79.205428`.

[258] R. Beams, L. G. Cançado, and L. Novotny. “Optical Measurement of the Phase-Breaking Length in Graphene.” In: *Nano Letters* 11.3 (Mar. 2011), pp. 1177–1181. ISSN: 1530-6984, 1530-6992. DOI: `10.1021/nl104134a`.

[259] C. Casiraghi, A. Hartschuh, H. Qian, S. Piscanec, C. Georgi, A. Fasoli, K. S. Novoselov, D. M. Basko, and A. C. Ferrari. “Raman Spectroscopy of Graphene Edges.” In: *Nano Letters* 9.4 (Apr. 2009), pp. 1433–1441. ISSN: 1530-6984, 1530-6992. DOI: `10.1021/nl8032697`.

[260] M. M. Lucchese, F. Stavale, E. H. Martins Ferreira, C. Vilani, M. V. O. Moutinho, R. B. Capaz, C. A. Achete, and A. Jorio. “Quantifying ion-induced defects and Raman relaxation length in graphene.” In: *Carbon* 48.5 (Apr. 2010), pp. 1592–1597. ISSN: 00086223. DOI: `10.1016/j.carbon.2009.12.057`.

[261] Z. Luo, T. Yu, Z. Ni, S. Lim, H. Hu, J. Shang, L. Liu, Z. Shen, and J. Lin. “Electronic Structures and Structural Evolution of Hydrogenated Graphene Probed by Raman Spectroscopy.” In: *The Journal of Physical Chemistry C* 115.5 (Feb. 2011), pp. 1422–1427. ISSN: 1932-7447, 1932-7455. DOI: `10.1021/jp107109h`.

[262] K. V. Zakharchenko, A. Fasolino, J. H. Los, and M. I. Katsnelson. “Melting of graphene: from two to one dimension.” In: *Journal of Physics: Condensed Matter* 23.20 (2011), p. 202202. ISSN: 0953-8984, 1361-648X. DOI: `10.1088/0953-8984/23/20/202202`.

[263] L. Yang, X. Wang, L. Zou, F. Ruan, and Q. Ni. “Effect of heat treatment on microstructures of magnetron sputtered amorphous carbon films.” In: *Diamond and Related Materials* 100 (Dec. 2019), p. 107572. ISSN: 0925-9635. DOI: `10.1016/j.diamond.2019.107572`.

[264] W.-J. Wu and M.-H. Hon. “Thermal stability of diamond-like carbon films with added silicon.” In: *Surface and Coatings Technology* 111.2–3 (Jan. 1999), pp. 134–140. ISSN: 02578972. DOI: `10.1016/S0257-8972(98)00719-1`.

[265] A. Pardo, J. G. Buijnsters, J. L. Endrino, C. Gómez-Aleixandre, G. Abrasonis, R. Bonet, and J. Caro. “Effect of the metal concentration on the structural, mechanical and tribological properties of self-organized a-C:Cu hard nanocomposite coatings.” In: *Applied Surface Science* 280 (Sept. 2013), pp. 791–798. ISSN: 0169-4332. DOI: `10.1016/j.apsusc.2013.05.063`.

[266] J. Choi, S. Nakao, S. Miyagawa, M. Ikeyama, and Y. Miyagawa. “The effects of Si incorporation on the thermal and tribological properties of DLC films deposited by PBII&D with bipolar pulses.” In: *Surface and Coatings Technology* 201.19–20 (2007), pp. 8357–8361. ISSN: 02578972. DOI: `10.1016/j.surfcoat.2006.02.084`.

[267] P. Wang, X. Wang, T. Xu, W. Liu, and J. Zhang. “Comparing internal stress in diamond-like carbon films with different structure.” In: *Thin Solid Films* 515.17 (June 2007), p. 6899. ISSN: 00406090. DOI: `10.1016/j.tsf.2007.02.069`.

[268] Š. Meškinis, A. Vasiliauskas, M. Andrulevičius, D. Peckus, S. Tamulevičius, and K. Viskontas. "Diamond Like Carbon Films Containing Si: Structure and Nonlinear Optical Properties." In: *Materials* 13.4 (Feb. 2020), p. 1003. ISSN: 1996-1944. DOI: `10.3390/ma13041003`.

[269] T. W. Scharf, J. A. Ohlhausen, D. R. Tallant, and S. V. Prasad. "Mechanisms of friction in diamondlike nanocomposite coatings." In: *Journal of Applied Physics* 101.6 (Mar. 2007), p. 063521. ISSN: 0021-8979, 1089-7550. DOI: `10.1063/1.2711147`.

[270] S. Lin, Z. Chen, L. Li, and C. Yang. "Effect of impurities on the Raman scattering of 6H-SiC crystals." In: *Materials Research* 15.6 (2012), pp. 833–836. ISSN: 1980-5373, 1516-1439. DOI: `10.1590/S1516-14392012005000108`.

[271] P. Yogi, M. Tanwar, S. K. Saxena, S. Mishra, D. K. Pathak, A. Chaudhary, P. R. Sagdeo, and R. Kumar. "Quantifying the Short-Range Order in Amorphous Silicon by Raman Scattering." In: *Analytical Chemistry* 90.13 (2018), pp. 8123–8129. ISSN: 0003-2700, 1520-6882. DOI: `10.1021/acs.analchem.8b01352`.

[272] A. Jena, S. K. Pattnaik, B. B. Palei, and S. K. Sarangi. "Synthesis of diamond crystal growth on tungsten carbide inserts by HFCVD using various seeding powders." In: *Applied Physics A* 128.4 (2022), p. 287. ISSN: 0947-8396, 1432-0630. DOI: `10.1007/s00339-022-05417-z`.

[273] M. Kan, J. Y. Wang, X. Li, S. Zhang, Y. Li, Y. Kawazoe, Q. Sun, and P. Jena. "Structures and Phase Transition of a MoS_2 Monolayer." In: *The Journal of Physical Chemistry C* 118 (Jan. 2014), pp. 1515–1522. DOI: `10.1021/jp4076355`.

[274] Q. H. Wang, K. Kalantar-Zadeh, A. Kis, J. N. Coleman, and M. S. Strano. "Electronics and optoelectronics of two-dimensional transition metal dichalcogenides." In: *Nature Nanotechnology* 7.11 (Nov. 2012), pp. 699–712. ISSN: 1748-3395. DOI: `10.1038/nnano.2012.193`.

[275] W. Jaegermann and D. Schmeisser. "Reactivity of layer type transition metal chalcogenides towards oxidation." In: *Surface Science* 165.1 (Jan. 1986), pp. 143–160. ISSN: 0039-6028. DOI: `10.1016/0039-6028(86)90666-7`.

[276] T. Y. Ko, A. Jeong, W. Kim, J. Lee, Y. Kim, J. E. Lee, G. H. Ryu, K. Park, D. Kim, Z. Lee, M. H. Lee, C. Lee, and S. Ryu. "On-stack two-dimensional conversion of MoS_2 into MoO_3." In: *2D Materials* 4.1 (Nov. 2016), p. 014003. ISSN: 2053-1583. DOI: `10.1088/2053-1583/4/1/014003`.

[277] M. Camacho-López, L. Escobar-Alarcón, M. Picquart, R. Arroyo, G. Córdoba, and E. Haro-Poniatowski. "Micro-Raman study of the m-MoO_2 to α-MoO_3 transformation induced by cw-laser irradiation." In: *Optical Materials* 33.3 (Jan. 2011), pp. 480–484. ISSN: 09253467. DOI: `10.1016/j.optmat.2010.10.028`.

[278] A. M. Chippindale and A. K. Cheetham. "The Oxide Chemistry of Molybdenum." In: *Studies in Inorganic Chemistry.* Vol. 19. Elsevier, 1994, pp. 146–184. ISBN: 978-0-444-88198-4. DOI: `10.1016/B978-0-444-88198-4.50008-5`.

[279] R. F. Sebenik, A. R. Burkin, R. R. Dorfler, J. M. Laferty, G. Leichtfried, H. Meyer-Grünow, P. C. H. Mitchell, M. S. Vukasovich, D. A. Church, G. G. Van Riper, J. C. Gilliland, and S. A. Thielke. "Molybdenum and Molybdenum Compounds." In: *Ullmann's Encyclopedia of Industrial Chemistry*. John Wiley & Sons, Ltd, 2000. ISBN: 978-3-527-30673-2. DOI: `10.1002/14356007.a16_655`.

[280] N. Cuando-Espitia, J. Redenius, K. Mensink, M. Camacho-López, S. Camacho-López, and G. Aguilar. "Influence of oxygen pressure on the fs laser-induced oxidation of molybdenum thin films." In: *Optical Materials Express* 8.3 (Mar. 2018), pp. 581–596. ISSN: 2159-3930. DOI: `10.1364/OME.8.000581`.

[281] M. A. Camacho-López, E. Haro-Poniatowski, L. Lartundo-Rojas, J. Livage, and C. M. Julien. "Amorphous-crystalline transition studied in hydrated MoO_3." In: *Materials Science and Engineering B: Solid-State Materials for Advanced Technology* 135.2 (Nov. 2006), pp. 88–94. ISSN: 0921-5107. DOI: `10.1016/j.mseb.2006.08.041`.

[282] A. T. Nelson, E. S. Sooby, Y. .-. Kim, B. Cheng, and S. A. Maloy. "High temperature oxidation of molybdenum in water vapor environments." In: *Journal of Nuclear Materials* 448.1 (May 2014), pp. 441–447. ISSN: 0022-3115. DOI: `10.1016/j.jnucmat.2013.10.043`.

[283] D. Godfrey and E. C. Nelson. *Oxidation Characteristics of Molybdenum Disulfide and Effect of Such Oxidation on Its Role as a Solid-Film Lubricant.* Washington, May 1949.

[284] H. E. Sliney. "Decomposition kinetics of some solid lubricants determined by elevated temperature X-ray diffraction techniques." In: *Proc. US Air Force Aerosp. Fluids Lubr Conf* (1963), pp. 350–367.

[285] C. Pan, L. Jiang, J. Sun, Q. Wang, F. Wang, K. Wang, Y. Lu, Y. Wang, L. Qu, and T. Cui. "Ultrafast optical response and ablation mechanisms of molybdenum disulfide under intense femtosecond laser irradiation." In: *Light: Science & Applications* 9.11 (May 2020), p. 80. ISSN: 2047-7538. DOI: `10.1038/s41377-020-0318-8`.

[286] M. Rouhani, Y. L. Foo, J. Hobley, J. Pan, G. S. Subramanian, X. Yu, A. Rusydi, and S. Gorelik. "Photochromism of amorphous molybdenum oxide films with different initial Mo^{5+} relative concentrations." In: *Applied Surface Science* 273 (May 2013), pp. 150–158. ISSN: 01694332. DOI: `10.1016/j.apsusc.2013.01.218`.

[287] M. Rouhani, J. Hobley, G. S. Subramanian, I. Y. Phang, Y. L. Foo, and S. Gorelik. "The influence of initial stoichiometry on the mechanism of photochromism of molybdenum oxide amorphous films." In: *Solar Energy Materials and Solar Cells* 126 (July 2014), pp. 26–35. ISSN: 0927-0248. DOI: `10.1016/j.solmat.2014.03.033`.

[288] N. T. McDevitt, J. E. Bultman, and J. S. Zabinski. "Study of Amorphous MoS_2 Films Grown by Pulsed Laser Deposition." In: *Appl. Spectrosc.* 52.9 (Sept. 1998), pp. 1160–1164. DOI: `10.1366/0003702981945165`.

[289] M. Chase. *NIST-JANAF Thermochemical Tables, 4th Edition.* American Institute of Physics, Aug. 1998.

[290] M. P. Thorgersen, W. A. Lancaster, B. J. Vaccaro, F. L. Poole, A. M. Rocha, T. Mehlhorn, A. Pettenato, J. Ray, R. J. Waters, R. A. Melnyk, R. Chakraborty, T. C. Hazen, A. M. Deutschbauer, A. P. Arkin, and M. W. W. Adams. "Molybdenum Availability Is Key to Nitrate Removal in Contaminated Groundwater Environments." In: *Applied and Environmental Microbiology* 81.15 (Aug. 2015), pp. 4976–4983. DOI: `10.1128/AEM.00917-15`.

[291] L. Mandrile, I. Cagnasso, L. Berta, A. M. Giovannozzi, M. Petrozziello, F. Pellegrino, A. Asproudi, F. Durbiano, and A. M. Rossi. "Direct quantification of sulfur dioxide in wine by Surface Enhanced Raman Spectroscopy." In: *Food Chemistry* 326 (Oct. 2020), p. 127009. ISSN: 03088146. DOI: `10.1016/j.foodchem.2020.127009`.

[292] L. Rintoul, K. Crawford, H. F. Shurvell, and P. M. Fredericks. "Surface-enhanced Raman scattering of inorganic oxoanions." In: *Vibrational Spectroscopy* 15.2 (Dec. 1997), pp. 171–177. ISSN: 09242031. DOI: `10.1016/S0924-2031(97)00034-9`.

[293] J. García-Gutiérrez, G. Fuentes, E. Maria, Hernández-Terán, P. García, F. Murrieta-Guevara, and F. Jimenez-Cruz. "Ultra-deep oxidative desulfurization of diesel fuel by the Mo/Al_2O_3 -H_2O_2 system: The effect of system parameters on catalytic activity." In: (Jan. 2008). DOI: `j.apcata.2007.10.024`.

[294] T. Sakurai, H. Ohno, S. Horikawa, Y. Iizuka, T. Uchida, and T. Hondoh. "A Technique for Measuring Microparticles in Polar Ice Using Micro-Raman Spectroscopy." In: *International Journal of Spectroscopy* 2010 (Aug. 2010), pp. 1–7. ISSN: 1687-9449, 1687-9457. DOI: `10.1155/2010/384956`.

[295] S. A. Khan, R. W. Hughes, and P. A. Reynolds. "Raman spectroscopic determination of oxoanions in aqueous polysulfide electrolyte solutions." In: *Vibrational Spectroscopy* 56.2 (July 2011), pp. 241–244. ISSN: 09242031. DOI: `10.1016/j.vibspec.2011.03.001`.

List of author's publications

[296] W. Tillmann, N. F. Lopes Dias, D. Stangier, W. Maus-Friedrichs, R. Gustus, C. A. **Thomann**, H. Moldenhauer, and J. Debus. “Improved adhesion of a-C and a-C:H films with a CrC interlayer on 16MnCr5 by HiPIMS-pretreatment.” In: *Surface and Coatings Technology* 375 (2019), pp. 877–887. ISSN: 02578972. DOI: 10.1016/j.surfcoat.2019.07.076.

[297] W. Tillmann, A. Wittig, D. Stangier, C.-A. **Thomann**, H. Moldenhauer, J. Debus, D. Aurich, and A. Brümmer. “Investigation of the Tribofilm Formation of HiPIMS Sputtered MoSx Thin Films in Different Environments by Raman Scattering.” In: *Lubricants* 7.11 (2019). ISSN: 2075-4442. DOI: 10.3390/lubricants7110100.

[298] W. Tillmann, H. Ulitzka, N. F. Lopes Dias, D. Stangier, C. A. **Thomann**, H. Moldenhauer, and J. Debus. “Effects of acetylene flow rate and bias voltage on the structural and tribo-mechanical properties of sputtered a-C:H films.” In: *Thin Solid Films* 693 (2020), p. 137691. DOI: 10.1016/j.tsf.2019.137691.

[299] W. Tillmann, N. F. Lopes Dias, D. Stangier, A. Nienhaus, C. A. **Thomann**, A. Wittrock, H. Moldenhauer, and J. Debus. “Effect of the bias voltage on the structural and tribo-mechanical properties of Ag-containing amorphous carbon films.” In: *Diamond and Related Materials* 105 (2020), p. 107803. ISSN: 0925-9635. DOI: 10.1016/j.diamond.2020.107803.

[300] W. Tillmann, A. Wittig, H. Moldenhauer, C.-A. **Thomann**, J. Debus, D. Aurich, and A. Bruemmer. “Nitrogen doping of MoSx thin films sputtered by reactive High Power Impulse Magnetron Sputtering.” In: *Thin Solid Films* 713 (2020), p. 138267. ISSN: 0040-6090. DOI: 10.1016/j.tsf.2020.138267.

[301] W. Tillmann, A. Wittig, D. Stangier, H. Moldenhauer, C.-A. **Thomann**, J. Debus, D. Aurich, and A. Bruemmer. “Influence of the bias-voltage, the argon pressure and the heating power on the structure and the tribological properties of HiPIMS sputtered MoSx films.” In: *Surface and Coatings Technology* 385 (2020), p. 125358. ISSN: 0257-8972. DOI: 10.1016/j.surfcoat.2020.125358.

[302] D. Aurich, A. Wittig, D. Stangier, J. Debus, C.-A. **Thomann**, W. Tillmann, and A. Brümmer. “MoS2-Dünnschichten für unsynchronisierte, trockenlaufende Schraubenmaschinen.” In: *Vakuum in Forschung und Praxis* 33.4 (2021), pp. 40–44. DOI: 10.1002/vipr.202100763.

[303] W. Tillmann, A. Wittig, D. Stangier, H. Moldenhauer, C.-A. **Thomann**, J. Debus, D. Aurich, and A. Bruemmer. “Temperature-dependent tribological behavior of MoS x thin films synthesized by HiPIMS.” In: *Tribology International* 153 (2021), p. 106655. ISSN: 0301679X. DOI: 10.1016/j.triboint.2020.106655.

[304] W. Tillmann, D. Grisales, D. Stangier, C.-A. **Thomann**, J. Debus, A. Nienhaus, and D. Apel. "Residual stresses and tribomechanical behaviour of TiAlN and TiAlCN monolayer and multilayer coatings by DCMS and HiPIMS." In: *Surface and Coatings Technology* 406 (2021), p. 126664. ISSN: 0257-8972. DOI: `10.1016/j.surfcoat.2020.126664`.

[305] W. Tillmann, N. F. Lopes Dias, C. Franke, D. Kokalj, D. Stangier, C. A. **Thomann**, and J. Debus. "Mechanical properties and adhesion behavior of amorphous carbon films with bias voltage controlled TixCy interlayers on Ti6Al4V." In: *Diamond and Related Materials* 115 (2021), p. 108361. ISSN: 0925-9635. DOI: `10.1016/j.diamond.2021.108361`.

[306] W. Tillmann, N. F. Lopes Dias, D. Stangier, S. Matveev, C.-A. **Thomann**, and J. Debus. "Structure and tribo-mechanical properties of Si- and W-containing amorphous carbon based multilayers." In: *Applied Surface Science Advances* 5 (2021), p. 100105. ISSN: 2666-5239. DOI: `10.1016/j.apsadv.2021.100105`.

[307] W. Tillmann, N. F. Lopes Dias, D. Stangier, S. Matveev, C. A. **Thomann**, and J. Debus. "Design of Cu- and Ag-containing amorphous carbon multilayers with improved tribo-mechanical properties." In: *Materials Letters* 284 (2021), p. 128905. ISSN: 0167-577X. DOI: `10.1016/j.matlet.2020.128905`.

[308] W. Tillmann, N. F. Lopes Dias, C. Franke, D. Kokalj, D. Stangier, V. Filor, R. H. Mateus-Vargas, H. Oltmanns, M. Kietzmann, J. Meißner, M. Hein, S. Pramanik, K.-P. Hoyer, M. Schaper, A. Nienhaus, C. A. **Thomann**, and J. Debus. "Tribo-mechanical properties and biocompatibility of Ag-containing amorphous carbon films deposited onto Ti6Al4V." In: *Surface and Coatings Technology* 421 (2021), p. 127384. ISSN: 0257-8972. DOI: `10.1016/j.surfcoat.2021.127384`.

[309] W. Tillmann, A. Wittig, D. Stangier, C.-A. **Thomann**, J. Debus, D. Aurich, and A. Bruemmer. "HiPIMS of MoS2 – Current-voltage characteristics." In: *Materials Letters* 320 (2022), p. 132340. ISSN: 0167-577X. DOI: `10.1016/j.matlet.2022.132340`.

[310] W. Tillmann, N. F. Lopes Dias, D. Stangier, J. Berndt, S. Klemme, L. Kesper, U. Berges, C. Westphal, C. A. **Thomann**, and J. Debus. "Rare-earth modified amorphous carbon films: Effects of erbium and gadolinium on the structural evolution and mechanical properties." In: *Diamond and Related Materials* 123 (2022), p. 108898. ISSN: 0925-9635. DOI: `10.1016/j.diamond.2022.108898`.

[311] W. Tillmann, A. Wittig, N. F. L. Dias, D. Stangier, C. A. **Thomann**, H. Moldenhauer, and J. Debus. "Silicon- and tungsten-containing hydrogen-free and hydrogenated amorphous carbon films for friction-reducing applications." In: *Diamond and Related Materials* 123 (2022), p. 108866. ISSN: 0925-9635. DOI: `10.1016/j.diamond.2022.108866`.

[312] W. Tillmann, A. Wittig, D. Stangier, C.-A. **Thomann**, J. Debus, D. Aurich, and A. Brümmer. "Structure and Tribo-Mechanical Properties of MoSx:N:Mo Thin Films Synthesized by Reactive dcMS/HiPIMS." In: *Journal of Materials Engineering and Performance* 31.4 (2022), pp. 3200–3207. ISSN: 1059-9495, 1544-1024. DOI: `10.1007/s11665-021-06447-z`.

[313] C. A. **Thomann**, A. Wittrock, A. Wittig, N. F. Lopes Dias, D. Stangier, W. Tillmann, and J. Debus. “Tuning of solid-to-solid structural transitions in amorphous carbon films by optical pumping and chemical modification.” In: *APL Materials* 11.3 (2023), p. 031106. ISSN: 2166-532X. DOI: `10.1063/5.0138362`.

Acknowledgements and personal notes

My physics studies in Dortmund (2013-2018) were mostly focussed on fundamental research and this dissertation (2019-2023) is my humble (and presumably final) contribution thereto. When I started - having only the physicist's view - I deeply enjoyed widening my perspective by working tightly with my colleagues Filipe, Alexandra, Daniel, and Dominic from the mechanical engineering department. With our common language and different views, both sides contributed to and enriched one another's work.

If there was only one distinctive fact I learnt as PhD candidate, I'd be to first reach out to and gain understanding for other people's perspectives before contributing oneself.

Acknowledgements

People I get to know during my studies left a priceless impression on me and I hold them dear. During my time as student, I benefited from the scholarship *Deutschlandstipendium* by the alumni association *PeP et al. e. V.*, where I happily volunteered with smaller projects throughout my studies, and by the foundation *Artur- und Lieselotte Dumcke-Stiftung*. For their support and the arising opportunities, I feel very grateful.

I would like to give my heartfelt thanks to my friends and colleagues. If they had not devoted their time for me the way they did, I perhaps would not have experienced half the pleasure that I have - my time as PhD student would not have been the same at all. As early as 2014 at *PeP et al.*, I met Henning Moldenhauer, who became my PhD predecessor. He first introduced me to the workgroup under Dr. Jörg Debus and its research interests, and later supported me beyond my training period and through rough times. Measuring the data for this work, sometimes meant spending hours and hours in the lab while being isolated in the COVID-19 lockdown. That period would not have been bearable if it was not for my master student Adrian Wittrock, who became an esteemed PhD candidate himself.

For his understanding and forbearance, and foremost for ambitious and rewarding co-operation throughout, I feel thoroughly grateful to have had Dr. Jörg Debus as doctoral supervisor. There is no doubt that my advance - both professional and personal - was pushed forward majorly.

Thank you, sincerely

When we have achievements that are based on theirs,
we remember them.
As long as we live, they too will live;
for they are now a part of us as we remember them.